



MINISTÉRIO DA CIÊNCIA, TECNOLOGIA E INOVAÇÃO  
**INSTITUTO NACIONAL DE PESQUISAS ESPACIAIS**

sid.inpe.br/mtc-m21b/2016/04.18.14.16-TDI

## STUDY OF LOW-THRUST ORBITAL MANEUVERS IN THE PRESENCE OF EXTERNAL DISTURBING FORCES

Thais Carneiro Oliveira

Doctoral Thesis of the Graduate Course in Space Engineering and Technology at the Space Mechanic and Control Division, supervised by the advisors Drs. Antonio Fernando Bertachini de Almeida Prado and Evandro Marconi Rocco, approved in April 19, 2016.

URL of the original document:

<<http://urlib.net/8JMKD3MGP3W34P/3LH65H8>>

INPE

São José dos Campos

2016

**PUBLISHED BY:**

Instituto Nacional de Pesquisas Espaciais - INPE

Gabinete do Diretor (GB)

Serviço de Informação e Documentação (SID)

Caixa Postal 515 - CEP 12.245-970

São José dos Campos - SP - Brasil

Tel.:(012) 3208-6923/6921

Fax: (012) 3208-6919

E-mail: pubtc@inpe.br

**COMMISSION OF BOARD OF PUBLISHING AND PRESERVATION  
OF INPE INTELLECTUAL PRODUCTION (DE/DIR-544):****Chairperson:**

Maria do Carmo de Andrade Nono - Conselho de Pós-Graduação (CPG)

**Members:**

Dr. Plínio Carlos Alvalá - Centro de Ciência do Sistema Terrestre (CST)

Dr. André de Castro Milone - Coordenação de Ciências Espaciais e Atmosféricas (CEA)

Dra. Carina de Barros Melo - Coordenação de Laboratórios Associados (CTE)

Dr. Evandro Marconi Rocco - Coordenação de Engenharia e Tecnologia Espacial (ETE)

Dr. Hermann Johann Heinrich Kux - Coordenação de Observação da Terra (OBT)

Dr. Marley Cavalcante de Lima Moscati - Centro de Previsão de Tempo e Estudos Climáticos (CPT)

Silvia Castro Marcelino - Serviço de Informação e Documentação (SID) **DIGITAL**

**LIBRARY:**

Dr. Gerald Jean Francis Banon

Clayton Martins Pereira - Serviço de Informação e Documentação (SID)

**DOCUMENT REVIEW:**

Simone Angélica Del Duca Barbedo - Serviço de Informação e Documentação (SID)

Yolanda Ribeiro da Silva Souza - Serviço de Informação e Documentação (SID)

**ELECTRONIC EDITING:**

Marcelo de Castro Pazos - Serviço de Informação e Documentação (SID)

André Luis Dias Fernandes - Serviço de Informação e Documentação (SID)



MINISTÉRIO DA CIÊNCIA, TECNOLOGIA E INOVAÇÃO  
**INSTITUTO NACIONAL DE PESQUISAS ESPACIAIS**

sid.inpe.br/mtc-m21b/2016/04.18.14.16-TDI

## **STUDY OF LOW-THRUST ORBITAL MANEUVERS IN THE PRESENCE OF EXTERNAL DISTURBING FORCES**

Thais Carneiro Oliveira

Doctoral Thesis of the Graduate Course in Space Engineering and Technology at the Space Mechanic and Control Division, supervised by the advisors Drs. Antonio Fernando Bertachini de Almeida Prado and Evandro Marconi Rocco, approved in April 19, 2016.

URL of the original document:

<<http://urlib.net/8JMKD3MGP3W34P/3LH65H8>>

INPE

São José dos Campos

2016

Cataloging in Publication Data

---

Oliveira, Thais Carneiro.  
O14s Study of low-thrust orbital maneuvers in the presence of external disturbing forces / Thais Carneiro Oliveira. – São José dos Campos : INPE, 2016.  
xxvi + 196 p. ; (sid.inpe.br/mtc-m21b/2016/04.18.14.16-TDI)

Thesis (Doctorate in Space Engineering and Technology at the Space Mechanic and Control Division) – Instituto Nacional de Pesquisas Espaciais, São José dos Campos, 2016.

Guiding : Drs. Antonio Fernando Bertachini de Almeida Prado and Evandro Marconi Rocco.

1. External disturbing forces. 2. Eletrodynamic tethers. 3. Solar sails. 4. Station-keeping maneuvers. 5. Pertubation integral.  
I.Title.

CDU 629.7.017.3:52-42

---



Esta obra foi licenciada sob uma Licença [Creative Commons Atribuição-NãoComercial 3.0 Não Adaptada](https://creativecommons.org/licenses/by-nc/3.0/).

This work is licensed under a [Creative Commons Attribution-NonCommercial 3.0 Unported License](https://creativecommons.org/licenses/by-nc/3.0/).

Aluno (a): **Thais Carneiro Oliveira**

Título: "STUDY OF LOW-THRUST ORBITAL MANEUVERS IN THE PRESENCE OF EXTERNAL DISTURBING FORCES"

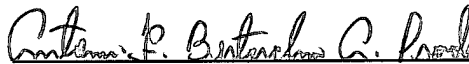
Aprovado (a) pela Banca Examinadora  
em cumprimento ao requisito exigido para  
obtenção do Título de **Doutor(a)** em  
**Engenharia e Tecnologia Espaciais/Mecânica  
Espacial e Controle**

Dr. Rodolpho Vilhena de Moraes



Presidente / UNIFESP / São José dos Campos - SP

Dr. Antonio Fernando Bertachini de Almeida Prado



Orientador(a) / INPE / SJC Campos - SP

Dr. Evandro Marconi Rocco



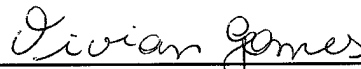
Orientador(a) / INPE / SJC Campos - SP

Dr. Othon Cabo Winter



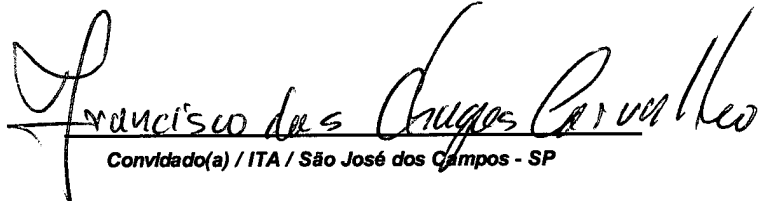
Membro da Banca / UNESP/GUARA / Guaratinguetá - SP

Dra. Vivian Martins Gomes



Convidado(a) / UNESP/GUARÁ / Guaratinguetá - SP

Dr. Francisco das Chagas Carvalho



Convidado(a) / ITA / São José dos Campos - SP

Este trabalho foi aprovado por:

( ) maioria simples

unanimidade

São José dos Campos, 19 de abril de 2016



“It is an old idea that the more pointedly and logically we formulate a thesis, the more irresistibly it cries out for its antithesis.”

*Hermann Hesse (1877-1962) - The Glass Bead Game (Romance published in 1943)*



## ACKNOWLEDGEMENTS

First of all, the author would like to thank her advisors Drs. Antonio Fernando Bertachini de Almeida Prado and Evandro Marconi Rocco for their patience, dedication, support and precious advices through the author's doctoral studies. The author would like also to thank Dr. Arun K. Misra, the student's advisor through the graduate research trainee program. The author feels privileged to have worked and collaborated with them and believes that, if she has seen further, it was by standing upon the shoulders of these giants.

The author would also like to express her gratitude for her professors of the graduate program at the space mechanics and control division at the National Institute for Space Research (INPE), who guided and tutored her for a solid knowledge of space engineering. Those professors provided more than the academic excellence that comes from books and she will always feel honored to have learned a lot from them. The author would also like to express her gratitude towards the secretary of the post-graduate course in space engineering and technology at the space mechanics and control division, Valdirene Moreira de Paula, who puts all her efforts and goodness to help the students.

The author's work was supported by the "Fundação de Amparo à Pesquisa do Estado de São Paulo (FAPESP)". The author gives a special thanks to FAPESP for the financial and institutional support, the appreciation of the Brazilian education, the research incentive and the ennoblement of the nation.

Finally, the author would like to express her gratitude towards her parents, José Fernando Azevedo de Oliveira and Elizabeth Cristina Carneiro, her grandmothers, Sônia Azevedo de Oliveira and Margarida Cristina Carneiro, and to her loyal and true friends for the love and support.



## ABSTRACT

One of the main objectives of this thesis is to study the magnitude of the disturbing forces received by a spacecraft for several orbits with the help of the method called Perturbation Integral. The Perturbation Integral can be the integral of the magnitude of the acceleration caused by the external disturbing forces that act on a spacecraft for one orbital period or the magnitude of the integral of the acceleration of the external disturbing forces for one orbital period. The study includes the behavior of different external disturbing forces for different orbits by varying the Keplerian elements. In this context, it is possible to find orbits that are less perturbed and create maps for various orbits that illustrate the magnitude of the perturbation behavior and the fuel consumption required to keep a spacecraft in a Keplerian orbit and the fuel consumptions required to perform orbital maneuvers after a period of time. Another main objective is to study low-thrust orbital maneuvers, known as station-keeping maneuvers, and to reduce the fuel consumption that may be used in the thrusters. The orbit of a spacecraft is deviated from the Keplerian orbit due to external perturbations. Propulsions systems can be used to correct the orbit with fuel expenditure. One of the proposals of this thesis is the use of electrodynamic tethers and solar sails to reduce the effects of the external perturbations to reduce the fuel consumption in station-keeping maneuvers. This study also includes the possibility to use the electrodynamic tethers as a drag force to optimize the time of the orbital decay of a spacecraft. The validation of the tether or solar sail usage is performed in two different environments. The first one is an orbital integrator that integrates the orbit of the spacecraft including the external disturbing forces. The second environment, used only for the solar sail validation, is an orbit simulator that can include a more realistic environment, like failures on the actuators, on the sensors, external disturbing forces non-predicted, etc. This last simulator is known as 'STRS' or "Spacecraft Trajectory Simulator".

Keywords: External Disturbing Forces. Electrodynamic Tethers. Solar Sails. Station-Keeping Maneuvers. Optimization. Perturbation Integral. STRS Simulator.



# **ESTUDO DE MANOBRAS ORBITAIS COM BAIXO EMPUXO NA PRESENÇA DE FORÇAS PERTURBADORAS**

## **RESUMO**

Um dos principais objetivos desta tese é estudar a magnitude das forças perturbadoras por várias órbitas com a ajuda de um método chamado Integral da Perturbação. A Integral da Perturbação pode ser a integral da magnitude da aceleração causada pelas forças perturbadoras externas que atuam sobre um veículo espacial por um período orbital ou a magnitude da integral da aceleração das forças perturbadoras externas por um período orbital. O estudo inclui o comportamento de diferentes perturbações externas para diferentes órbitas variando os elementos Keplerianos. Neste contexto, é possível encontrar órbitas que são menos perturbadas e criar mapas para diversas órbitas que ilustram o comportamento da magnitude da perturbação, o consumo de combustível necessário para manter um veículo espacial em uma órbita Kepleriana e o consumo de combustível para realizar manobras orbitais após um período de tempo. Outro objetivo principal é estudar manobras orbitais de baixo impulso, conhecidas como manobras de manutenção orbital, e diminuir o consumo de combustível utilizado nos propulsores. A órbita de um veículo espacial é desviada da órbita Kepleriana devido às perturbações externas. Sistemas de propulsão podem ser usados a fim de corrigir os desvios consumindo combustível. A proposta da tese abrange o uso de cabos eletrodinâmicos e de velas solares a fim de reduzir os efeitos das perturbações externas e diminuir o consumo de combustível em manobras de manutenção. Este estudo também inclui a possibilidade de utilizar os cabos eletrodinâmicos como uma força de arrasto de modo a otimizar o tempo de decaimento orbital de um veículo espacial. A validação do cabo eletrodinâmico ou da vela solar é realizado em dois ambientes distintos. O primeiro é um integrador orbital que integra a órbita do veículo espacial, incluindo as perturbações externas. O segundo ambiente, usado somente para a validação de vela solar, é um simulador de órbita que apresenta um ambiente mais realista capaz de considerar falhas nos atuadores, nos sensores, forças perturbadoras externas não previstas, etc. Este último simulador é conhecido como 'STRS 'ou "Simulador de Trajetória de um Satélite".

Palavras-chave: Forças Perturbadoras Externas. Cabos Eletrodinâmicos. Velas Solares. Manobra de Manutenção Orbital. Otimização. Integral de Perturbação. STRS Simulador.



## LIST OF THE FIGURES

	<u>Pág.</u>
Figure 2.1 – Architecture of PID controller design STRS with the solar sail use as a non-fuel consumer thruster.....	34
Figure 2.2 – The light bean interaction of the solar radiation pressure with a smooth surface with the incident light bean, the reflection light bean and the force produced by the solar radiation pressure. ....	37
Figure 2.3 – Illustration of the umbra, penumbra and illuminated areas.....	38
Figure 2.4 – The representation of the spacecraft with a rectangular shape with one of its face pointed towards the radial direction and the solar sail representation. ....	39
Figure 2.5 – Exemplification of the zonal terms.....	41
Figure 2.6 – Exemplification of the tesseral terms.....	41
Figure 2.7 – Exemplification of the sectorial terms.....	42
Figure 2.8 – Representation of the coordinates systems OXYZ and O'X'Y'Z' with respect to the centre of the Earth and the center of mass of the spacecraft or the system. ....	52
Figure 2.9 – Definition of the pitch and roll angles at the orbital coordinate system O'X'Y'Z'. ....	52
Figure 2.10 – The representation of the coordinates systems OXYZ and O`er, eθ eφ with respect to the centre of the Earth and the center of mass of the spacecraft or the system. ....	53
Figure 2.11 – Magnetic field geometry. ....	55
Figure 2.12 – Design of the insulated tether.....	58
Figure 2.13 – Representation of the electrical circuit for the insulated tether. ..	58
Figure 2.14 – Tether motion through the magnetic field of the Earth.....	59
Figure 2.15 – The design of the bare tether. ....	61
Figure 3.1 – PI of the atmospheric drag as a function of the semi-major axis from 6700 to 7000km. ....	66

Figure 3.2 – The semi-major axis time evolution in the presence of the atmospheric drag.....	70
Figure 3.3 – PI of the atmospheric drag with $\pm 5\%$ of error of the density as a function of the semi-major axis from 6700 to 6800 km. ....	71
Figure 3.4 – PI of the atmospheric drag with $\pm 10\%$ of error of the density as a function of the semi-major axis from 6700 to 6800 km. ....	72
Figure 3.5 – PI of the several disturbing forces as a function of the semi-major axis from 6700 to 7000km. ....	73
Figure 3.6 – PI of $J_2$ disturbing force as a function of the semi-major axis from 6700 to 7000 km.....	75
Figure 3.7 – $PI_{MAG}$ of several disturbing forces as a function of the semi-major axis from 6700 to 7000 km. ....	76
Figure 3.8 – PI of $J_n$ 's and $C_{22}$ disturbing forces as a function of the semi-major axis from 6700 to 7000 km. ....	78
Figure 3.9 – $PI_{MAG}$ of the $J_n$ 's and $C_{22}$ disturbing forces as a function of the semi-major axis from 6700 to 7000 km. ....	79
Figure 3.10 – $PI_{MAG}$ of $J_2$ and $J_4$ disturbing forces as a function of the semi-major axis from 6700 to 7000 km. ....	80
Figure 3.11 – PI of $J_2$ and $C_{22}$ disturbing force as a function of the semi-major axis from 11000 to 27000 km. ....	81
Figure 3.12 – PI of several disturbing forces except $J_n$ and $C_{22}$ as a function of the semi-major axis from 11000 to 27000 km.....	82
Figure 3.13 – PI of several disturbing forces as a function of the semi-major axis from 32000 to 52000 km. ....	84
Figure 3.14 – PI of several disturbing forces as a function of the eccentricity from 0 to 0.3636. ....	86
Figure 3.15 – PI of the solar radiation pressure as a function of the eccentricity from 0 to 0.3636. ....	87
Figure 3.16 – PI value of $J_2$ and $C_{22}$ as a function of the eccentricity from 0 to 0.3636. ....	88

Figure 3.17 – PI of the atmospheric drag as a function of the eccentricity from 0 to 0.3636. ....	89
Figure 3.18 – PI of several disturbing forces as a function of the inclination change from 0 to $\pi$ rad. ....	90
Figure 3.19 – PI value of $J_2$ as a function of the inclination change from 0 to $\pi$ rad. ....	91
Figure 3.20 –The study of the Ace acceleration as a function of the co-latitude from 0 to $\pi/2$ rad. ....	93
Figure 3.21 –The study of the mean magnitude of Ace as a function of the co-latitude from 0 to $\pi/2$ rad. ....	94
Figure 3.22 – PI of $J_2$ as a function of the inclination from 0 to $\pi$ rad. ....	95
Figure 3.23 – PI of several disturbing forces as a function of the inclination from 0 to $\pi$ rad. ....	96
Figure 3.24 – Third-body and the reference system Oijk. ....	98
Figure 3.25 – PI of the solar radiation pressure as a function of the inclination from 0 to $\pi$ rad. ....	99
Figure 3.25b – Acceleration of the solar sail and the disturbing forces for a system with 100 kg and maximum area of $500\text{m}^2$ . ....	102
Figure 3.26 – Acceleration of the solar sail and the disturbing forces for a system with 50 kg and maximum area of $500\text{m}^2$ . ....	103
Figure 3.27 – Area of the solar sail for one orbit period. ....	104
Figure 3.28 – The angle of incidence of the solar sail for one orbit period. ....	105
Figure 3.29 – Versor for the X axis of the solar sail and of the disturbing forces for one orbit period. ....	106
Figure 3.30 – Normal of the solar sail with reflectivity of 0.9 and the versor of the disturbing forces for X axis. ....	107
Figure 3.31 – Normal of the solar sail with reflectivity of 0.9 and the versor of the disturbing forces for Y axis. ....	108
Figure 3.32 – Normal of the solar sail with reflectivity of 0.7 and the versor of the disturbing forces for X axis. ....	109

Figure 3.33 – Normal of the solar sail with reflectivity of 0.7 and the versor of the disturbing forces for Y axis. ....	110
Figure 3.34 – Acceleration of the solar sail and the disturbing forces for a system with 50 kg and fixed area of 400m <sup>2</sup> . ....	111
Figure 3.35 – Acceleration of the solar sail and the disturbing forces with the solar sail for a system with 50 kg and fixed area of 400m <sup>2</sup> . ....	112
Figure 3.36 – Acceleration of the solar sail and of the disturbing forces with a semi-major axis of 10.000 km. ....	114
Figure 3.37 – Parameter for the luminosity of the orbital path. ....	115
Figure 3.38 – Acceleration of the solar sail and of the disturbing forces for a geostationary orbit. ....	116
Figure 3.39 – Angle of Incidence of the solar sail for the geostationary orbit. ....	117
Figure 3.40 – PI of the disturbing forces with the solar sail use as a function of the semi-major axis from 3500 to 55000 km. ....	118
Figure 3.41 – PI of the disturbing forces and the solar sail as a function of the eccentricity from 0 to 0.3. ....	119
Figure 3.42 – PI of the disturbing forces and the solar sail as a function of the inclination from 0 to $\pi$ rad. ....	120
Figure 3.43 – $\Delta V$ value for the solar sail, the perturbations and the thrust for one orbital period with a variable area for the solar sail. ....	122
Figure 3.44 – The fuel consumption evolution for one orbital period with a variable area for the solar sail. ....	123
Figure 3.45 – The angle of incidence for one orbital period with a variable area for the solar sail. ....	124
Figure 3.46 – The area of the solar sail evolution for one orbital period with a variable area for the solar sail. ....	125
Figure 3.47 – The magnitude of the thrust of the propulsion system for one orbital period with a variable area for the solar sail. ....	126
Figure 3.48 – The velocity increment of the perturbations in the OXYZ reference system evolution for one orbital period with a variable area for the solar sail. ....	127

Figure 3.49 – The versors of the solar sail and the perturbations in the X axis for one orbital period.....	128
Figure 3.50 – The versors of the solar sail and the perturbations in the Y axis for one orbital period.....	128
Figure 3.51 – The versors of the solar sail and the perturbations in the Z axis for one orbital period.....	129
Figure 3.52 – $\Delta V$ values for the solar sail, the perturbations and the thrust for one orbital period with a fixed area for the solar sail. ....	130
Figure 3.53 – The fuel consumption evolution for one orbital period with a fixed area for the solar sail. ....	131
Figure 3.54 – The average EMF for insulated and bare tethers for tether lengths from 5 to 20 km. ....	134
Figure 3.55 – The average current for insulated tether for lengths from 5 to 20 km. ....	135
Figure 3.56 – The average current for bare tether for lengths from 5 to 20 km. ....	136
Figure 3.57 – The acceleration on the Y' axis for insulated tether from lengths from 5 to 20 km. ....	137
Figure 3.58 – The acceleration on the Y' axis for bare tether from lengths from 5 to 20 km.....	138
Figure 3.59 – The acceleration on the Z' axis for insulated tether from lengths from 5 to 20 km. ....	139
Figure 3.60 – The acceleration on the Z' axis for bare tether from lengths from 5 to 20 km.....	140
Figure 3.61 – The average EMF for insulated and bare tethers from 6500 to 9500 km of semi-major axis.....	141
Figure 3.62 – The average current for insulated tether from 6500 to 9500 km of semi-major axis. ....	142
Figure 3.63 – The average current for bare tether from 6500 to 9500 km of semi-major axis. ....	143

Figure 3.64 – The acceleration on the Y' axis for insulated tether from 6500 to 9500 km of semi-major axis.....	144
Figure 3.65 – The acceleration on the Y' axis for bare tether from 6500 to 9500 km of semi-major axis. ....	145
Figure 3.66 – The acceleration on the Z' axis for insulated tether from 6500 to 9500 km of semi-major axis.....	146
Figure 3.67 – The acceleration on the Z' axis for bare tether from 6500 to 9500 km of semi-major axis. ....	147
Figure 3.68 – The average EMF for insulated and bare tethers from 0 to $\pi$ rad of inclination. ....	149
Figure 3.69 – The average current for insulated tether from 0 to $\pi$ rad of inclination. ....	150
Figure 3.70 – The average current for bare tether from 0 to $\pi$ rad of inclination. ....	151
Figure 3.71 – The acceleration on the Y' axis for insulated tether from 0 to $\pi$ rad of inclination. ....	152
Figure 3.72 – The acceleration on the Y' axis for bare tether from 0 to $\pi$ rad of inclination. ....	153
Figure 3.73 – The acceleration on the Z' axis for insulated tether from 0 to $\pi$ rad of inclination. ....	154
Figure 3.74 – The acceleration on the Z' axis for bare tether from 0 to $\pi$ rad of inclination. ....	155
Figure 3.75 – The PI of the disturbing forces for different eccentric orbits as a function of the semi-major axis from 6500 to 7900 km. ....	158
Figure 3.76 – The PI of the disturbing forces for different eccentric orbits as a function of the altitude from 150 to 1500 km.....	159
Figure 3.77 – The decay of the tethered system over the days from zero to 18 days.....	160
Figure 3.78 – The acceleration of the tether and the disturbing forces for one orbital period.....	162

Figure 3.79 – The ionospheric density, umbra and illuminated areas for one orbital period.....	163
Figure 3.80 – The pitch and roll angles for one orbital period.....	164
Figure 3.81 – The power and current of the tether for one orbital period. ....	165
Figure 3.82 – Acceleration of the tether and all the perturbations on the X axis for one orbital period. ....	168
Figure 3.83 – Acceleration of the tether and all the perturbations on the Y axis for one orbital period. ....	169
Figure 3.84 – Pitch angle for one orbital period.....	170
Figure 3.85 – PI of several disturbing forces and the tether as a function of the semi-major axis from 6678 to 6978 km. ....	172
Figure 3.86 – Current and power of the tether as a function of the semi-major axis from 6678 to 6978 km. ....	173
Figure 3.87 - PI for several disturbing forces as a function of the semi-major axis from 6978 to 7278 km. ....	174
Figure 3.88 – PI for several disturbing forces and the tether as a function of the semi-major axis from 6978 to 7278 km. ....	175
Figure 3.89 – PI for the disturbing forces and tether as a function of the inclination from 0 to 90 degrees. ....	176
Figure 3.90 – Pitch and roll angles for one orbital period. ....	177
Figure 3.91 – Current and power of the tether as a function of the inclination from 0 to 90 degrees. ....	178
Figure 3.92 – Altitude decay in days due to the disturbing forces with and without the tether control. ....	179



## LIST OF THE TABLES

	<b><u>Pág.</u></b>
Table 2.1 – Standard Atmosphere Derived from 1976 and 1962 U. S Standard Atmospheres. ....	48
Table 3.1 – Initial Parameters of the Spacecraft for the Perturbation Integrals studies. ....	65
Table 3.2 – Initial Parameters of the Orbit for the PI and PI <sub>MAG</sub> studies. ....	65
Table 3.3 – Initial Parameters of the Orbit for the PI study. ....	85
Table 3.4 – Initial Parameters of the Orbit for the PI study. ....	89
Table 3.5 – Initial parameters of the orbit solar sail study. ....	101
Table 3.6 – Initial Parameters of the Spacecraft for the solar sail study. ....	101
Table 3.7 – PI values for the solar sail study. ....	112
Table 3.8 – Initial Parameters of the Spacecraft for the STRS study. ....	121
Table 3.9 – Initial Parameters of the Orbit for the STRS study. ....	122
Table 3.10 – Parameters of the spacecraft system ....	131
Table 3.11 – Parameters of the Tether Cable ....	131
Table 3.12 – Electron Density Profile ( $e^-/m^3$ ). ....	132
Table 3.13 – Initial Physical and Orbital Parameters. ....	132
Table 3.14 – Time of decay for different eccentricities. ....	157
Table 3.15 – Time of decay for different eccentricities. ....	159
Table 3.16 – PI values based on Equation 2.1. ....	166
Table 3.17 – PI value based on Equation 2.1. ....	170



## LIST OF ACROBYMS AND ABBREVIATIONS

AU	Astronomical Unit
EDT	Electrodynamic Tether
EMF	Electromotive Force
GEO	Geostationary Orbits
GPS	Global Positioning System
HEO	High Earth Orbits
ISS	International Space Station
LEO	Low Earth Orbits
MEO	Medium Earth Orbits
STEPS	Station Tethered Express Payload System
STRS	Spacecraft Trajectory Simulator
TSS	Tethered Satellite System



## SUMMARY

	<b><u>Pág.</u></b>
1 INTRODUCTION .....	1
1.1. Objectives .....	1
1.2. Perturbation Integral .....	2
1.3. Solar Sails.....	8
1.4. Tethered Systems.....	14
1.4.1. Eletrodynamic Tether .....	17
1.5. Spacecraft Trajectory Simulator.....	20
1.6. Orbital Motion And Disturbing Forces .....	24
2 MATHEMATICAL MODELS.....	27
2.1. Perturbation Integrals.....	27
2.2. The Spacecraft Trajectory Simulator.....	33
2.3. The Solar Radiation Pressure .....	35
2.3.1. The Solar Sail.....	38
2.4. The Spherical Harmonics $J_n$ And $C_{22}$ .....	40
2.5. The Third-Body Perturbation.....	44
2.6. The Atmospheric Drag .....	45
2.7. The Electrodynamic Tether .....	51
2.7.1. The Magnetic Field Of The Earth .....	54
2.7.2. The Insulated Tether .....	57
2.7.3. The Bare Tether .....	61
3 RESULTS .....	65
3.1. Perturbation Integrals.....	65
3.1.1. The Semi-Major Axis Variation .....	65
3.1.2. The Eccentricity Variation.....	85
3.1.3. The Inclination Variation .....	89
3.2. The Solar Sail Study .....	100
3.3. The Electromagnetic Tether Study.....	131
3.3.1. The Tether Length Study.....	133

3.3.2.	The Tether Semi-Major Axis Study.....	141
3.3.3.	The Tether Inclination Study.....	148
3.3.4.	The De-Orbiter EDT Effect In Orbital Motion And Perturbation Integrals .....	156
3.4.	The Electrodynamic Tether Use For Reducing The Disturbing Forces ..	161
3.4.1.	The Perturbation Integrals Results For The EDT .....	171
3.4.2.	The Orbital Propagator Results.....	178
4	CONCLUSION .....	181
	REFERENCES.....	183

# 1 INTRODUCTION

This introduction chapter includes the main topics of the thesis, like electrodynamic tethers, solar sails, the Perturbation Integral method and the Spacecraft Trajectory Simulator (STRS) software. The objectives of the thesis are also included in this chapter.

The overview containing all the important points about the introduction is given as follows:

- a) objectives;
- b) preliminaries remarks related to the thesis topics;
- c) previous, current and future missions related to solar sails and electrodynamic tethers;
- d) the potential space applications of the solar sails, the electrodynamic tethers, the Perturbations Integral method and the STRS software;
- e) literature review.

## 1.1. Objectives

This thesis involves several different topics that vary from electrodynamic tethers to solar sails. It also contains different tools that are used to achieve and analyze the results of low-thrust maneuvers in the presence of external disturbing forces.

The principal tools used in this work are the Perturbation Integral and the STRS. The Perturbation Integral is focused on the analysis of the variation of velocity that the disturbing forces can deliver to the system and the efficiency of the low-thrusters to reduce or overcome the effects of these disturbing forces.

The STRS simulator main focus in this thesis is to study some maneuvers in a more realistic approach. The low-thrusters used in this simulator are the solar

sail and electric thruster. The low-thrusters are combined together to reduce the effects of the disturbing forces at every step of the time and to optimize the fuel consumption. The greatest advantage of using this software is the possibility of computing errors, failures, delays and so forth in the actuators, sensors, etc. The results can be more realistic and reliable with the STRS ambience.

The maneuvers proposed are strictly related to orbital maintenance of the spacecraft in its nominal orbit. The disturbing forces included in this work shift away the spacecraft from its nominal position.

The low-thrusters proposed in this work to maneuver the spacecraft are based on two non-fuel consumer thrusters: the electrodynamic tether (EDT) and the solar sail. Others thrusters are also considered in this work to maneuver the spacecraft, if no free-fuel thruster is used or if the solar sail or the EDT cannot fully reduce or compensate the effects of the disturbing forces.

## 1.2. Perturbation Integral

The Perturbation Integral is the magnitude of the velocity deviation caused by the disturbing forces that act on a spacecraft for one orbital period of a Keplerian orbit. The Perturbation Integral method is subdivided in two integrals. The first one, abbreviated by PI, is the integral for one orbital period of the magnitude of the disturbing accelerations. The second one, abbreviated by  $PI_{MAG}$ , is the magnitude of the integral for one orbital period of the disturbing accelerations.

The concept of the Perturbation Integral, the PI to be more specifically, was first introduced by [Prado \(2013\)](#).

The PI can also be used to evaluate the efficiency of the EDT or the solar sails as they can cause a velocity variation of the spacecraft's Keplerian orbit. If the EDT or the solar sail is used to reduce or compensate the effects of the disturbing forces by applying a force in the opposite direction of the disturbing

forces, then the PI of the low-thrust propulsion system is the magnitude of the velocity reduction that needs to be delivered to the spacecraft. Otherwise, if they are used as a drag in the direction of the orbital velocity, then the PI provides the magnitude of the velocity increase that these non-fuel-consumption thrusters can deliver to the system. The PI of the disturbing forces itself represents the total variation of velocity that the thrust must apply in one orbital period to keep the spacecraft in a Keplerian orbit.

At a first glance, the PI is an approximation of the reality. Indeed, the cost to keep a spacecraft in a Keplerian orbit all the time can be highly fuel-demanding. It means that missions with this goal are not very popular, but situations like that may occur in specific cases.

The same occurs to the  $PI_{MAG}$ . The  $PI_{MAG}$  assumes that the deviations caused by the disturbing force can be negligible for one orbital period. The  $PI_{MAG}$ , differently from the PI, includes the compensations due to the variations in the direction of the forces for one orbital period.

Even if the Perturbation Integral is an approximated method, this tool is proven in this thesis to be a powerful tool that can:

- a) measure the magnitude of the velocity deviation coming from the disturbing forces added together or individually;
- b) create maps of the magnitude of the velocity deviation of the system caused by the disturbing forces for different orbits, as a function of the Keplerian elements of the orbit;
- c) measure the magnitude reduction of the velocity deviation that the disturbing forces could deliver to the Keplerian orbit if EDT or solar sail is used to compensate the effects of the disturbing forces. The magnitude increase can also be analyzed if those fuel-free low-thrusters are used to increase the effects of the disturbing forces;

- d) be used to estimate the cost of station-keeping maneuvers based on the characteristics of the orbit and on the set of perturbations considered, with no dependence on the type of engine used as a thruster;
- e) evaluate the pattern of the disturbing forces as a function of the Keplerian elements and find orbits with minimal values of Perturbation Integrals. Minimal values for the Perturbation Integrals mean the best potential orbits for the low-cost orbital maintenance.

All of these features of the Perturbation Integral are proven and explained in the results chapter of this thesis. The mathematical model chapter provides the mathematical formulation of the Perturbation Integral method.

Besides [Prado \(2013\)](#), there are many references that used the PI as an important mechanism to achieve several purposes, as described below.

[Oliveira and Prado \(2013\)](#) provide an estimative of the station-keeping maneuver cost to maintain a spacecraft in its nominal position. The orbits studied are close to the geostationary orbits (GEO). The method used is the PI. The result of this integral is the velocity variation that the spacecraft needs to perform all the time to compensate the deviations caused by the perturbing forces. The perturbing forces considered are the lunisolar perturbation and the  $J_2$  effect of the gravitational field of the Earth. This paper covers the study of the variation of the nominal semi-major axis, the eccentricity and the inclination.

[Oliveira et al. \(2013\)](#) propose a procedure to map orbits with respect to the perturbation forces with the goal of finding orbits that may use the solar radiation pressure for station-keeping maneuvers. The calculations are made based on the PI. The paper shows different types of integrals of the perturbing forces over the time. Solar radiation pressure,  $J_2$  to  $J_4$  zonal harmonics terms of the geopotential, and lunisolar perturbations are considered. The results provide the magnitude of each perturbing forces, so it is possible to see if the radiation pressure can be used to control the effect of other forces, or at least to help in

reducing the cost of the control. This paper is the first one written by the authors that introduces the idea of using the solar radiation pressure to reduce the effects of the disturbing forces and to analyze its efficiency with the PI values.

[Oliveira and Prado \(2014a\)](#) search for orbits that have great potentials to require low-fuel consumption for station-keeping maneuvers for constellations of spacecrafts. The method used to study the problem is based on the PI as well. For this search, it is analyzed the integral of orbits with different values of the Keplerian elements in order to find the best ones with respect to the PI values. The perturbations considered are the ones caused by the third body, which includes the Sun and the Moon, and the  $J_2$  term of the geopotential. The Global Positioning System (GPS) and the Molniya constellations are used as examples for those calculations.

Moreover, [Prado \(2014\)](#) maps orbits with the PI around the Asteroid 2001SN<sub>263</sub>. This asteroid is a triple system, which center of mass is in an elliptic orbit around the Sun. The perturbations considered in the present model are the ones due to the oblateness of the central body, the gravity field of the two satellite bodies (Beta and Gamma), the Sun, the Moon, the asteroids Vesta, Pallas and Ceres and all the planets of the Solar System. This mapping is important because it shows the relative importance of each force for a given orbit of the spacecraft, helping the mission planning team to make a decision about which forces need to be included in the model for a given accuracy and nominal orbit.

[Sanchez et al. \(2014a\)](#) provide a useful new method to determine minimum and maximum range of values for the degree and order of the geopotential coefficients required for simulations of spacecraft's orbits around the Earth. The method is based on the PI. There are some constraints in the degree and order of the terms which are present in the geopotential formula, saving computational efforts compared to the integration of the full model. In this paper, it is studied quasi-circular orbits and it is presented several simulations showing

the bounds for the maximum degree and order that should be used in the geopotential for different situations.

[Carvalho et al. \(2014\)](#) propose less perturbed circular orbits around Europa. This search is made based on the PI. The perturbing forces considered are the third-body perturbation that comes from Jupiter and the  $J_2$ ,  $J_3$ , and  $C_{22}$  Jupiter's non-sphericity and terms of the gravitational potential of Europa. Several numerical studies are performed and the results show the locations of the less perturbed orbits. The results show that it is possible to find near-circular frozen orbits with smaller amplitudes of variations of the orbital elements.

[Sanchez et al. \(2014b\)](#) study gravitational captures of a spacecraft by the Pluto-Charon system, searching configurations where the loss of energy of the spacecraft to Pluto is maximized in a time interval that keeps the viability of the mission. The method use the three-dimensional restricted three-body problem and takes into account the perturbation of the Pluto and Charon gravitational potentials ( $J_2$  and  $C_{22}$ ), the perturbation of the Sun and the gravity of the minor satellites of Pluto (Styx, Nix, Kerberos, and Hydra). The initial conditions which lead to captures of probes that remain in orbit around Pluto for 10 years or more is considered as stable regions. The PI is used to calculate the total velocity variation received by the spacecraft, in the stable regions, due to the Sun, Charon, the small satellites of Pluto and the  $J_2$  and  $C_{22}$  terms of the potential of Pluto and Charon.

[Oliveira et al. \(2014\)](#) aim to map orbits based on the PI. Particularly, the effects of the inclination and the eccentricity of the orbit in those mappings are studied. The perturbation forces considered here are the solar radiation pressure, the lunisolar perturbation, the zonal harmonics  $J_2$  to  $J_4$  and the atmospheric drag. The possibility of using a solar sail to reduce the effects of the other perturbations acting on the satellite is considered under this approach. The problem is stated to find the necessary and sufficient conditions to use the solar

sail as a low-thrust propulsion to reduce the effects of the disturbing forces. This study is a continuation of [Oliveira et al. \(2013a\)](#).

[Oliveira and Prado \(2014b\)](#) find the necessary and the sufficient conditions to use solar sails in order to compensate or to reduce the perturbation effects due to external forces received by a satellite. This study considers a satellite with the following disturbing forces: the solar radiation pressure, the zonal harmonic perturbation  $J_2$  to  $J_4$  and the third body perturbation due to the Sun and the Moon. The necessary and the sufficient conditions are, for a given orbit, the area and the attitude that the solar sail must have in order to compensate or to reduce the effects of the other perturbation forces. In this way, the cost of the station keeping maneuver can be reduced in terms of the fuel consumption, since there is less perturbation acting on the satellite. This last study includes also the attitude restrictions the solar sail can have.

[Oliveira and Prado \(2014c\)](#) study potential orbits for missions to the asteroid 2001SN<sub>263</sub>, a triple system. Currently, there are several institutions in Brazil studying a mission to this asteroid. This mission is called ASTER and it is planned for a one year duration in the asteroid system. The goal of this paper is to study the forces acting in that system, and then verify the possibility of using the solar radiation pressure to make station-keeping maneuvers. The dynamical model considers the gravitational forces of the three bodies of the system, the  $J_2$  perturbation of the main body and the solar radiation pressure. For a given orbit, the optimal direction of the solar sail attitude along the orbit is found, as well as the size that the solar sail must have in order to compensate the disturbing forces. Optimal solutions are found by allowing variations of the size of the solar sail. Also, a sub-optimal analysis is considered by fixing the area of the solar sail, but maintaining the optimal solar sail attitude. The necessity of a propulsion system to complement the maneuvers is considered.

[Venditti and Prado \(2015\)](#) study orbital dynamics around irregular shaped cube body. The cube shape is a promising study, since the shape of an asteroid is

currently modeled by the sum of several known geometric shapes, and the cube is one of the most basic ones. The PI is used to map orbits and find less perturbed ones, which are good candidates for station-keeping maneuvers. Points in the orbit that minimizes the perturbations are found and they can be used for constellations of nanosatellites.

[Lara \(2016\)](#) studies the  $PI_{MAG}$  for the gravitational perturbation due to the zonal harmonic  $J_2$  using an analytical approach. The study also includes numerical simulations and first order approximations of the algebraic results.

### 1.3. Solar Sails

Johannes Kepler once wrote to his friend Galileo Galilei a letter which contained the following quote: “[...] Let us create vessels and sails adjusted to the heavenly ether, and there will be plenty of people unafraid of the empty wastes [...]” ([KOESTLER, 1986](#)).

The idea proposed by Kepler can be seen as a reality of today. The vessels can be understood as the spacecrafts. The sails can be understood as the chemical thrusters, the electrical thrusters, or even the tether propulsion or solar sails. The humankind is also unafraid of the empty wastes as there are humans orbiting the Earth, visiting the Moon and planning Mars colonization.

Kepler was right in proposing sails through the space, since solar sails missions has already been proved to work using propulsion systems with no fuel consumption. Nevertheless, he was wrong about the ether, but this is another great story that runs out of the scope of this work.

Solar sails are used as a propulsion system by the interaction of the solar photons with the surface of the solar sail. This interaction is known as solar radiation pressure, a kind of long-term external disturbing force that acts on the surface of any spacecraft.

Solar sails use the solar radiation pressure as a free-fuel propulsion system. The solar radiation force occurs when a light beam falls upon a surface and causes a loss of energy resulting in a force acting on the surface of the spacecraft. This transference of energy may result on a torque, if the center of the mass of the spacecraft is not the center of pressure. The solar radiation pressure can be used in solar sails for attitude control, orbital maintenance or in interplanetary missions.

Optimized solar sails must have a large area that is illuminated by the Sun. Since the solar radiation pressure is its working principle, a large area means that the surface can intercept a larger numbers of photons and create more pressure (MCINNES, 2004). Furthermore, to optimize the magnitude of the solar radiation acceleration, the mass of the solar sail must be as light as possible. This means that solar sails are projected with a small mass per unit area, just like a paper sheet, thin and large (MCINNES, 2004). The material of the solar sail also influences its performance. Solar sails must have surface as near as possible to perfect reflectors. In this way, it is optimized the momentum transferred to it. If the solar sail has a perfect reflection, then the momentum transferred to the sail is two times the momentum transported by the incident photons. The solar sail orientation is also fundamental to maneuver correctly the system and achieve the trajectory goals.

The solar sail concept has a long and rich history with scientists and science fiction authors as pioneers. Maxwell (1873) proved mathematically that the light can exert a pressure on a surface and it was demonstrated experimentally later by Lebedew (1901). Between the work of these two scientists, Le Faure and De Graffigny (1889) wrote a fiction novel about spacecrafts propelled by mirrors.

K. Tsiolkovsky and his co-worker F. Tsander, from the former soviet union are believed to be the first scientists to write about the solar sailing (MCINNES, 2004). Tsiolkovsky (1921,1936) discussed practical solar sails as a non-rocket form of space travel. Tsander (1924) proposed interplanetary space missions

using tremendous mirrors of very thin sheets, capable of achieving favorable results. By the time of Tsiollovksy and Tsander, the solar sails were not so popular and yet a really primitive idea.

Later on, [Wiley \(1951\)](#) wrote, under the pseudonym of Russel Sanders, an article that discussed the design of a feasible solar sail and some strategies for orbit rising. He wrote it under a pseudonym to protect his professional credibility. He stated that solar sails must be more practical than rocket propulsion, with no fuel consumption and long life-time. He was optimistic about its benefits.

An important paper written by [Garwin \(1958\)](#) studied also the feasibility of solar sails with elegant features, advantages of solar sail propulsion and the possibility to achieve high velocity increments for a long period of time. [Garwin \(1958\)](#) was the first to use the term “solar sailing” and, after that, the name became popular and it is used until now.

The solar sailing discussion after the 1960s became a vast study to contribute to the solar sail understanding and technology. The mirror concept, back to the early literature, has been improved over the years to thin, large and light reflective solar sails.

A brief idea of the most enrichment studies about solar sails are given as follows.

[Tsu \(1959\)](#) studies the benefits of the solar sail, like no fuel or propellant requirements, no power plant needed aboard ship and no waste-heat disposal problem. This paper presents the characteristics of a solar sail in details and the equations of motion. The orientation of the solar sail is optimized and the time travel computed and compared with chemical thrusters.

[London \(1960\)](#) uses the exact differential equations of motion instead of the approximated one applied by [Tsu \(1959\)](#). The logarithmic spiral trajectory is one of the maneuvers studied.

[Sands \(1961\)](#) presents escape maneuvers with solar sail usage for initially circular orbits. The flat sail is rotated about its axis at half of the revolution rate about the planet. The orbits are in the plane of the ecliptic of a planetary gravitational field.

[Fimpe \(1962\)](#) presents the same idea of [Sands \(1961\)](#), but he includes the three-dimensional trajectories for the planetary escape.

[Wright and Warmke \(1972\)](#) present solar sail missions. The paper proposes missions that use solar sail vehicles to deliver large payloads throughout the solar system, like Jupiter, Saturn or Mars. It is also stated that a reusable sail could be returned to Earth.

[Svitek et al. \(1982\)](#) were not the first ones to propose spinning solar sails, but his work presents a complete guide with detailed characteristics of them and other types of solar sail. This paper studies rigid solar sail with stiffening performed by composite beams curing in space and by a network of tubes filled with gas. The soft solar sail is also studied with a spinning sail, a parachute-like sail and a solar sail reinforced by gravity gradient. All of the solar sails proposed are compared and its performance is discussed based on the application of the mission.

The study of solar sails and disturbing forces is also considered in the scientific research. One of the notorious and pretentious studies about solar sails and disturbing forces is given by [Forward \(1991\)](#). The idea of this paper is to have a spacecraft static (with no orbit). The idea is to use a solar sail propulsion to maintain itself in a desired “non-orbiting” static equilibrium position adjacent to the Earth by balancing light pressure and gravitational force. The idea of a spacecraft not orbiting a gravitational field may be playful, but yet the idea

behind the paper contributed to the idea of using solar sails to reduce undesired forces.

[McInnes et al. \(1994\)](#) study stationary solutions for the restricted three-body problem for spacecraft with a solar sail in the Earth-Sun and Earth-Moon systems. It is found that the usual five Lagrange points are extended to a continuum of new artificial points that form level surfaces parameterized by the sail mass per unit area. Analytic expressions for the sail mass per unit area and the sail attitude required for these stationary solutions are obtained and the stability of the solutions examined.

[Maccone \(1994\)](#) proposes space missions outside the solar system to exploit the gravitational lens of the Sun. It is proposed that the spacecraft can achieve its final orbit to study the gravitational lens phenomena of the Sun with solar sail propulsion through the solar system.

[Carroll \(1998\)](#) proposes an economical planetary space travel with a small solar sail to provide thrust to the spacecraft. The idea behind the paper is to create lighter spacecrafts that can exploit the solar system with no fuel, just using the light solar sail as a propulsion system.

[Liu et al. \(2014\)](#) study the attitude dynamics for the highly flexible solar sail with control vanes, sliding masses, and a gimbaled control boom. The vibration equations are derived considering the geometric nonlinearity of the sail structure, subjected to the forces generated by the control vanes, solar radiation pressure, and sliding masses. Then, the dynamic models for attitude and vibration controller design and dynamic simulation are obtained, respectively.

[Oliveira and Prado \(2014b\)](#) propose an investigation about potential low-cost orbits with reduced external perturbations and the use of solar sails to reduce even more the external perturbations. Many different solar sails concept is proposed, like variable solar sails, fixed area solar sails and attitude restrictions for the control of them.

[Oliveira and Prado \(2014c\)](#) study a solar sail concept to reduce the perturbations around a triple asteroid, which is related to the ASTER Brazilian mission. The study finds potential low-station keeping orbits and proposes solar sails to reduce the external perturbations.

[Zeng et al. \(2014\)](#) study the concept of fast solar sail rendezvous missions to near Earth asteroids by considering the hyperbolic launch excess velocity as a design parameter. After introducing an initial constraint on the hyperbolic excess velocity, a time optimal control framework is derived and solved by using an indirect method.

[Jin et al. \(2014\)](#), based on the coupling effect of the orbit and the attitude, state a theory of time-optimal control that is used to design the transfer trajectory from an earth-centric orbit to a heliocentric polar orbit. This paper establishes the reduced dynamic model for a flexible solar sail with foreshortening deformation and coupling of its attitude and vibration. In the process of attitude control, it is considered that the sail craft generates orbital deviations from the designed orbit, as well as structural vibration.

[Visagie et al. \(2015\)](#) propose the use of drag augmentation from a deployable drag-sail to de-orbit a satellite in LEO, to lead to a reduction in collision risk.

Next, it follows a description of some solar sails missions.

The IKAROS (interplanetary Kite-craft accelerated by Radiation of the Sun) mission was conceived by JAXA (Japan Aerospace Exploration Agency). This mission was launched in May 21, 2010. This mission was the first one to demonstrate the solar sail technology in interplanetary missions. The main propulsion is the solar sail and the other propulsion system is the photon-propulsion. The mission performed a fly-by in Venus ([JAPAN AEROSPACE EXPLORATION AGENCY, ...](#)).

The mission called NanoSail-D composed by a nanosatellite and a solar sail orbited the Earth for 240 days. This was the first nanosatellite with solar sail in Low-Earth Orbit (LEO). The mission was successfully launched to space in November, 2010, as a payload on NASA's FASTSAT (Fast, Affordable, Science and Technology SATellite). The NanoSail-D's sail was deployed on January 20. This mission was launched to determine how future satellites can use this new technology ([NATIONAL AERONAUTICS AND SPACE AGENCY, 2012](#)).

The mission called LightSail was launched on May 20, 2015. Unfortunately, the final orbit of the spacecraft was not the nominal one. Nevertheless, the mission still could test the deployment sequence and capture pictures. The atmosphere did not allow the solar sailing tests ([PLANETARY SOCIETY, ...](#)).

A pretentious mission called Sunjammer was planned to launch the first solar sail mission to deep space and the largest sail ever flown so far. The mission Sunjammer would be equipped with technologies to provide Earth with its earliest warning to the potential hazardous of solar activities. Unfortunately, the mission was cancelled because of the lack of confidence on its contractor's ability, in 2015 ([SPACE NEWS, 2014](#); [SUNJAMMER, 2015](#)).

The information about missions using solar sail in this chapter is brief, since there are many others current and future missions that have been postponed or canceled.

The solar sail is a vast topic and the literature review given in this thesis does not represent even by far all the related topics and applications it can have. The idea behind the literature review is to introduce the reader to the solar sail world and its potential applications. Regarding the solar sails, the solar system is the limit.

#### **1.4. Tethered Systems**

A tethered satellite system (TSS) consists of two or more rigid bodies with tether or tethers connecting these bodies ([ASLANOV; LEDKOV, 2012](#)).

The TSS can have many different applications. The main applications of the TSS are explained next and later the EDT is explained in detail.

The concept of TSS started in 1895 with the work of [Tsiolkovsky \(1959\)](#). He envisioned a giant tower stretching from the ground to geostationary orbit (GEO), from which the satellites could be put in orbit. The idea of [Tsiolkovsky \(1959\)](#) became the famous TSS, known as space elevators.

Although space elevators are still a theory, mainly because of the lack of technology to build them and dangerous space debris impacts, the subject is still present in conferences and papers. Like in [Edwards \(2004\)](#) who presents an overview about the advances of the technology and the impact on the space elevator design of the advances of technology. He also presents the tasks that must be overcome to build space elevators.

[Pearson \(2007\)](#) examines lunar space elevators, a concept originated by the lead author, for lunar development. Lunar space elevators are flexible structures connecting the lunar surface with counterweights located beyond the  $L_1$  or  $L_2$  Lagrangian points in the Earth-Moon system. The application of lunar tether is to transfer lunar objects to high altitude orbits around the Earth.

[Pearson et al. \(2010\)](#) study the probability of a space elevator to collide with space debris. The study covers many different altitudes from LEO to GEO.

Another TSS application is the creation of an artificial gravity on board a space system. The idea is to use the centrifugal force of inertia for the creation of artificial gravity ([COSMO; LORENZINI, 1997; FORWARD et al., 1997](#)). The TSS can be two spacecrafts connected by a chain and the magnitude of this force is proportional to the length of the chain and the square of the angular velocity ([ASLANOV; LEDKOV, 2012](#)).

The first experiment to create artificial gravity was carried out by NASA in 1966 during the Gemini-11 mission ([HACKER; GRIMWOCK, 1977](#)). The spacecraft, Gemini-11, was connected with a target satellite with a 30 m tether length. The TSS Gemini 11 spun around its centre of mass with an angular velocity of  $1.6 \cdot 10^{-2} \cdot s^{-1}$  ([ASLANOV; LEDKOV, 2012](#)).

The spin resulted in an artificial gravity of  $10^{-4}$  g onboard Gemini. Although the magnitude of the artificial gravity is really low, it has a great potential to create artificial gravity and help the humankind to explore the space. Artificial gravity can help humans in space exploration by avoiding the atrophy of the muscles, bone decalcification, etc.

Another tether application is to use a spinning space tethering system for lifting a payload into a high-altitude orbit or/and decaying a payload. If the tether properly swing, the conservation of the angular momentum makes one end of the TSS body increase its orbit, while the other one decays if the tether between these bodies are disconnected ([ASLANOV; LEDKOV, 2012](#)).

Another approach is the use of space escalators. The tether consists of two end bodies, one in a higher altitude than the other. A spacecraft is collected by one of these end bodies and then the tether itself will work as an escalator, lowering or raising the orbit of the spacecraft. Not only the spacecraft will have its orbit altered, but also the tether, due to the conservation of the energy.

The STEPS (Station Tethered Express Payload System) calls for a novel with this approach for the ISS (International Space Station) ([COSMOS; LORENZINI, 1997](#)). The payload that is wished to be lowered is one of the ends of the end bodies and the other one is the ISS. The tether, in a correct swing, can lower the payload attitude and increase the ISS's altitude by cutting the tether ([TIESENHAUSEN, 1985](#)).

There are two successful experiments of payload delivery by means of a tether: the SEDS 1 experiment in 1993 ([SMITH, 1995](#)) and the YES2 in 2007

([WILLIAMS, 2009](#)). The first one used a static deployment and the second one a dynamic one.

There are many other applications of tethers, like placing a spacecraft into an orbit; the creation of a traffic artery linking Earth and the Moon; gravity stabilization; generation of electrical energy by a conductive tether, the use of electrical energy for maneuvering; the use of electrodynamic tether for debris descending; etc ([ASLANOV; LEDKOV, 2012](#)). The main importance of the TSS is to perform orbital maneuvers or attitude control without any or minimum fuel expenditure.

There are many TSS experiments that have been carried out, like: GEMINI 11, GEMINI 22, TPE 1, TPE 2, CHARGE 1, CHARGE 2, OEDIPUS A, TSS 1, SEDS 1, SEDS 2, PMG, TSS 1R, Tips, YES, YES2, T-REX, etc ([ASLANOV; LEDKOV, 2012](#)). The next sub-section introduces briefly some EDT missions and experiments.

The TSS topic is a vast and promising topic with different applications, dynamics and working principles. The reader is encouraged to read the references to understand in more details the tether's world.

The EDT is the next topic on this sub-section. Since this thesis proposes the use of electrodynamic tethers to maneuver spacecrafts, it is given a special section for it.

#### **1.4.1. Eletrodynamic Tether**

The electrodynamic tether has a conductive tether that allows a current to flow through it. The EDT has special end bodies, one of them that have a contact with the plasma of the atmosphere. This end body is known as an electron collector. The collectors can be electronic guns, hollow cathodes or the tether itself ([PARKS; KATZ, 1987](#); [WILBUR; LAUPA, 1988](#)). The other end must be an electron emitter.

The EDT with a conductor tether moving in a magnetic field causes a voltage induction (COSMO; LORENZINI, 1997). As the electron collector provides the electrons and the emitter emits the electrons, there is a current flowing through the tether. The current flow through the tether induces a Lorentz force on the system (COSMO; LORENZINI, 1997).

The EDT can also use a battery to overcome the voltage induction and create an opposite Lorentz force to the opposite current flow.

There are many tether flights that has been launched to study the EDT. The TSS-1 mission was launched on July 31, 1992 (COSMO; LORENZINI, 1997). Although this mission does not involve EDT experiments, the mission accomplished a better understating of the TSS, like the basic concept of long gravity-gradient, safety concerns, the feasibility of deploying a satellite to long distances and the feasibility to the TSS-1R (COSMO; LORENZINI, 1997).

The TSS-1R mission was launched on February 22, 1996. This mission had a satellite that was deployed 20.7 km above the Space Shuttle on a conducting tether. It remained there for more than 20 hours performing science experiments. After that it stayed more hours making experiments at a deployed distance of 2.5 km. The goals of the TSS-1R mission were to demonstrate the research of EDT and space plasma physics. Although this mission could not perform all the experiments planned, the TSS-1R was able to measure the motional EMF, the satellite potential, the current in the tether, the charged particle distributions, and the electric and magnetic fields. The TSS-1R contributed for a better understating of the EDT with the experimental results. (COSMO; LORENZINI, 1997)

The other two missions that helped scientists understand better the TSS and EDT tethers are the SEDS missions: SEDS-1 AND SEDS-2. The SEDS-1 objectives were to demonstrate that SEDS hardware could be used to deploy a payload at the end of a 20 km tether long and study its reentry after the cut of the tether. SEDS-2 mission objectives were to demonstrate the feasibility of

deploying a payload with a closed-loop control law and to study the long term evolution of a TSS. Unfortunately, the SEDS-2 mission failed, as debris or a micrometeoroid collided with the system after 5 days of the mission. ([COSMO](#); [LORENZINI, 1997](#))

The PMG (or Plasma Motor Generator) experiment tested the ability of a hollow cathode assembly to provide a low impedance bipolar electrical current between a spacecraft and the ionosphere. The EDT length was 500 m. The experiment aimed at demonstrating that this configuration could function either as orbit-boosting motor or as a generator converting orbital energy into electricity. This mission was launched on June 26, 1993 ([COSMO](#); [LORENZINI, 1997](#)). The data confirmed that the experiment was a success.

There are many other missions that have been launched or proposed to be launched using TSS and EDT. The author encourages the reader to learn more about those missions in the references cited in this work.

The EDT has a vast literature. Some of them are given below.

[Anderson et al. \(1979\)](#) study the potential use of an EDT built with metal, either uncoated or coated with a dielectric. The electrodynamic interaction with the magnetoionic medium of the Earth and the ionosphere generates effects that can be used by the spacecraft.

[Arnold and Grossi \(1983\)](#) study the natural damping the EDT has. The results obtained are of great importance to study the long-term of the dynamics of the EDT. In the same year, [Grossi \(1983\)](#) argues about the feasibility of electric power generation and electromagnetic wave injection by electrodynamic tethers.

A great compact study about EDT is given by [Lanoix \(1999\)](#). This thesis includes a mathematical model for the long-term dynamics of a tethered spacecraft. There are two approaches studied in this work, the analytical

approximation and the numerical results. The insulated and the bare tethers are studied. This last reference is a complete guide for the dynamics of the motion and the attitude that the EDT can experience in space.

### 1.5. **Spacecraft Trajectory Simulator**

The STRS is a software that was first developed by Dr. Evandro M. Rocco and then it has been constantly improved by him and his doctoral students through many years. The software itself is a complex tool that propagates the orbit and the attitude of a spacecraft over the time. The software can also perform maneuvers. There are many external disturbing forces that can be considered in this simulator, like atmospheric drag, solar radiation pressure,  $J_n$ ,  $C_{nn}$  and  $S_{nn}$  due to the non-sphericity of the Earth and the albedo perturbation. The STRS has some other extensions for the propagation of a spacecraft orbiting the Moon, Jupiter and so on.

The STRS can also consider many non-linearities due to failures, errors, noise, malfunctioning or external perturbations of the actuators, sensors and other subsystems that complete the spacecraft system.

In this way, the STRS is capable of propagating orbits and simulate orbits in a more realistic environment if many aspects of the orbit were not modeled with a simple orbit propagator and found by optimal solutions. The model can include all the specifications of the subsystems, like errors and noise and it includes all the external disturbing forces. The STRS is also capable of including non-predictable failures that may occur during the mission. The time-consuming cost to find an optimal maneuver including all the potential failures, all the external perturbations and the error propagation can make the project unfeasible and the use of the STRS to include them is a must.

The STRS can perform impulsive and non-impulsive maneuvers. The STRS is a control loop feedback mechanics which is essential for low-thrust maneuvers

(MARCELINO, 2009). Therefore, the STRS is a PID controller (or proportional integral derivative controller).

There are two orbits that the STRS integrates simultaneously. One is the desired orbit and the other one is the real orbit that the satellite has for the same integration step of time. For many reasons, like not expected external perturbations or failures in the sensors or actuators, there may have a difference between the measured position of the spacecraft and the desired position. The controller acts in order to minimize the error over the time by using the actuators of the systems.

The basic working principle of the software STRS is explained next:

- a) The simulation occurs in a discrete-event simulation, or, in other words, the integration occurs in a discrete sequence of events in time. At each step of time, the state of the spacecraft (position and velocity) is computed. In this step, all the disturbing forces, non-linearities, errors and failures must be set;
- b) Because the STRS works in a control loop feedback, there are two states for the system. One of them is the desired state for the satellite and the other one is the real state that includes the sets stipulated in the previous step;
- c) An error signal is then computed in the PID controller with the difference between the desired state and the real state of the spacecraft;
- d) The controller attempts to minimize the error according to the PID settings, like the damper parameters, the power supplied, etc;
- e) The control signal acts on the actuator (propulsion system). At this step the non-linearities of the actuator can be considered;

- f) Finally, the actuation signal is sent to the dynamics of the system. At this step, the actuation signal can be added to the velocity deviation due to the disturbing forces. The result provided by the dynamics is the current state or the real state of the system;
- g) Sensors are used to determine the new state of the system and to compare this state with the desired state to close the loop.

There are many references that have been published with the use of the STRS.

[Rocco \(2008a\)](#) begins to build up the first steps of the STRS. This paper details the software design for the Earth albedo with models and the architecture of the software. This system is available as a new and complex disturbing force that the satellite can suffer. This project is funded by Marie Curie Program of the European Commission in partnership with the Stanford and Cambridge Universities. Their main objectives were the development of methods for trajectories and attitude reconstruction, considering the spacecraft dynamics identification, and apply these methods to scientific missions like Gravity Probe B (NASA) and GAIA (ESA). The model of the Earth is albedo is based on the reflectivity data measured by NASA's Earth Probe satellite, which is part of the TOMS project (Total Ozone Mapping Spectrometer).

[Rocco \(2008b\)](#) considers the disturbance on the spacecraft orbit due to the terrestrial albedo using the Earth's albedo model and the orbital dynamics model developed as part of the previous work, [Rocco \(2008a\)](#). In this paper, it is studied the deviations the spacecraft can suffer due to the albedo disturbing force for some specific missions.

[Rocco \(2009\)](#) presents a complete set and architecture for the STRS software. The PID controller is explained with details and more disturbing forces are added in the results. The controller wishes to reduce the deviations caused by the disturbing forces. Several orbits are studied.

[Santos \(2011\)](#) includes in the STRS software a new tool that uses the atmospheric drag to create a lift and perform maneuvers. The controller finds the optimal solution with the best angles of attack to perform maneuvers that reduces the energy of the orbit.

[Oliveira et al. \(2013b\)](#) specify the boundaries of the Van-Allen belts to study the time of the passage through these dangerous regions, using a plasma engine developed by [Ferreira et al. \(2016\)](#).

[Gonçalves et al. \(2013a\)](#) include the lunar trajectories for spacecrafts in the STRS simulator. In this paper, the gravitational disturbances are included in optimal maneuvers.

[Venditti et al. \(2013\)](#) include non-spherical central bodies as the main gravitational field of a spacecraft's orbit. The trajectory and the control around these bodies are modeled by parallelepipeds.

[Rocco \(2013\)](#) proposes an on-board automatic control of the Keplerian elements of an orbit in a closed loop system.

[Santos and Rocco \(2013\)](#) study the control of trajectories with continuous thrust applied to rendezvous maneuvers. The PID controller was once used in the STRS to perform the rendezvous with a low-thrust continuous system. The problem involves a multi-optimization problem as the fuel, the time and the precision have to be minimized.

[Gonçalves et al. \(2013b\)](#) include in the STRS the model of the albedo of the Moon. The work involves the same working principles as used in [Rocco \(2008a\)](#). The magnitude of this perturbation is analyzed and compared for different Moon's orbit and other disturbing forces.

[Santos et al. \(2011\)](#) study the trajectory control of an aeroassisted maneuver between two coplanar circular orbits. The simulator developed for this paper considers a reference trajectory and a trajectory perturbed by external

disturbances combined with non-idealities of sensors and actuators. It is able to operate in closed loop, controlling the trajectory (drag-free control) at each instant of time using a Proportional-Integral-Derivative (PID) controller and propulsive jets.

Once more, [Rocco \(2015\)](#) studies the automatic correction of the semi-major axis with an on-board control system for orbital maneuvers, but this time around Mars. The disturbing forces considered are due to the gravitational influence of the Sun, Phobos and Deimos.

[Gonçalves et al. \(2015a\)](#) study the deviations the disturbing forces can cause on a Moon's orbit and the necessary control that must be applied to correct the shifts caused by the disturbing forces. In [Gonçalves et al. \(2015b\)](#), it is included the evaluation of the uncertainty in the trajectory simulations of a lunar satellite due to the adopted model for the lunar gravitational field. This uncertainty may cause error predictions in the orbital trajectory and the STRS is used to correct those uncertainties.

### **1.6. Orbital Motion And Disturbing Forces**

A Keplerian orbit is known as a negligible point mass moving under the sole influence of the gravity of the attractor, which is also a point mass with a significant mass. The centre of the mass of the system is therefore the point with the significant mass. The trajectory of the negligible mass is a conic section, which can be a circle, an ellipse, a parabola or a hyperbola.

On the other hand, there are other forces influencing the spacecraft trajectory and they can deviate the orbit of the spacecraft. Their effects on the motion are usually small, but still noticeable as the orbit does not keep a Keplerian orbit. There are many kinds of perturbation like air lift, atmospheric drag, Earth asphericity, solar radiation pressure, third body perturbation of the Moon and the Sun, electromagnetic forces, albedo effects and so on.

The magnitude of each perturbation depends on the system itself and the state of the spacecraft.

The main effect of the air lift and drag is the decay of the semi-major axis (COSMO; LORENZINI, 1997; JACCHIA, 1977; SANTOS, 2011). The decay rate depends on the state of the spacecraft, the ballistic coefficient, the solar activity effect on the atmosphere, etc. The estimation of the decay of the satellites can be computed with interpolation and analytical formulation (COSMO; LORENZINI, 1997; JACCHIA, 1977; SANTOS, 2011), but the exact calculation with a good precision requires very detailed models that includes the altitude propagation and the solar activity acting on the atmosphere (HUGHES, 1986; WARNOCK; COCHRAN, 1993). The electrodynamic tether can also work as a drag, if the current flows in the induced EMF (electromotive force) direction. Warnock and Cochran (WARNOCK; COCHRAN, 1993) investigated the effect of several parameters, like semi-major axis, inclination, argument of latitude and tether length a tethered mission.

The Earth asphericity perturbation forces are due to a non-homogeneous mass distribution and aspherical shape of the Earth. The main result of this disturbing force is a drift in the ascending node and in the argument of perigee (COSMO; LORENZINI, 1997; KAPLAN, 1976).

The solar radiation pressure is due to the impact of the solar radiation in the surface of the spacecraft. It has been proved that the magnitude of the solar radiation pressure becomes larger than the atmospheric lift for altitudes beyond 800 km (BAKER, 1967). The solar radiation pressure causes periodic changes on all of the orbital elements (CHOBOTOV, 1991).

The lunisolar attraction is the interaction of the gravity force of the Sun, and the Moon in the Earth and in the spacecraft. In Chobotov (1991), it has been set that, for altitudes beyond 26000 km, the lunisolar perturbation becomes non-negligible. The lunisolar perturbation is known as the third-body perturbation of the Sun and the Moon.

The electromagnetic or Lorentz force is due to the motion of an electric current flowing in the magnetic field of the Earth (COSMO; LORENZINI, 1997, FORWARD et al., 1997; JOHNSON; HERRMANN, 1998; estes et al.,1997; LORENZINI et al., 1997). The current flow can be from the payload system itself or from the electrodynamic tether. The payload system can generate the Lorentz forces and produce internal torques (ZANARDI et al., 2004). The internal torque produced by the Lorentz force can also be produced by a magnetic torque, but in this case this system would be used for an altitude control (TORCZYNSKI et al., 2010). The electromagnetic tether itself can be used to create drag or increase the altitude of the satellite or even to control the disturbing forces and maneuver the system (COSMO AND LORENZINI, 1997, FORWARD et al., 1997, JOHNSON; HERRMANN, 1998, ESTES et al., 1997, LORENZINI et al. 1997, LANOIX, 1999, OLIVEIRA; PRADO, 2015).

## 2 MATHEMATICAL MODELS

This section introduces the mathematical models used in this thesis to obtain the results. The mathematical models chapter is divided by the following topics: Perturbation Integrals, STRS, EDT, solar sail, solar radiation pressure, spherical harmonic perturbation, atmospheric drag and third-body perturbation from the Sun and the Moon.

### 2.1. Perturbation Integrals

The integral approach is subdivided in two forms. The first one that shall be introduced is the PI. The PI is based on the integral of the magnitude of the disturbing forces per unit mass along the orbit for one orbital period. The mathematical formulation for this integral approach is given as follows (PRADO, 2013)

$$PI = \int_0^T |\mathbf{a}| dt \quad (2.1)$$

where  $\mathbf{a}$  is the acceleration caused by the disturbing force or forces,  $t$  is the time and  $T$  is the period of the orbit.

The  $PI$  [ $m/s$ ] is actually the total velocity, for one orbital period, that a propulsion system must apply in order to keep the spacecraft in a Keplerian orbit all the time.

Note that Equation 2.1 can evaluate the acceleration caused by the disturbing forces added together or separately. If all the disturbing forces considered in this work needs to be computed, then the net acceleration  $\mathbf{a}$  would be in the form given by Equation 2.2

$$\mathbf{a} = \mathbf{a}_{drag} + \mathbf{a}_{Moon} + \mathbf{a}_{Sun} + \mathbf{a}_{Jn} + \mathbf{a}_{C22} + \mathbf{a}_{radiation} \quad (2.2)$$

where the sub index *drag* is related to the atmospheric drag; *Moon* and *Sun* are related to the third-body perturbations of the Moon and the Sun, respectively;  $J_n$  is related to the zonal harmonic of  $n^{\text{th}}$  order;  $C_{22}$  is related to the sectorial harmonic of order  $n=2$  and  $m=2$ ; and the *radiation* is related to the solar radiation pressure.

The PI can also evaluate the reduction or the increase in the fuel expenditure that a propulsion system needs by simply adding the desired accelerations. Therefore, the acceleration caused by the solar sail or the electromagnetic tether can be included in order to evaluate its efficiency in Equation 2.2 (OLIVEIRA; PRADO, 2014b; OLIVEIRA; PRADO, 2015)

The PI assumes that the spacecraft is in a Keplerian orbit all the time, even though there are disturbing forces acting on it. The calculations are performed for only one orbital period, which justify this approximation. The values obtained would represent the cost to keep a Keplerian orbit all the time. The idea is to use those numbers for comparisons of the magnitude of the forces, not to really keep the spacecraft in a Keplerian orbit all the time.

So, it is assumed that the variations of the orbital elements during one orbital period, the duration of the integration, is not too large, then this approach is an easy way to estimate the magnitude of the disturbing forces with no orbit propagation including the disturbing forces. It gives less time-consuming numerical calculations.

Moreover, if the direction of the disturbing force is in the direction of the velocity of the orbit or opposite to it, like when considering the atmospheric drag or an EDT with radial attitude for equatorial orbits, then the pi is actually the total velocity variation the spacecraft receives in one orbital period. The pi would be, in this case, the total velocity variation the propulsion system must apply in order to raise or decrease its altitude and to compensate these perturbation effects.

The second formulation for the Perturbation Integral method is the  $PI_{MAG}$ . This integral is an essential key used to analyze the forces that can be compensated during one orbital period of the spacecraft. The magnitude of the  $PI_{MAG}$  is different from the PI for forces that can be compensated during one orbital period. The  $PI_{MAG}$  value can be understood as an approximation of the velocity increment a propulsion system must apply instantly to compensate the deviations caused by the disturbing forces after one orbital period of the spacecraft.

The  $PI_{MAG}$  formulation is given as follows

$$PI_{MAG} = \left| \int_0^T \mathbf{a} dt \right| \quad (2.3)$$

The  $PI_{MAG}$  calculates the magnitude of the vector after the integral is computed. The great difference between  $PI_{MAG}$  and PI is that the former allows the compensation of the disturbing forces if the directions of the accelerations along one orbital period are not orthogonal or if they do not have the same direction.

It is also possible to create maps for different orbits by varying the Keplerian elements of the orbits. The maps are the key to evaluate the behavior of the disturbing forces and to evaluate the cost of orbital maintenance for different orbits. It allows a fast and easy way to find or compare different orbits based on the maps that show the Perturbation Integrals. Orbits that have lower PI values are orbits with a good potential to require less fuel for station-keeping maneuvers ([PRADO, 2013](#)). Moreover, the results in this work show that the  $PI_{MAG}$  can show critical inclinations for the  $J_2$  perturbation. It indicates that both versions can be useful, depending on the goal of the study.

The mathematical equation for the Perturbation Integral given by Equation 2.1 or Equation 2.3 can be rewritten in order to allow the numerical integration to be faster and more precise. The reformulation is the change of the variable of integration from the time  $t$  to the eccentric anomaly “E”. This change of the

integration variable is easily made since it is assumed that the orbit is Keplerian. The time  $t$  is related to the mean anomaly  $M$  as given by Equation 2.4

$$M = M_0 + n(t - t_0) \quad (2.4)$$

where  $M_0$  is the initial mean anomaly,  $n$  is the mean motion and  $t_0$  is the initial time. The mean motion is the time-average angular velocity over an orbit and it is given by Equation 2.5

$$n = \left( \frac{\mu}{a_s^3} \right)^{1/2} \quad (2.5)$$

where  $\mu$  is the multiplication of the universal gravitational constant with the mass of the main body and  $a_s$  is the semi-major axis. In this thesis,  $\mu$  is given by  $3.986 \times 10^5 \text{ km}^3/\text{s}^2$ , which is the value for the Earth. The variable  $M$  can be replaced by the eccentric anomaly  $E$  with the help of the following Equation 2.6

$$dM = (1 - e \cos E) dE \quad (2.6)$$

where  $e$  is the eccentricity of the orbit.

Therefore, the Equation 2.1 can be written as (PRADO, 2013)

$$PI = \frac{1}{n} \int_0^{2\pi} |\mathbf{a}| (1 - e \cos E) dE \quad (2.7)$$

The  $PI_{MAG}$  can be written similarly, but the magnitude should be computed after the integration, not before.

The use of the eccentric anomaly as the integration variable instead of the time leads the integration into an analytical step-size regulation in an efficient way to compute elliptic orbits. Therefore, the integration in  $E$  allows more accuracy than the integration in  $t$  for the same number of steps for the integration.

The PI, as described by Equation 2.1 or 2.7, or the  $PI_{MAG}$ , in Equation 2.3, may depend on some initial parameters such as the position of the Sun, and the Moon. In order to evaluate the PI with no dependence on the initial position of the Sun and/or the Moon, an averaging technique is applied in the Perturbation Integral. The Perturbation integral with the averaging technique becomes a mean value that does not depend on the initial time of the integration and the relative position of the Sun or the Moon.

For example, if the perturbation caused by the Moon needs to be computed in the PI with the averaging technique, then the PI becomes

$$PI = \frac{1}{2\pi n} \iint_0^{2\pi} |\mathbf{a}|(1 - e \cos E) dE df_{0Moon} \quad (2.8)$$

where  $f_{0Moon}$  is the initial anomaly of the Moon.

The integration shown in Equation 2.8 considers the mean value of the PI taking into account all the possible initial positions of the Moon. The method to find a mean value of the PI with all the possible initial configurations of the Moon is given by integrating the PI in Equation 2.7 from 0 to  $2\pi$  with the integration variable being the initial anomaly of the Moon. Then after the integration, the result is divided by  $2\pi$  to obtain an average value of all the possible values that the PI could have.

Similarly, it is possible to compute the  $PI_{MAG}$  with the averaging technique for the perturbation due to the Moon.

If the Sun is the cause of the perturbation or if the solar radiation pressure (which includes the solar sail) needs to be computed in the PI with the averaging technique, whether they are added together or separated, the formulation is given as follows

$$PI = \frac{1}{2\pi n} \iint_0^{2\pi} |\mathbf{a}|(1 - e \cos E) dE df_{0Sun} \quad (2.9)$$

where  $f_{0Sun}$  is the initial anomaly of the Sun.

Similarly, it is possible to compute the  $PI_{MAG}$  with the averaging technique for the Sun perturbation or the others disturbing forces that depends on the position of the Sun.

If the lunisolar perturbation needs to be computed, then the PI with the averaging technique becomes (PRADO, 2013)

$$PI = \frac{1}{4\pi^2 n} \iiint_0^{2\pi} |\mathbf{a}|(1 - e \cos E) dE df_{0Sun} df_{0Moon} \quad (2.10)$$

Similarly, it is possible to compute the  $PI_{MAG}$  with the averaging technique for the lunisolar perturbation.

The PI can also include the perturbation caused by the EDT, but the inclusion of the EDT in the PI with the averaging technique cannot be conceived, since the magnetic field of the Earth is not constant and it changes over the time.

In this thesis, the PI and  $PI_{MAG}$  may be used with or without the averaging technique. It is specified each time if the averaging technique is used or not.

For the averaging technique, the orbit of the Sun and the Moon is simplified, in order to guarantee a fast numerical integration for the Perturbation Integrals and, therefore, a fast creation of maps based on them. For the averaging technique, the Sun and the Moon are assumed to be in circular orbits around the Earth with semi-major axis of 384.399 km for the Moon and 149.597.870 km for the Sun. The inclination of the orbit of the Sun is 23.5 degrees and the inclination of the orbit of the Moon (with respect to the Earth's equator) is 18 degrees. In fact, the inclination of the Moon varies from 18 to 28 degrees, but this variation does not produce important changes on the PI values and, for this reason, it was fixed in 18 degrees (PRADO, 2013).

The mass of the Moon is assumed to be  $7.349 \times 10^{22}$  kg, so  $G_{mMoon} = 4.9383 \times 10^3 \text{ km}^3/\text{s}^2$  and the mass of the Sun is assumed to be  $1.98892 \times 10^{30}$  kg,

so  $G_{mSun} = 1,33 \times 10^{11} \text{ km}^3/\text{s}^2$ . The orbit propagation of the Sun and the Moon is computed for each step of the integration.

For values of the Perturbation Integrals with no averaging technique, a more detailed method is used based on the time and the ephemeris model of the Sun and the Moon. The ephemeris model is based on the Julian dates, to provide the accurate position of the Sun and the Moon ([TAMBURRO et al., 1968](#)). The ephemeris model of the Sun is based in [Capó-Lugo and Bainun \(2011\)](#) and for the Moon it is based in [Simpson \(1999\)](#).

The averaging technique is an easy numerical method that can consider a mean value of the PI or  $PI_{MAG}$  that does not depend of the initial position of the Sun and the Moon. The method conceives a mean value of the Perturbation Integral with no dependence in the initial conditions of the position of the Sun and the Moon, or the date and time of the initial integration.

The disturbing forces due to the third-body perturbation and the solar radiation pressure are extremely dependable on the initial position of the Sun or the Moon. If the averaging technique was not considered, then the results of the Perturbation Integrals would be based on the initial parameter of the time and the position of those bodies.

The averaging technique is used to obtain a Perturbation Integral value that would be the average value if all the initial positions of the Sun and the Moon would be considered in the Perturbation Integral and then calculated its mean value. In this way, the result of the Perturbation Integral would not depend on the initial time or date.

## **2.2. The Spacecraft Trajectory Simulator**

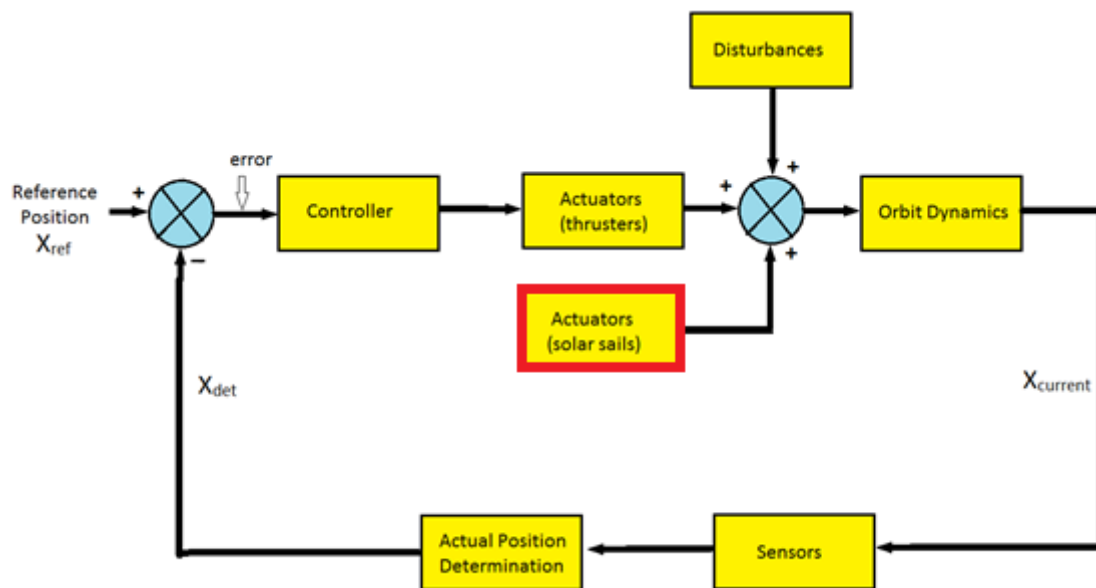
The software STRS is used in this work to validate the solar sail in a realistic environment. The realistic environment can set different parameters, failures,

errors and more at the actuators, orbital dynamics, sensors, controller, etc (ROCCO, 2009).

This section is concerned with the STRS working principle used in this thesis. The solar sail actuates due to the solar radiation pressure in the opposite direction of the disturbing forces that need to be reduced. The working principle of the solar sail is given in section 2.3.1.

There are many initial conditions that the user can set to simulate an orbit or a maneuver in the STRS, as explained in the introduction section. Figure 2.1 shows the architecture of the STRS with the solar sail use.

Figure 2.1 – Architecture of PID controller design STRS with the solar sail use as a non-fuel consumer thruster.



The work of the thesis related to the STRS is the development of the solar sail actuator in the STRS ambience. Therefore, the block named actuators (solar sails) in Figure 2.1 with the red contour was the major contribution for the STRS topic.

Figure 2.1 shows the PID control with the solar sail use. The Gregorian date is converted to Julian Date. From the Julian Date, it is possible to estimate the

position of the Sun, the Moon and the latitude at the ground track of the spacecraft. The disturbing forces are set as the initial conditions, as well as the time and date. The disturbing forces generate a disturbance in the orbital dynamics. The solar sail is used as an actuator that reduces the magnitude of the disturbing forces. This thesis uses the Keplerian orbit as the reference orbit to be maintained. The orbital dynamics integrates for one step of time with the disturbing forces acting on it. The sensors are used to analyze the state of the spacecraft given by the position and velocity. The perturbed state is different from the Keplerian state (the nominal orbit) and the difference between these two states creates an error signal. The controller acts to correct this error signal and it activates the actuator (propulsion system with fuel-consumption) to reduce the error signal to zero. The loop is closed and the cycle starts again.

The STRS is used in this thesis as a simulator with a PID controller that corrects the shifts caused by the disturbing forces at every step of the time. The solar sail is used as an actuator to reduce the disturbing forces and, in this way, to reduce the error signal from the reference state. The fuel propulsion acts as an additional actuator that reduces the disturbing forces if the solar sail cannot make it zero.

The purpose of this thesis is to study the feasibility of the solar sail in the STRS ambience. Some specific working principles of the software can be read in the literature given before. Some other parameters that may not be explicit in the results with the STRS use were considered to be irrelevant for the scope of this work.

### **2.3. The Solar Radiation Pressure**

The solar radiation pressure is one of the perturbation forces that act on the spacecraft, deviating the orbit of the spacecraft to a non-Keplerian orbit. The solar radiation pressure occurs when the radiation emitted by the Sun collides with the surface of the spacecraft, resulting in a force acting on that surface. The solar radiation pressure can not only change the orbital motion of the

spacecraft, but it can also change the attitude of the spacecraft, if the solar radiation pressure force is not directed to the center of mass of the spacecraft (ANDERSON, 2001).

Although the solar radiation pressure is a disturbing force, there are some cases where it can be used for the attitude control to help the maintenance of the orientation of the spacecraft or even for orbital maintenance (POLYAKA, 1963; WILLIAMS; WANG, 2000; KUMAR et al., 2004; BORGRAAFE et al., 2014).

The magnitude of the solar radiation pressure acceleration applied to a spacecraft or a solar sail is given by (FIESELER, 1998):

$$\mathbf{a}_{radiation} = \tau(1+\epsilon) \frac{P_s A_s}{c m} \left(\frac{k}{k_0}\right)^2 \cos^2 \varnothing \hat{f} \quad (2.11)$$

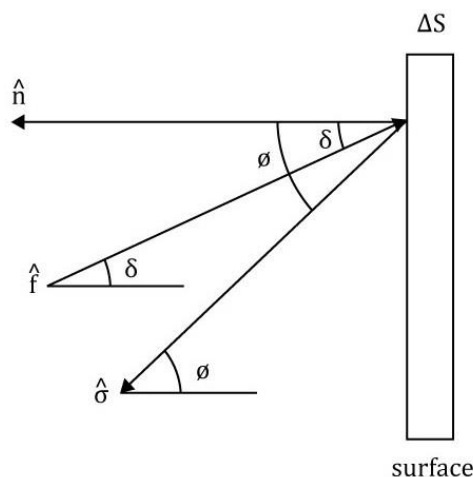
where  $\epsilon$  is the reflectivity of the surface, assuming values from 0 to 1;  $P_s$  is the power delivered from the Sun per square meters at one AU (Astronomical Unit) ( $\approx 1360\text{W/m}^2$ );  $A_s$  is the projected area of the spacecraft or the solar sail that is illuminated by the Sun;  $m$  is mass of the spacecraft;  $\varnothing$  is the angle between the opposite direction of the light flux and the normal direction of the surface,  $c$  is the speed of light,  $\tau$  determines the Earth's shadow/penumbra/illuminated region,  $k$  is the distance from the spacecraft to the Sun and  $k_0$  the mean distance from the Earth to the Sun ( $\approx 1\text{AU}$ ). The unit vector  $\hat{f}$  represents the direction of the force applied to the surface of the body and it is given by (CAPÓ-LUGO et al., 2011):

$$\hat{f} = -\frac{(1-\epsilon)\hat{\sigma} + 2\epsilon \cos\varnothing \hat{n}}{\sqrt{(1-\epsilon)^2 + 4\epsilon \cos^2\varnothing}} \quad (2.12)$$

where  $\hat{\sigma}$  is the unit vector with the opposite direction to the light flux and  $\hat{n}$  is the unit vector pointing to the normal of the surface.

Figure 2.2 shows the light interaction with a smooth surface of the body with the unit vectors  $\hat{\sigma}$ ,  $\hat{n}$ ,  $\hat{f}$  and the angles  $\delta$  and  $\varnothing$  (CAPÓ-LUGO et al., 2011).

Figure 2.2 – The light beam interaction of the solar radiation pressure with a smooth surface with the incident light beam, the reflection light beam and the force produced by the solar radiation pressure.



Source: Adapted from Tewari (2007).

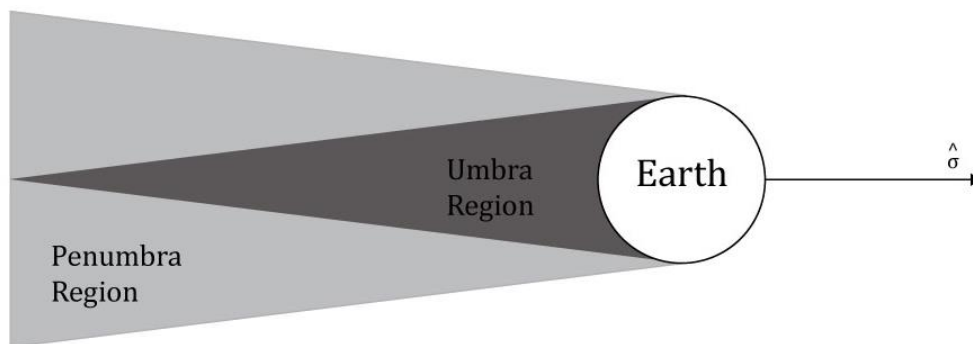
The angle  $\delta$  provides the direction of the solar radiation pressure force and it is the angle between the unit vectors  $\hat{n}$  and  $-\hat{f}$ . In the way shown in Equation 2.12 and Figure 2.2, the direction of the force caused by the solar radiation pressure is related to the reflectivity of the surface  $\epsilon$  and the angle between the directions of the light flux  $\varnothing$  with the normal of the surface. If the value of the reflectivity of the surface is different from one, some of the energy of the light flux is absorbed by the surface and then the direction of the solar radiation force is not the opposite to the normal unit vector  $\hat{n}$ . Nevertheless, if the value of the reflectivity of the surface is one, then the direction of the solar radiation pressure force is opposite to the normal unit vector.

The shadow regions given by  $\tau$  is determined by conical projections of the umbra and penumbra shadows, given the position and the shape of the Earth, the Sun and the distance between those two celestial bodies (LONGO et al., 1995). The coefficient  $\tau = 1$  occurs when the spacecraft is in the illuminated

region. If  $\tau = 0.5$ , then the spacecraft is located at the penumbra region and if  $\tau = 0$ , the spacecraft is in the umbra region. A schematic illustration of this configuration is given in Figure 2.3 (LONGO et al., 1995)

For practical reasons, since this thesis is concerned with a conceptual design and first analysis of spacecraft's orbits, the shape of the spacecraft was considered to be very simple. The spacecraft has a square shape area. The surface of the spacecraft is smooth. For the attitude of the spacecraft, it is considered that one of the sides is always pointing to the center of the Earth if the electrodynamic tether is not used. When the electrodynamic tether is used, the attitude of the system is given by the optimal attitude the system must have in order to reduce the disturbing forces effects or to de-orbit.

Figure 2.3 – Illustration of the umbra, penumbra and illuminated areas.



Source: Adapted from Longo et al. (1995).

### 2.3.1. The Solar Sail

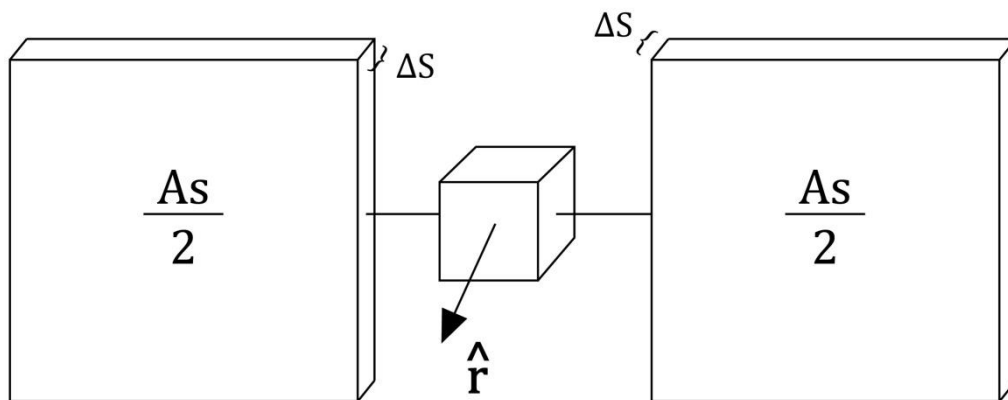
This thesis may use the solar radiation pressure in order to reduce the shifts caused by the other perturbation forces. The solar sail is used here to expand the effects of the solar radiation pressure and to create a solar sail actuation in the opposite direction of the other disturbing forces. To achieve this purpose, the attitude of the solar sail is an important key to guarantee that the disturbing forces of the solar sail and the external forces acting on the spacecraft are opposite (OLIVEIRA et al., 2013a; OLIVEIRA et al., 2014).

The direction of the disturbing force or forces that needs or need to be reduced is set, then its opposite direction is the direction that the solar sail radiation force must be applied in order to reduce the shifts. The attitude of the solar sail is given by the unit vector  $\hat{n}$  and the direction of the force given by the solar sail  $\hat{f}$  is opposite to the disturbing forces. The solution of the optimal attitude of the solar sail is accomplished by applying the Newton's method for non-linear systems with the help of Equation 2.12 and the fact that  $\cos \phi = \hat{\sigma} \cdot \hat{n}$  (RUGGIERO et al., 1996; OLIVEIRA; PRADO, 2014b).

For the solar sail, the shape considered is a smooth surface with negligible base area  $\Delta s$ , as shown in Figure 2.4 . Once the solar sail has a smooth surface, there is no need to define the shape of the solar sail surface. It is only necessary to define the area of the smooth surface  $A_s$  and the normal unit vector of the solar sail for its attitude.

The solar sail is used to compensate the other perturbation forces effects, which deviates the orbit of the spacecraft. Therefore, it is considered that the spacecraft is able to change the attitude of the solar sail at every instant of time, compensating the torques and other perturbations that the attitude motion suffers.

Figure 2.4 – The representation of the spacecraft with a rectangular shape with one of its face pointed towards the radial direction and the solar sail representation.



It is proposed two types of solar sails in this thesis: an optimal sail and a sub-optimal one. The optimal one has an optimal attitude and variable area  $A_s$ . The optimal attitude means that the solar sail can freely change its attitude to guarantee that the solar sail perturbation force is always opposite to the disturbing force that needs to be reduced. The variable area is capable of controlling the magnitude of the sail and adjusting its magnitude according to the magnitude of the disturbing forces.

The sub-optimal case considers that the area  $A_s$  is fixed, but the attitude of the solar sail is optimal. The sub-optimal case cannot guarantee that the magnitude of the sail has the same magnitude of the disturbing forces to be compensated.

There are some parts of the orbit where the solar radiation pressure cannot control the other perturbation forces, whether because the spacecraft is on the shadow of the Earth or because the optimal angle of the incident of the flux of the Sun radiation  $\vartheta$  is larger than  $\pi/2$  rad. Whenever the solar radiation cannot help to control the other perturbation forces, the solar sail becomes inactive by rotating the panels to a direction perpendicular to the normal of the surface of the solar sail with the direction of the light flux. In this way, the light flux collides with the neglected base area of the solar sail and it becomes inactive. (OLIVEIRA; PRADO, 2014b).

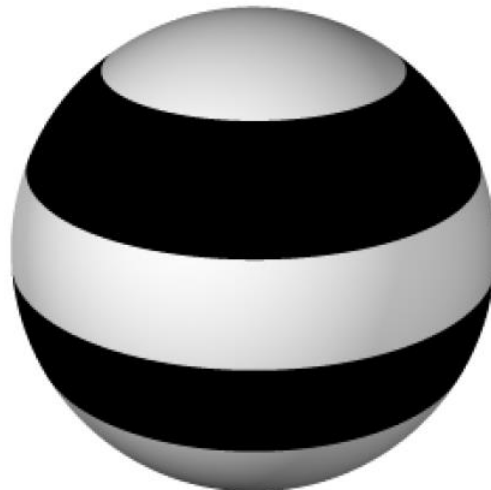
#### 2.4. The Spherical Harmonics $J_n$ And $C_{22}$

Planets do not have a perfect symmetry of a spherical shape. The most important reason for that is the mass displacement due to the rotation about an axis. This mass displacement causes a bulging at the equator of the body and a flattened at the poles, resulting in an oblate body. The Earth is not different and its non-symmetry can cause a non-Keplerian orbit for the spacecraft.

The second prominent mass displacement is due to the flattening at the equator. This flattening is well observed, in particular in the geostationary orbits, where the longitude of the orbit is dragged to Sri Lanka.

The non-symmetry of the Earth is usually described with the spherical harmonics. The gravity is a conservative force, therefore, it has no influence on the total energy of the system and it can be written as a gradient of a scalar function. The scalar function, known as geogravitational potential is a sum of zonal and tesseral terms in an equation. The zonal terms are related to the different zones of the spherical shape, as shown in Figure 2.5. The tesseral terms are related to different zones, cutting the spherical shape in a longitudinal form, as shown in Figure 2.6. A special case of the tesseral terms are known as sectorial terms, shown in Figure 2.7.

Figure 2.5 – Exemplification of the zonal terms.



Source: [Kuga et al. \(2011\)](#).

Figure 2.6 – Exemplification of the tesseral terms.



Source: [Kuga et al. \(2011\)](#).

Figure 2.7 – Exemplification of the sectorial terms.



Source: [Kuga et al. \(2011\)](#).

This thesis includes the zonal terms ( $J_2$ ,  $J_3$  and  $J_4$ ) and the sectorial term ( $C_{22}$ ). The most important non-symmetry comes from the zonal term that is related to an oblate planet ( $J_2$ ) and the flatter at the equator ( $C_{22}$ ).

The geogravitational potential  $P_{JC}$  of the Earth due to the zonal terms and the sectorial term considered in this work can be written as (TEWARI, 2007; KUGA et al., 2011)

$$P_{JC}(r, \varphi, \theta) = -\frac{\mu}{r} \left\{ \sum_{n=2}^4 \left( \frac{R_e}{r} \right)^n J_n P_n(\cos \theta) - \left( \frac{R_e}{r} \right)^2 C_{22} \cos(2 \cdot \varphi) P_{22} \right\} \quad (2.13)$$

where  $\theta$  is the co-latitude and  $\varphi$  is the longitude of the spacecraft according to the centre of the mass of the system,  $r$  is the distance of the spacecraft from the centre of mass,  $R_e$  is the equatorial radius of the planet,  $J_n$  is the zonal coefficients,  $C_{22}$  is a sectorial coefficient,  $P_n$  is the Legendre polynomials and  $P_{22}$  is an associated Legendre function.

The coefficients  $J_n$  and  $C_{22}$  are unique for each body. They represent the spherical harmonics of the planetary mass distribution, and they reduce in magnitude as the order  $n$  increases for the Earth. In his way, the largest one is the term  $J_2$ , due to the oblate symmetry. It denotes a non-dimensional difference between the moments of inertia about the polar axis and an axis in the equatorial plane. The next higher-order form is the term  $J_3$ , which indicates the pear-shaped, or triangular.  $J_4$  and  $J_5$  are the measures of a square and a pentagonal shaped harmonics, respectively. The  $C_{22}$  represents an oblate symmetry as well, flatted at the Equator. The four spherical harmonics normalized considered in this work are given by  $\bar{J}_2 = -484.16555 \times 10^{-6}$ ,  $\bar{J}_3 = 0.95848 \times 10^{-6}$ ,  $\bar{J}_4 = 0.53997 \times 10^{-6}$  and  $\bar{C}_{22} = 0.24394 \times 10^{-5}$  (TEWARI, 2007; KUGA et al., 2011).

The acceleration caused by the spherical harmonics is obtained by taking the gradient of the geogravity potential given in Equation 2.13 with respect to the position vector, as follows (TEWARI, 2007; KUGA et al., 2011).

$$\mathbf{a}_{JnC22} = -\left( \frac{\partial P_{JC}}{\partial \mathbf{r}} \right)^T = -\left( \frac{\partial P_{JC}}{\partial r} \right) \mathbf{i}_r - \left( \frac{1}{r \sin \theta} \frac{\partial P_{JC}}{\partial \varphi} \right) \mathbf{i}_\varphi - \left( \frac{1}{r} \frac{\partial P_{JC}}{\partial \theta} \right) \mathbf{i}_\theta \quad (2.14)$$

or,

$$\frac{\partial P_{JC}}{\partial r} = \frac{GM}{r^2} \left[ \begin{aligned} &3\bar{J}_2 \left(\frac{Re}{r}\right)^2 \bar{P}_2(\sin \theta) + 4\bar{J}_3 \left(\frac{Re}{r}\right)^3 \bar{P}_3(\sin \theta) + \\ &5\bar{J}_4 \left(\frac{Re}{r}\right)^4 \bar{P}_4(\sin \theta) - 3 \left(\frac{Re}{r}\right)^2 \bar{C}_{22} \cos 2\varphi \bar{P}_{22} \end{aligned} \right] \quad (2.15)$$

$$\frac{\partial \varphi_{JC}}{\partial \theta} = \frac{GM}{r} [2\bar{C}_{22} \sin 2\varphi \bar{P}_{22}] \quad (2.16)$$

$$\frac{\partial P_{JC}}{\partial \theta} = -\frac{GM}{r} \left[ \begin{aligned} &\bar{J}_2 \left(\frac{Re}{r}\right)^2 \sin \theta \bar{P}'_2(\sin \theta) + \bar{J}_3 \left(\frac{Re}{r}\right)^3 \sin \theta \bar{P}'_3(\sin \theta) + \\ &\bar{J}_4 \left(\frac{Re}{r}\right)^4 \sin \theta \bar{P}'_4(\sin \theta) + \left(\frac{Re}{r}\right)^2 \sin \theta \bar{C}_{22} \cos 2\varphi \bar{P}'_{22} \end{aligned} \right] \quad (2.17)$$

where  $\bar{P}_n$  and  $\bar{C}_{22}$  are the Legendre polynomials and the normalized associated function of Legendre, respectively; and the sub-index " ' " means the derivative in terms of  $\theta$ .  $G$  is the universal gravitational constant (assumed to be  $6.67259 \times \frac{10^{-11}m^3}{kg \cdot s^2}$ )

The position vector  $\mathbf{r}$  is given as follows

$$\mathbf{r} = r\mathbf{i}_r + r \varphi \sin \theta \mathbf{i}_\varphi + r\theta\mathbf{i}_\theta \quad (2.18)$$

in the reference system  $(r, \varphi, \theta)$ .

The unit vector denotes the radial, longitudinal, and southward directions, in the local horizon frame attached to the spacecraft.

## 2.5. The Third-Body Perturbation

In its simplest form, an orbit model can be created by assuming that only two bodies are involved, both of them behaving as spherical point-masses. One of them with negligible mass, the other one with significant mass, and no other force acting in the bodies. For this case, the model is simplified to a Keplerian orbit.

Nevertheless, in our solar system, there are not only two bodies involved. There are the presence of other gravitational bodies such as the Sun, the Moon and

planets. The gravitational influence of those bodies deviates the spacecraft from the Keplerian orbit. Therefore, they can be considered as disturbing forces.

The third-body perturbation comes from a third massive body with gravitational influence strong enough to disturb the Keplerian orbit of a two-body problem. For spacecrafts orbiting the Earth, it is usually studied the gravitational perturbation of the Sun and the Moon.

In mathematical terms, if the spacecraft mass is neglected and the masses of the Earth and the third-body ( $m_{tb}$ ) cannot be neglected, then the acceleration due to the third-body perturbation becomes (TEWARI, 2007; PRADO, 2013)

$$\mathbf{a}_{third-body} = -Gm_{tb} \left( \frac{1}{r_{etb}^3} \mathbf{r}_{etb} + \frac{1}{r_{tbs}^3} \mathbf{r}_{tbs} \right) \quad (2.19)$$

where  $\mathbf{r}_{etb}$  is the vector from the Earth to the third-body,  $\mathbf{r}_{tbs}$  is the vector from the third-body to the spacecraft and  $m_{tb}$  is the mass of the third-body (assumed to be  $7.349 \times 10^{22}$  kg for the Moon and  $1.98892 \times 10^{30}$  kg for the Sun).

The third-body perturbation is a conservative perturbation force since its nature comes from gravitational forces. So, it can be written as a scale function or as a potential. The scalar function due to the third-body perturbation is given as (TEWARI, 2007; PRADO, 2013)

$$P_{tb} = Gm_{tb} \left( -\frac{1}{r_{etb}} + \frac{\mathbf{r} \cdot \mathbf{r}_{tbs}}{r_{tbs}^3} \right) \quad (2.20)$$

where  $\mathbf{r}$  is the vector from the Earth to the spacecraft.

The potential is related to the acceleration as follows

$$\mathbf{a}_{third-body} = \left( \frac{\partial P_{tb}}{\partial \mathbf{r}} \right)^T \quad (2.21)$$

## 2.6. The Atmospheric Drag

The atmosphere can be understood as several layers of gases around the planetary surface linked to the planet by the gravitational force.

A spacecraft passing through the atmosphere is influenced by the atmospheric drag. This perturbation is non-conservative and causes orbital decay.

It is highly important to define the atmosphere in order to define later the atmospheric drag perturbation.

In the lowest layer, less than 15 km, the atmosphere can be regarded as in a thermal equilibrium with negligible external influences, such as electromagnetic disturbances and chemical reaction. However, this layer is under constant perturbation by horizontal winds and non-equilibrium phenomenon due to the presence of vapors. This layer comprehends the weather as we know it.

At low attitudes, from 0 to 86 km, it is possible to define the atmosphere with thermal and hydrostatic equilibrium with layers having a linear variation of the temperature with the altitude ([TEWARI, 2007](#)).

There are some commonly well-defined layers for low altitudes from 0 to 86 km. The troposphere extends from 0 to 11 km and it has a linear decrease the temperature with the altitude. The next level, known as stratosphere, consists of three layers with constant and linearly increasing temperature at different rates, respectively (from 11 to 47 km). Above this point there is the mesosphere, with isothermal layers along two consecutive layers with linearly decreasing temperature. ([TEWARI, 2007](#))

In the altitude from 86 to 500 km, there is the thermosphere, which experiences a nonlinear behavior due to the solar radiation and sun-spot activities. Beyond that layer lies the exosphere. This region also has a nonlinear behavior, due to the electromagnetic effects of ionized gas due to the interaction of the solar wind and the atmosphere.

The atmosphere is highly non-linear and dependable of external conditions such as solar activity and the magnetic field of the Earth. The model that should be included for the atmosphere at these altitudes must be a complex one that comprehends and predicts the magnetic field and the sun activity with great precision. This model is not within the scope of this work and it is used a less precise, but still valid model for the orbital analysis presented here.

The Jacchia Reference Atmosphere is an atmospheric model that covers the altitude from 90 to 2500 km. This model is more complex and it includes latitudinal, seasonal, geomagnetic and solar effects ([JACCHIA, 1977](#)). This model was developed in 1970 and updated in 1971 and 1977. Jacchia's models are based mostly on spacecraft drag data ([JACCHIA, 1971](#)). Assuming diffusive equilibrium, the atmospheric profiles are defined by the exospheric temperature. It contributed with the thermospheric part (110 km to 200 km) to the CIRA-72 model. [Jacchia \(1964\)](#) was the first to point out the coupling between solar wind and atmosphere.

The MSIS Model 1986 or Mass-Spectrometer-Incoherent-Scatter (MSIS) model describes the neutral temperature and densities in the upper atmosphere (above about 100 km). The most important difference between the MSIS model and the Jacchia one is the new data analyzed and computed in the newest model. The new data sources include measurements from several rockets, spacecrafts (OGO 6, San Marco 3, AEROS-A, AE-C, AE-D, AE-E, ESRO 4, and DE 2), and incoherent scatter radars ([BATTEN et al., 1987](#)).

There is a new version of the MSIS Model 1986, the MSISE Model 1990. Above 72.5 km MSISE-90 is essentially a revised MSIS-86 model taking into account data derived from space shuttle flights and newer incoherent scatter results. For someone interested only in the thermosphere (above 120 km), the author recommends the MSIS-86 model. MSISE is also not the model of preference for specialized tropospheric work. It is better for studies that reach across several atmospheric boundaries ([HEDIN, 1991](#)).

This thesis uses a Standard Atmosphere Model that comprises consecutive layers of specified temperature ( $T_e$ ) variation with the altitude ( $h$ ),  $T_e(h)$ . It is chosen a convenient model with a linear variation of temperature vs. altitude for each nominal temperature at each layer. The model is divided in 21 layers and each layer has a nominal temperature that provides a linear variation of the temperature with the altitude. In Table 2.1 it is shown the standard atmosphere derived from the model implemented.

Table 2.1 – Standard Atmosphere Derived from 1976 and 1962 U. S Standard Atmospheres.

$i$	$h_i$ (km)	$T_i$ (K)	$R$ (J/kg*K)	$b$ (K/km)
1	0	288.15	287.0	-6.5
2	11.0191	216.65	287.0	0.0
3	20.0631	216.65	287.0	1.0
4	32.1619	228.65	287.0	2.8
5	47.3501	270.65	287.0	0.0
6	51.4125	270.65	287.0	-2.8
7	71.8020	214.65	287.02	-2.0
8	86	186.946	287.02	1.693
9	100	210.02	287.84	5.0
10	110	257.0	291.06	10.0
11	120	349.49	308.79	20.0
12	150	892.79	311.80	15.0
13	160	1022.2	313.69	10.0
14	170	1103.4	321.57	7.0

15	190	1205.4	336.68	5.0
16	230	1322.3	366.84	4.0
17	300	1432.3	416.88	3.3
18	400	1487.4	463.36	2.6
19	500	1506.1	493.63	1.7
20	600	1506.1	514.08	1.1
21	700	1507.6	514.08	0.0

Source: [Tewari, 2007](#).

The atmosphere model is a blend of two conventions for the atmosphere model, the 1976 U.S Standard Atmosphere ([COESA, 1976](#)), in the range  $0 \leq h \leq 86 \text{ km}$  of altitude, and the 1962 U.S Standard Atmosphere ([COESA, 1962](#)) up to  $h = 2000 \text{ km}$ .

The temperature variation  $T_e(h)$  is given as follows

$$T_e(h) = T_i + b(h + h_i) \quad (2.22)$$

where the subscript  $i$  refers to the quantities at the base of the layer (the nominal temperature),  $b$  is the thermal lapse rate and  $T_e$  is the temperature at altitude  $h$ .

The thermal lapse rate is given as follows

$$b = -\frac{(j-1)g}{nR} \quad (2.23)$$

where  $g$  is the acceleration due to gravity,  $R$  is the specific gas constant and  $j$  is the polytropic exponent, which is equal to the specific heat at the hydrostatic equilibrium. The pressure of the atmosphere  $p$  is given by the hydrostatic equation ([TEWARI, 2007](#))

$$p = p_i e^{-\left[\frac{g_0(h-h_i)}{RT_i}\right] \left[1 - \frac{\beta(h-h_i)}{2}\right]} \quad (2.24)$$

where  $g_0$  is the acceleration of the gravity at the sea level ( $\approx 9.81 \text{ m/s}$ ), and  $\beta$  is given by the expression  $\beta = \frac{2}{R_e}$ .

Once the pressure is set, the density is given by (TEWARI, 2007)

$$\rho = \frac{p}{RT_e} \quad (2.25)$$

The acceleration caused by the atmospheric drag is proportional to the product of the atmospheric density  $\rho$  and the square of the relative speed of the system  $v_r$ . It opposes the orbital motion. The acceleration is given as follows (TEWARI, 2007)

$$\mathbf{a}_{drag} = -qv_r \mathbf{v}_r \quad (2.26)$$

where

$$q = \frac{1}{2} \rho \frac{C_D A_D}{m} \quad (2.27)$$

where  $C_D$  is the drag coefficient (usually this value is  $\approx 2$ ),  $A_D$  is the area that is in contact with the atmosphere at the opposed direction of the orbital motion and  $m$  is the mass of the spacecraft (KUGA et al., 2011).

The relative speed of the system is given in Equation 2.28. It is assumed that the atmosphere rotates with the Earth at the same speed and rate (KUGA et al., 2011)

$$\mathbf{v}_r = \dot{\mathbf{r}} - \boldsymbol{\omega}_r \times \mathbf{r} \quad (2.28)$$

where  $\boldsymbol{\omega}_r$  is the angular velocity of the Earth's rotation and  $\dot{\mathbf{r}}$  is the velocity of the spacecraft relative to the inertial system.

## 2.7. The Electrodynamic Tether

There are two types of conductive tethers: the insulated wires and the bare ones. This thesis includes the study of both of them. This section of electrodynamic tethers covers the model of the magnetic field and the characteristics of the tethers.

The tether consists of two spacecraft of mass  $m_1$  and  $m_2$  linked by an inelastic tether of mass  $m_t$ . The tether is assumed to remain straight. The sub-satellites of the tether are given by rectangular shapes with area  $A_1$  and  $A_2$ .

The attitude (or orientation) of the tether is given by the in-plane pitch angle  $\alpha$  and the out-plane roll angle  $\gamma$ .

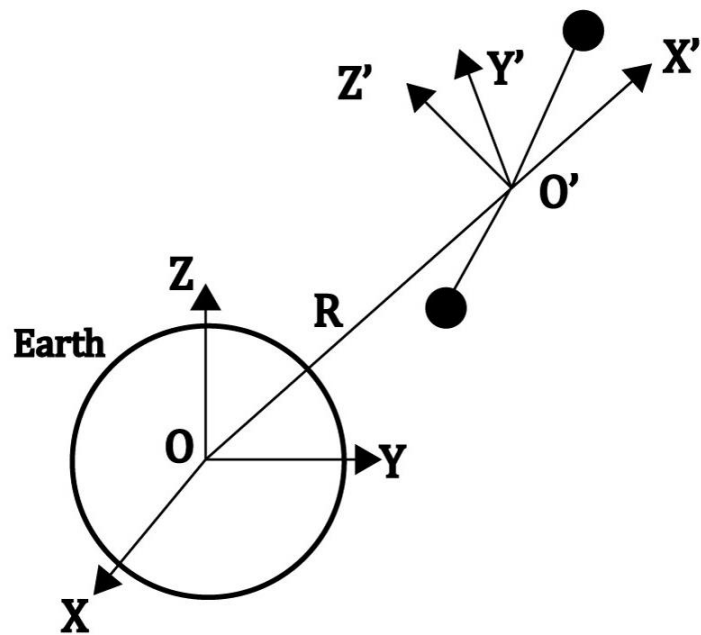
The rotation of the system about an axis parallel to the tether elongation does not have an effect on the dynamics of the EDT (LANOIX, 1999). For this reason, the rotation angle (yaw) is ignored in this thesis.

There are three main coordinate systems used in this thesis. The first one is the vernal coordinate system. The vernal coordinate system OXYZ is the inertial system of the thesis and it is used to calculate most of the perturbation forces. The OXYZ describes the position and velocity of the centre of mass of the system. The origin is at the centre of the Earth. The Z-axis points in the direction of the celestial North Pole. The X-axis points toward the vernal equinox. The Y-axis completes the right-handed set OXYZ.

The second coordinate system  $O'X'Y'Z'$  is used to describe the attitude of the tether. The EDT perturbation is strictly related to the attitude of the system. The  $X'$ -axis is parallel to the local vertical, that is, the position vector of the system centre of mass of the system from the centre of the Earth. The  $Z'$ -axis points in the direction of the angular momentum of the orbit and the  $Y'$ -axis completes the right-handed frame  $O'X'Y'Z'$ . The angle between the projection of  $m_2$  on the  $X'Y'$ -plane and the  $X'$ -axis gives the pitch angle  $\alpha$ . The angle between the

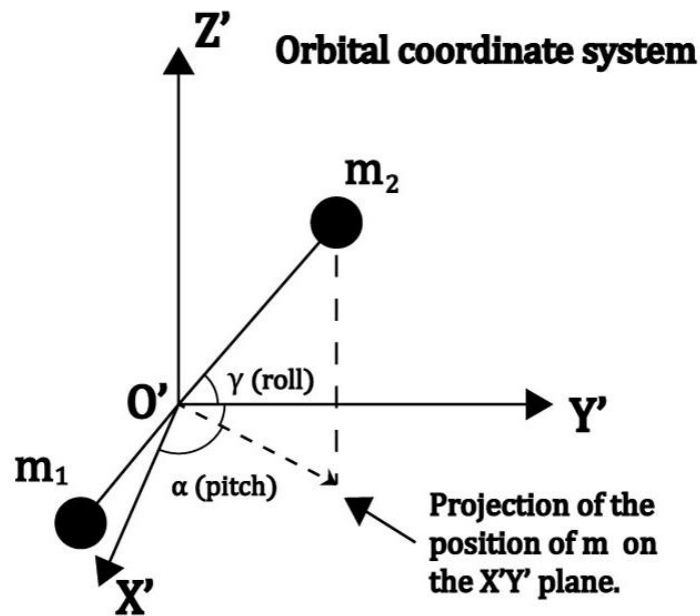
position vector of  $m_2$  relative to  $O'$  and its projection on the  $X'Y'$ - plane gives the roll angle  $\gamma$ . Figure 2.8 shows the  $OXYZ$  and  $O'X'Y'Z'$  coordinate systems. Figure 2.9 illustrates the definition of the pitch and roll angles.

Figure 2.8 – Representation of the coordinates systems  $OXYZ$  and  $O'X'Y'Z'$  with respect to the centre of the Earth and the center of mass of the spacecraft or the system.



Source: [Lanoix, 1999](#).

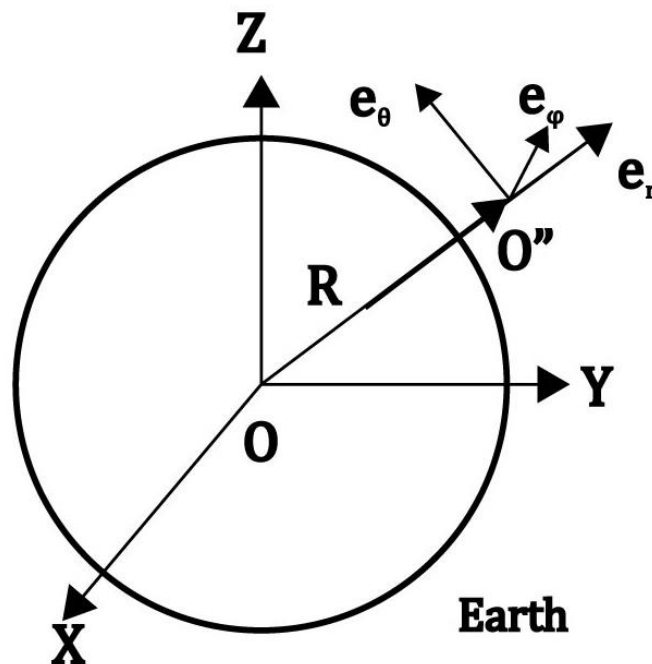
Figure 2.9 – Definition of the pitch and roll angles at the orbital coordinate system  $O'X'Y'Z'$ .



Source: [Lanoix, 1999](#).

The third coordinate system is used specially for the magnetic field model and the  $J_n$  and  $C_{22}$  perturbation. The geocentric coordinates are to  $r, \theta, \varphi$ , which are the radius, the co-latitude and the longitude, respectively. The direction  $e_r$  is parallel to the local vertical,  $e_\theta$  points eastward in the direction of the increasing longitude and  $e_\varphi$  lies in the direction of the increasing latitude (see Figure 2.10).

Figure 2.10 – The representation of the coordinates systems  $OXYZ$  and  $O''e_r, e_\theta, e_\varphi$  with respect to the centre of the Earth and the center of mass of the spacecraft or the system.



Source: [Lanoix, 1999](#).

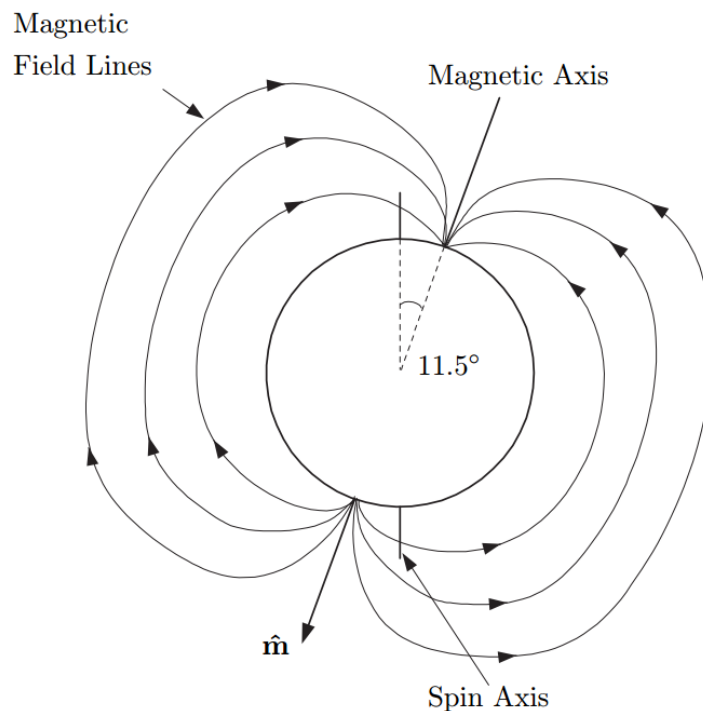
The tether is studied for two distinct and opposite goals. One of them is the use of an EDT to create a drag force to decay the system faster. The EDT is used as a de-orbiter. The second study investigates the EDT as a propulsion system capable of reducing the disturbing forces. This study is similar to the solar sail. In this case, the EDT can also reduce the atmospheric drag effect. The optimal attitude of the tether is given by finding the attitude that the tether should have at the centre of the mass of the system to create a Lorentz force on the opposite direction of the disturbing forces that needs to be reduced. The direction of the EDT perturbation and the disturbing forces are not exactly opposite, since the method based on the centre of the mass of the system does not consider the anomalies that the magnetic field may have. The magnetic field is not constant and it changes over the time. Nevertheless, the attitude is easily calculated with this method and does not require an optimization tool to find the optimal attitude. The method can be easily computed on-board to reduce or to increase the perturbation or drag effects.

### 2.7.1. The Magnetic Field Of The Earth

The motion of a conductive wire across the magnetic field of the Earth induces an EMF and, if there is a current passing through the wire, the Lorentz force is induced by the system. The induced Lorentz force can also occur when there is a battery that runs against the EMF and overcomes it. In this case, the direction of the force would be opposite to the force induced by the EMF.

In order to predict the EDT it is necessary to model the magnetic field of the Earth. The Earth's magnetic field generally resembles the field around a magnetized sphere, or a tilted dipole, as seen in Figure 2.11.

Figure 2.11 – Magnetic field geometry.



The geometry of the magnetic field of the Earth with  $\hat{m}$  axis as the magnetic axis and the spin axis inclined  $11.5^\circ$  from the last one.

Source: [Davis, 2004](#).

The magnetic axis is inclined around  $11.5^\circ$  from the spin axis, from the centre of the Earth.

The most used and well accepted model for the magnetic field of the Earth is the International Geomagnetic Reference Field (IGRF), and it is the model used in this thesis. The IGRF is based on the Gaussian coefficients,  $g_n^m$  and  $h_n^m$ , that are updated each 5 years. The present model of this thesis is the IGRF2010, which is good from 2010 to 2015 ([INTERNATIONAL GEOMAGNETIC... 2007](#)).

The magnetic field coefficients are given after several proposals and the best values that fit the data available by the International Association of Geomagnetism and Aeronomy (IAGA). The model includes secular variations and they are used to extrapolate the Gaussian coefficients to the date in question. The reader is encouraged to read more about the modeling of the magnetic field in the references cited here. The IGRF consists of 120 coefficients for each epoch (5 years) with 80 of them related to the secular variation ([DAVIS, 2004](#))

The IGRF considers the extrapolations and random variation in the magnetic field. The randomness is caused by external factors like the temporal variations that occur about every 27 days, when the active solar area of the Sun faces the Earth ([KRISTIN, 2001](#)). These variations can last from seconds to days. The other type of variation is caused by the interaction of the plasma of the ionosphere with the magnetic field. The auroral electrojet can cause significant changes in the magnetic field. Solar flares can also create temporal changes in the magnetic field of the Earth. The mathematics of the IGRF is given below ([KRISTIN, 2001](#)).

The magnetic field  $\mathbf{B}$  of the earth can be written as a negative gradient of a scalar potential  $V$  ([DAVIS, 2004](#))

$$\mathbf{B} = -\nabla V \quad (2.29)$$

The scalar potential  $V$  can be modeled by a spherical harmonic expansion as shown below ([DAVIS, 2004](#))

$$V(r, \theta, \varphi) = Re \sum_{n=1}^k \left(\frac{Re}{r}\right)^{n+1} \sum_{m=0}^n (g_n^m \cos m\varphi + h_n^m \sin m\varphi) P_n^m(\cos\theta) \quad (2.30)$$

where  $r, \theta, \varphi$  are the geocentric coordinates, which EW the radius, the co-latitude and the longitude, respectively. The coefficients  $g_n^m$  and  $h_n^m$  are the Gaussian coefficients and  $P_n^m(\theta)$  represents the Schmidt quasi-normalized associated Legendre functions with degree  $n$  and order  $m$ .

The magnetic field of the Earth can be computed by taking the gradient of Equation 2.30 for the geocentric coordinates, as given by Equations 2.31 to 2.33 (DAVIS, 2004)

$$B_r = \sum_{n=1}^k \left(\frac{Re}{r}\right)^{n+2} (n+1) \sum_{m=0}^n (g_n^m \cos m\varphi + h_n^m \sin m\varphi) P_n^m(\cos\theta) \quad (2.31)$$

$$B_\theta = - \sum_{n=1}^k \left(\frac{Re}{r}\right)^{n+2} \sum_{m=0}^n (g_n^m \cos m\varphi + h_n^m \sin m\varphi) \frac{\partial P_n^m(\cos\theta)}{\partial \theta} \quad (2.32)$$

$$B_\varphi = - \frac{1}{\sin\theta} \sum_{n=1}^k \left(\frac{Re}{r}\right)^{n+2} \sum_{m=0}^n m (-g_n^m \sin m\varphi + h_n^m \cos m\varphi) P_n^m(\cos\theta) \quad (2.33)$$

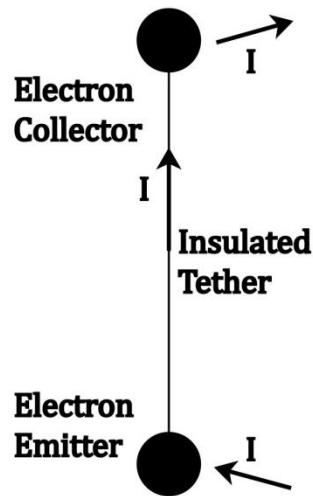
where the  $B_r$ ,  $B_\theta$  and the  $B_\varphi$  represents the field strength in local tangential coordinates and the other variables were defined before.

### 2.7.2. The Insulated Tether

The insulated tether can only exchange electrons with the ionosphere using the sub-satellites. The wire that connects these two sub-satellites is covered with an insulator. Since the wire is insulated, there is the Debye-sheath shielding (ESTES et al., 1997; SANMARTIN et al., 1993) effect. This effect limits the current of the wire. Lower currents produce lower induced Lorentz force. On the other hand, the system itself is efficient on releasing the electron using a hollow cathode or an electro gun (LANOIX, 1999).

Figures 2.12 and 2.13 show the design of the insulated tether and the electrical circuit for it, respectively.

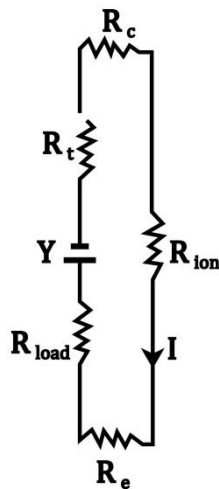
Figure 2.12 – Design of the insulated tether.



The design of the insulated tether with an electron emitter, an electron collector and the current flow along the tether.

Source: [Lanoix, 1999](#).

Figure 2.13 – Representation of the electrical circuit for the insulated tether.



The representation of the electrical circuit of the insulated tether with constant current flow and the resistances the system may have, like the impedance load, the tether resistance, the resistances of the tether emitter and collector.

Source: [Lanoix, 1999](#).

where  $R_{load}$  is the impedance of the load (which depends on the application);  $R_t$  is the tether resistance,  $R_e$  is the resistance of the tether emitter and the

resistance  $R_c$  of the tether collector. As in many other references, like [Johnson and Hermann \(1998\)](#), [Estes et al. \(1997\)](#), [Lorenzini et al. \(1997\)](#) and [Sanmartin et al. \(1993\)](#), the tether resistance  $R_t$  is neglected. Although the tether resistance is different from zero, this assumption is made due to the complexity of the equations and the minor differences on the results obtained with and without this assumption.

If  $R_{load}$  is negative, then there is a battery that drives the current against the induced EMF. If  $R_{load}$  is positive, then the current flows according to the EMF.

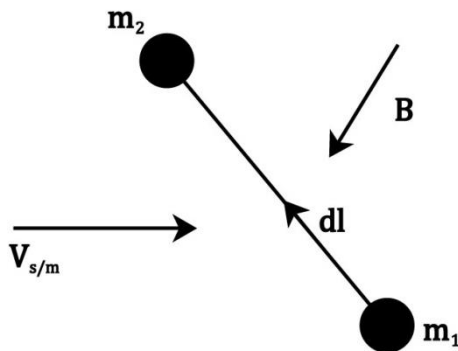
The induced EMF  $\gamma$ , or electrical potential induced in the system by the motion of a wire in the presence of a magnetic field, is given as follows ([LANOIX, 1999](#))

$$\zeta = \int_0^{L_{total}} \mathbf{v}_r \times \mathbf{B} \cdot d\mathbf{l} \quad (2.34)$$

where  $\mathbf{B}$  is the magnetic field,  $\mathbf{v}_r$  is the relative velocity of the system (the same presented in Equation 2.28),  $d\mathbf{l}$  is the infinitesimal vector element pointing along the tether from  $m_1$  to  $m_2$  and  $L_{total}$  is the length of the tether.

Figure 2.14 represents the end masses of the tether, the relative velocity and the magnetic field of the Earth.

Figure 2.14 – Tether motion through the magnetic field of the Earth.



Source: [Lanoix, 1999](#).

The EMF  $\zeta$  is positive whenever  $m_2$  has an electrical potential higher than  $m_1$  and the current  $I$  that passes through the tether is positive when the electrons flow from  $m_2$  to  $m_1$ .

If a battery is used to overcome the EMF, then  $m_1$  has an electrical potential higher than  $m_2$  and the current is negative with the electrons flowing from  $m_1$  to  $m_2$ .

The maximum current that can flow from the insulated tether with a zero  $R_{load}$  is given by the Parker-Murphy law (PARKER; MURPHY, 1976) with the help of the TSS-1R mission (THOMPSON et al. 1997):

$$I_{max} \approx K_1 n_e \sqrt{T_\infty} \left[ \frac{1}{2} + \left( \frac{\gamma}{\gamma_0} \right)^{0.528} \right] \quad (2.35)$$

where  $K_1 = 5.1255 \times 10^{-15} \text{ Amp} * \text{m}^3 / \text{K}^5$ ,  $n_e$  denotes the ionospheric electron density. This density can vary from  $10^{12} \text{ e}^-/\text{m}^3$  during the day to  $10^{10} \text{ e}^-/\text{m}^3$  at night.  $T_\infty$  is the undisturbed ionospheric plasma temperature and  $\gamma_0$  is given by (LANOIX, 1999)

$$\gamma_0 = \frac{AB^2 e^-}{8\pi m_e} \quad (2.36)$$

where  $A$  is the total surface area of the collecting electron body,  $B$  is the magnitude of the magnetic field,  $e^-$  represents the elementary electron charge and  $m_e$  is the electron mass.

The current flowing through the tether induces a Lorentz force that is given by (LANOIX, 1999)

$$\mathbf{F}_{mag} = \int_0^{L_{total}} I d\mathbf{L} \times \mathbf{B} \quad (2.37)$$

The current  $I$  can be factored out of the integral in Equation 2.37, since the current is constant across the system.

### 2.7.3. The Bare Tether

The bare tether consists on a bare wire that collects itself the electrons. The bare tether cannot release the electrons as efficiently as the insulated one. The bare tether system has one sub-satellite that acts as an electron emitter and the other end mass that serves as a ballast to keep the tether taut.

The bare tether does not have an insulated wire and, for that reason, the tether radius is much smaller and does not suffer from the Debye shielding effect. The Debye shielding effect limits the current of the tether for insulated systems. Therefore, the bare tether is capable of collecting more electrons and achieving greater currents (ESTES et al., 1997).

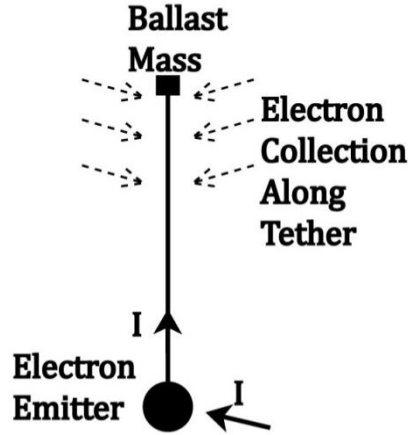
The bias voltage  $V^*$  for the bare tether is given by

$$V^*(l) = E_0 l - I_{max} R_{load} \quad (2.38)$$

where  $E_0$  is the motional electric field. The bias voltage can be understood as the difference between the motional EMF at the distance  $l$  of the tether from  $m_1$  and the voltage drop or rise for the load or battery, respectively (ESTES et al., 1997).

Figure 2.15 shows the design for a bare tether with the current flowing through the induced EMF and with a battery, respectively.

Figure 2.15 – The design of the bare tether.



The design of the bare tether with a ballast mass, the tether itself as an electron collector and the electron emitter.

Source: [Lanoix \(1999\)](#).

In mathematical terms, the electron collection in bare tethers, when the bias is positive, is given as follows ([ESTES et al., 1997](#); [SANMARTIN et al., 1993](#)).

$$I(l) = \frac{2}{3} K_2 n_e r_t \sqrt{E_0} \left[ l_c^{\frac{3}{2}} - \left( l - \frac{I_{max} R_{load}}{E_0} \right)^{\frac{3}{2}} \right] \quad (2.39)$$

where  $K_2 = 1.9 \times 10^{-13} C^{1.5} / kg^{0.5}$ ,  $n_e$  denotes the ionospheric electron density,  $r_t$  is the tether radius,  $E_0$  is the motional electric field [V/m],  $l_c$  is the electron collection length,  $I_{max}$  is the maximum value of the current and it does not change after the voltage bias becomes negative and  $R_{load}$  is the impedance load ([LANOIX, 1999](#)).

The tether electron collection length  $l_c$  is given by ([LANOIX, 1999](#)).

$$l_c = l_{tot} - \frac{I_{max} R_{load}}{E_0} \quad (2.40)$$

For the interval where the voltage bias is negative, the maximum current is given by Cosmo and Lorenzini (1997) as follows.

$$I_{max} = \frac{2}{3} K_2 n_e r_t \sqrt{E_0} l_c^{\frac{3}{2}} \quad (2.41)$$



### 3 RESULTS

This section provides the results of this thesis, obtained based on the mathematical formulations given before.

#### 3.1. Perturbation Integrals

This section presents the disturbing forces in the perturbation integrals analysis. The behavior of the disturbing forces is analyzed as a function of the Keplerian elements. Therefore, several orbits are included and the pattern of the disturbing forces is analyzed.

The shape of the spacecraft is considered to be rectangular with the area of each side equal and given by Table 3.1 . It is considered also that one of the faces of the spacecraft is always pointing towards the centre of the Earth.

In this section, the averaging technique for the PI and  $PI_{MAG}$  are used. Table 3.1 presents the initial parameters for the Perturbation Integral study.

Table 3.1 – Initial Parameters of the Spacecraft for the Perturbation Integrals studies.

Mass (kg)	$\epsilon$	$C_D$	Area (m <sup>2</sup> )
1000	0.8	2	6

##### 3.1.1. The Semi-Major Axis Variation

In order to guarantee that the results of the PI and  $PI_{MAG}$  are independent of the time of the integration, or the period of the orbit, the PI and  $PI_{MAG}$  results are multiplied by the period of a nominal orbit and divided by the period of the orbit under study.

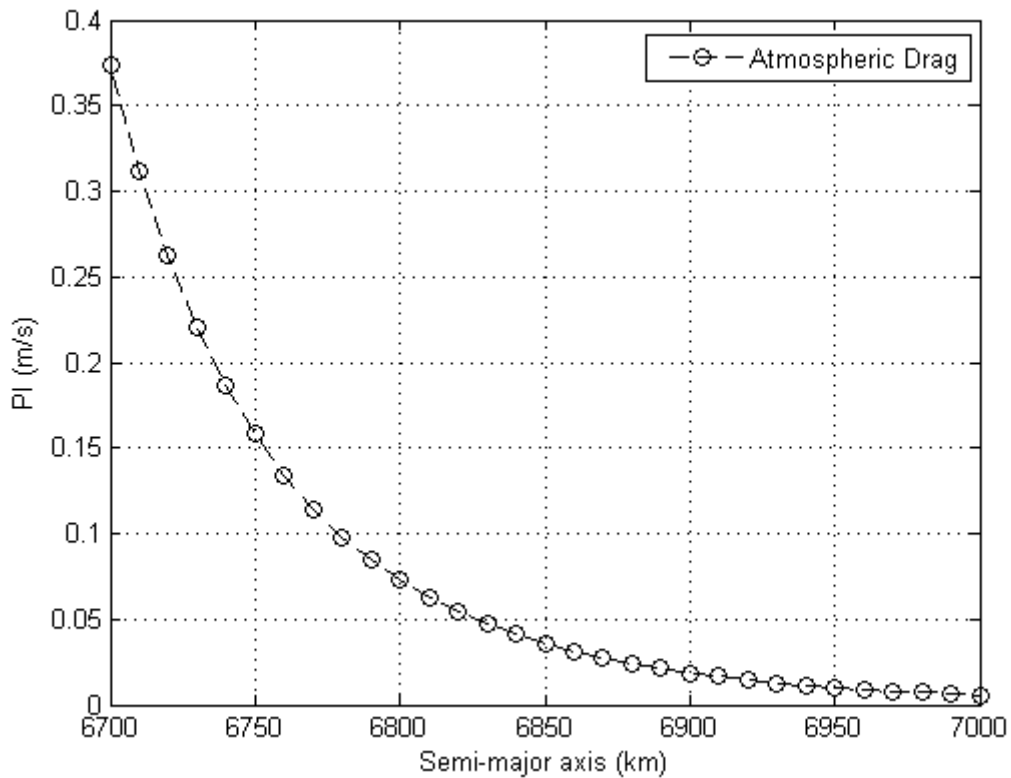
Table 3.2 – Initial Parameters of the Orbit for the PI and  $PI_{MAG}$  studies.

Eccentricity	Inclination	Argument of	Ascending
--------------	-------------	-------------	-----------

		Perigee	Node
0	0	0	0

Figure 3.1 shows the behavior of the disturbing forces change given by the PI as the semi-major axis varies from 6700 to 7000 km. The nominal orbit used has semi-major axis of 7000 km.

Figure 3.1 – PI of the atmospheric drag as a function of the semi-major axis from 6700 to 7000km.



The atmospheric drag decreases as the semi-major axis increases. This behavior occurs because the atmospheric density decreases exponentially with the altitude. In addition, the atmospheric drag is also related to the relative speed of the system (see Equation 2.28), so as the semi-major axis increases, this velocity decreases and so does the atmospheric drag acceleration.

It is hard to predict analytically the exponential decay without computing all the parameters since the density given by Equation 2.25 is related exponentially to the temperature, the thermal lapse and the altitude. Moreover, the drag acceleration is also related to the relative speed of the system (see Equation 2.25). On the other hand, Figure 3.1 shows the exponential decay as the altitude of the orbit is raised. The greatest advantage of the PI maps is that it is possible to interpolate easily the results and to estimate the disturbing force behavior by only accessing Figure 3.1. In other words, it gives a quantification of the effects of the drag force in terms of removing energy from the spacecraft.

If the PI of the atmospheric drag is interpolated as a polynomial function  $PI_{poly}$  of fourth degree, the result would be:  $PI_{poly}(x) = 1.6025 \cdot 10^{-10} x^4 - 4.4259 \cdot 10^{-6} x^3 + 4.5839 \cdot 10^{-2} x^2 - 2.1101 \cdot 10^2 x + 3.6424 \cdot 10^5$ , where  $x$  is the semi-major axis. This polynomial of fourth order leads to a precision of  $|PI_{poly} - PI| \leq 0.003$  m/s. it means that it is possible to obtain an analytical equation to predict the effects of the drag.

The PI is the magnitude of the velocity variation that a propulsion system must apply in order to keep the spacecraft in a Keplerian orbit all the time. Therefore, as the semi-major axis is increased, the velocity change required is reduced. As given by Equation 2.26, the atmospheric drag applies a force that is always on the opposite direction of the orbital motion.

Since the acceleration caused by the drag is always opposite to the direction of motion, it gives an interesting result: the estimative of the orbital decay based on the PI value for the atmospheric drag. The process that explains how it is possible is given as follows.

The equation of motion of the spacecraft with a non-impulsive disturbing acceleration or with a propulsion acceleration ( $F/m$ ) is given by Equation 3.1

$$\ddot{\mathbf{r}} = -\mu \frac{\mathbf{r}}{r^3} + \frac{\mathbf{F}}{m} \quad (3.1)$$

If the direction of the force  $\mathbf{F}$  is opposite to the direction of the orbital motion, then Equation 3.1 becomes

$$\ddot{\mathbf{r}} = -\mu \frac{\mathbf{r}}{r^3} + \frac{F \dot{\mathbf{r}}}{m \dot{r}} \quad (3.2)$$

Multiplying Equation 3.2 by a dot product of  $\dot{\mathbf{r}}$ , the equation becomes

$$\ddot{\mathbf{r}} \cdot \dot{\mathbf{r}} = -\mu \frac{\mathbf{r} \cdot \mathbf{v}}{r^3} + \frac{F \dot{\mathbf{r}} \cdot \dot{\mathbf{r}}}{m \dot{r}} \quad (3.3)$$

where  $\ddot{\mathbf{r}} \cdot \dot{\mathbf{r}} = \frac{1}{2} \frac{dv^2}{dt}$  and  $\mu \frac{\mathbf{r} \cdot \mathbf{v}}{r^3} = -\frac{d}{dt} \left( \frac{\mu}{r} \right)$ . Therefore, Equation 3.3 can be written as

$$\frac{d}{dt} \left( \frac{v^2}{2} - \frac{\mu}{r} \right) = \frac{F}{m} v \quad (3.4)$$

where  $v = \dot{r}$ .

The energy of an orbit is given by  $E = \frac{v^2}{2} - \frac{\mu}{r}$ .

If the orbit is circular, it is possible to reduce the Equation 3.4 to the following equation:

$$\frac{d}{dt} \left( \frac{\mu}{2r} - \frac{\mu}{r} \right) = \frac{F}{m} \sqrt{\frac{\mu}{r}} \quad (3.5)$$

Separating the variables, it is obtained

$$\frac{d\left(\frac{\mu}{r}\right)}{\sqrt{\frac{\mu}{r}}} = -2 \frac{F}{m} dt \quad (3.7)$$

Integrating both sides of Equation 3.7, the equation becomes

$$v_{final} - v_{initial} = -\frac{F}{m}\Delta t \quad (3.8)$$

The term  $\frac{F}{m}$  in Equation 3.8 can be approximated by  $PI/T$  if it is considered that the acceleration of the disturbing force (drag) is constant. The difference  $v_{final} - v_{initial}$  is the difference of the velocity of the spacecraft in the final orbit and in the initial orbit.

The force caused by the atmospheric drag is constant for the same altitude.

The approximation to estimate the time of the decay can be obtained by substituting  $\frac{F}{m}$  in Equation 3.8 by  $PI_{poly} / T$  and the velocity of the circular orbit  $v$  per  $\sqrt{\frac{\mu}{a}}$ , where  $a$  is the semi-major axis of the orbit. In this way, Equation 3.8 becomes

$$\Delta t_N = -\left(\sqrt{\frac{\mu}{a_{N+1}}} - \sqrt{\frac{\mu}{a_N}}\right) \frac{T_N}{PI_{poly(a)N}} \quad (3.9)$$

where  $N$  is the order of the step and  $T_N$  is the period of the orbit given by the orbit related to  $N$  step. If the result is given by  $M$  steps, then the total decay time  $t_{decay}$  is  $t_{decay} = \sum_{N=1}^M \Delta t_N$ .

As the order of steps is reduced, the precision is increased.

The idea to estimate the time of the decay based on the  $PI$  value is a rough approximation, since the correct way would be to integrate the motion equation as update the Keplerian elements over the time. As the orbit decay, for example, the eccentricity of the orbit increases and this method does not consider this fact. This rough approximation can be valid for small orbital decays or when the magnitude of the disturbing force is relatively large in a short time period. Nevertheless, this approximation always leads to errors.

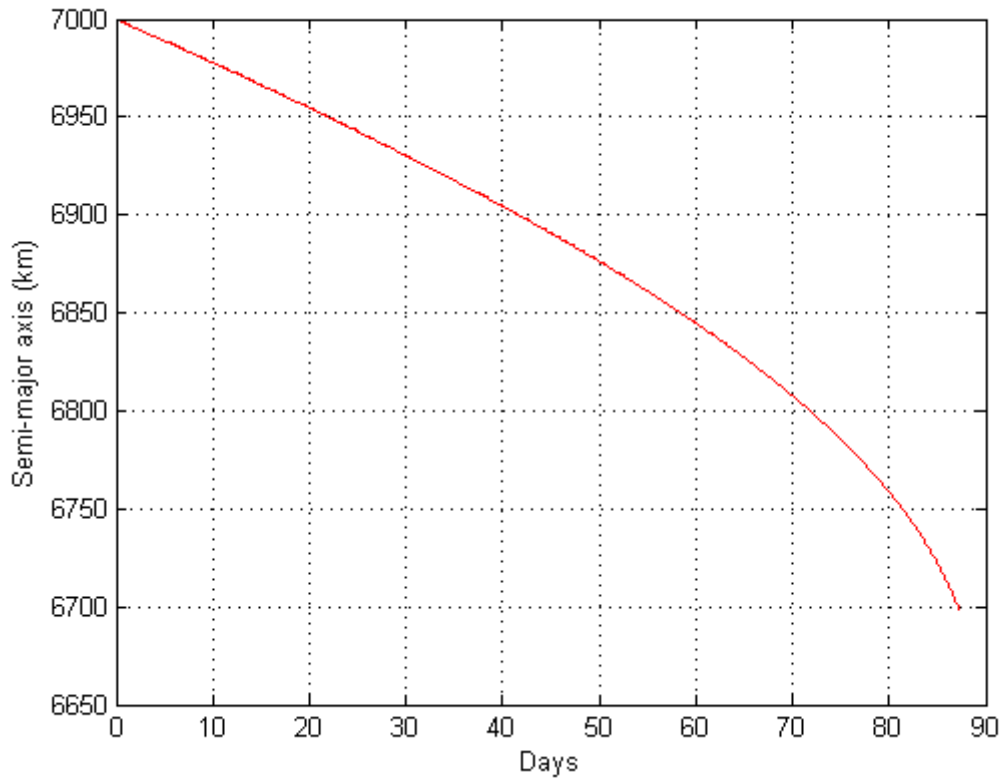
The idea of this thesis is to present the estimation of the orbit decay as a simple and practical tool, just like the PI method, for a first estimate the time of decay that a force in the opposite direction of motion would provoke in a spacecraft, if no propulsion system is used to regain its altitude. This tool does not require a sophisticated integration and atmosphere model or any simulator with numerical integration. Equation 3.9 and the map based on the PI are capable of estimating the time of decay.

This thesis is also not concerned with the analysis of the errors and the study of the boundaries that this method could be valid. It is just presented a potential new, fast and powerful method. The orbit analysts should study carefully if this method could be used to estimate the orbit decay for a first mission analysis according to the numerical errors and other effects.

If the method based on Equation 3.9 is applied with the help of Figure 3.1 for  $M = 31$  (number of steps), then the estimated time of decay would be 86.95 days from 7000 to 6700 km of semi-major axis.

In order to validate this method, the same initial parameters were computed in an orbit integrator. The orbit integrator estimated 88.78 days for the orbit to decay from 7000 to 6700 km of semi-major axis. The results are relatively close. This result, as many others that are included in this thesis, validate this method (see the electrodynamic section). But, once more, this method is not always valid as an estimative if the time of the integration is long enough to change drastically the Keplerian elements like eccentricity or argument of perigee. Figure 3.2 shows the semi-major axis decay as a function of time obtained by the orbit integrator.

Figure 3.2 – The semi-major axis time evolution in the presence of the atmospheric drag.



The atmospheric model used in this work may have some errors. The solar activity is not considered in this model and this activity can change drastically the upper layers of the atmosphere, especially the exosphere. Some other approximations considered in the atmospheric model may also lead to some errors.

Figures 3.3 and 3.4 show two hypothetical cases of errors in this model based on Figure 3.1. The first one considers an error on the density of the atmosphere of  $\pm 5\%$ , and the next one considers  $\pm 10\%$ . The error is based in the mathematical formulation of the atmosphere given in the last chapter.

Figure 3.3 – PI of the atmospheric drag with  $\pm 5\%$  of error of the density as a function of the semi-major axis from 6700 to 6800 km.

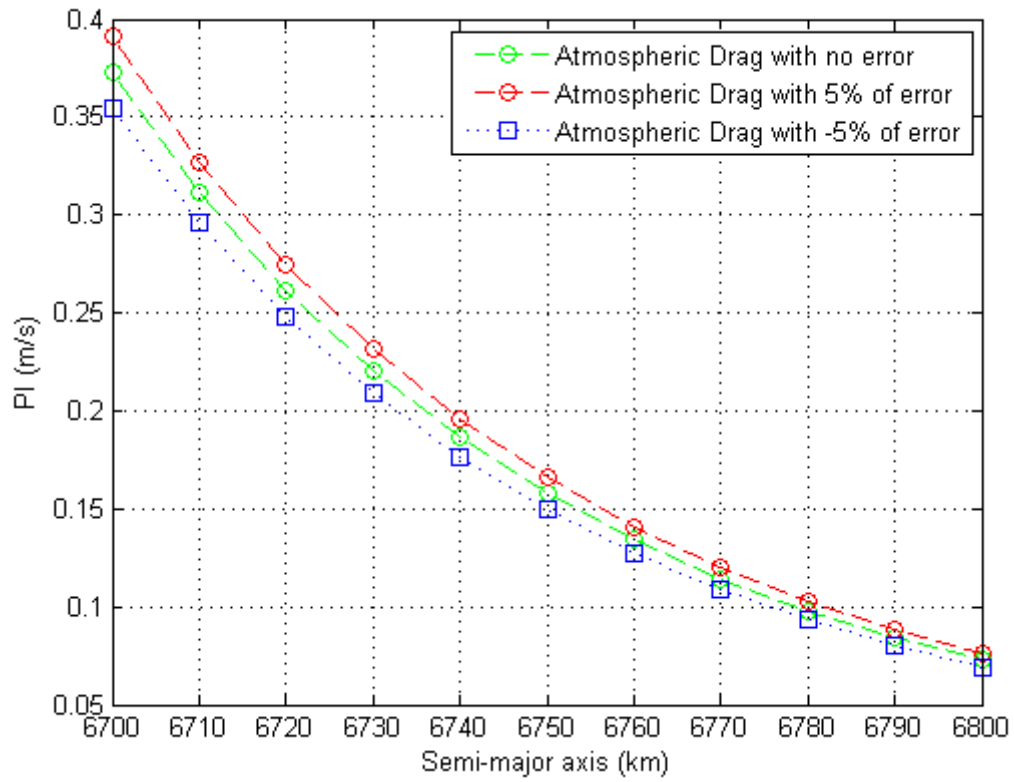
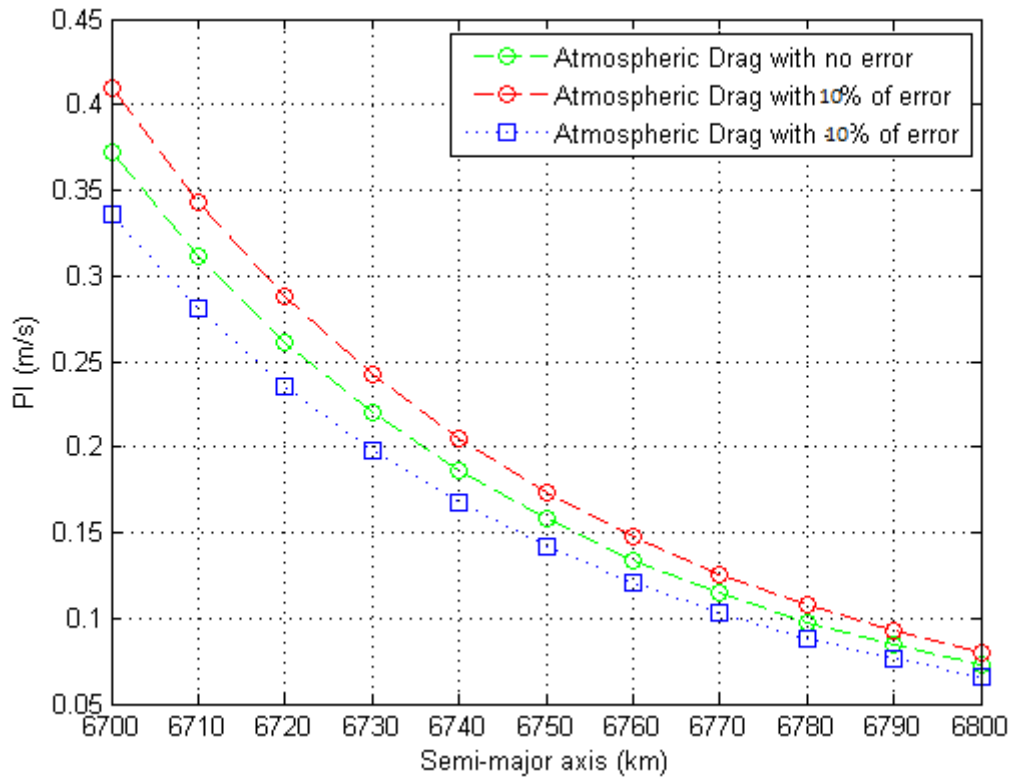


Figure 3.4 – PI of the atmospheric drag with  $\pm 10\%$  of error of the density as a function of the semi-major axis from 6700 to 6800 km.



The error in the density leads to different values of the PI. As the semi-major axis decreases, the altitude of the orbit decreases. Consequently, the density of the atmosphere increases. The error proposed in this analysis is based on the density of the atmosphere. It means that when the density increases, the error related to the magnitude of the atmospheric drag is also increased.

The analysis of the error in a model that is not accurate is essential to estimate the potential difference the PI must have and to study the viability of the mission before the launch, even if the atmospheric model is not 100% accurate.

The PI values for the other disturbing forces are given in Figures 3.5 and 3.6 .

Figure 3.5 – PI of the several disturbing forces as a function of the semi-major axis from 6700 to 7000km.

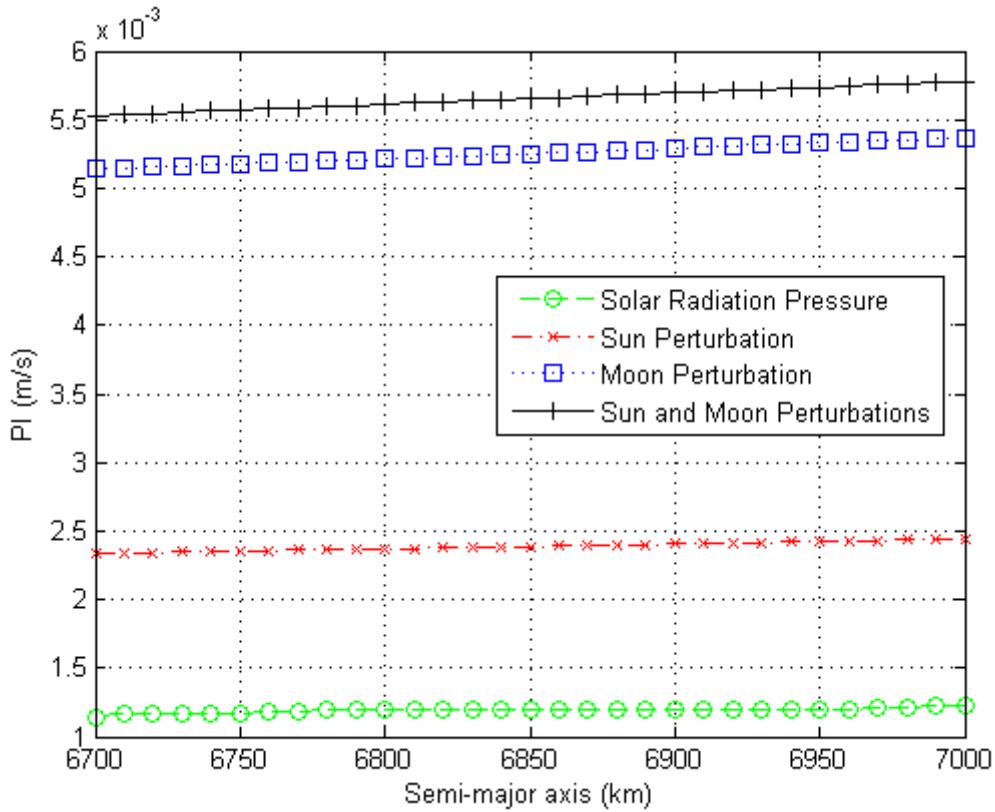


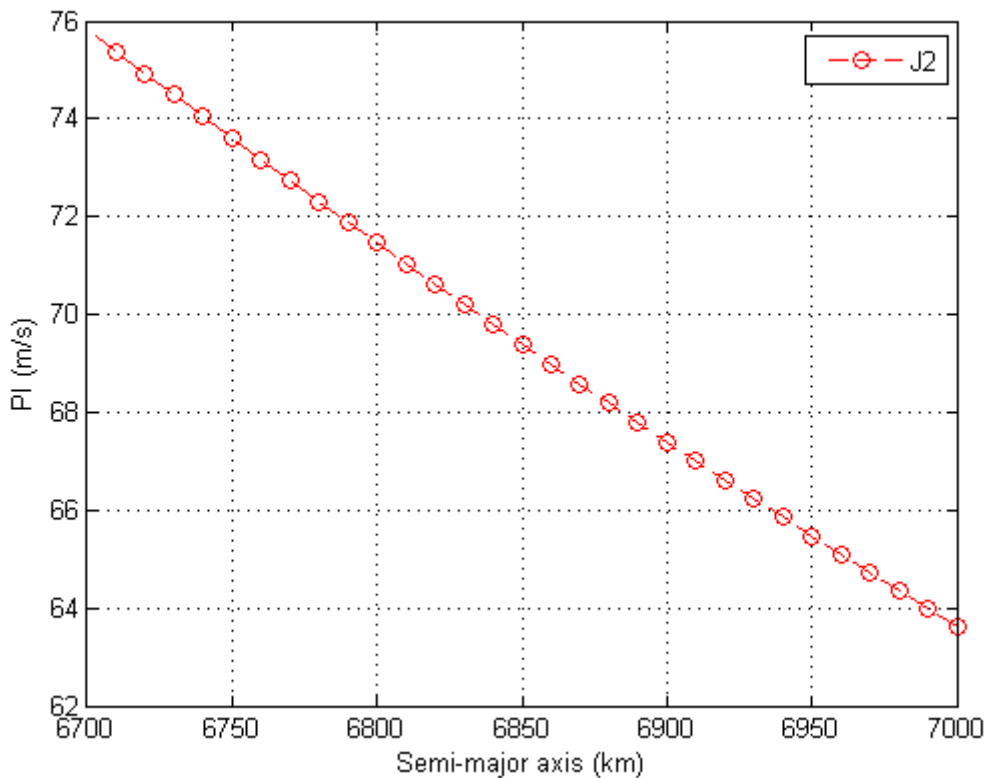
Figure 3.5 presents the variation of the PI for the disturbing forces of the Moon, the Sun and the solar radiation pressure. The magnitude of the perturbation of the Moon is more than two times larger than the Sun for this range of semi-major axis. The increase of the disturbing forces occurs gradually as the semi-major axis increases. As the semi-major axis increases, the mean distance from the spacecraft to the third-body (Sun and Moon) decreases, and, therefore, the magnitude of the perturbation, related to the square of the distance of the spacecraft to the third-body (see Equation 2.19) is decreased ( $\frac{1}{r_{tbs}^2}$ ).

The total velocity variation that must be applied to the spacecraft for one orbital period to eliminate the effects of the solar radiation pressure and the third-body perturbation is significantly low, in the order of  $\approx 10^{-3} m/s$ . This means that, for the orbits studied here, the low-thrust propulsion system is a good candidate to overcome those perturbing forces.

The sum of the solar and luni perturbation separately has different results from the computation of both effects together in the PI. This occurs because the Moon can sometimes compensate the solar radiation pressure effect and the Sun perturbation, depending on the geometry of the problem. In this way, the lunisolar perturbation is smaller than the third-body perturbation of the Sun and the Moon computed separately.

The range from the semi-major axis from 6700 to 7000 km includes LEO. For these orbits, the magnitude of the disturbing forces of the  $J_2$  is much larger if compared to the other disturbing forces, as shown in Figure 3.6 .

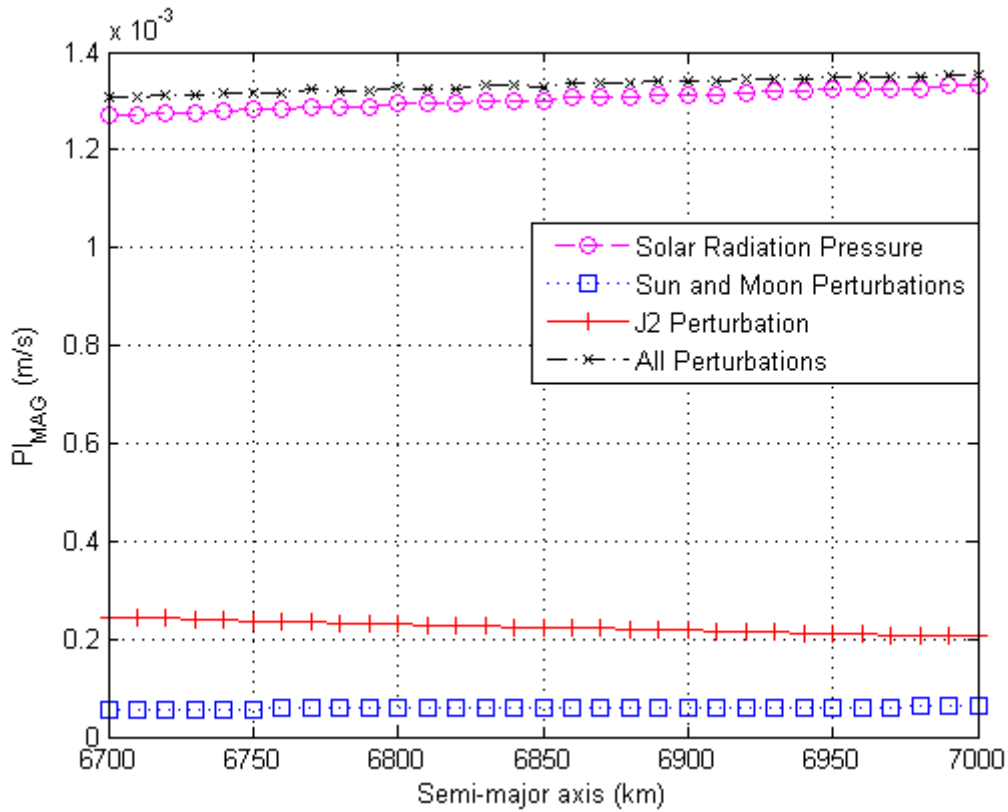
Figure 3.6 – PI of  $J_2$  disturbing force as a function of the semi-major axis from 6700 to 7000 km.



The magnitude of the perturbation caused by the  $J_2$  term is much larger than the atmospheric drag for this range. So, the range from 64 to 76 m/s of the PI becomes unviable for the propulsion system to correct the shifts caused by this perturbation.

Moreover, even though the  $J_2$  perturbation has the larger magnitude, this force is conservative and it requires less attention than the atmospheric drag. The atmospheric drag for this simulation can decay the spacecraft up to 300 km in approximately 85 days. The atmospheric drag is a non-conservative force and requires constant maneuvers. The  $J_2$  perturbation effect added to the  $J_3$ ,  $J_4$  and  $C_{22}$  can easily be maneuvered after several orbits since there are some compensations of the force for one orbital period. The same occurs for the third-body perturbation. Figure 3.7 shows the  $PI_{MAG}$  for the same simulation with the  $J_2$ , third-body and the solar radiation pressure perturbations.

Figure 3.7 –  $PI_{MAG}$  of several disturbing forces as a function of the semi-major axis from 6700 to 7000 km.



Since the third-body and the  $J_2$  perturbations are conservative forces, the  $PI_{MAG}$  of these forces is much smaller than the  $PI$  (compare Figures 3.5, 3.6 and 3.7). Even if the forces are conservative, the  $PI_{MAG}$  values are not zero. The  $PI$  and  $PI_{MAG}$  of the solar radiation pressure are similar, since the nature of this force is

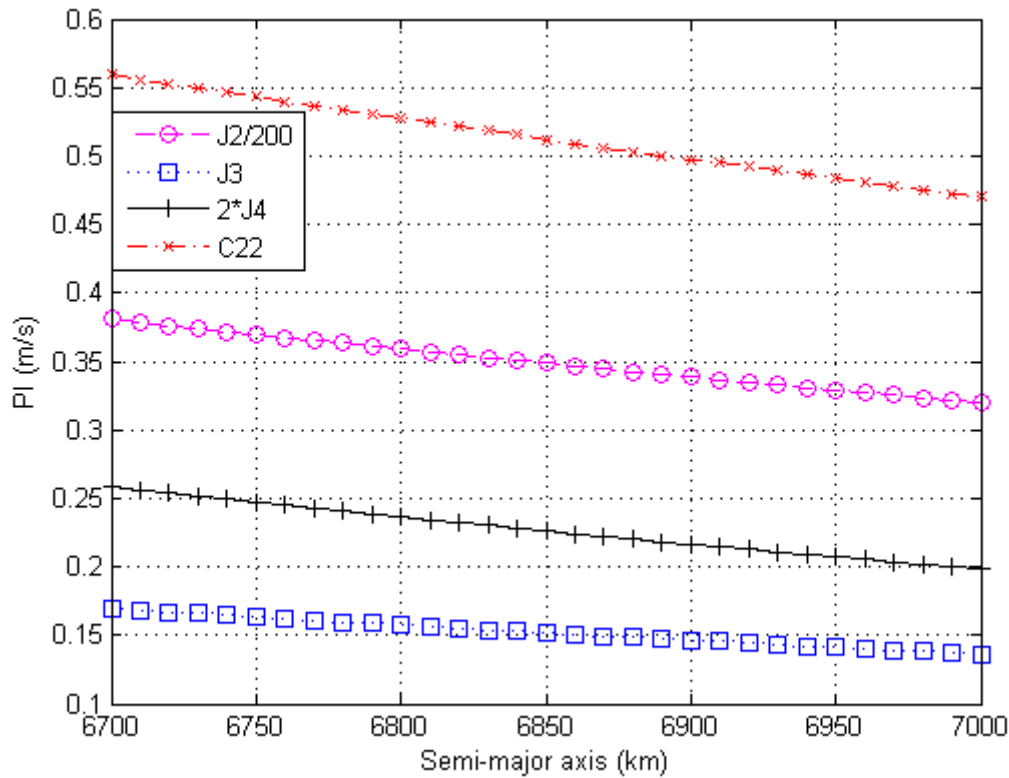
non-conservative and the integration occurs for one orbital period. The solar radiation force for the  $PI_{MAG}$  has the largest magnitude in Figure 3.7. The atmospheric drag and the solar radiation force are adequate for the  $PI_{MAG}$  since these forces are non-conservative. The atmospheric drag always acts on the direction of the motion of the spacecraft, so it changes the energy of the system. The best evaluation for the atmospheric drag and solar radiation pressure perturbations is the PI.

The pattern of the  $J_2$  perturbation, which decreases with the semi-major axis, also occurs for the  $PI_{MAG}$ . This occurs because any spherical harmonic perturbation of order “n” is inversely proportional to the distance to the centre of the Earth at the power “n”.

Nevertheless, the magnitude of  $PI_{MAG}$  from the  $J_2$  perturbation must be analyzed carefully. Figures 3.9 and 3.10 explain this point.

Figure 3.8 shows the PI of the disturbing forces of  $J_2$ ,  $J_3$  and  $J_4$  and  $C_{22}$  separately.

Figure 3.8 – PI of  $J_n$ 's and  $C_{22}$  disturbing forces as a function of the semi-major axis from 6700 to 7000 km.



Note that the values of the PI for  $J_2$  and  $J_4$  are modified in order to have the same disturbing forces in the same magnitude range. The  $J_2$  value is divided by 200. This means that the  $J_2$  magnitude perturbation is around 200 times larger than the  $J_3$  perturbation for this simulation. In Equations 2.15 and 2.17, it is possible to see that, if the order “n” of the  $J_n$  is increased, the magnitude of the disturbing force is decreased because of the multiplication of the term  $\left(\frac{Re}{r}\right)^n$ , where  $Re < r$  or even  $Re \ll r$ . It is also noted that the  $J_n$  coefficients as the degree and order increases.

Even if the coefficients  $J_3$  and  $J_4$  are much smaller than  $J_2$ , at this range, the  $J_3$  and  $J_4$  have a magnitude of the PI larger than the solar radiation pressure and the lunisolar perturbation.

The magnitude of the  $C_{22}$  perturbation is more than 3 times larger than the  $J_3$  perturbation for this simulation. Figure 3.8 shows that the PI values for  $J_2$  and  $C_{22}$  are the most prominent perturbations due to the spherical harmonics.

Figures 3.9 and 3.10 show the  $PI_{MAG}$  of the disturbing forces of  $J_2$ ,  $J_3$ ,  $J_4$  and  $C_{22}$ , separately.

Figure 3.9 –  $PI_{MAG}$  of the  $J_n$ 's and  $C_{22}$  disturbing forces as a function of the semi-major axis from 6700 to 7000 km.

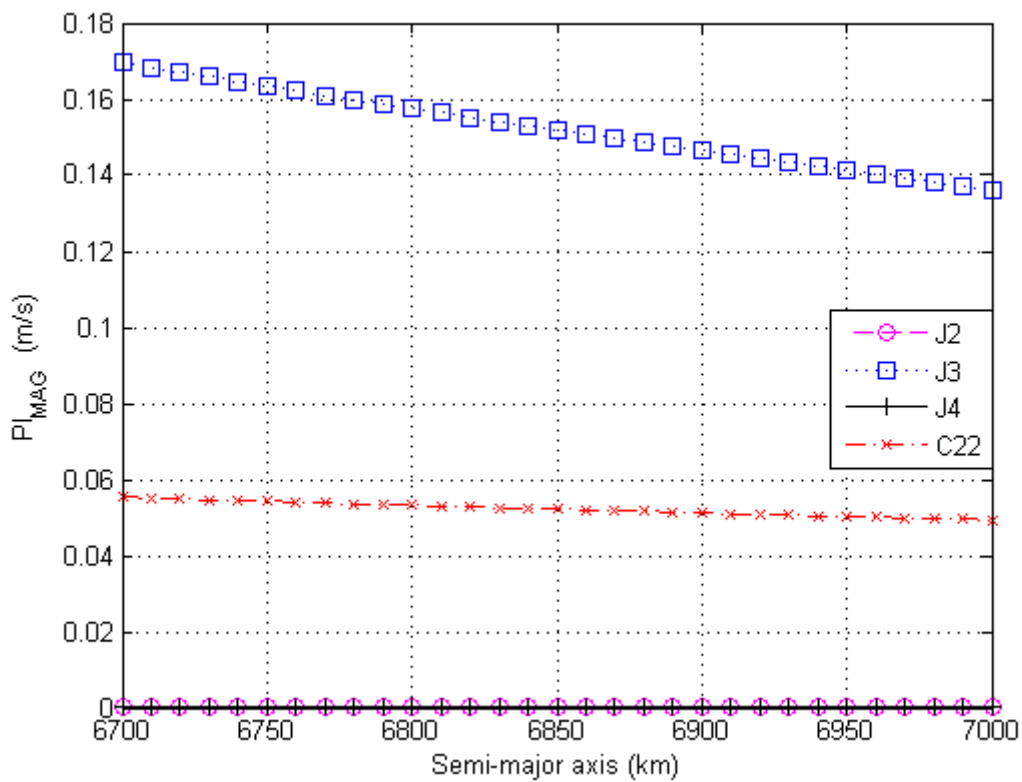
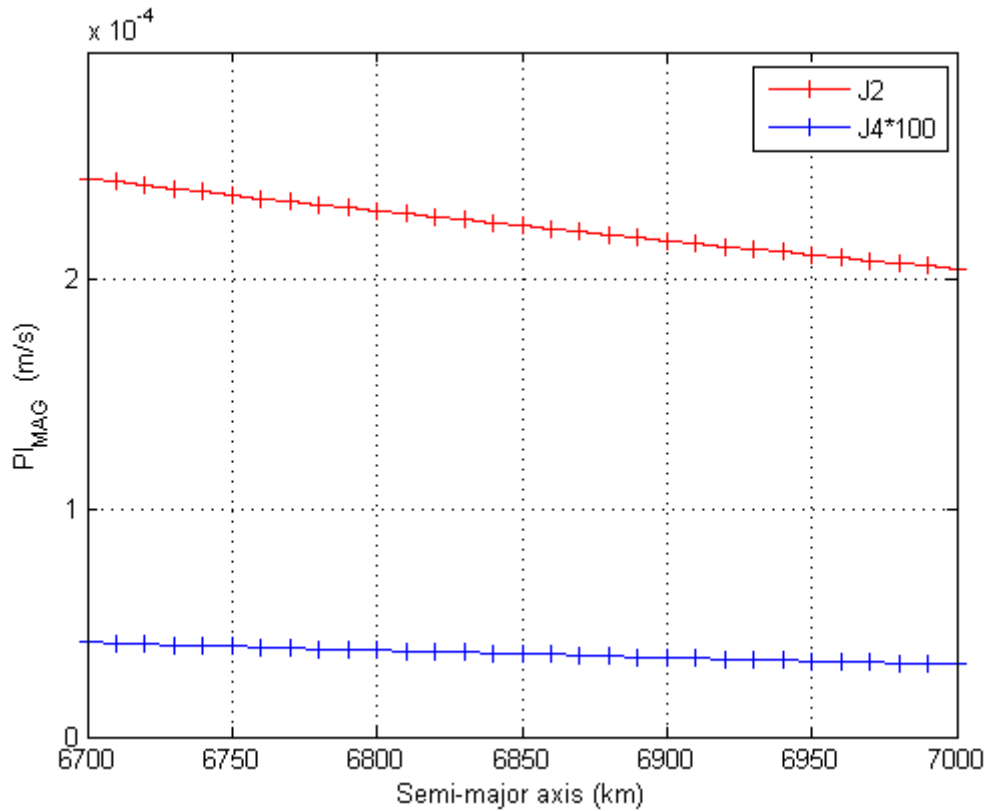


Figure 3.10 –  $PI_{MAG}$  of  $J_2$  and  $J_4$  disturbing forces as a function of the semi-major axis from 6700 to 7000 km.

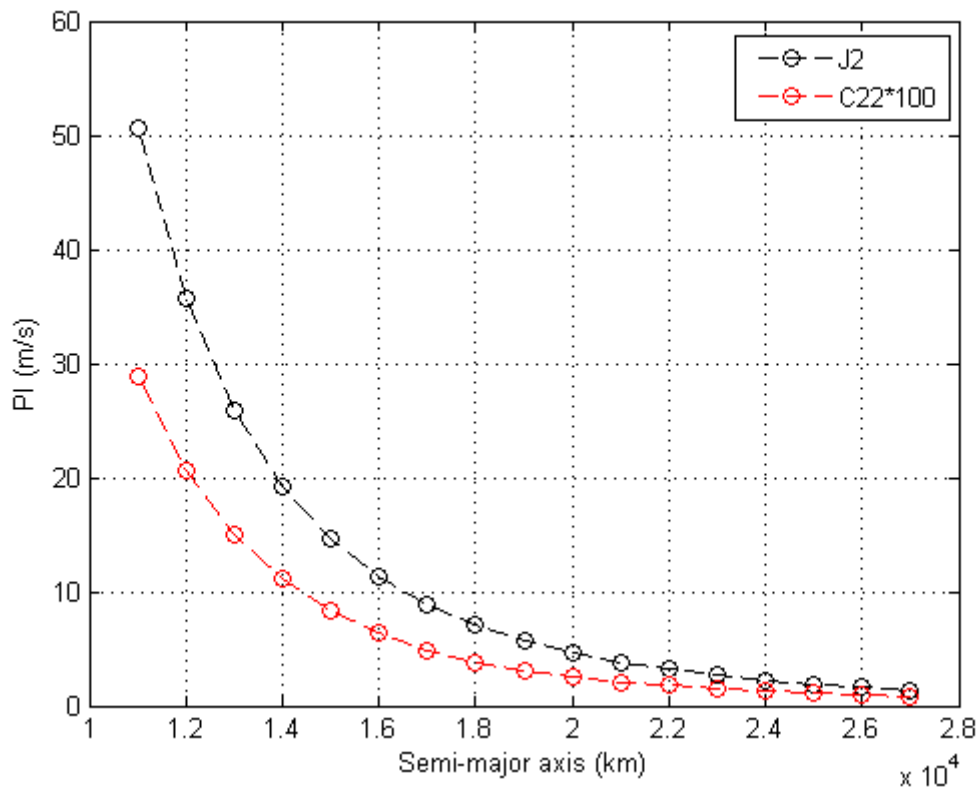


Figures 3.9 and 3.10 show an interesting result and the proof that the value of the  $PI_{MAG}$  should be studied in details. The magnitude of the  $PI_{MAG}$  of the  $J_3$  perturbation and  $C_{22}$  are much larger than the  $J_2$  and  $J_4$  perturbations. The  $PI_{MAG}$  considers the compensations of the perturbations for one orbital period. The most important difference from  $J_2$  and  $J_4$  perturbations compared to  $J_3$  and  $C_{22}$  perturbations is the shape of the perturbations. While the  $J_2$  and  $J_4$  perturbations comes from ellipsoid and square shapes, the  $J_3$  is a pear-shaped perturbation and  $C_{22}$  is asymmetric. The geometries of the pear shape and of the uniform shape of  $C_{22}$  at the  $PI_{MAG}$  allow less compensations of the perturbations, since the geometric nature of this perturbation is not symmetric, as the ellipsoid or the square for orbits with zero inclination.

The  $PI_{MAG}$ , later on in this thesis, will prove to be extremely valuable to find less perturbed orbits when a symmetric perturbation is considered and centered in the centre of the inertial coordinate system.

The behavior of the disturbing forces is not always like the range of 6700 to 7000 km. The next investigations regarding the semi-major axis include the range from 11000 to 27000 of the MEO (Medium Earth Orbits), with a nominal orbit of 20000 km and from 32000 to 52000 for the HEO (High Earth Orbits), with a nominal orbit of 45000 km of semi-major axis. The MEO and HEO orbits are not at all influenced by the atmospheric drag.

Figure 3.11 – PI of  $J_2$  and  $C_{22}$  disturbing force as a function of the semi-major axis from 11000 to 27000 km.

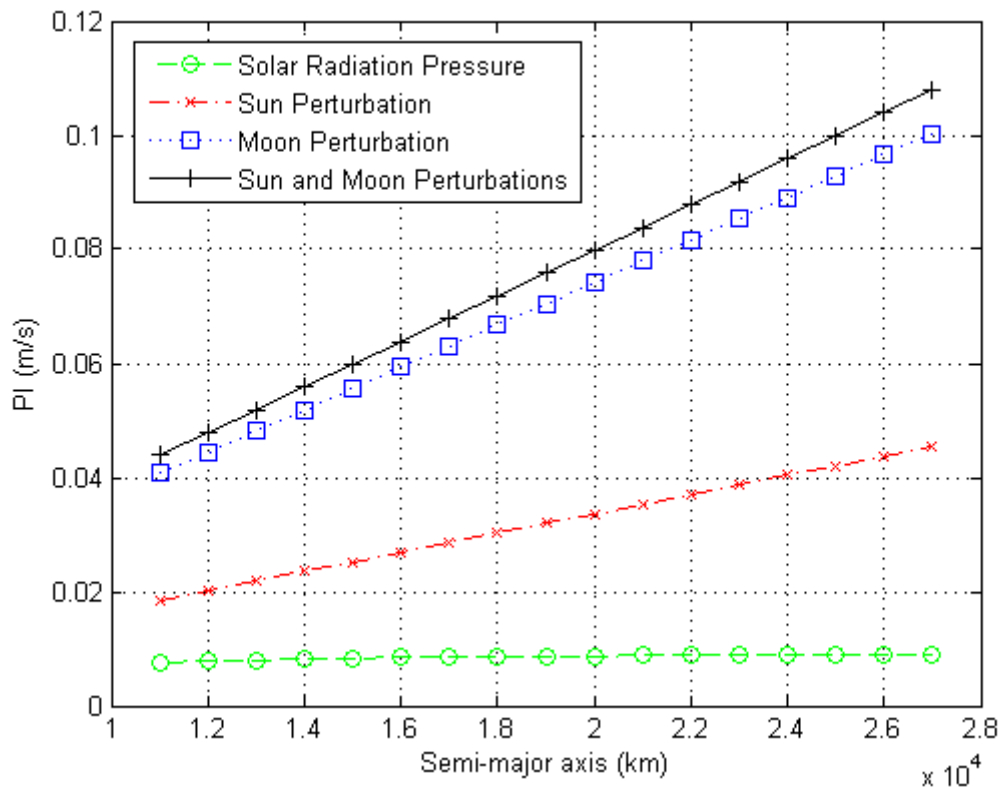


In Figure 3.11, it is shown the  $J_2$  and  $C_{22}$  perturbations as the semi-major axis increases. The decay of the PI is mainly related to  $1/r^4$ . The PI follows the decay related to  $J_2$  and  $C_{22}$  shown in Equations 2.15, 2.16 and 2.17. Since  $J_n$  and

$C_{22}$  perturbations decrease exponentially, it is possible also to extrapolate the results and predict others PI values for different semi-major axis.

The PI related to  $J_2$  has the same magnitude decay of the  $C_{22}$ . As shown before, the value of the PI for the  $J_2$  perturbation is much larger than the other perturbations. The PI for the  $J_2$  is more than 100 times larger than the  $C_{22}$  for this simulation.

Figure 3.12 – PI of several disturbing forces except  $J_n$  and  $C_{22}$  as a function of the semi-major axis from 11000 to 27000 km.



There is an illusion created in Figure 3.12. It seems that the rate that the Moon and the Sun increases is linear and that the inclination of the curve related to the Moon is larger than the Sun. The rate either of the Sun or the Moon is not linear, as the acceleration of the third-body is related to the square distance of the spacecraft to the third-body. In this way, as the spacecraft approximates from the third-body, it would be clearer that the rate is exponential, and not linear. Figure 3.12 has a range of the semi-major axis small if compared to the

distance from the spacecraft to the third-body, and in this way, there is an almost linear relation. The magnitude of the Moon perturbation is larger than the Sun, since the Moon is much closer. As the semi-major axis increases until the orbit of the Moon and a little bit beyond, the magnitude of the Moon perturbation will always overcome the Sun. Prado (2013) shows the PI results for orbits close to the Moon.

The solar radiation pressure slowly increases, but the rate of the increase is much smaller, if compared to the rate due to the third-body. The magnitude of the solar radiation pressure is a sensitive perturbation that is proportional to  $\left(\frac{k}{k_0}\right)^2$ , as given in Equation 2.11. A noticeable increase of the solar radiation pressure in the PI maps would require a large value for the  $k$  distance, from one semi-major axis to another. In others words, the range of semi-major axis should be much larger to give differences in this value.

Figure 3.13 shows all the disturbing forces as the semi-major axis varies from 32000 to 52000 km.

Figure 3.13 – PI of several disturbing forces as a function of the semi-major axis from 32000 to 52000 km.

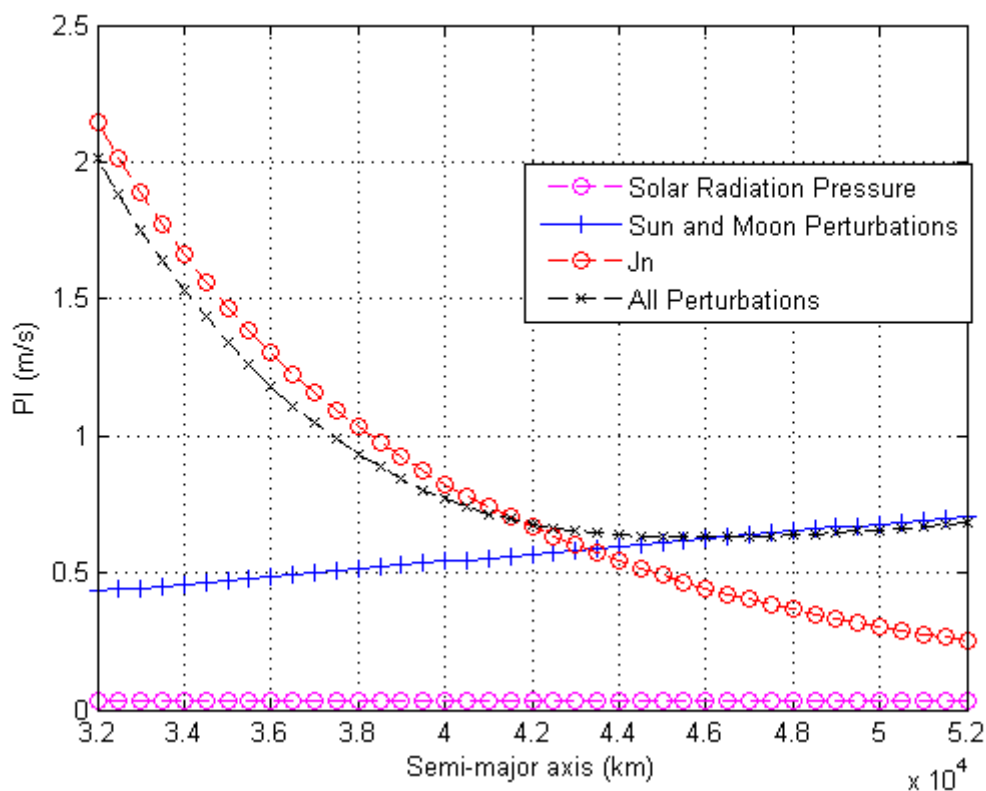


Figure 3.13 has an important behavior. The sum of all perturbations, given by the black line, has a minimum at the semi-major axis of 46000 km. The minimum occurs when the  $J_n$  perturbation decreases exponentially and the lunisolar perturbation overcomes the  $J_n$  perturbation effect.

The magnitude of the acceleration of each perturbation can be easily computed and it might change for several different positions of the Moon and the Sun. The PI uses the averaging technique to provide a result that is independent of the position of the Sun or the Moon. In other words, the mean value that PI can have for different initial positions of these bodies can have.

This averaging technique shows the minimum value of the magnitude of the disturbing forces considering several orbits. It is interesting to note that the

magnitude of the third-body perturbation becomes larger than the  $J_n$  perturbation at the semi-major axis of 43000 km, approximately.

This map is very important also for MEO and HEO, searching for orbits that are as Keplerian as it can be. The deviations of the orbit are strictly related to the magnitude of the disturbing forces and, if it is possible to choose the semi-major axis of the orbit, Figure 3.13 is capable of estimating the best one from the point of view of having less perturbations.

If not only  $J_n$  is computed in Figure 3.13, but also the  $C_{22}$  perturbation, the minimum would occur at the same semi-major axis of Figure 3.13. This means that the  $J_2$  perturbation is the largest perturbation of the spherical harmonics, as expected

### 3.1.2. The Eccentricity Variation

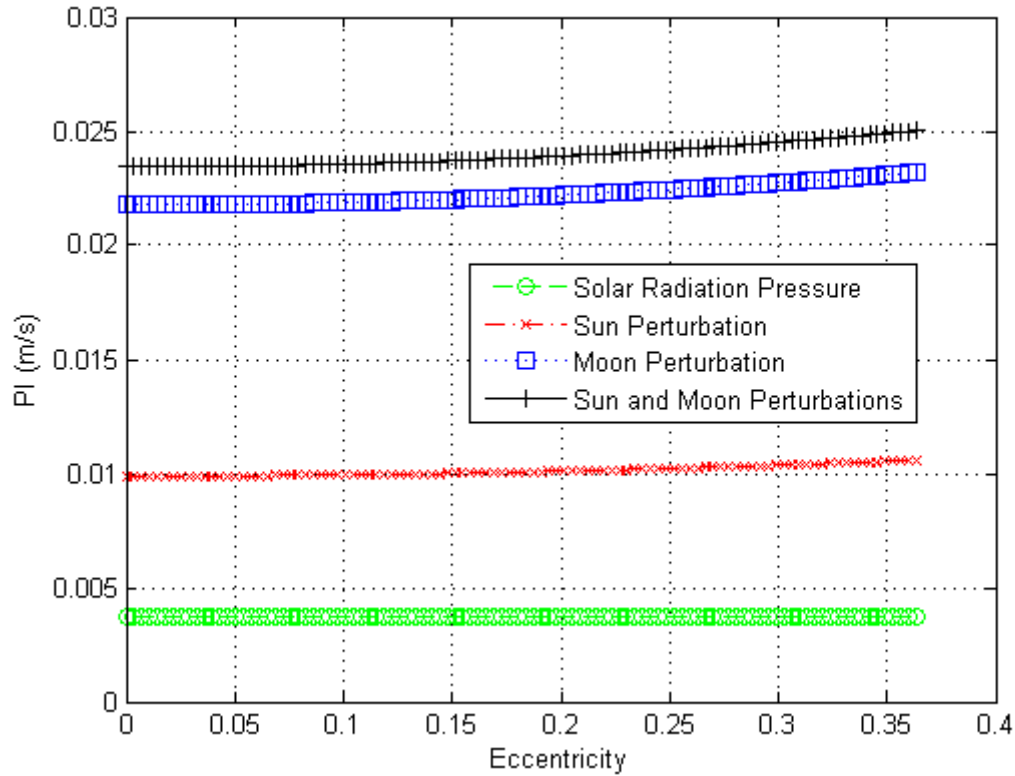
The eccentricity variation section maps orbits for on different eccentricities. It means that the magnitude of the disturbing forces acts different from circular orbits, which the values depending on the true anomaly of the spacecraft.

Table 3.3 – Initial Parameters of the Orbit for the PI study.

Semi-major axis	Inclination	Argument of Perigee	Ascending Node
12,252 km	0	0	0

The semi-major axis of 12,252 km is carefully chosen, so the maximum perigee distance of the orbit would be 7000 km and the apogee 15000 km, with an eccentricity of 0.3636. In this way, there is a passage through the atmosphere along the orbit.

Figure 3.14 – PI of several disturbing forces as a function of the eccentricity from 0 to 0.3636.



The disturbing forces of the third-body perturbation increase with the eccentricity, as shown in Figure 3.14. As the eccentricity of the orbit increases, the apogee distance increases and the time that the spacecraft passes near the apogee increases as well. This means that the distance from the third-body decreases, along with the time spent at a lower distance from the third-body. Those facts make the magnitude of the third-body perturbation to increase.

The solar radiation pressure remains almost constant with the variation of the eccentricity. There is a slight decrease of the perturbation with the eccentricity increases, because the perigee decreases, then the trajectory passes more time through the shadow region, reducing the solar radiation pressure. Figure 3.15 shows this effect.

Figure 3.15 – PI of the solar radiation pressure as a function of the eccentricity from 0 to 0.3636.

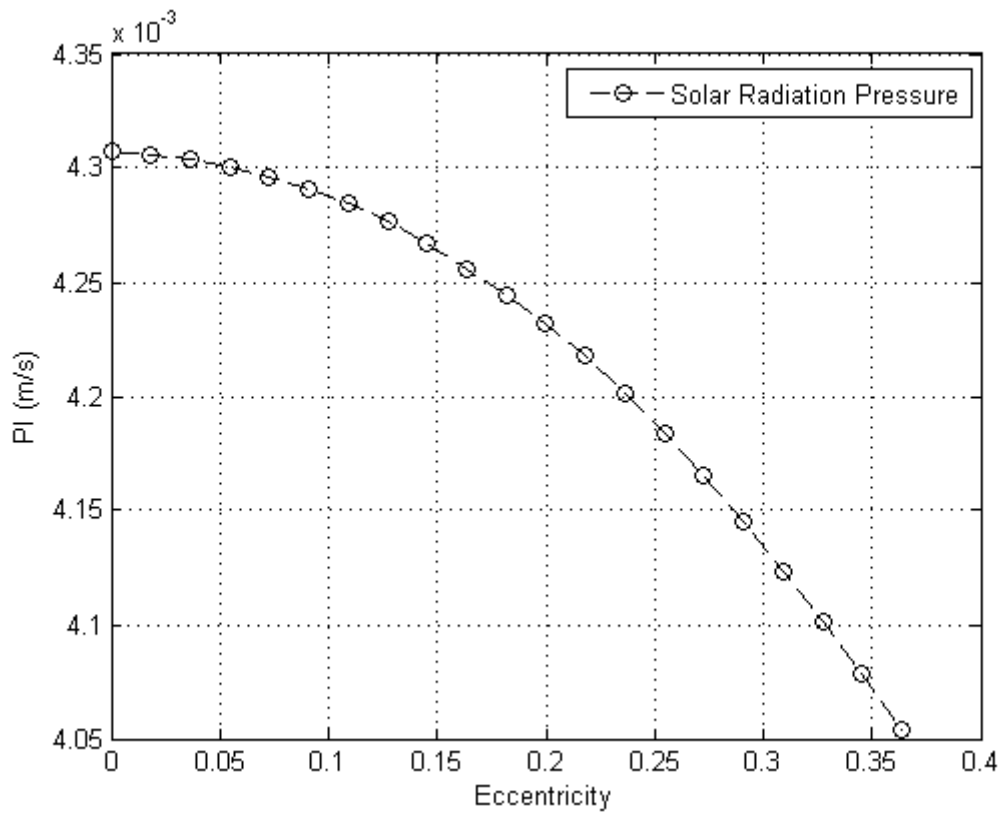
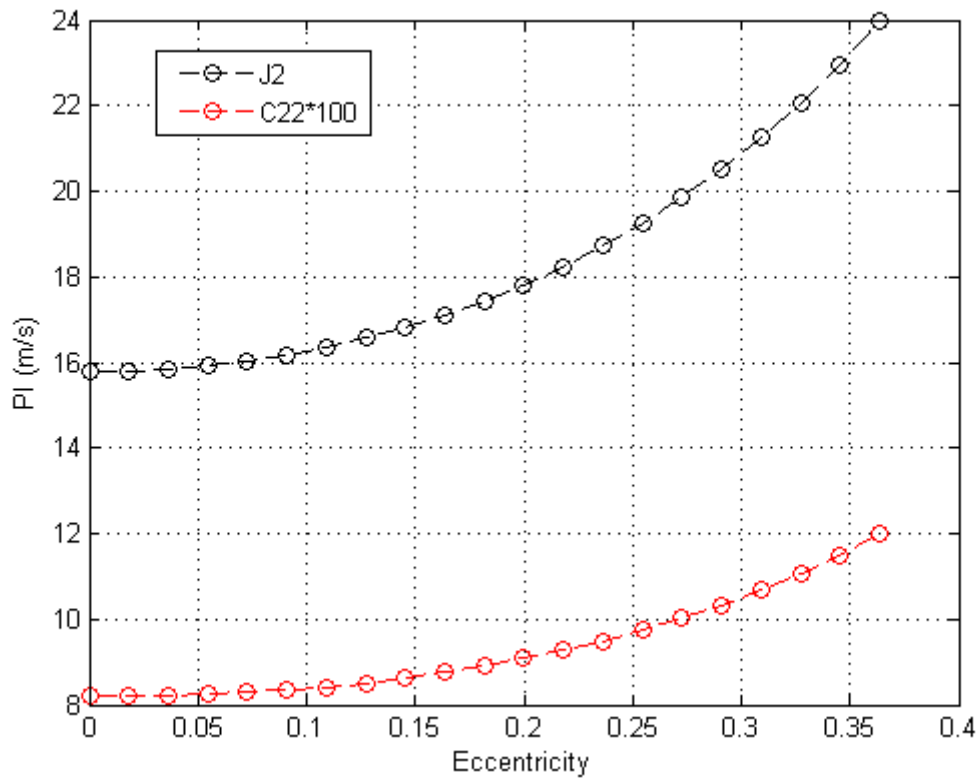


Figure 3.16 – PI value of  $J_2$  and  $C_{22}$  as a function of the eccentricity from 0 to 0.3636.



The  $J_2$  and  $C_{22}$  perturbations increase exponentially with the eccentricity as well. As the eccentricity increases, the  $J_2$  and  $C_{22}$  accelerations increase, since the perigee distance decrease. The accelerations of the  $J_2$  and  $C_{22}$  are proportional to the square distance from the centre of the Earth. The magnitude of the  $J_2$  perturbation, for this range of semi-major axis, is high and the cost to reduce this perturbation effect can be very fuel consuming. Nevertheless, Figure 3.16 illustrates the  $J_2$  pattern as a function of the eccentricity of the orbit. The pattern is the same for the eccentricity variation at any nominal semi-major axis for the  $J_2$  and  $C_{22}$ . It increases exponentially.

Figure 3.17 – PI of the atmospheric drag as a function of the eccentricity from 0 to 0.3636.

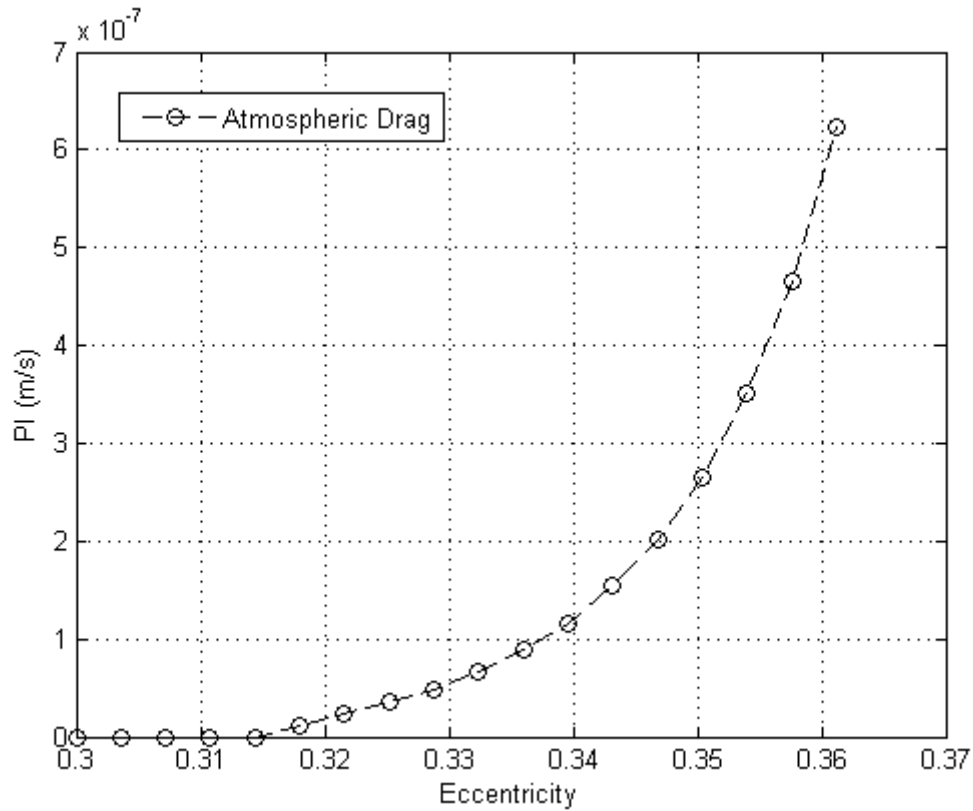


Figure 3.17 shows the PI for this orbit as the eccentricity increases. The decrease of the perigee is related to passages through more dense layers of the atmosphere, and, therefore, the atmosphere drag increases exponentially. The eccentricity of 0.315 for this simulation has a perigee smaller than 2000 km. This means that for eccentricities equal or larger than 0.315, the atmospheric drag perturbation begins to act.

### 3.1.3. The Inclination Variation

This last study involves the inclination, both for the PI and  $PI_{MAG}$ . The semi-major axis chosen is based on the geostationary orbit. The change of the inclination is from 0 to 180 degrees.

Table 3.4 – Initial Parameters of the Orbit for the PI study.

Semi-major axis	Eccentricity	Argument of Perigee	Ascending Node
42164 km	0	0	0

Figure 3.18 – PI of several disturbing forces as a function of the inclination change from 0 to  $\pi$  rad.

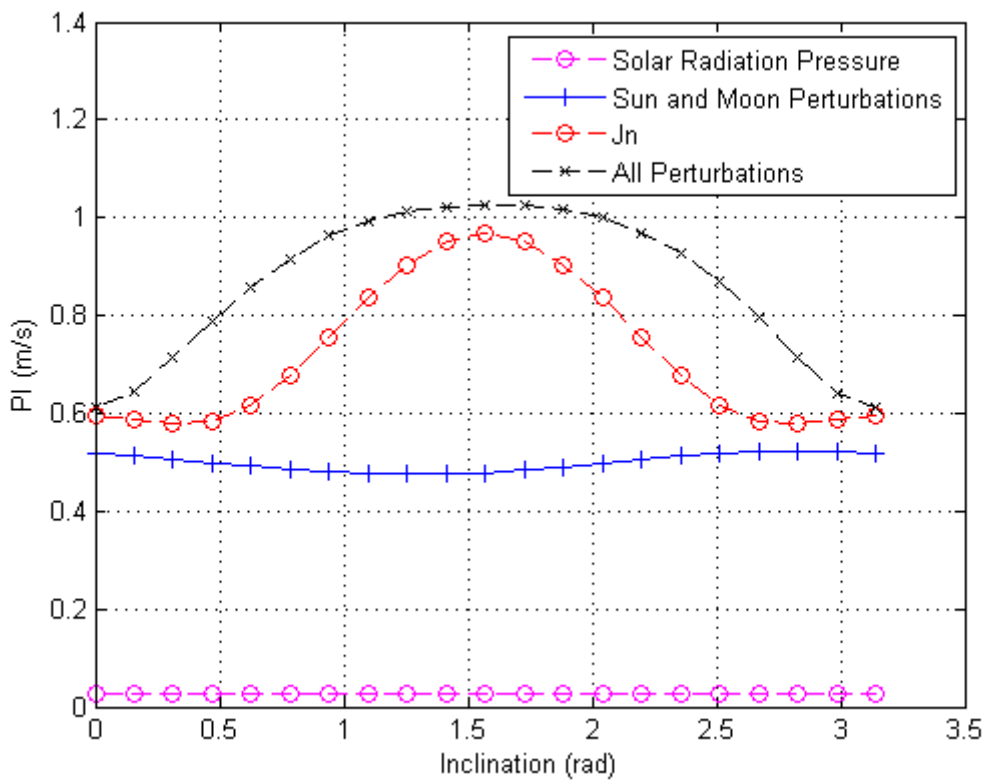


Figure 3.18 shows different pattern behaviors for each disturbing force. Even the solar radiation pressure has a unique pattern as a function of the inclination. It is not clear in the figure due to the scale. The next figures will present in more details the patterns and explanations for that.

Figure 3.19 – PI value of  $J_2$  as a function of the inclination change from 0 to  $\pi$  rad.

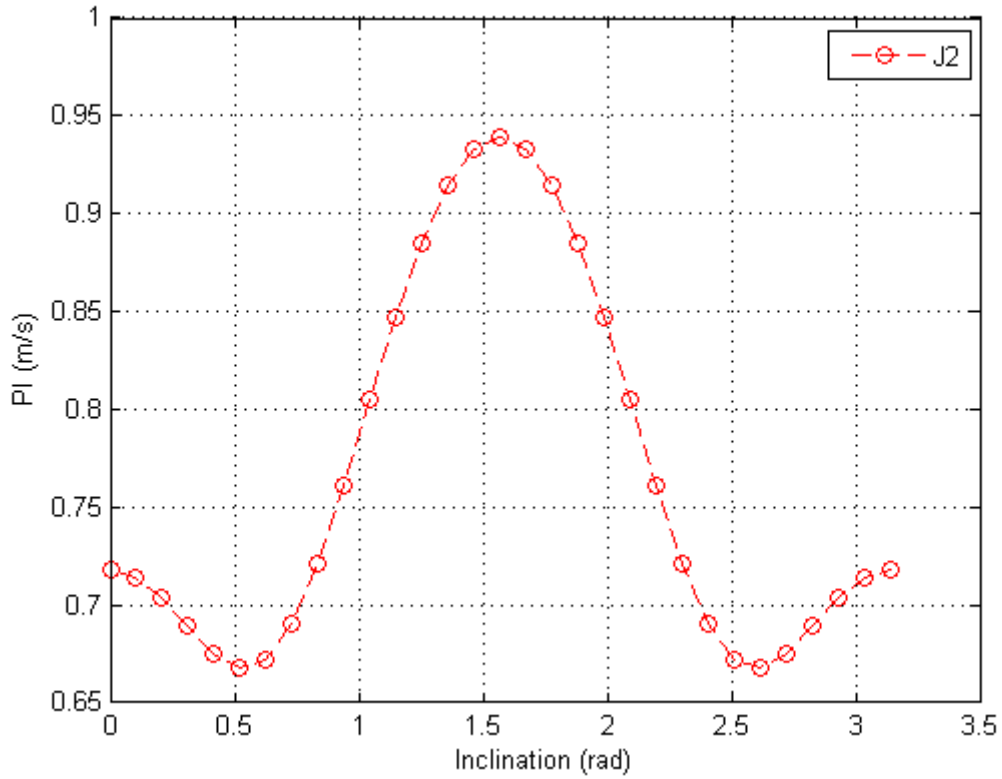


Figure 3.19 has two interesting minimums at  $26.46^\circ$  and  $153.44^\circ$  inclination degrees. The explanation for these minimums is given bellow.

The PI of the  $J_2$  is the norm of the acceleration at every step of the time. In this way, the first step is to take the norm of the Equation 2.14 with the  $J_2$  coefficient only ( $|\mathbf{a}_{J_2}|$ ).

$$|\mathbf{a}_{J_2}| = \left\{ \left( \frac{3GMJ_2}{r^2} \right)^2 \left( \frac{Re}{r} \right)^4 \left[ \frac{1}{4} (3 \cos^2 \theta - 1) + \sin^2 \theta \cos^2 \theta \right] \right\}^{1/2} \quad (3.10)$$

Figure 3.19 changes only the inclination. Therefore, the  $r$  is constant. The change of the acceleration must be due to  $\theta$ , which is the co-latitude of the system and the minimum or maximum must occur at  $\frac{d|\mathbf{a}_{J_2}|}{d\theta} = 0$ . After some manipulations, the last derivate can be reduced to

$$\cos\theta = \sqrt{1/5} \quad (3.11)$$

or

$$\cos\theta = \pm 1 \quad (3.12)$$

or

$$\sin\theta = \pm 1 \quad (3.13)$$

This means that  $\theta = 63.4349^\circ$  or  $116.5^\circ$ . Since  $\theta$  is the co-latitude, the latitude ( $90 - \theta$ ) would be effectively  $26.46^\circ$  and  $153.44^\circ$ . But, this result does not prove why the PI for the  $J_2$  has a minimum at  $26.46^\circ$ . It just proves that, at this latitude, there is a minimum or a maximum magnitude acceleration.

The prove of the minimum for the PI comes from plotting the coefficients of Equation 3.10, given by  $Ace = \left[ \frac{1}{4}(3 \cos^2 \theta - 1) + \sin^2 \theta \cos^2 \theta \right]^{1/2}$ , as a function of the co-latitude. Those coefficients are related to the magnitude of the acceleration of the  $J_2$  with a constant factor multiplying it. Those coefficients shall be called ace.

Figure 3.20 –The study of the Ace acceleration as a function of the co-latitude from 0 to  $\pi/2$  rad.

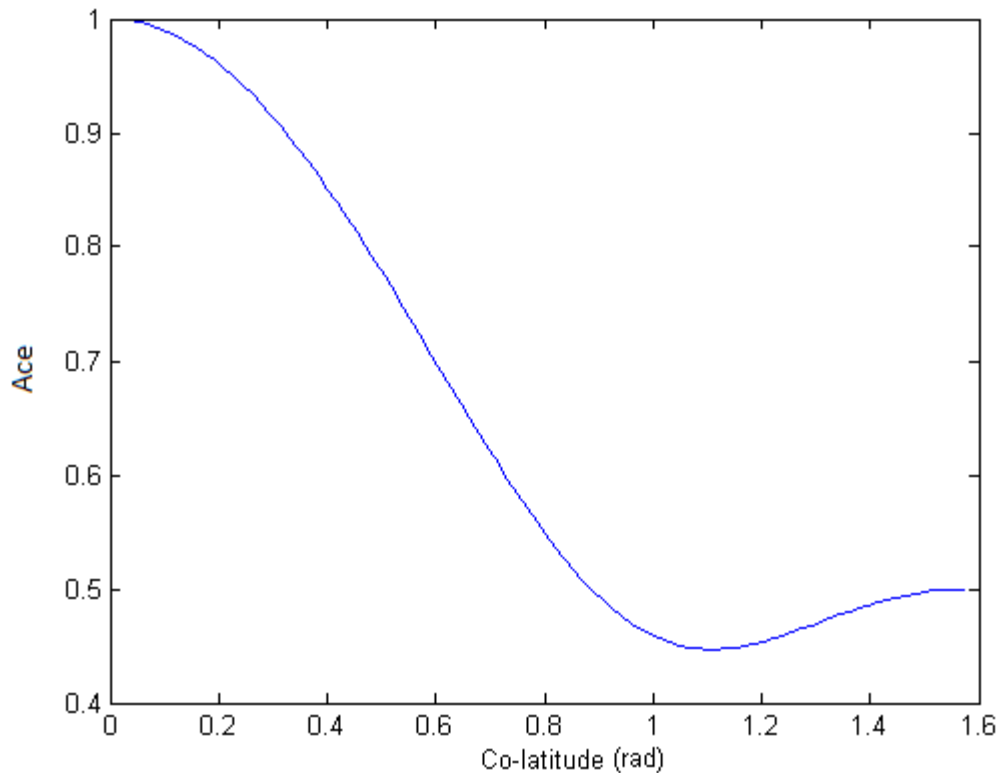
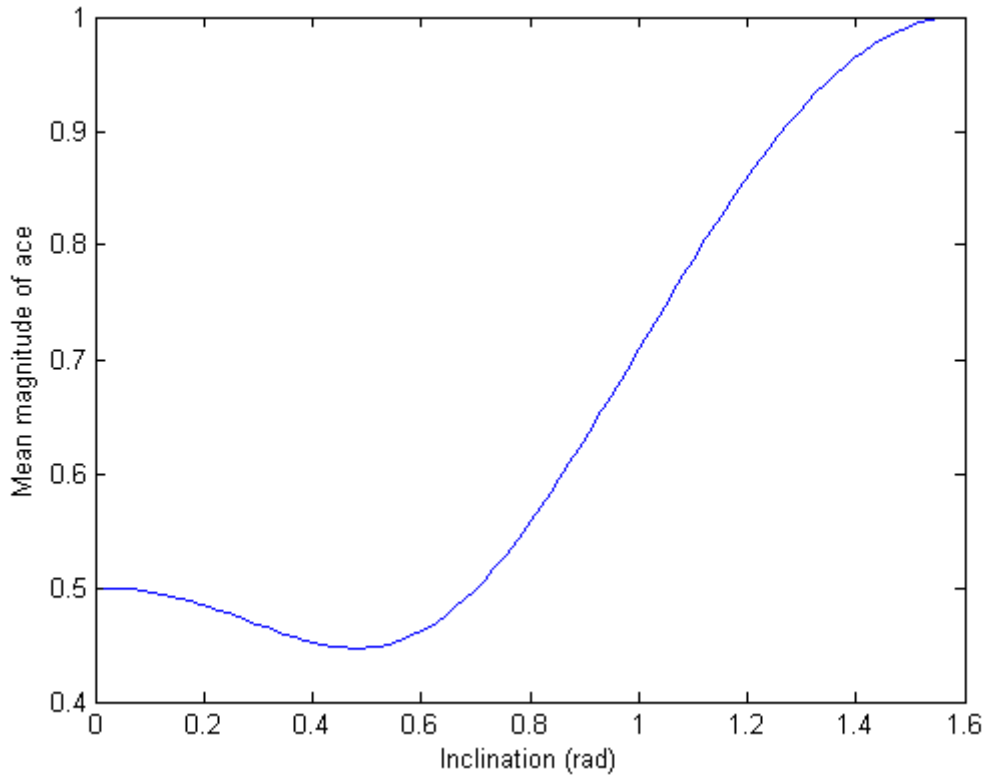


Figure 3.20 shows the magnitude of the acceleration due to  $J_2$  as a function of the co-latitude. An equatorial orbit may have the latitude constant at 0 degrees and the inclination as well. A polar orbit must have the latitude in the range 90 to -90 degrees. The inclination would be 90 or -90 degrees. The maximum latitude of the orbit is the inclination of the orbit. The minimum occurs when the latitude is 0.48 rad, or 27.5 degrees.

In this way, the inclination of the orbit can be related to the maximum latitude of the orbit. The mean magnitude area of the Ace is shown in Figure 3.20 for each different latitude. The orbit inclination is related to the maximum latitude the orbit can have. Figure 3.21 plot the mean ace acceleration for different inclinations.

Figure 3.21 –The study of the mean magnitude of Ace as a function of the co-latitude from 0 to  $\pi/2$  rad.

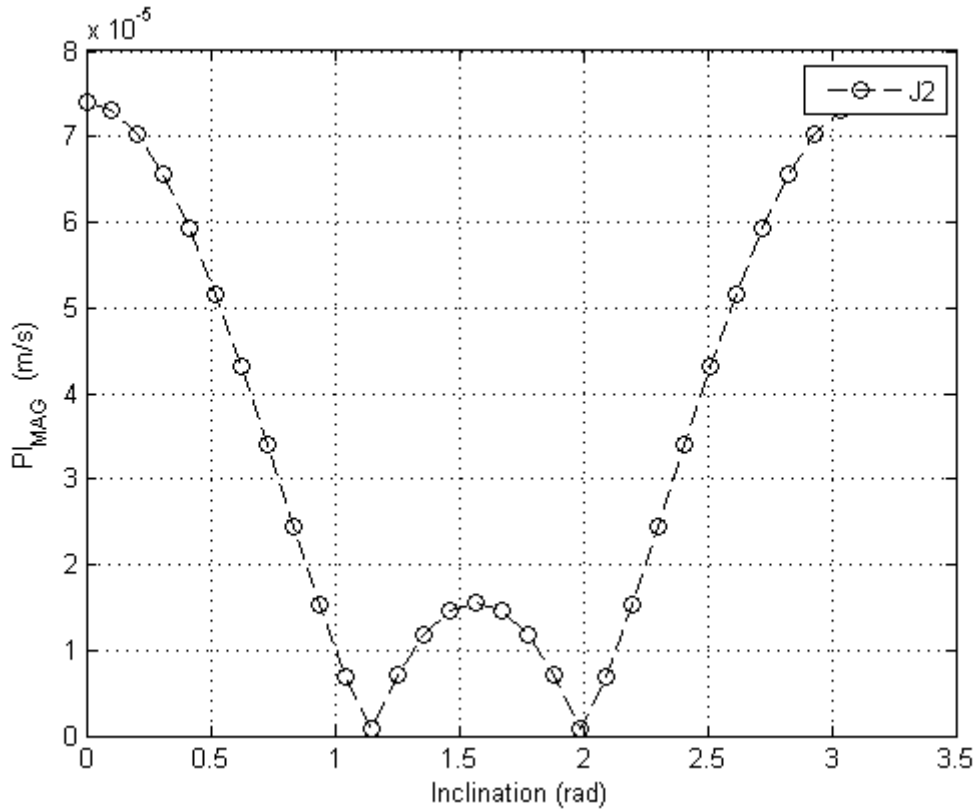


The PI pattern in Figure 3.20 is coherent with Figure 3.21. The assumption that the minimum occurs because of the  $J_2$  is proven in Figure 3.21.

The maximum value occurs at the polar orbit, when the inclination is 0 or  $180^\circ$ . The minimum of Figure 3.20 is also the minimum in Figure 3.21.

The next Figure 3.22 presents now an interesting result for the  $J_2$  perturbation with the  $PI_{MAG}$ .

Figure 3.22 – PI of  $J_2$  as a function of the inclination from 0 to  $\pi$  rad.



The minimum values of the  $PI_{MAG}$  occur exactly at the critical inclinations,  $63.43^\circ$  and  $116.56^\circ$ . It should be mentioned that the  $PI_{MAG}$  is not zero at the minimums. Figure 3.22 shows the critical inclination of the  $J_2$  perturbation with an easy and fast method of integration. The  $PI_{MAG}$  does not use any algebraic analysis, just the numerical integration. The minimum occurs exactly at the critical inclination. Many readers may ask the advantage of the  $PI_{MAG}$ , since Figure 3.22 shows what it already known in the previous literature.

It is important to remember, first of all, that  $PI_{MAG}$  can show minimums for different perturbations, whether they are added together or studied separately. The  $PI_{MAG}$  does not require any algebraic analysis, just numerical analysis.

The perturbations, orbits and stability of spacecrafts orbiting the Earth are well known. Nevertheless, the study of irregular bodies like asteroids and comets is intriguing and challenging for the researchers today. The  $PI_{MAG}$  can be a useful

method to find less perturbed orbits with no algebraic calculation, just the numerical integration.

The problem with the  $J_3$  and  $C_{22}$  perturbation is that they are asymmetric and therefore the magnitude of the  $PI_{MAG}$  are larger. The  $J_4$  is a symmetric perturbation but was omitted here since the magnitude of this perturbation does not show any significant result isolated. The sum of the  $J_2$  and  $J_4$  perturbation did not change the critical inclination value.

Figure 3.23 – PI of several disturbing forces as a function of the inclination from 0 to  $\pi$  rad.

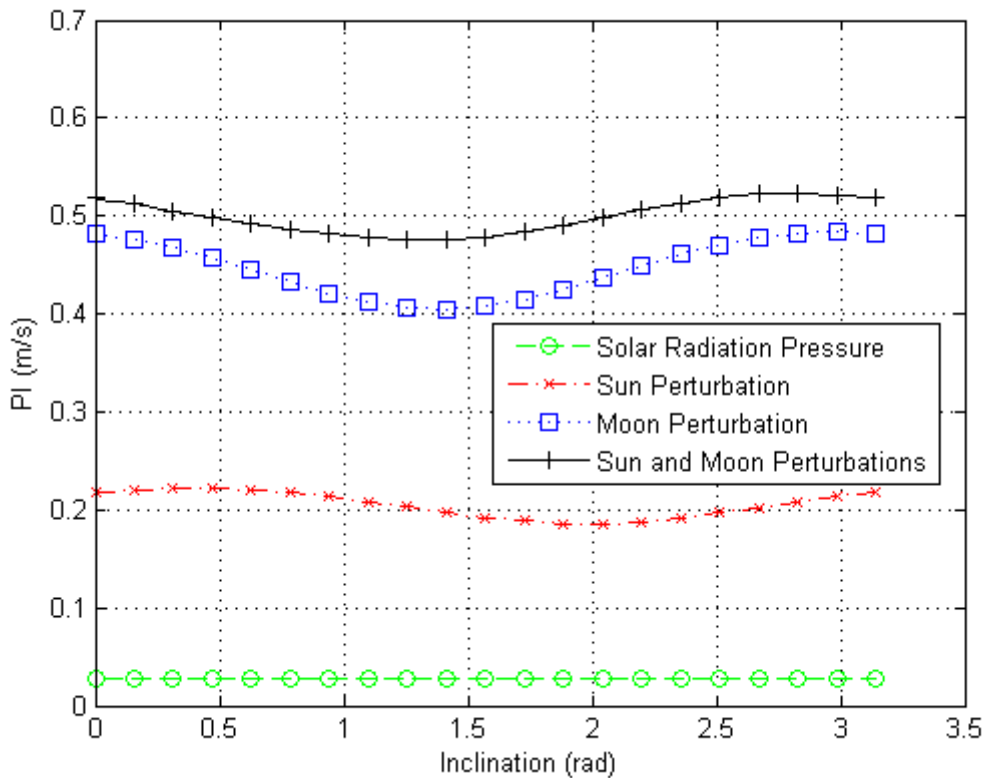


Figure 3.2 shows an interesting behavior. The maximum value of the third-body perturbation occurs when the inclination of the spacecraft is aligned with the inclination of the third-body and the minimum occurs when the inclinations of the orbit of the spacecraft is perpendicular to the third-body perturbation. The inclination of the Moon is 18 degrees and the Sun is 23.5 degrees.

The higher values for the mean PI appear for the cases where the orbit is coplanar with the third-body, either prograde or retrograde. They have about the same values, which mean that, regarding costs for station keeping maneuvers, prograde and retrograde orbits are similar. The orbits with minimum values are the ones that lie in a plane that is perpendicular to the plane of the orbit of the third-body. This is expected, because the co-planar orbits are the ones that pass closer to the third-body, compared with the inclined orbits. Of course, the perpendicular orbit is the one that makes the spacecraft to stay at a longer distance from the third-body, and therefore, the minimum occurs there.

The point now is that if the mean distance of an orbit co-planar to the third-body is the same compared to an orbit perpendicular to this plane. The third-body is a perturbation that is related to the square distance from the third-body. The proof that the PI values are different at co-planar and perpendicular orbits can be evaluated by a line integral of the trajectory of the orbit (let's state as  $\mathbf{k}$ ) and the acceleration of the third-body  $\mathbf{a}_{Third-body}$ , as given below

$$Mag = \int_{k0}^{kf} d\mathbf{k} \cdot \mathbf{a}_{Third-body} \quad (3.14)$$

where  $k0$  is the initial position of the trajectory and  $kf$  is the final position of the trajectory, after one orbital period.

If the PI values are correct, then the  $Mag$  values would follow the PI pattern. But, it is important to remember that the PI considers the averaging technique. The integration in Equation 3.14 would have to consider the averaging technique, when the inclination of the orbit is changed.

On the other hand, there is an easier and fast way to demonstrate the difference on the PI values for the planar and perpendicular orbits.

Let's consider a reference system Oijk (see Figure 3.24 ). The third-body lies in the i axis. There are two circular orbits to be compared; a planar one (Orbit 1), that lies in the ik plane and a perpendicular one (Orbit 2), that lies in the jk

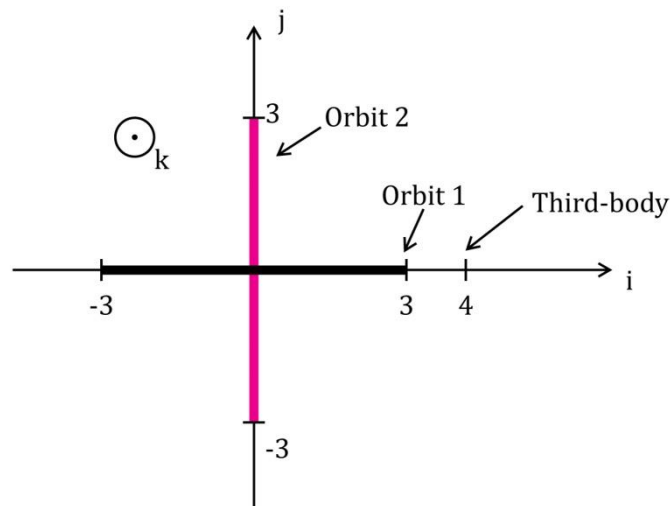
plane. The radius of the orbits is 3 and the centre of the orbit is the centre of the reference system. The distance from the third-body to the centre of the reference system is 4.

The acceleration of the third-body perturbation is related to square distance of the spacecraft to the third-body. Let's compute the acceleration in 4 points of each orbit to compare them. The points for the Orbit 1 are  $\mp 3i$  and  $\mp 3k$ . The points for the Orbit 2 are  $\mp 3j$  and  $\mp 3k$  (see Figure 3.24 ).

Let's state that the magnitude of the acceleration is related to  $1/r'^2$ , where  $r'$  is the distance from the third-body to the spacecraft.

Then the magnitude of the acceleration of the Orbit 1 would be 1 at  $3i$ ;  $1/7^2$  at  $-3i$ ; and  $1/5^2$  at  $\mp 3k$ . The magnitude of the acceleration of the Orbit 2 would be  $1/5^2$  at  $\mp 3j$  and at  $\mp 3k$ . If it is summed all the 4 magnitude accelerations of each orbit, Orbit 1 would have the value  $1348/1225$  and the Orbit 2 would have  $196/1225$ .

Figure 3.24 – Third-body and the reference system Oijk.



This easy calculation shows that, at planar orbits, the magnitude acceleration when the orbit is planar is larger compared to the case where the orbit is perpendicular. The planar orbits are the ones that pass closer to the third-body

and the magnitude increase of the acceleration is larger than in perpendicular orbits.

Figure 3.25 – PI of the solar radiation pressure as a function of the inclination from 0 to  $\pi$  rad.

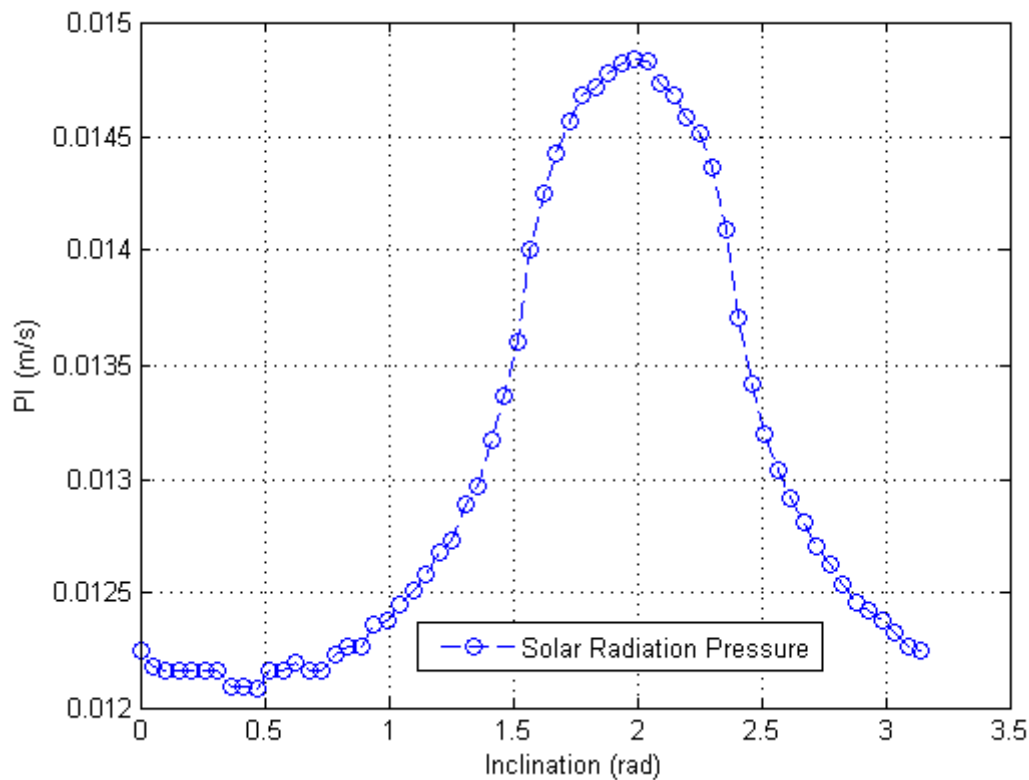


Figure 3.25 has the mass of the system of 100 kg. The mass was changed in order to amplify the magnitude of the solar radiation pressure. Also, the semi-major axis of this orbit was considered to be 7000 km. The semi-major axis was reduced so there would be more time and passages through the umbra and penumbra areas of the geometric configuration of the Sun, Earth and the spacecraft. Figure 3.25 shows clearly that the minimum value occurs when the inclination of the orbit is the same of the Sun. This means that there are more passages through the umbra region, where the solar radiation pressure perturbation drops to zero. The maximum occurs, evidently, when the orbits are perpendicular. This means that the spacecraft receives more frequently the

radiation of the Sun and there are fewer passages even through penumbra regions.

It is insignificant the variation of  $\left(\frac{k}{k_0}\right)^2$  in Equation 2.11 as the spacecraft approaches the Sun. When the spacecraft closer to the Sun, it receives more radiation, and the solar radiation pressure should increase the magnitude (coplanar orbits). When the orbit is perpendicular to the Sun's orbit, the solar radiation magnitude would decrease. The logic is the same of the third-body perturbation pattern. Nevertheless, the passages through the umbra and penumbra areas overcome this effect. In many references ([KUGA et al., 2011](#); [CAPÓ-LUGO; BAINUN, 2011](#)), the power radiation that comes from the Sun in an Earth orbit is considered to be constant, because its change due to the distance of the spacecraft to the Sun is negligible.

### 3.2. The Solar Sail Study

The solar sail is used, in this section, to reduce the disturbing forces effects. The solar sail can have a variable flat area or a fixed area. The solar sail is used to reduce one or more disturbing forces. The initial parameters of this section include the initial time and date of the simulation. The time and date provides the position of the Sun and the Moon. The PI studied in this section has the averaging technique. The solar sail finds, at every step of time, the optimal position it must have in order to reduce the disturbing forces by applying a solar radiation pressure perturbation in the opposite direction. The initial position and the time and date are essential to predict the optimal attitude of the solar sail. The magnitude reduction is extremely dependent on these parameters. Therefore, the averaging technique is used in this section for the PI to find average results with no dependence on the initial parameters.

The initial time for the integration is 1<sup>st</sup> of January, 2016, at 17:30 00' for the cases that do not use the averaging technique.

Table 3.5 – Initial parameters of the orbit solar sail study.

Semi-major axis	Inclination	Eccentricity	Argument f Perigee	Ascending Node
26000 km	0	0	0	0

Table 3.6 – Initial Parameters of the Spacecraft for the solar sail study.

Mass (kg)	$\epsilon$	Area (m <sup>2</sup> )
200	0.8	6

The reflectivity parameters for the solar sail is  $\epsilon_{solar\ sail} = 0.9$ .

Figure 3.25b shows the magnitude of the solar sail and the magnitude of all the disturbing forces (lunisolar,  $J_n$  and solar radiation pressure) considered for one orbital period. The solar sail was considered to have a variable area, with the maximum area of 500 m<sup>2</sup>.

Figure 3.25b– Acceleration of the solar sail and the disturbing forces for a system with 100 kg and maximum area of 500m<sup>2</sup>.

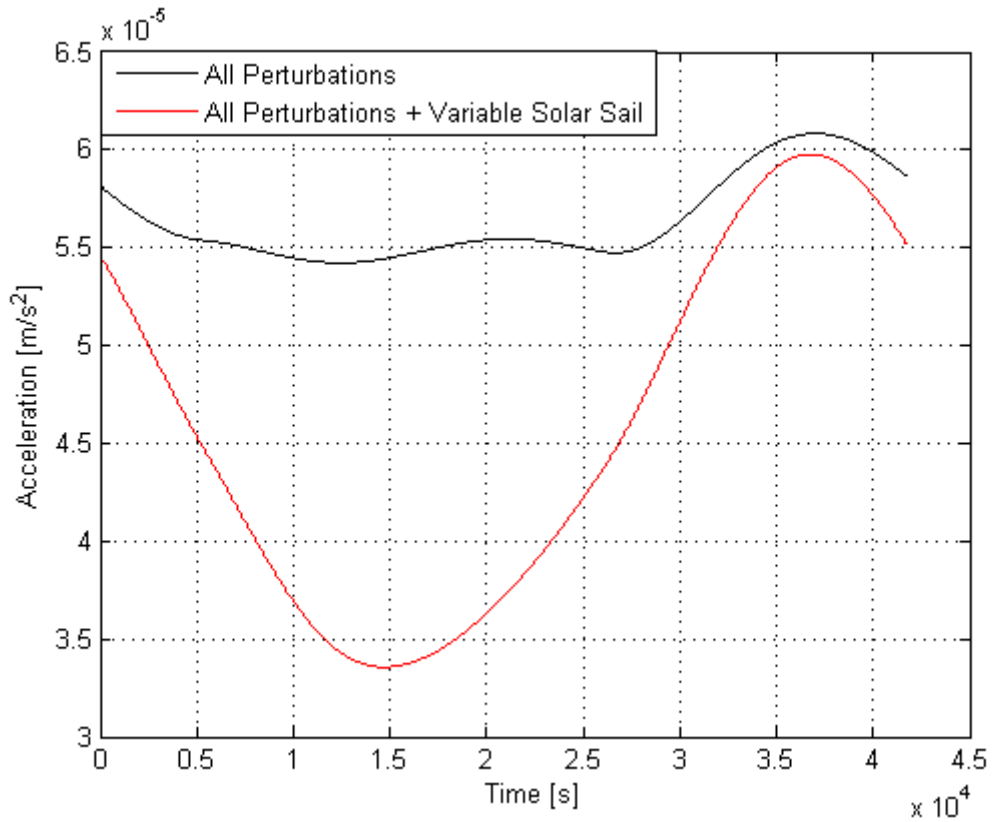
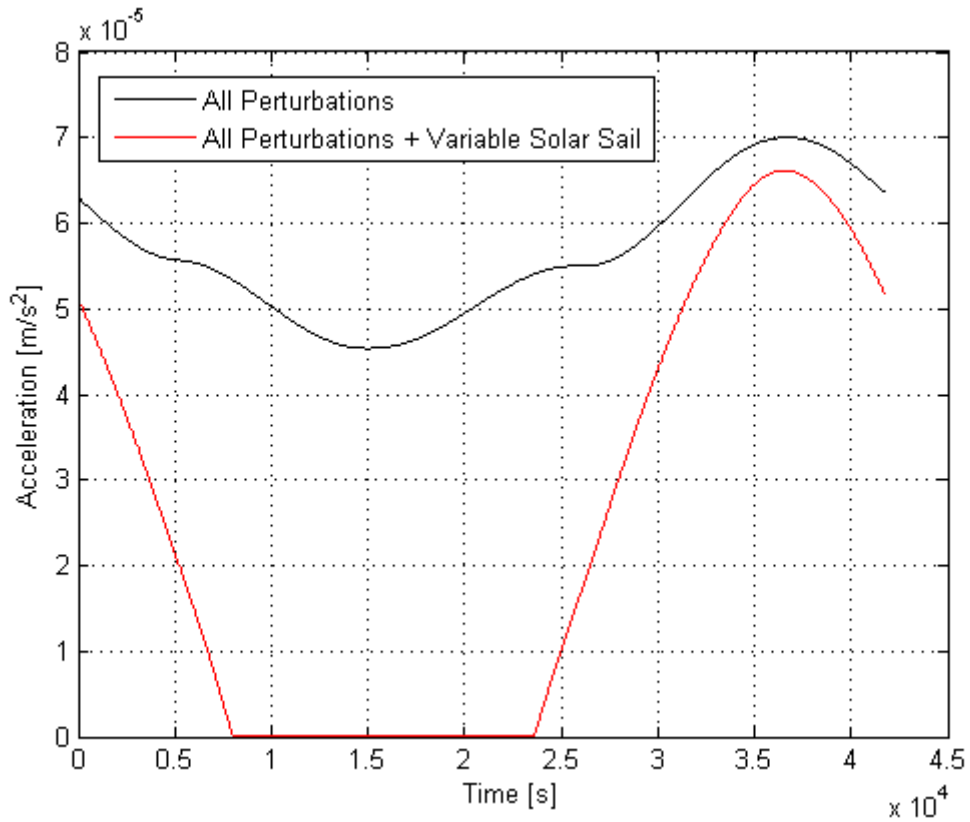


Figure 3.25b shows that the solar sail can reduce the effects of the disturbing forces. Nevertheless, the maximum area of the solar sail in this simulation is 500 m<sup>2</sup>, even if the necessary area to overcome the sum of all the disturbing forces effect is much larger than 500 m<sup>2</sup>.

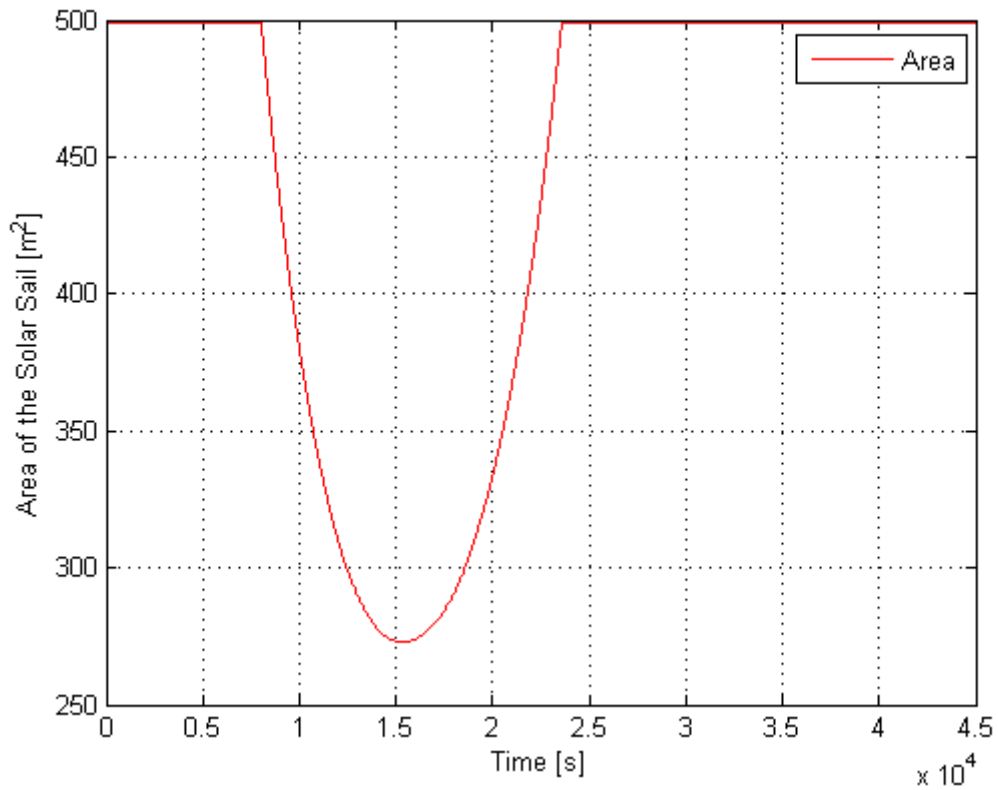
Figure 3.26 considers the mass of the spacecraft of 50 kg. The mass reduction is related to the magnitude of the solar radiation pressure or the efficiency of the solar sail.

Figure 3.26 – Acceleration of the solar sail and the disturbing forces for a system with 50 kg and maximum area of 500m<sup>2</sup>.



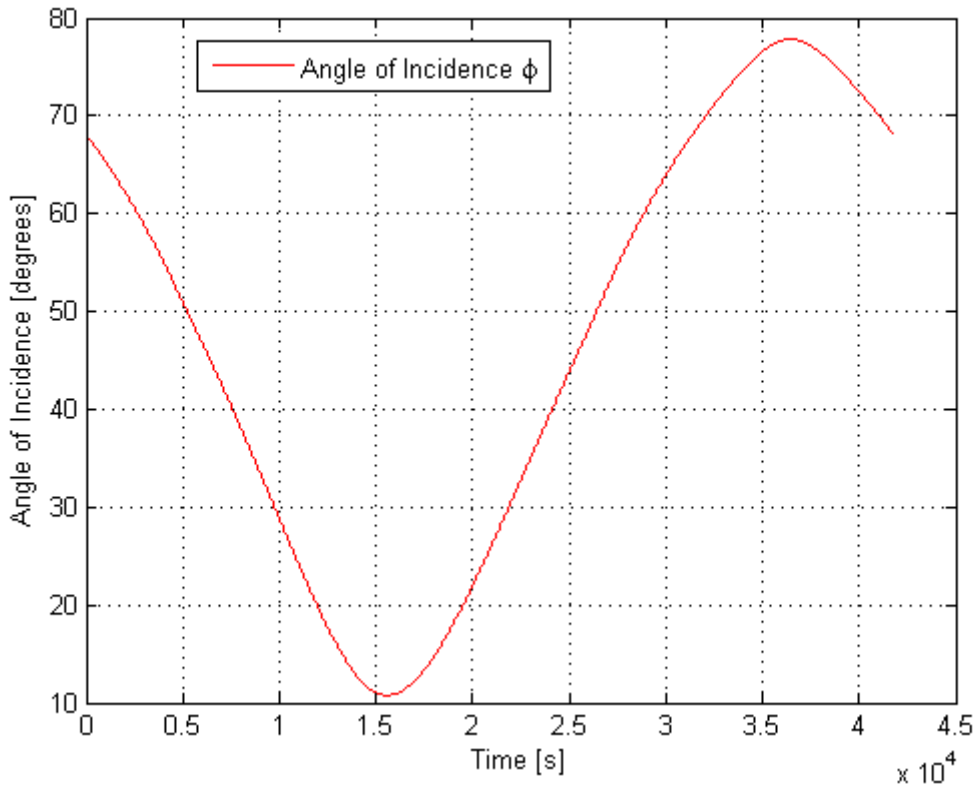
The lighter spacecraft allows the solar sail to increase its efficiency, since the smaller mass is related to less inertia and the increase of the magnitude of the solar radiation pressure. The period of the time where the red line of the acceleration is zero is the period of the time where the solar radiation pressure can overcome totally the disturbing forces effects. This means that the solar radiation pressure can cancel the disturbing forces during a short interval. Figure 3.27 shows the area of the variable solar sail for the spacecraft of 50 kg.

Figure 3.27 – Area of the solar sail for one orbit period.



The same interval where the solar sail can reduce the disturbing forces is the interval where the area of the solar sail is smaller than  $500 \text{ m}^2$ . At this interval, the area required to overcome the disturbing forces effects is smaller than the maximum area and, for that reason, the magnitude of the perturbation is zero. The next Figure shows why the area of this simulation is not always smaller than the maximum area and that there are some intervals where the solar sail cannot reduce the disturbing forces, since the area achieves its maximum value.

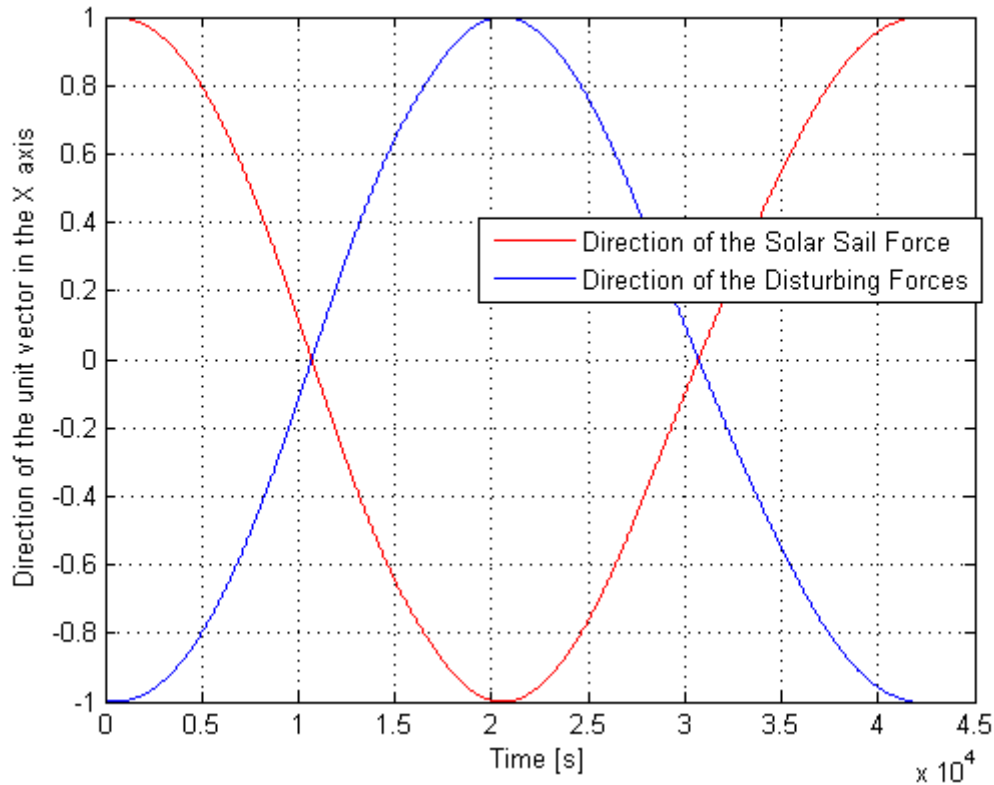
Figure 3.28 – The angle of incidence of the solar sail for one orbit period.



Equation 2.11 shows that the magnitude of the solar radiation pressure is proportional to  $\cos^2\phi$ . Due to this correlation, as the angle of incidence increases, the magnitude of the solar radiation pressure reduced. The interval of the time where the solar sail can reduce the disturbing forces effects is the interval where the angle of incidence has its lowest values. The angle of incidence shown in Figure 3.28 guarantees that the direction of the disturbing forces that needs to be compensated and the direction solar sail are opposite. Even if the magnitude is not the same, the direction of the solar sail is optimized.

Figure 3.29 shows the direction of the acceleration caused by the sum of all the disturbing forces and the acceleration caused by solar sail for the X axis in the inertial reference system.

Figure 3.29 – Versor for the X axis of the solar sail and of the disturbing forces for one orbit period.



The direction of the solar sail and the disturbing forces are opposite. This means that the solar radiation pressure could create a disturbing force that is totally opposite to the other forces. But this is not always true. If there is a passage through the umbra region, than the solar sail becomes inactivate because there is no solar radiation. There is also another exception, when the angle of incidence is larger than 90 degrees, which means that the solar radiation pressure cannot reduce the disturbing forces and must be inactive until this angle drops below 90 degrees. It is impossible that an angle of incidence is above 90 degrees, but the numerical solutions can be found in Equation 2.11. The angle of incidence above 90 degrees means that the geometry of the position of the Sun and the direction of the disturbing forces does not allow the solar sail to reduce the disturbing forces.

Figure 3.29 shows also the normal direction of the solar sail at the X axis if  $\epsilon_{solar\ sail} = 1$ . A surface 100% reflective means that the normal of the solar sails is opposite to the direction of the force of the solar radiation pressure. It is convenient to consider a solar sail with 100% of efficiency, since the numerical calculations become easier and there is no need to solve a non-linear system of equations. Unfortunately, up to now, the solar sail efficiency is around 90%. This means  $\epsilon_{solar\ sail} = 0.9$ . The method used in this thesis with a non-perfect solar sail reflector requires that the software solves the nonlinear system of equations given by Equation 2.12. The attitude of the solar sail for non 100% reflective solar sails are given by the norm of the solar sail  $\hat{n}$ .

The next figures show the attitude of the solar sail  $\hat{n}$  for  $\epsilon_{solar\ sail} = 0.9$  and the direction of the disturbing forces.

Figure 3.30 – Normal of the solar sail with reflectivity of 0.9 and the versor of the disturbing forces for X axis.

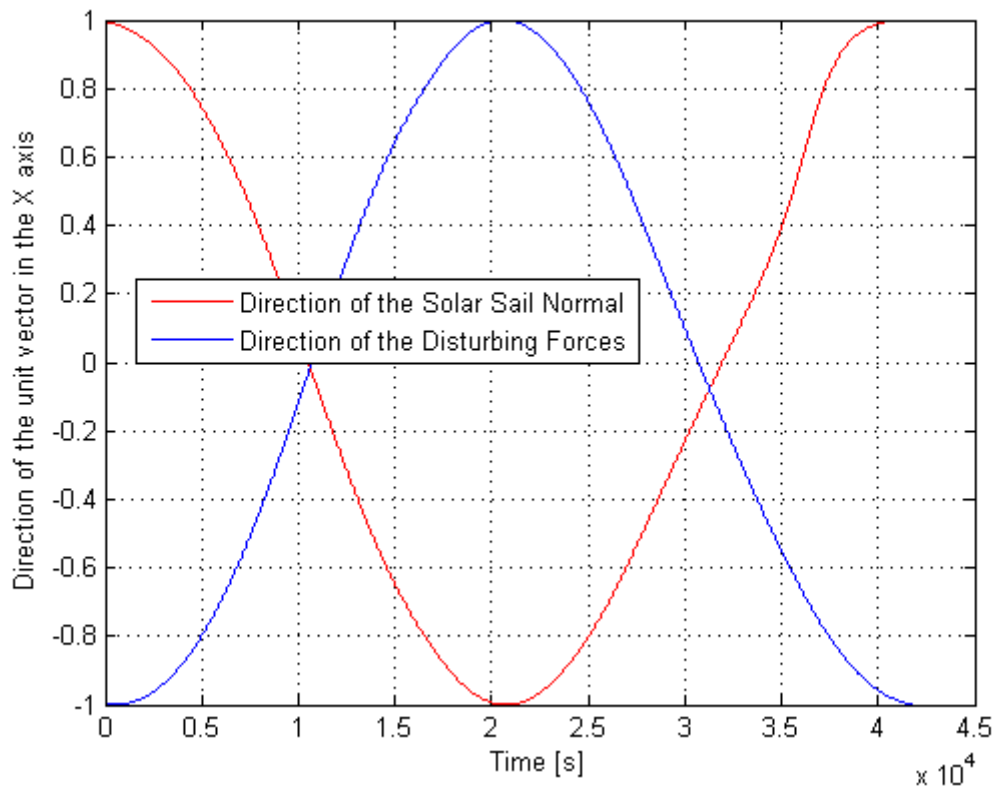
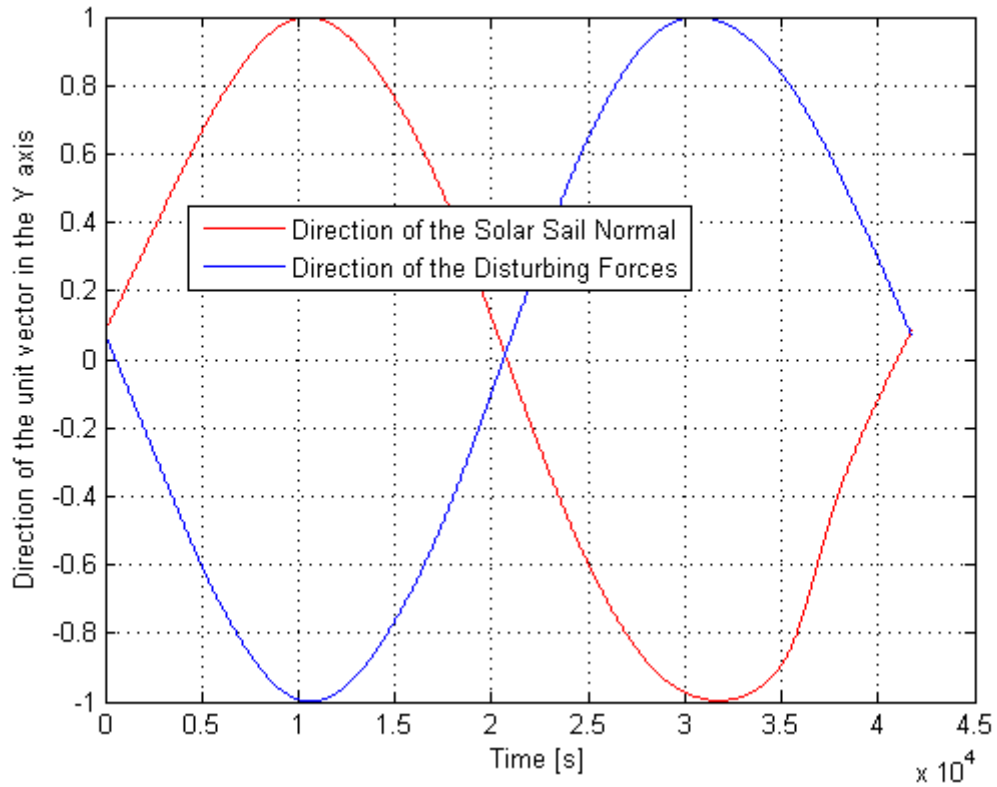


Figure 3.31 – Normal of the solar sail with reflectivity of 0.9 and the versor of the disturbing forces for Y axis.



The direction on the Z axis was omitted because the magnitude of this direction is much lower, if compared to the X and Y axis.

It is possible to see in Figures 3.30 and 3.31 that the directions are not always opposite for of the normal and the disturbing forces, since the solar sail is not 100 reflective. As the efficiency of the solar sail drops, the direction of the normal deviates more from the direction of the disturbing forces. Figures 3.32 and 3.33 show the directions, for the same simulation but with  $\epsilon_{solar\ sail} = 0.7$

Figure 3.32 – Normal of the solar sail with reflectivity of 0.7 and the versor of the disturbing forces for X axis.

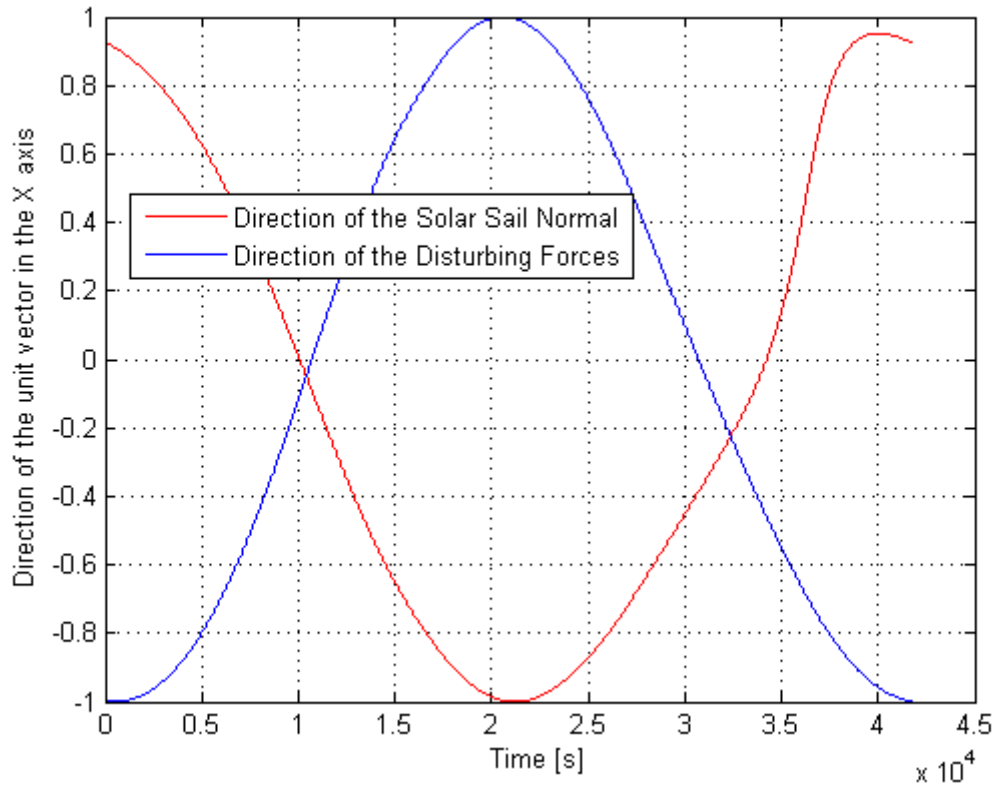


Figure 3.33 – Normal of the solar sail with reflectivity of 0.7 and the versor of the disturbing forces for Y axis.

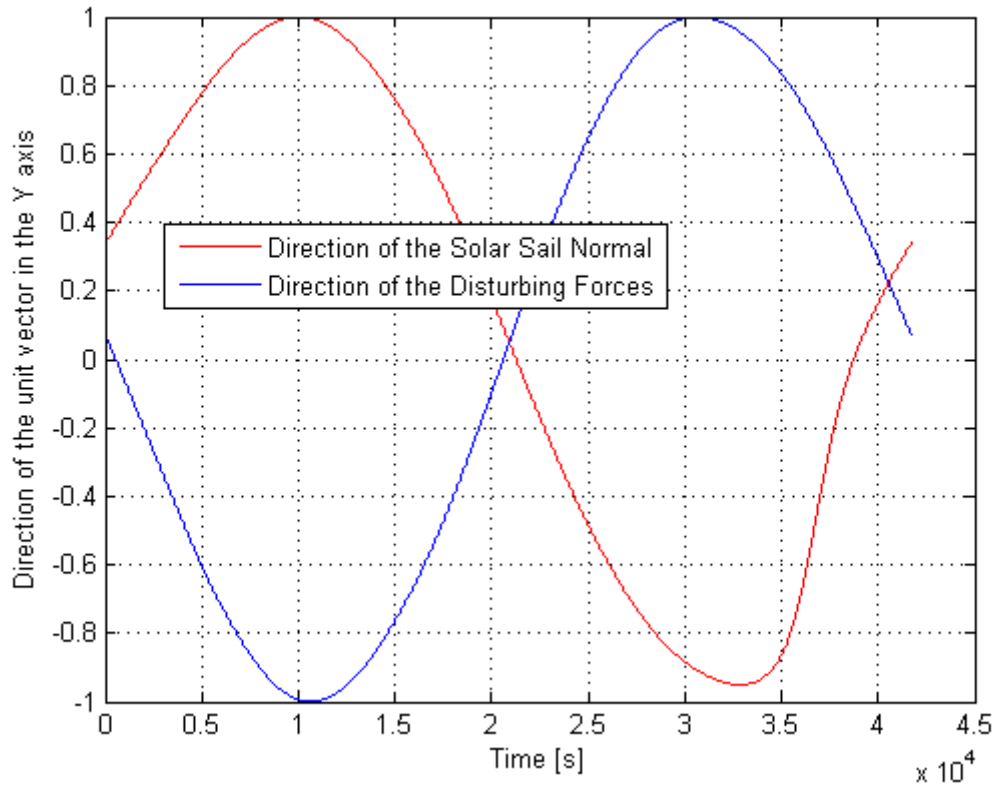
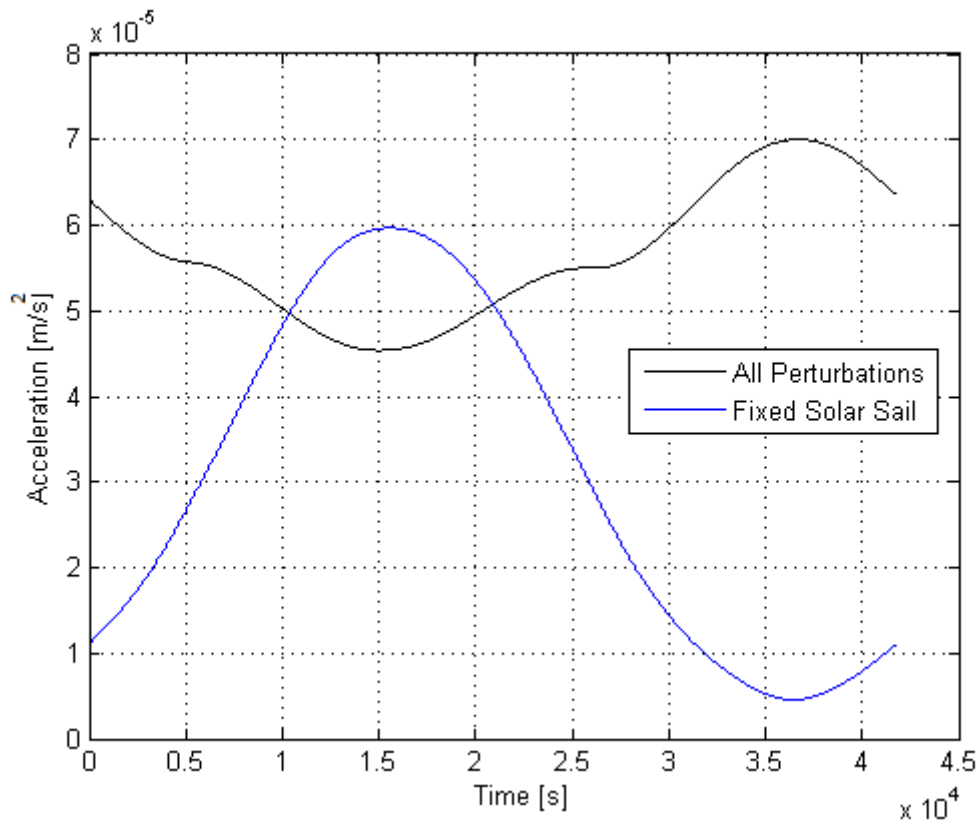


Figure 3.34 shows the efficiency of the solar sail with a fixed area, now of 400 m<sup>2</sup>, and mass of the system of 50 kg.

Figure 3.34 – Acceleration of the solar sail and the disturbing forces for a system with 50 kg and fixed area of 400m<sup>2</sup>.



There is an interval where the acceleration of the solar sail is larger than the disturbing forces. The problem with a fixed area for the solar sail is that the magnitude of the solar sail perturbation cannot be controlled and may overcome the disturbing forces. This means that, at the interval where the solar sail perturbation is larger, the solar sail not only overcomes the disturbing forces effects but it also creates a perturbation on the opposite direction. Even if the solar radiation pressure with fixed area can exceed the perturbation that needs to be reduced, this excess may represent a reduction of the total magnitude of the disturbing force. Figure 3.35 shows the same simulation of Figure 3.34 , but with the sum of all the perturbations with the solar sail acceleration.

Figure 3.35 – Acceleration of the solar sail and the disturbing forces with the solar sail for a system with 50 kg and fixed area of 400m<sup>2</sup>.

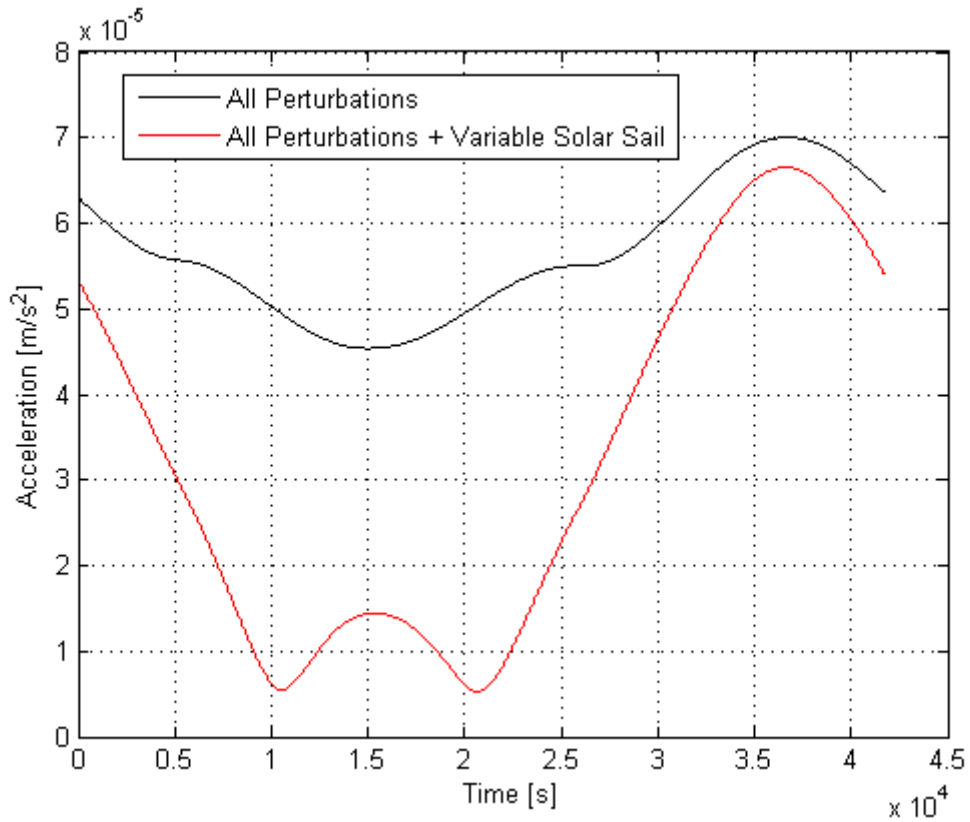


Figure 3.35 shows that even if the solar radiation pressure exceeds the disturbing forces magnitude, it stills compensates the effects caused by them in this simulation.

The PI value without the averaging technique for this simulation is given in Table 3.7 for the mass of 50 kg for the system.

Table 3.7 – PI values for the solar sail study.

PI <sub>all perturbations</sub>	PI <sub>all perturbations + variable solar sail</sub>	PI <sub>all perturbations + fixed solar sail</sub>
2.3585 m/s	1.1699 m/s	1.3499 m/s

Table 3.7 shows that the solar sail with the variable area could reduce almost half of the magnitude of the perturbation. The fixed area for the solar sail is not that efficient as the variable one, but it can still reduce considerably the perturbations effects.

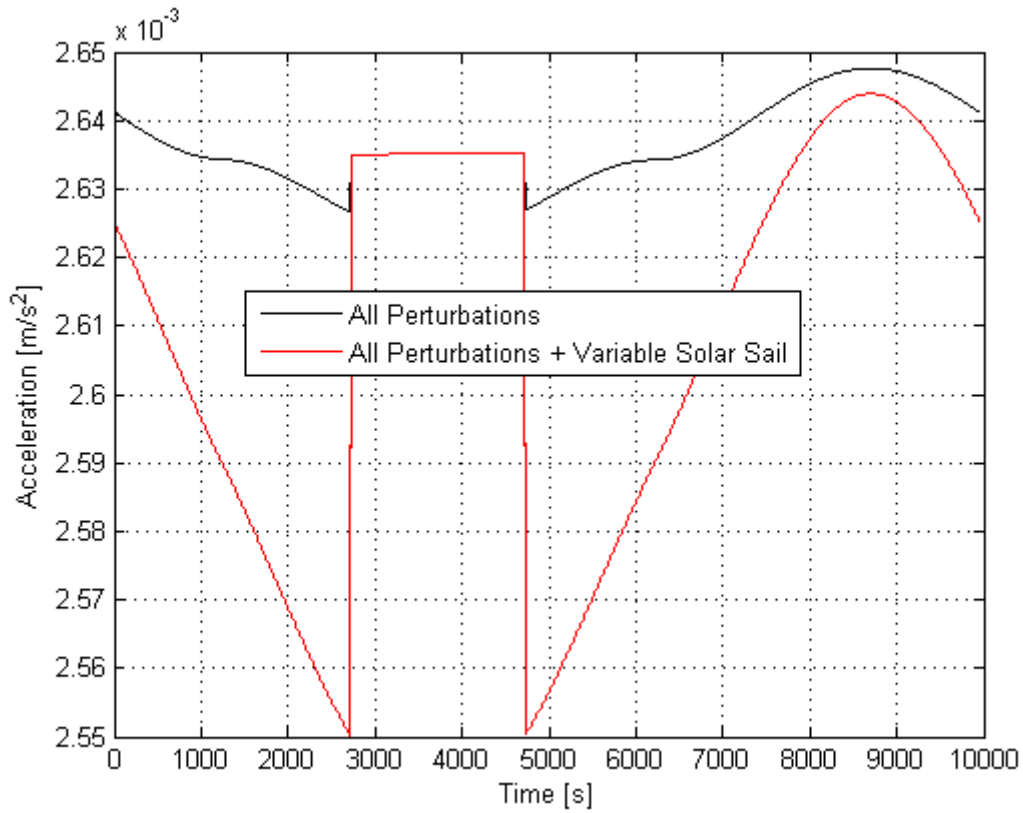
The solar sail used to reduce the other disturbing forces demonstrates to be efficient and a promising concept for future missions.

The mission must evaluate carefully the disturbing forces that are needed to be reduced and also the area that the solar sail must have in order to make the compensation.

The idea of the results is to show the reader the potential use the solar sail can have and the optimal results it can achieve. Nevertheless, the results can only be used as first mission analysis, since many other factors must be taken in account, like the physical parameters of the actuators, the internal torques, the failures, etc.

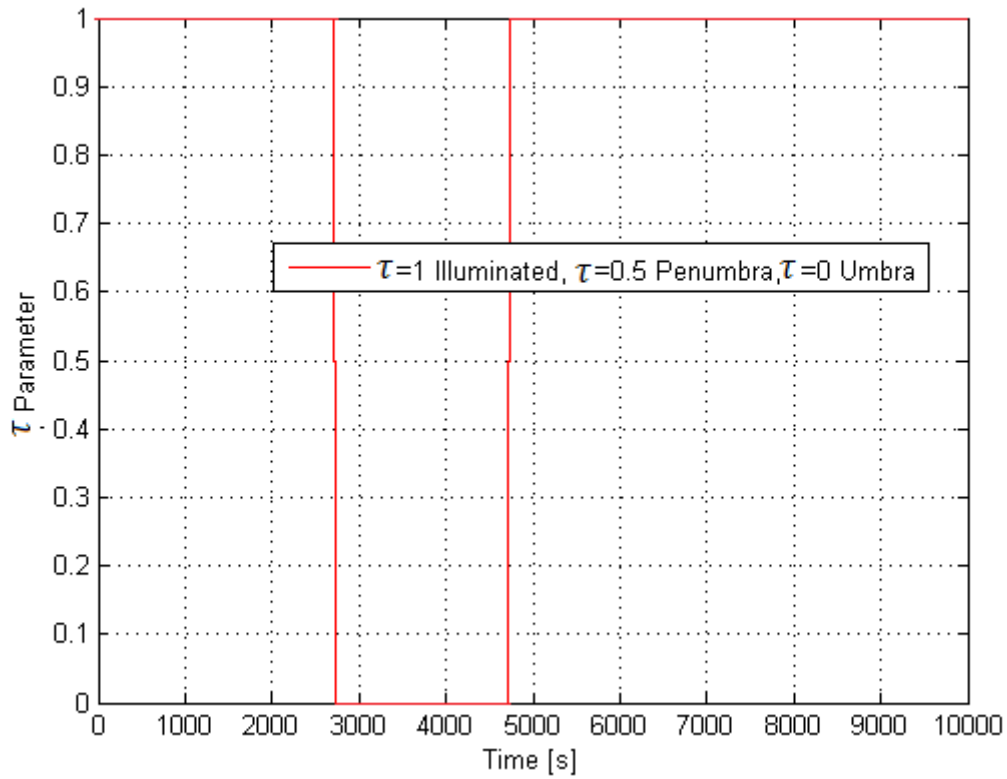
Figure 3.36 shows a passage through an umbra region and the drop of the efficiency of the solar sail. The semi-major axis chosen for this simulation was 10000 km.

Figure 3.36 – Acceleration of the solar sail and of the disturbing forces with a semi-major axis of 10.000 km.



In Figure 3.36 it is possible to see that there is a range where the solar sail cannot reduce the perturbations effects. This is due to the passage through the umbra, as it is shown in Figure 3.37.

Figure 3.37 – Parameter for the luminosity of the orbital path.



The next two Figures, 3.38 and 3.39, consider the solar sail use at a geostationary orbit. The magnitude of the solar sail acceleration reduction is shown in Figure 3.38, while the angle of incidence is shown in Figure 3.39.

Figure 3.38 – Acceleration of the solar sail and of the disturbing forces for a geostationary orbit.

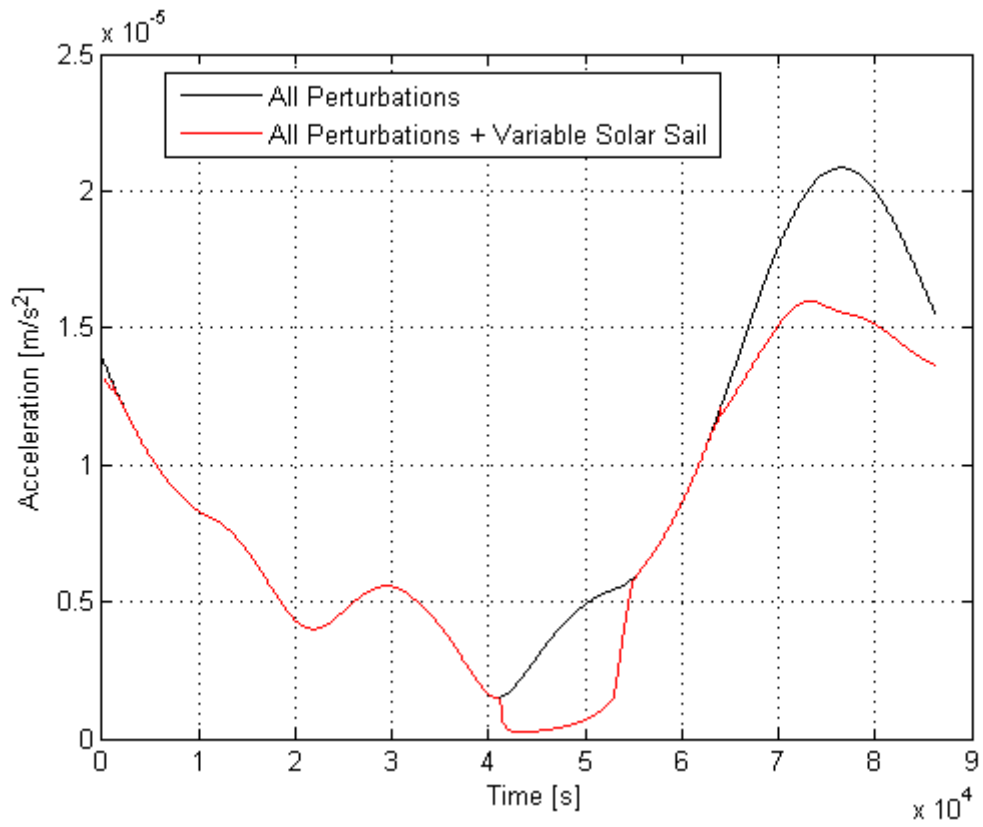
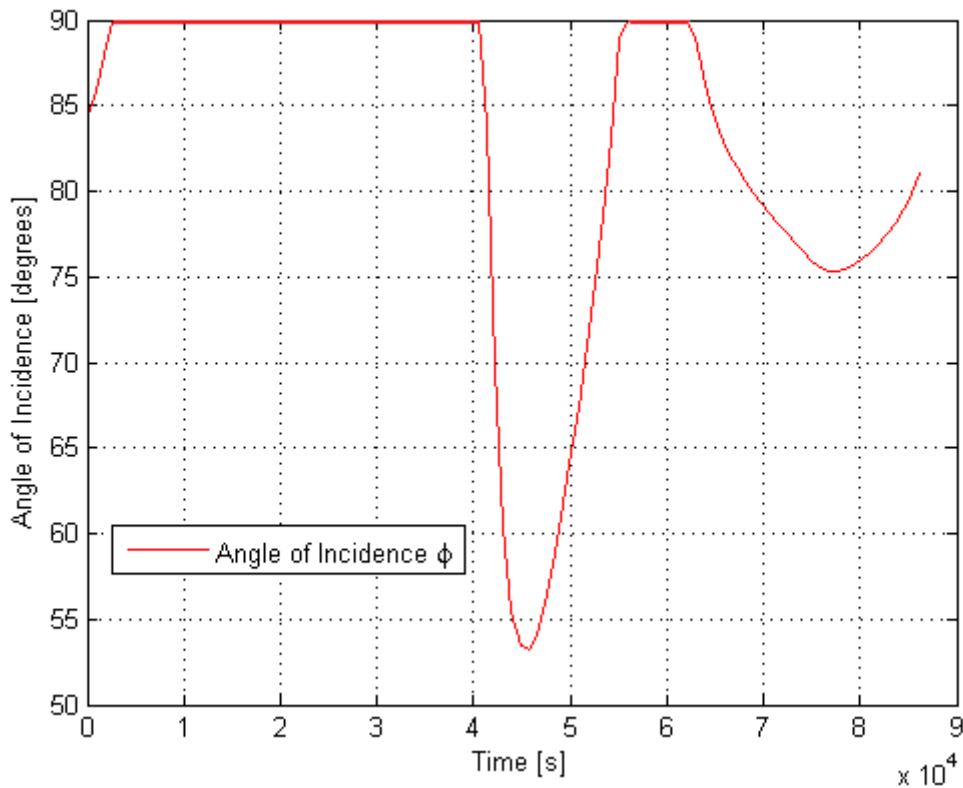


Figure 3.39 – Angle of Incidence of the solar sail for the geostationary orbit.



In Figure 3.39, the necessary angle of incidence achieves values beyond 90 degrees. Physically, it is impossible to conceive an angle of incidence larger than 90 degrees, and therefore the solar sail is inactivated.

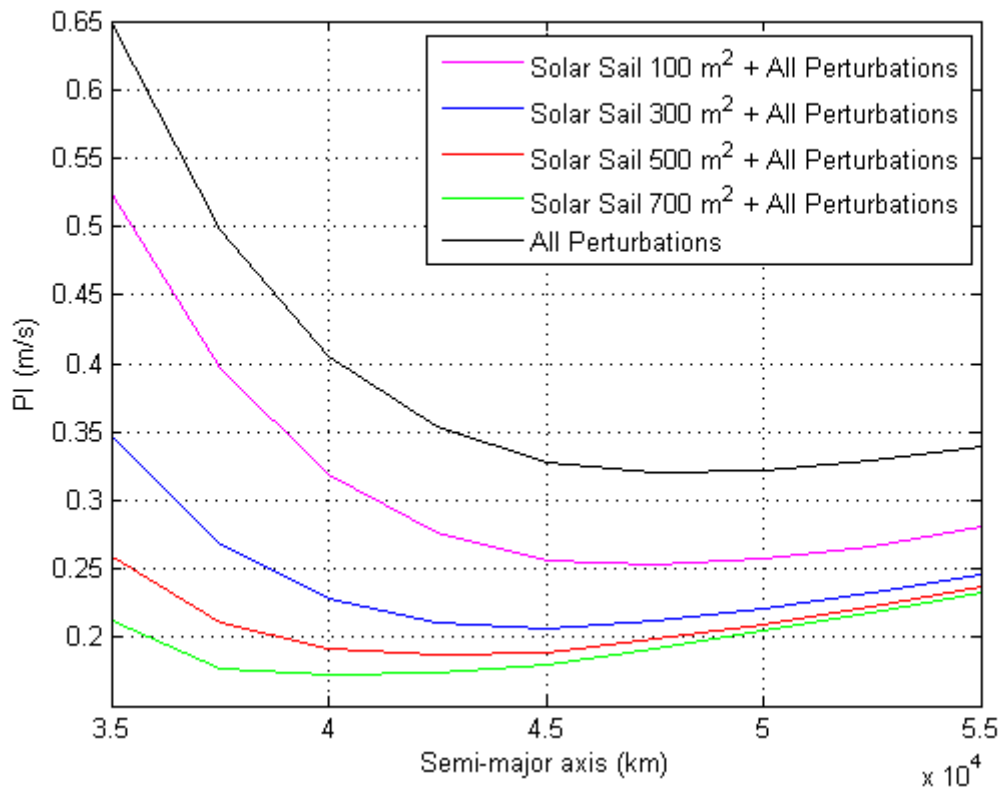
As the semi-major axis changes, or other Keplerian elements, the magnitude of the perturbation changes as well. Not only the area that the solar sail must have to compensate the effects of disturbing forces changes just the Keplerian elements, but also the angle of incidence. At the geostationary orbit, the magnitude of the third-body perturbation becomes more prominent (see Figure 3.13) than the  $J_n$  perturbation. The direction of the disturbing forces changes as the source change (Earth or third-body) or when the magnitude of the forces changes.

With the working principles of the solar sail introduced, the next results show the PI to evaluate the efficiency of the solar sail as a function of some

Keplerian elements of the orbit. Only the solar sail with variable area will be presented, since the results are optimized.

For the next Figure 3.40, the values of the PI using the averaging technique is considered as a function of the semi-major axis. The mass of the spacecraft is considered to be 100 kg. Many different maximum areas were considered for the variable solar sail.

Figure 3.40 – PI of the disturbing forces with the solar sail use as a function of the semi-major axis from 3500 to 55000 km.



It is possible to see that when the maximum area increases, the minimum value of PI and the semi-major axis also decrease. When the maximum area of the solar sail increases, the solar sail is capable of reducing more efficiently the perturbations.

Figures 3.41 and 3.42 show the variable solar sail with the maximum area of 500 m<sup>2</sup> and the total mass of the system of 100 kg considering variations in the eccentricity and inclination.

Figure 3.41 – PI of the disturbing forces and the solar sail as a function of the eccentricity from 0 to 0.3.

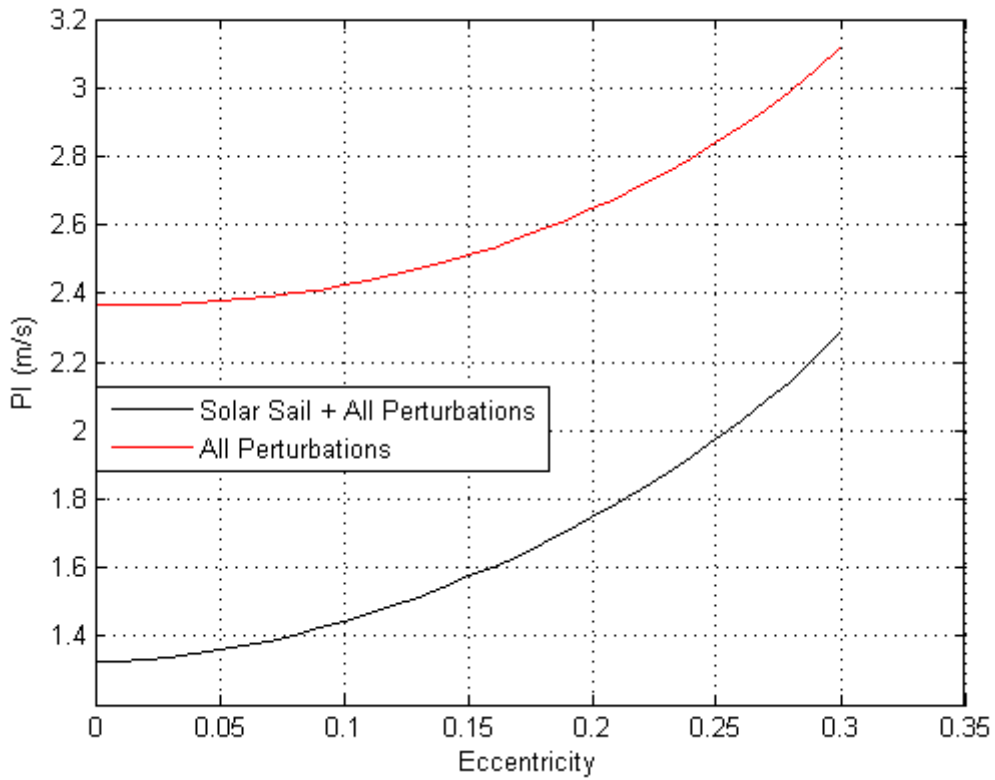
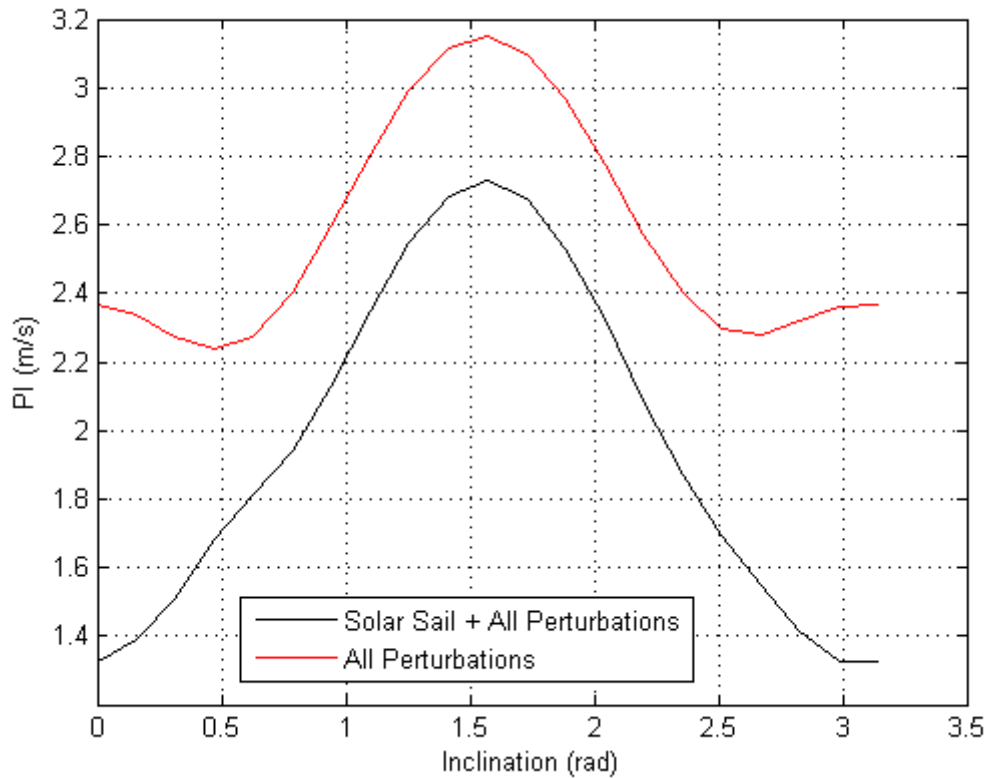


Figure 3.42 – PI of the disturbing forces and the solar sail as a function of the inclination from 0 to  $\pi$  rad.



The solar sail is efficient in reducing the magnitude of the disturbing forces. The minimum  $J_2$  perturbation vanishes as the solar sail is used to reduce the disturbing forces effects. But, as the inclination achieves the polar orbits, the efficiency decreases if compared to equatorial orbits. When the inclination increases, the angle of incidence increases and the efficiency of the solar sail decrease.

When the eccentricity increases, the magnitude of the perturbation increases and the efficiency of the solar sail decreases. The increase of the eccentricity, grows the magnitude of the disturbing forces. The solar sail area is fixed and, for that reason, the magnitude of the solar sail perturbation cannot increase.

The PI maps with the solar sail are a good tool to analyze the efficiency of the solar sail in reducing the total perturbations. It is a simple method that can

predict the magnitude reduction for many different orbits as a function of the Keplerian elements. It is possible to study different solar sails with different areas and to analyze the efficiency of each one. The solar sail proposed here is capable of reducing the magnitude of the perturbation in an efficient way. This solar sail can become a great future propulsion system, with no fuel consumption, to reduce the disturbing forces effects.

The last topic of the solar sail is to validate it in the STRS. The STRS can provide a realistic environment for the solar sail use with a PID control.

The STRS used the solar sail to reduce the disturbing forces effects. And, if the solar sail cannot cancel the magnitude of the perturbation, then the propulsion system acts on the system to zero the perturbation. As the simulator is a PID controller, at each step of time, the orbit is constantly trying to keep the Keplerian orbit. The solar sail acts like a primary propulsion system that reduces the perturbation effect with no fuel consumption. The second propulsion system is an actuator that consumes fuel in the maneuvers.

It is assumed that the propulsion system can actuate at every direction. The propulsion system considered is based on the plasma engine named PHALL 2 studied and developed by Dr. Leonardo Ferreira at UnB (University of Brasilia). The specific impulse is 1607 s and the average measured thrust is 120 mN. (FERREIRA et al., 2016)

The orbit studied is the geostationary orbit. Table 3.8 shows the initial parameters for the simulations. The disturbing forces included are: the solar radiation pressure, the  $J_2$  perturbation and the third-body perturbation of the Sun and the Moon.

Table 3.8 – Initial Parameters of the Spacecraft for the STRS study.

Mass (kg)	$\epsilon$	$C_D$	Area (m <sup>2</sup> )
500	0.9	2	10

Table 3.9 – Initial Parameters of the Orbit for the STRS study.

Semi-major axis	Eccentricity	Inclination	Argument of Perigee	Ascending Node
42164 km	0	0	0	0

The initial time and date of the simulation is 05/01/2013 at 0:00:00'.

Figures 3.43 to 3.51 show the results for the solar sail with maximum area of 500m<sup>2</sup>.

Figure 3.43 –  $\Delta V$  value for the solar sail, the perturbations and the thrust for one orbital period with a variable area for the solar sail.

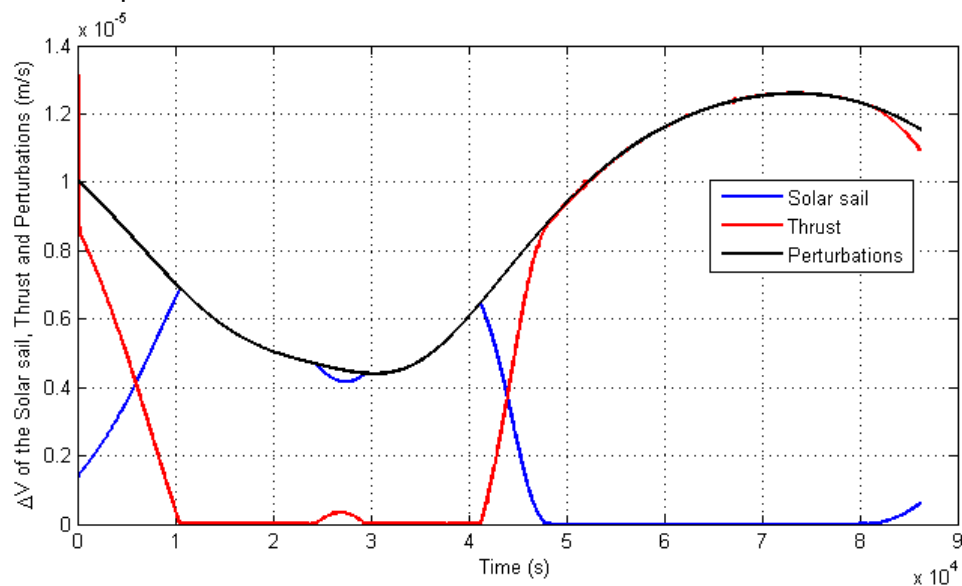
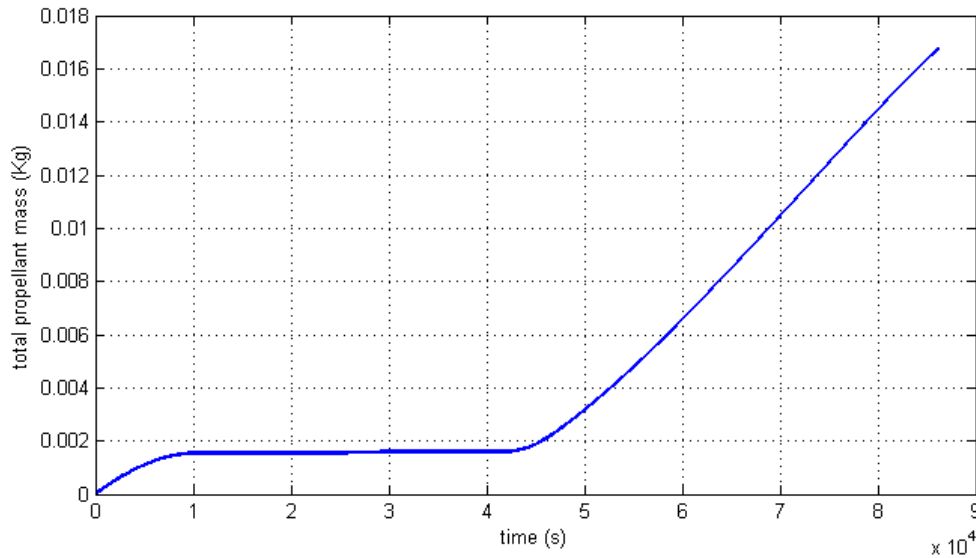


Figure 3.43 shows the  $\Delta V$  of the solar sail, the thrust and the perturbations. The  $\Delta V$  thrust decays as the solar sail  $\Delta V$  increases. At the length of the time where the solar sail can fully control the perturbations the thrust is off. There is a small portion of the interval where the solar sail is reducing the perturbations that the solar sail fails to reduce them. The explanation for this factor comes in Figure

3.45. At the end of the simulation, the solar sail perturbation is zero and the thrust begins to act again to reduce the disturbing forces effects.

Figure 3.44 – The fuel consumption evolution for one orbital period with a variable area for the solar sail.



At Figure 3.44 is possible to see the total propellant mass as the time pass by. The total mass consumed by the thrust is steady when the solar sail is active. The solar sail can reduce the disturbing forces for a range of time and no fuel is used. As the solar sail efficiency drops, the thrust begins to act again and the fuel is consumed. The total fuel consumption with the solar sail use and the thrust engine for one orbital period is 0.01675 kg. If the solar sail was inactive and only the thruster was active to reduce the disturbing forces effects, then the fuel consumption for one orbital period would be 0.02356. The solar sail reduced up to 29% of the fuel consumption in this simulation.

Figure 3.45 – The angle of incidence for one orbital period with a variable area for the solar sail.

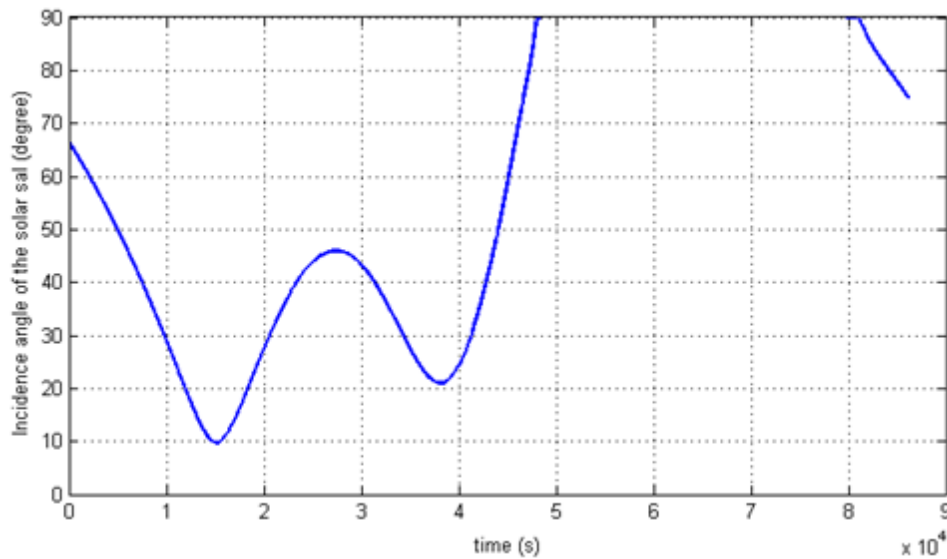


Figure 3.45 shows the angle of incidence of the sail. The interval where the solar sail can fully control the disturbing forces is when the angle of incidence is low. Lower angle of incidence requires smaller areas to guarantee that the magnitude of the solar sail perturbation is equal to the magnitude of the disturbing forces. The “belly” that occurs around  $2.75 \times 10^4$  s has an increase of the angle of incidence and this increase requires that the solar sail area is larger than the maximum one imposed. In this way, the solar sail cannot fully control the disturbing forces in this region. The angle of incidence for the second part of the period of the orbit goes to 90 degrees. This means that the solar sail cannot reduce the disturbing forces. Nevertheless, there are some small intervals that the angle of incidence drops and the solar sail can slightly reduce the disturbing forces effects.

Figure 3.46 – The area of the solar sail evolution for one orbital period with a variable area for the solar sail.

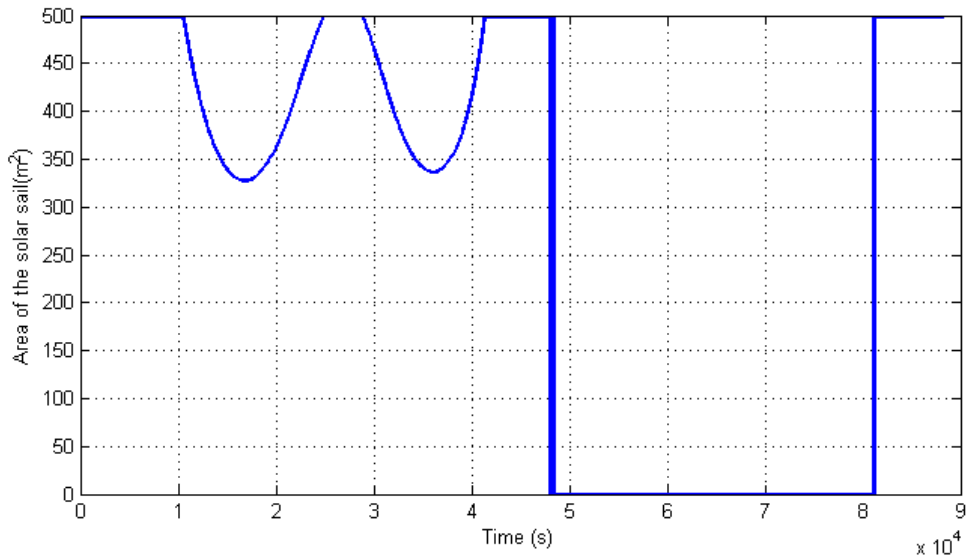


Figure 3.46 shows that the area of the solar sail is strictly related to the angle of incidence. As the angle of incidence decreases, the required area to reduce the disturbing forces decreases as well. The area achieves the maximum for the solar sail when the angle of incidence increases. The area drops to zero when the angle of incidence is equal to 90 degrees. The area of the solar sail does not have to necessary drop to zero, but the area that is illuminated by the Sun must drop to zero. If the maximum area of the solar sail were larger than 500 m<sup>2</sup>, the solar sail could reduce the disturbing forces more efficiently when the angle of incidence increased.

Figure 3.47 – The magnitude of the thrust of the propulsion system for one orbital period with a variable area for the solar sail.

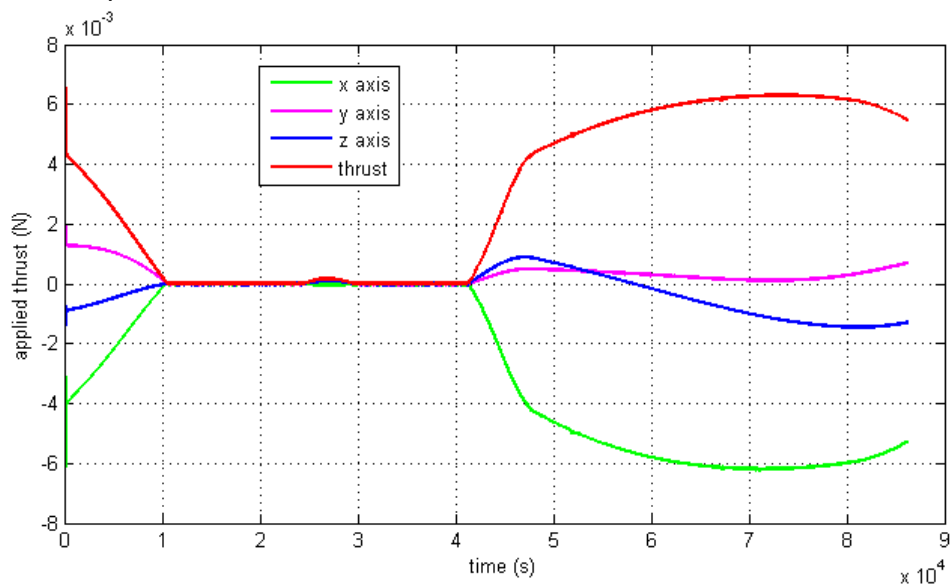


Figure 3.47 shows the thrust applied in Newton for each different axis and for the magnitude of the thrust. It is possible to see that for the interval that the solar sail reduces almost to zero the disturbing forces effects, the thrust is inactive. For the other periods of the orbit, the thrust is active and the maximum force applied was  $6.5 \times 10^{-3}$  N. This means that, for the PHALL 2 plasma thruster used in this simulation, the magnitude of only one thruster is capable of controlling the disturbing forces.

Figure 3.48 – The velocity increment of the perturbations in the OXYZ reference system evolution for one orbital period with a variable area for the solar sail.

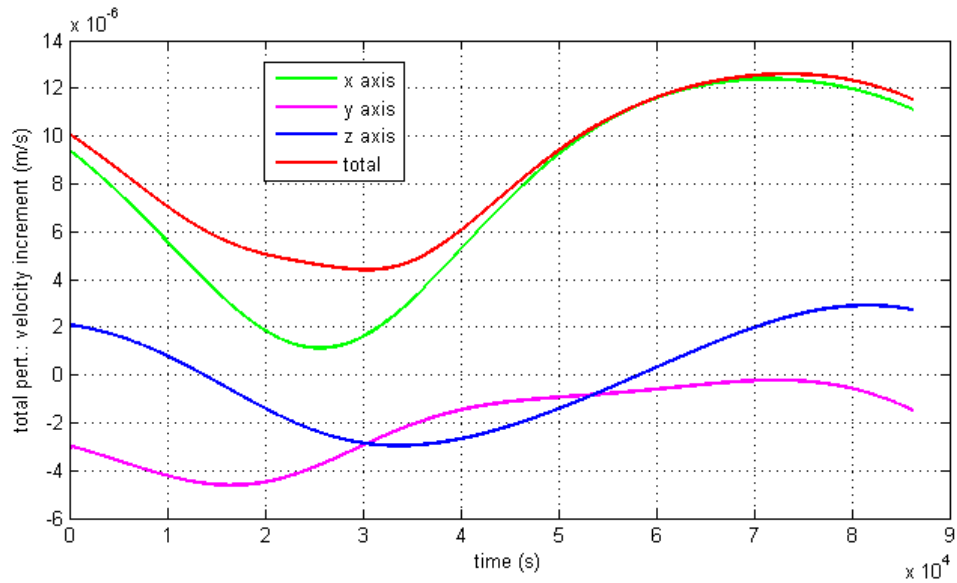


Figure 3.48 shows the velocity increment due to the disturbing forces in each inertial axes and the magnitude of the disturbing forces. It is possible to note that the pattern of the thrust + solar sail is the pattern of the magnitude increment of the disturbing forces.

The Figures 3.49 to 3.51 show the versors, on the inertial frame, of the solar sail perturbation direction and the sum of all the disturbing forces that needs to be cancelled.

Figure 3.49 – The versors of the solar sail and the perturbations in the X axis for one orbital period.

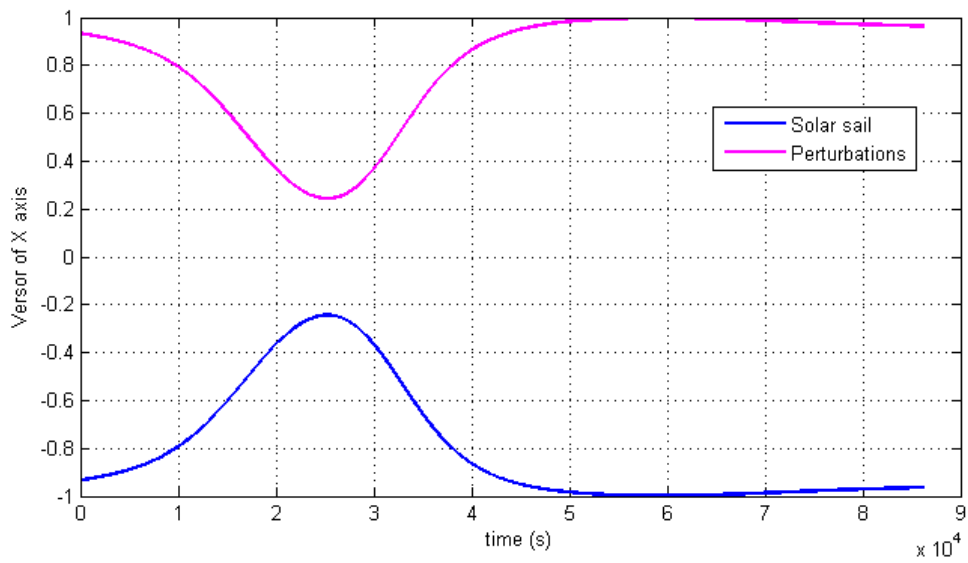


Figure 3.50 – The versors of the solar sail and the perturbations in the Y axis for one orbital period.

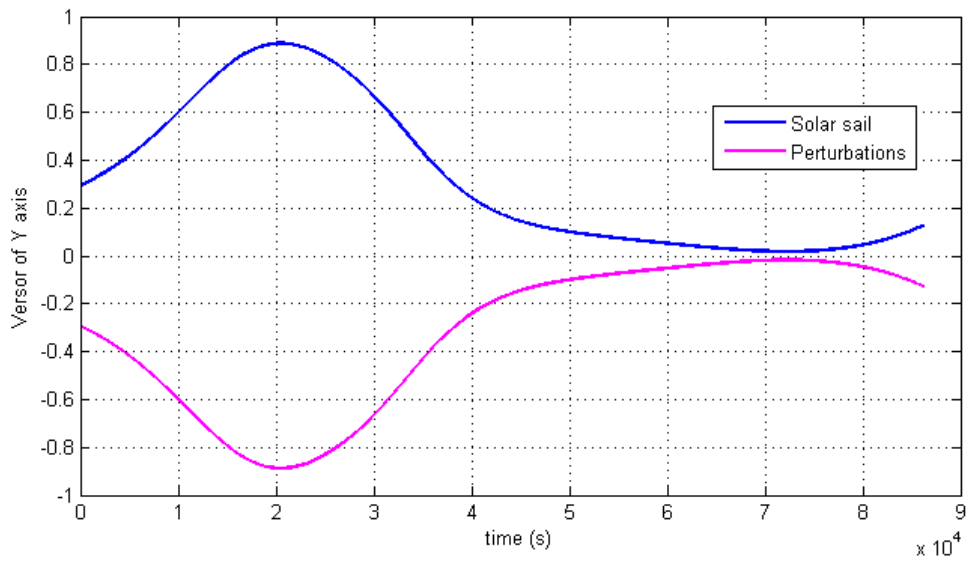
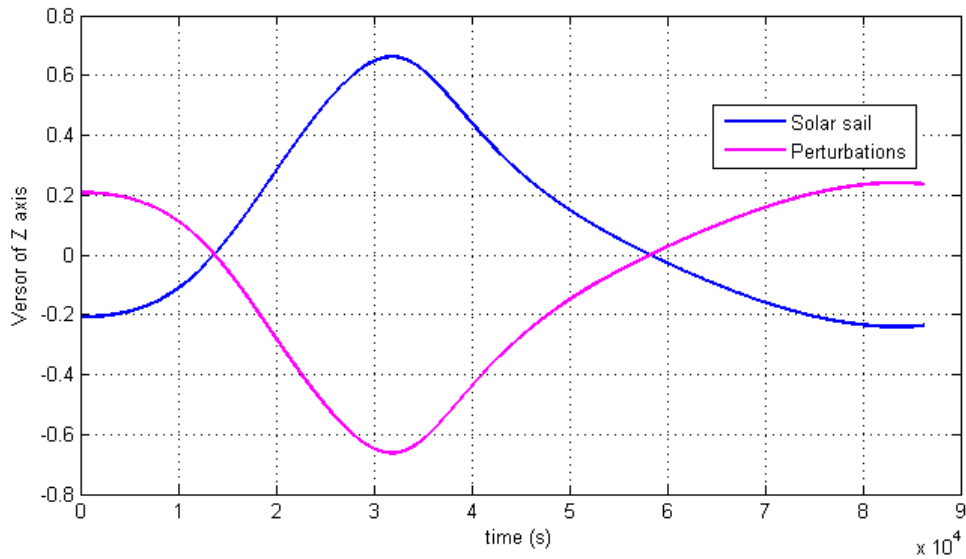


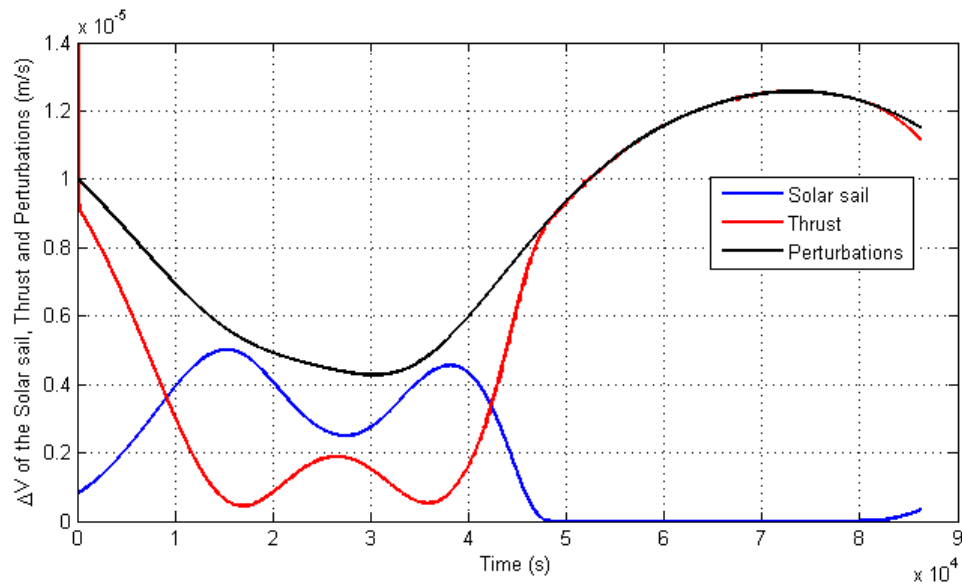
Figure 3.51 – The versors of the solar sail and the perturbations in the Z axis for one orbital period.



The station-keeping maneuver for the Keplerian orbit is achieved successfully for this simulation. The thruster is capable of reducing the disturbing forces when the solar sail is not active and the PID controller is capable of keeping the spacecraft following the nominal trajectory with small errors.

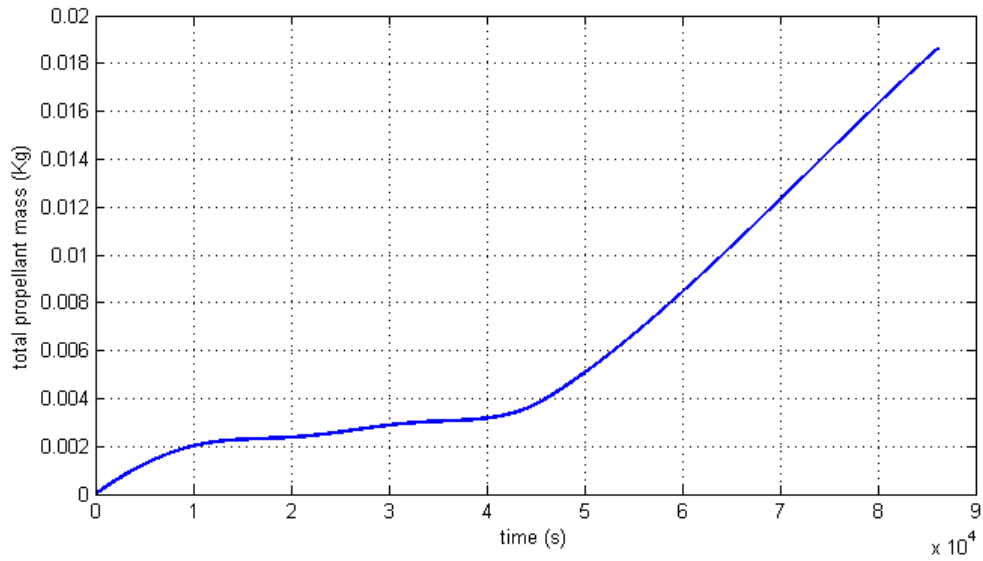
Figures 3.52 and 3.53 show the solar sail with a fixed area of  $300 \text{ m}^2$ . Figure 3.45 shows that the angle of incidence is the same for the fixed area of the solar sail. The angle of incidence is the same when the propulsion system is capable of reducing the disturbing forces effects.

Figure 3.52 –  $\Delta V$  values for the solar sail, the perturbations and the thrust for one orbital period with a fixed area for the solar sail.



The  $\Delta V$  now differs from the solar sail with the variable area for the thrust and the solar sail perturbation. The solar sail with fixed area follows clearly the pattern of the angle of incidence. When the angle of incidence of the solar sail is low, the  $\Delta V$  achieves its highest values; when the angle of incidence increases, the magnitude decreases. The propulsion system is active all the time reducing the disturbing forces to guarantee that the perturbations are compensated. The fuel consumption for this maneuver is 0.01863 kg. The reduction of the fuel consumption is 20%, if compared to the maneuver with the thrust usage only.

Figure 3.53 – The fuel consumption evolution for one orbital period with a fixed area for the solar sail.



### 3.3. The Electromagnetic Tether Study

This section includes the electromagnetic tether study. The initial parameters for the simulations are given in Table 3.10. The results in this section are related to de-orbit employment of the tether, when the tether current runs in the direction of the induced EMF. The tether attitude is the radial attitude (vertically oriented).

Table 3.10 – Parameters of the spacecraft system

Dimensions ( $A_{sub1}$ , $A_{sub2}$ )	6 m <sup>2</sup> , 0.6m <sup>2</sup>
Mass ( $m_1$ , $m_2$ )	100 kg, 5 kg
Load resistance (Ohm)	0

Table 3.11 – Parameters of the Tether Cable

Tether core material	Aluminium
Core density (kg/m <sup>3</sup> )	2850
Core resistivity	27.4 x 10 <sup>-9</sup>
Tether radius (mm)	0.2

The resistance of the tether is neglected, although the system described in Table 3.11 would generate a non-negligible resistance. The resistance complicates the tether modeling and it is neglected in most of the investigations like in [Johnson and Hermann \(1998\)](#), [Estes et al. \(1997\)](#), [Lorenzini et al. \(1997\)](#) and [Sanmartin et al. \(1993\)](#).

Table 3.12 – Electron Density Profile (e<sup>-</sup>/m<sup>3</sup>).

Illuminated region	2 x 10 <sup>12</sup>
Penumbra region	1 x 10 <sup>11</sup>
Umbra region	0.1 x 10 <sup>11</sup>

Table 3.13 – Initial Physical and Orbital Parameters.

Semi-major axis (km)	6978 (600 km of altitude)
Eccentricity	0
Inclination	0

Tether length (km)	5
Pitch and Roll angles for the de-orbit	0
Initial time of the simulation	12:00
Date of the simulation	01/01/2015

Several simulations are carried out to study the effect of the EDT. The effect of each factor is determined by varying its value and keeping the other parameters as given by the tables above.

The angles of pitch and roll are zero and it results in the component of the Lorentz force along the  $x'$ -axis to be zero. The results in this section are given in the orbital coordinates. The explanation of the zero axis perturbation is given in Equation 3.15. The direction of the Lorentz force given in Equation 2.37 is given by the cross product  $d\mathbf{L} \times \mathbf{B}$ .

$$d\mathbf{L} \times \mathbf{B} = (L_{y'}B_{z'} - L_{z'}B_{y'})\hat{x}' + (L_{z'}B_{x'} - L_{x'}B_{z'})\hat{y}' + (L_{x'}B_{y'} - L_{y'}B_{x'})\hat{z}' \quad (3.15)$$

The tether with radial attitude direction (pitch = 0 and roll = 0) does not have any perturbation for this integral, since  $d\mathbf{L} = L_1\hat{x}'$  and  $|d\mathbf{L} \times \mathbf{B}|_{\hat{x}'} = 0$ .

### 3.3.1. The Tether Length Study

[Forward et al. \(1997\)](#) et al. states that the EDT should have a length of 5 to 20 km in order to guarantee that the tether remains taut all the time. The Figures shows the average EMF, the mean current at  $m_1$  and the average Lorentz force

for the insulated and bare tethers. The average value means the mean value for one orbital period.

Figure 3.54 – The average EMF for insulated and bare tethers for tether lengths from 5 to 20 km.

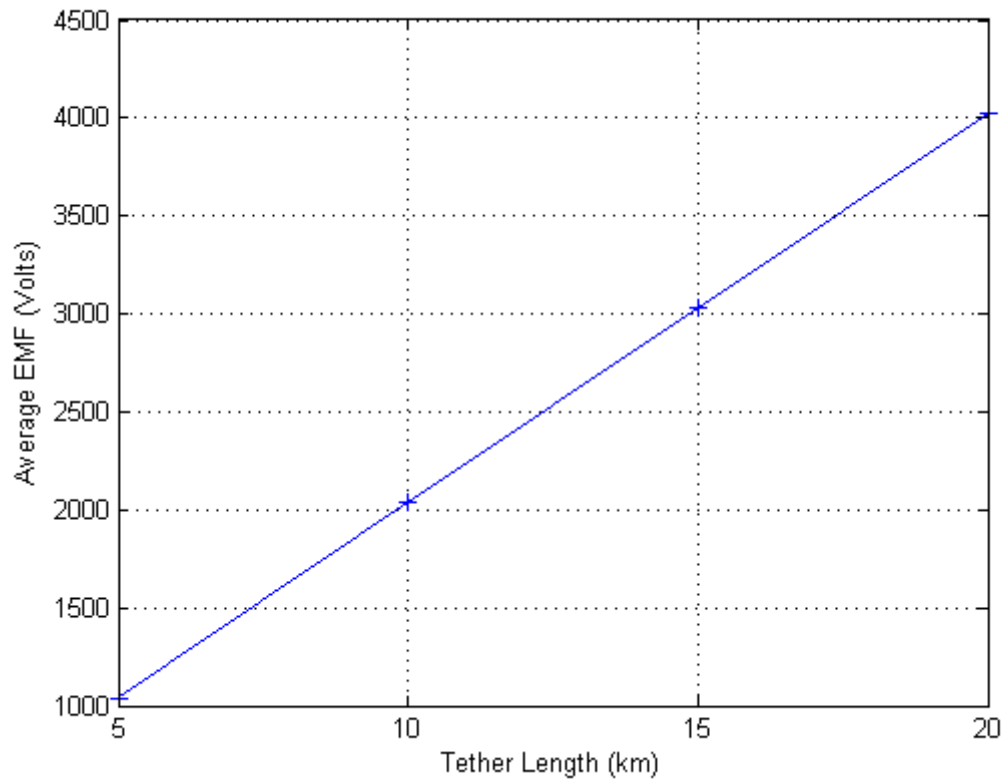


Figure 3.55 – The average current for insulated tether for lengths from 5 to 20 km.

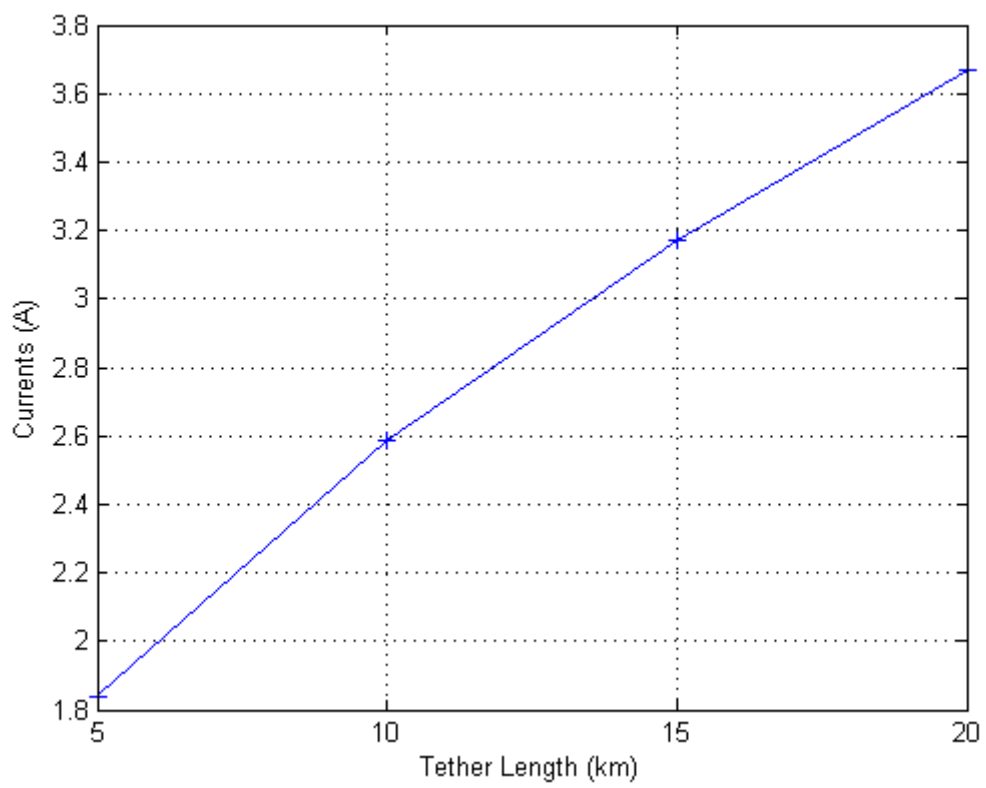


Figure 3.56 – The average current for bare tether for lengths from 5 to 20 km.

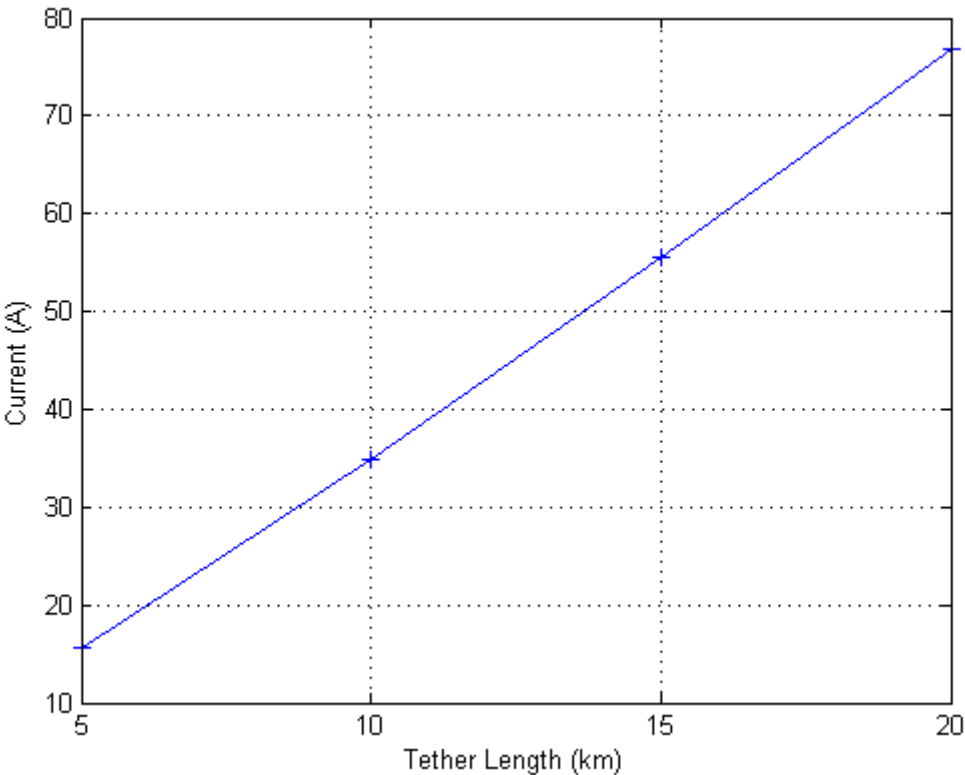


Figure 3.57 – The acceleration on the Y' axis for insulated tether from lengths from 5 to 20 km.

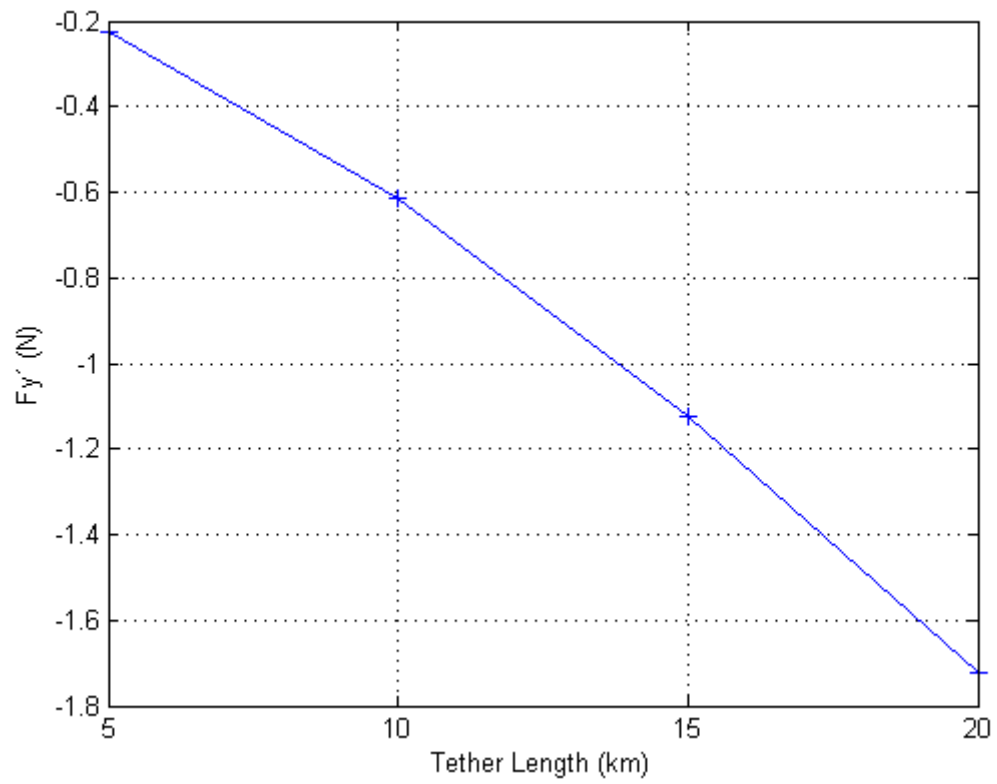


Figure 3.58 – The acceleration on the Y' axis for bare tether from lengths from 5 to 20 km.

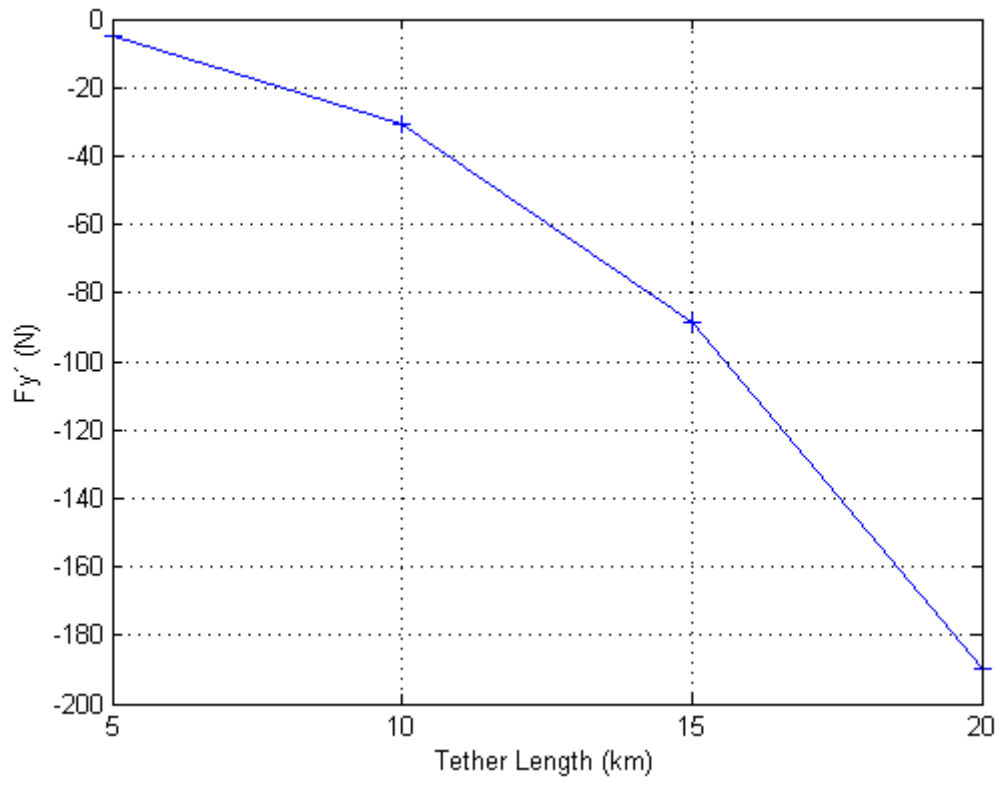


Figure 3.59 – The acceleration on the Z' axis for insulated tether from lengths from 5 to 20 km.

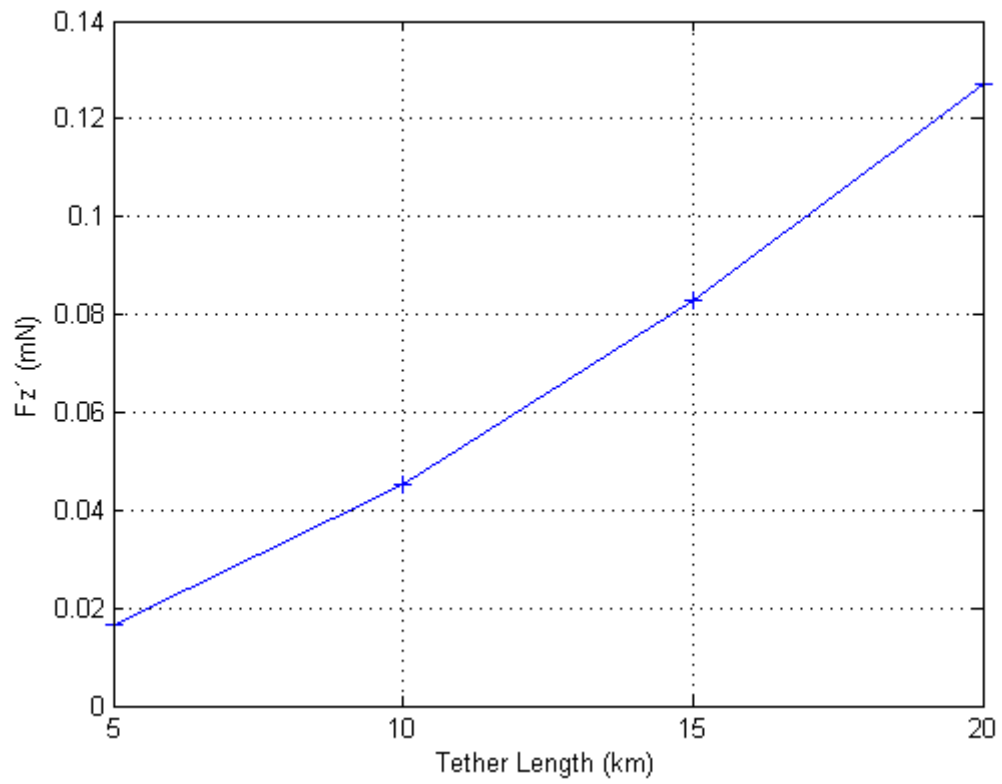
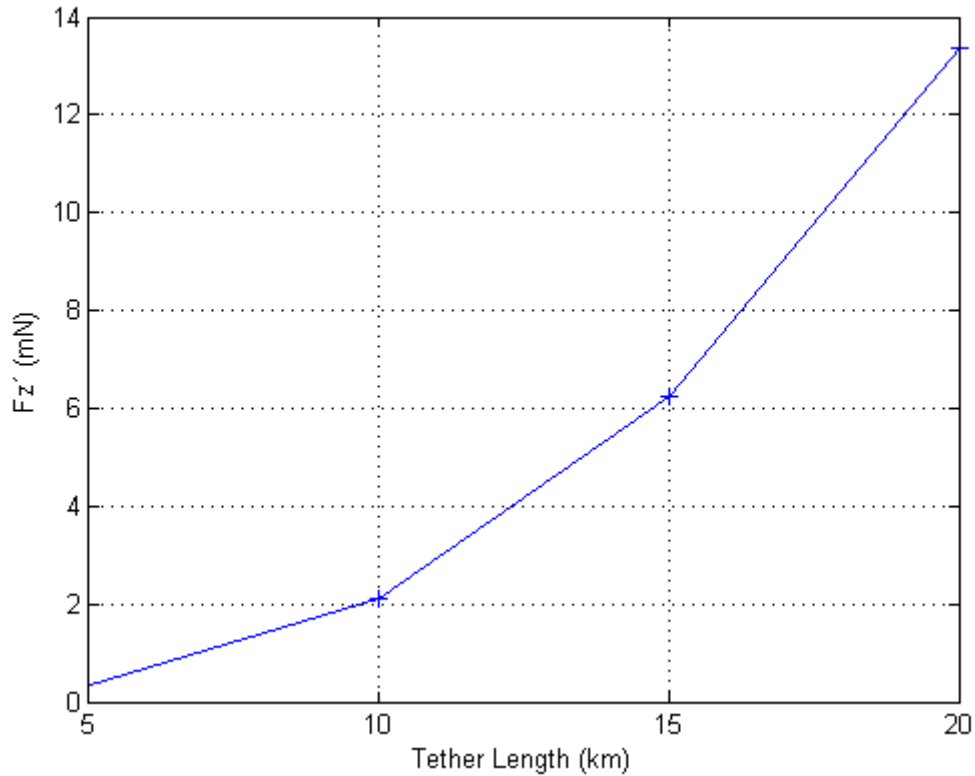


Figure 3.60 – The acceleration on the Z' axis for bare tether from lengths from 5 to 20 km.



The average EMF in Figure 3.54 is the same for both of the tethers, because it depends only on  $v_r$ ,  $\mathbf{B}$ ,  $d\mathbf{l}$  and total length  $L_{total}$  (see Equation 2.34).

The current for the insulated tether follows the 0.528<sup>th</sup> power law behavior given by Equation 2.35 in Figure 3.55. The Lorentz forces in Figures 3.57 and 3.59 approximately follow the 1.528<sup>th</sup> power law, since the force is proportional to both the current and tether length (see Equations 2.35 and 2.37).

The induced current for the bare tether follows the 1.5<sup>th</sup> power law behavior of the tether length in Figure 3.56, related to Equations 2.39 and 2.41. The Lorentz force given by Figures 3.58 3.60 grows with 2.5<sup>th</sup> power of the tether length.

The results are consistent with the mathematical model and the growth power of the bare tethers, in terms of the current and the Lorentz forces. It is a major advantage of the bare tethers.

### 3.3.2. The Tether Semi-Major Axis Study

This section studies the current, average EMF and the induced Lorentz force in tethers as a function of the semi-major axis.

Figure 3.61 – The average EMF for insulated and bare tethers from 6500 to 9500 km of semi-major axis.

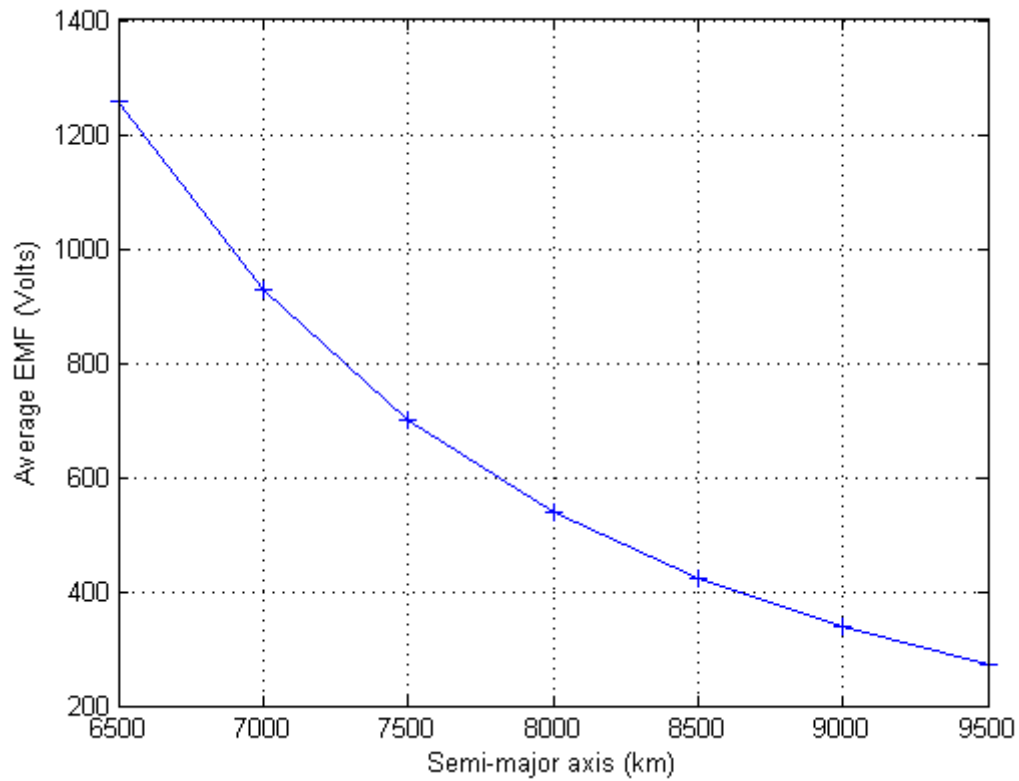


Figure 3.62 – The average current for insulated tether from 6500 to 9500 km of semi-major axis.

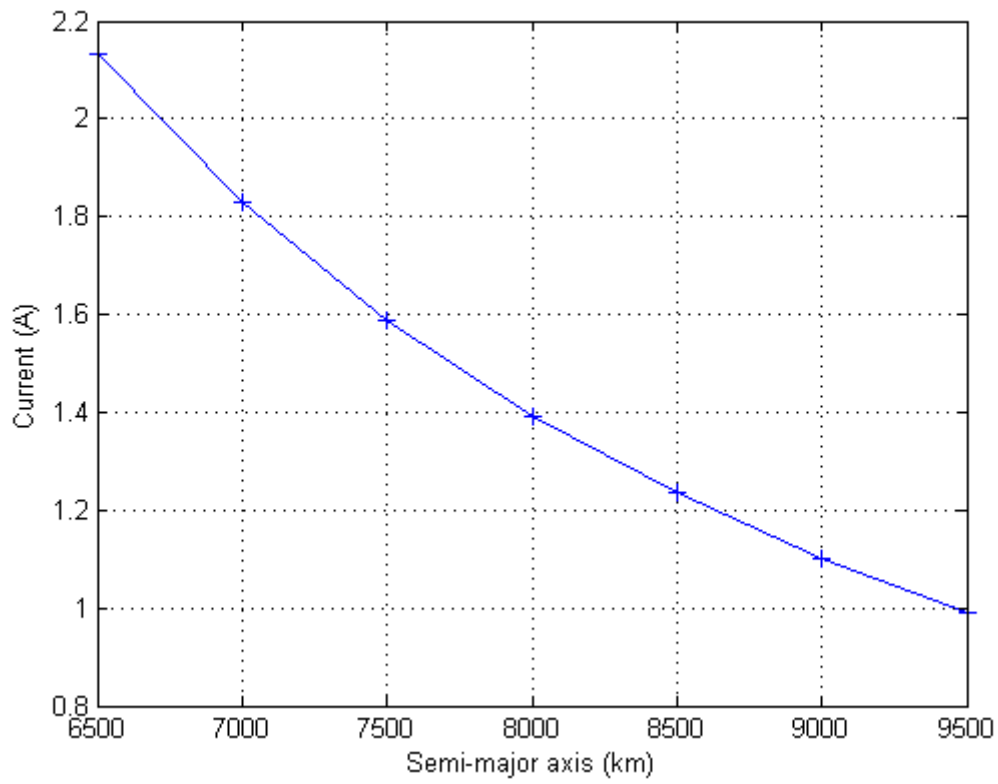


Figure 3.63 – The average current for bare tether from 6500 to 9500 km of semi-major axis.

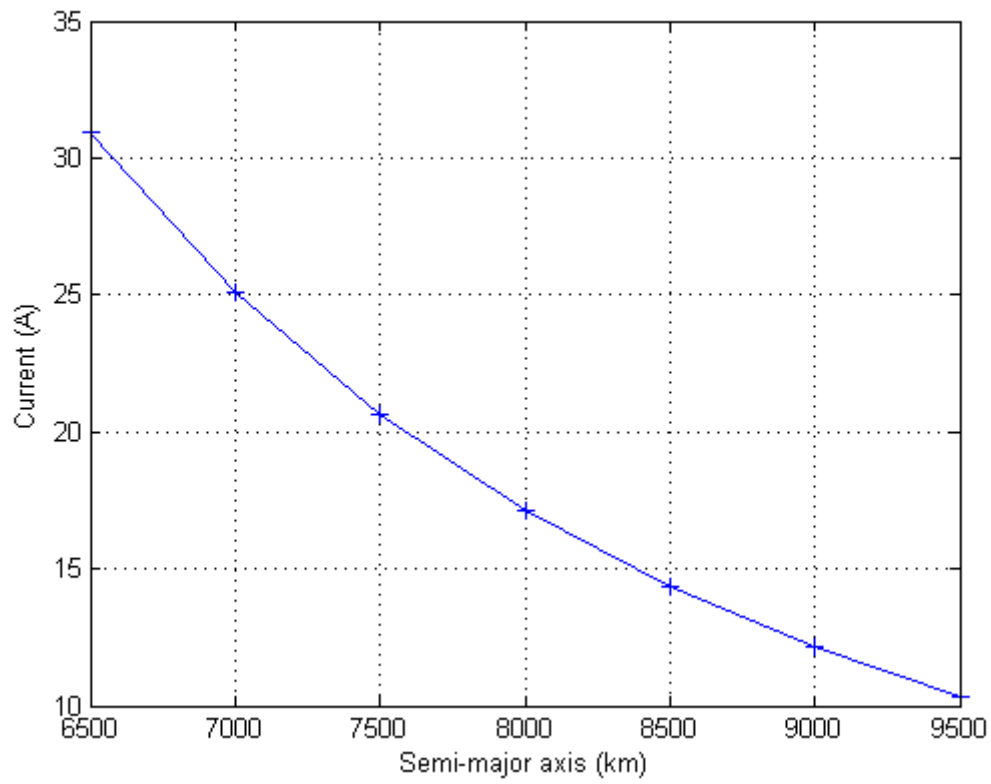


Figure 3.64 – The acceleration on the Y' axis for insulated tether from 6500 to 9500 km of semi-major axis.

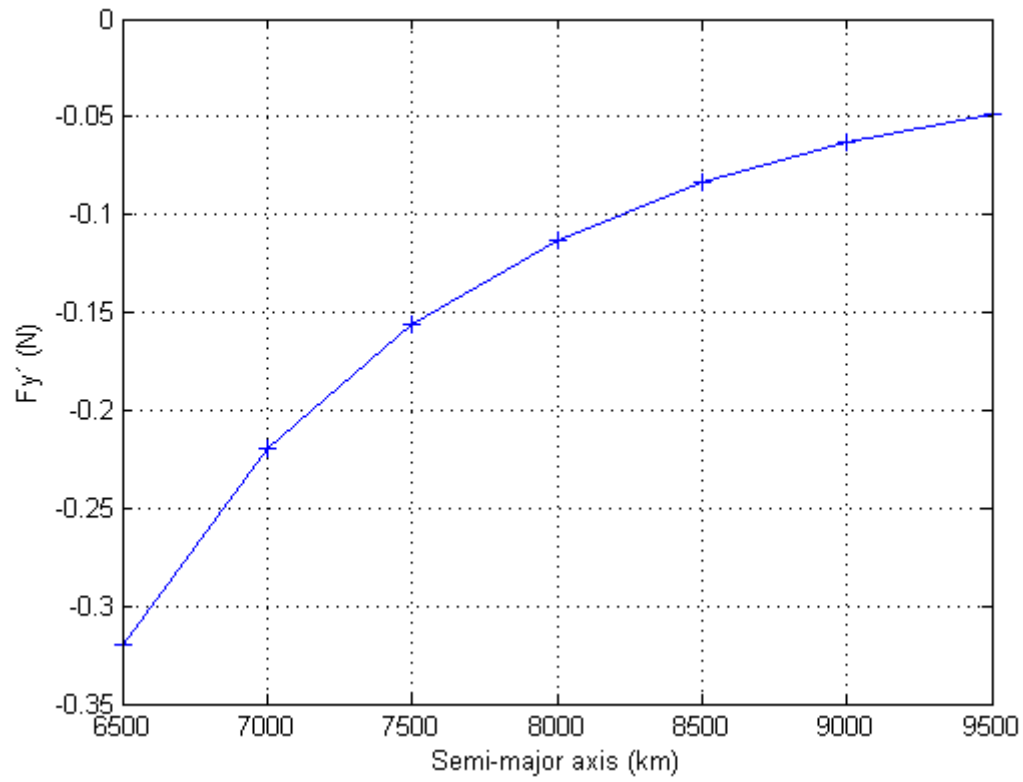


Figure 3.65 – The acceleration on the Y' axis for bare tether from 6500 to 9500 km of semi-major axis.

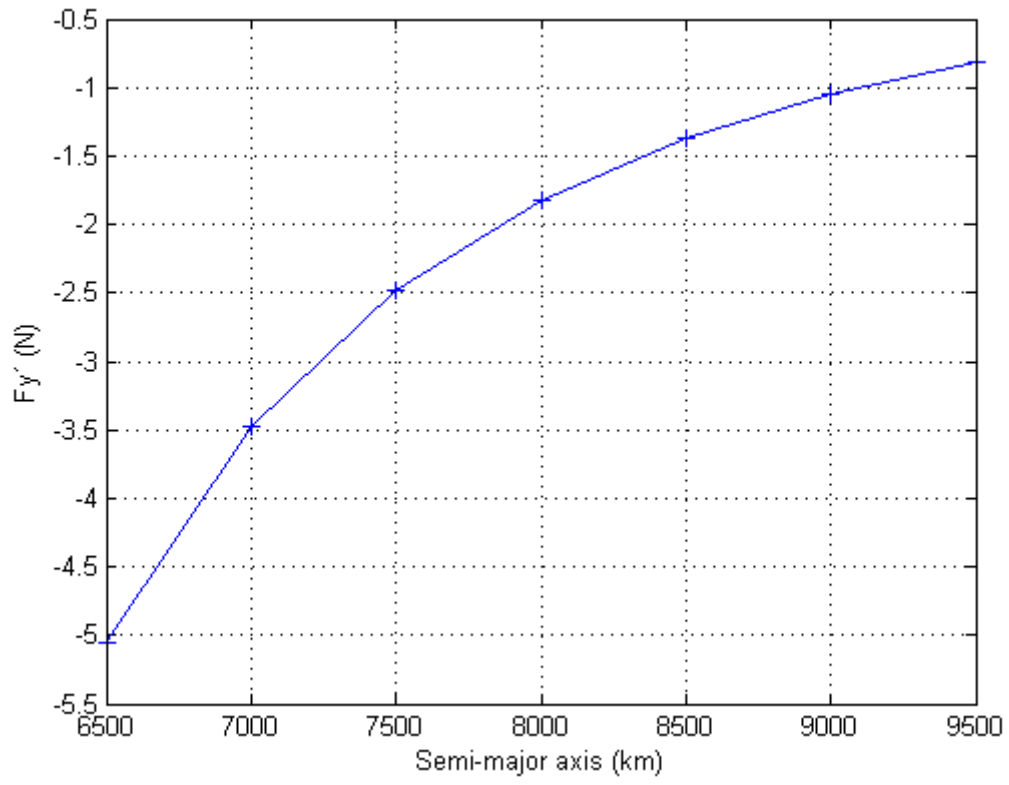


Figure 3.66 – The acceleration on the Z' axis for insulated tether from 6500 to 9500 km of semi-major axis.

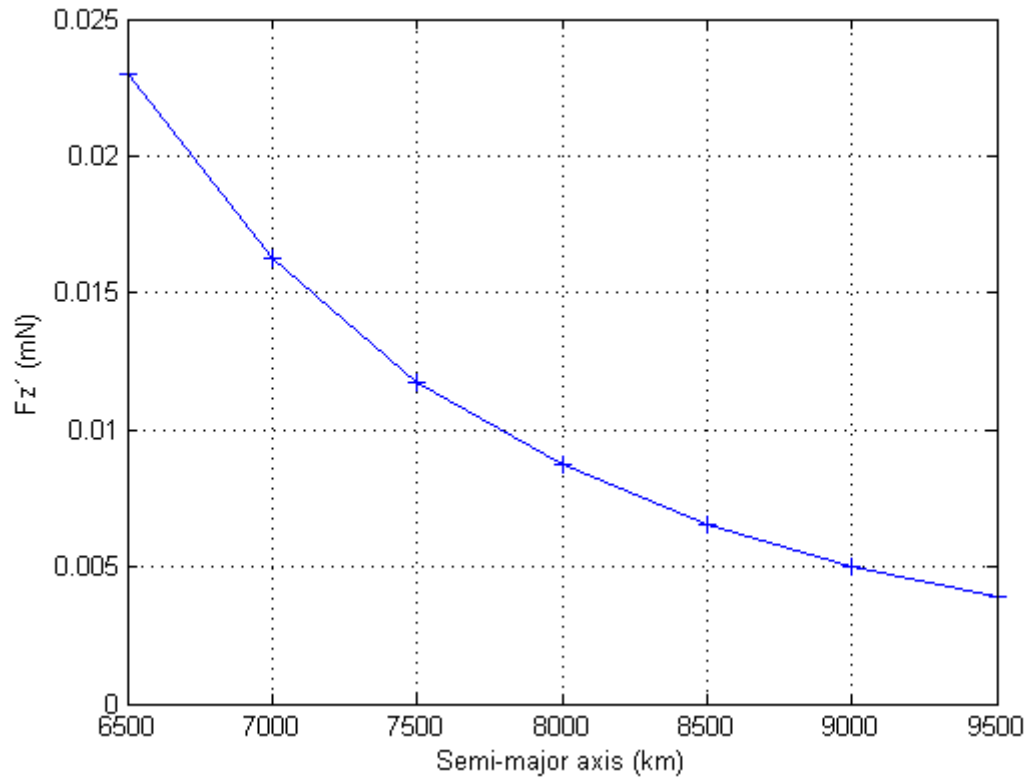
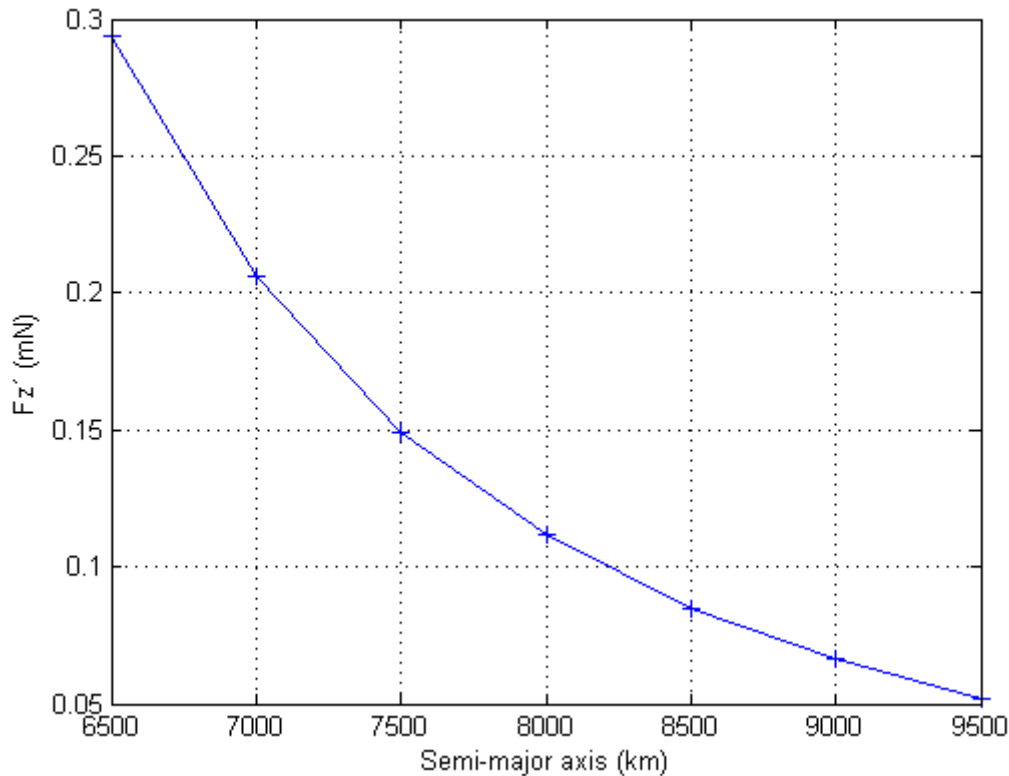


Figure 3.67 – The acceleration on the Z' axis for bare tether from 6500 to 9500 km of semi-major axis.



Once again, the EMF does not depend if the tether is bare or insulated, as shown in Figure 3.61. The decay on the EMF force as the altitude increase follows the decay of 3.67<sup>th</sup> power of the altitude. The decay is due to the prominent term of the magnetic field of the Earth ( $\approx 3^{\text{rd}}$  power of decay) added with the 0.5<sup>th</sup> power decay of the orbital speed (COSMO AND LORENZINI, 1997). The difference between the decay of the results of 3.67<sup>th</sup> and the expected decay of 3.5<sup>th</sup> is due to the higher order terms of the magnetic field model (see Figure 3.61).

The insulated current varies with the 0.528<sup>th</sup> power of the EMF. The current would decay with the 1.85<sup>th</sup> power of altitude ( $3.5 \times 0.528 = 1.85$ ) for the first order of approximation. The result obtained with a current and refined model lead to a decay with the 1.78<sup>th</sup> power as shown in Figure 3.62 .

For bare system, the decay of the current would be with the  $1.84^{\text{th}}$  order for the first approximation, with the multiplication of  $3.5^{\text{th}}$  due to the prominent term of the magnetic field and 0.5 due to the velocity decay, as the altitude increases. The results obtained in this thesis with the IGRF10 have the  $1.83^{\text{th}}$  power law of decay, as shown in Figure 3.56.

The Lorentz force is related to the current and the magnetic field of the Earth. In this way, the expected decay, at first order approximation, would be  $5.54^{\text{th}}$  and  $5.25$  of the semi-major axis for insulated and bare wires, respectively. Nevertheless, the results obtained were  $4.91^{\text{th}}$  and  $5.02^{\text{th}}$  power of semi-major axis, respectively (see Figures 3.64 3.65 3.66 and 3.67 ).

### **3.3.3. The Tether Inclination Study**

This study is related to the orbital inclination change. As the inclination of the orbit changes, the orbit goes from direct to retrograde, the EMF and the current reverse their directions (see Figures 3.68 to 3.7). The current, EMF and force magnitudes are larger in orbital inclination of  $\pi-i$  than in  $i$ , since the retrograde orbits have larger velocity magnitudes.

Figure 3.68 – The average EMF for insulated and bare tethers from 0 to  $\pi$  rad of inclination.

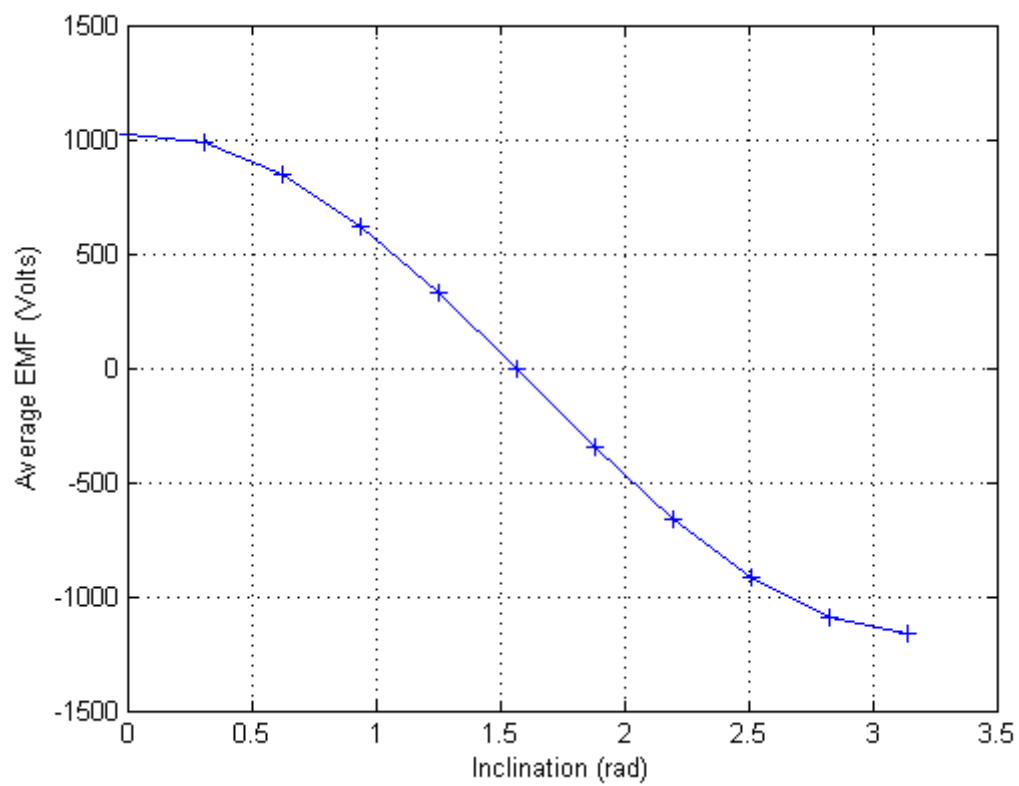


Figure 3.69 – The average current for insulated tether from 0 to  $\pi$  rad of inclination.

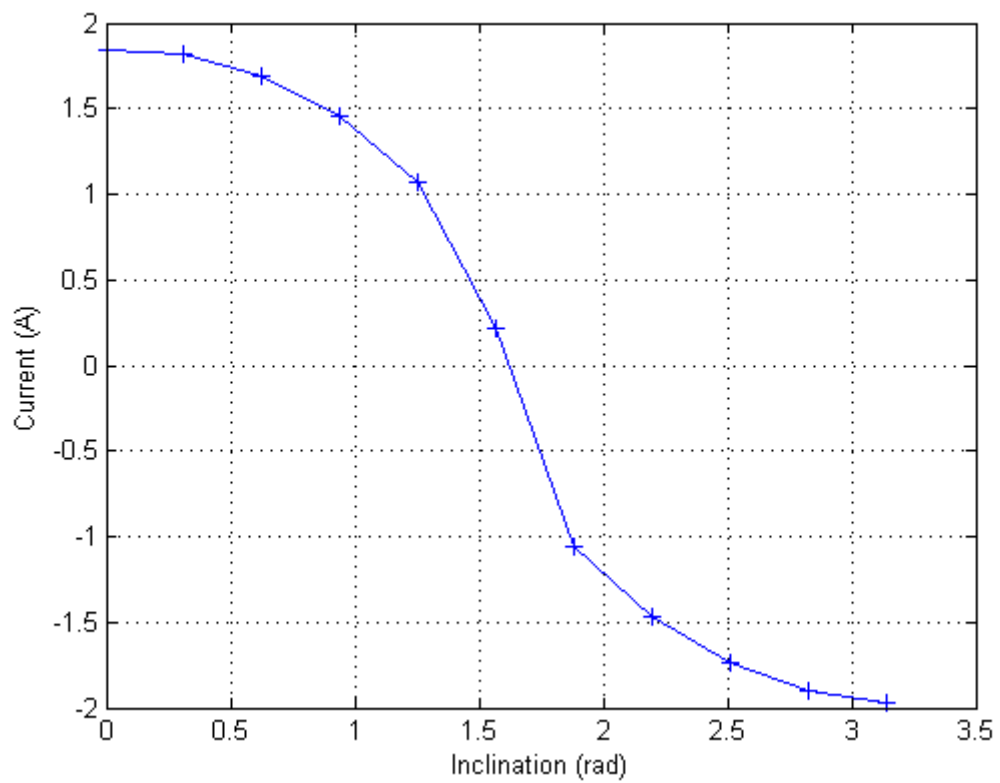


Figure 3.70 – The average current for bare tether from 0 to  $\pi$  rad of inclination.

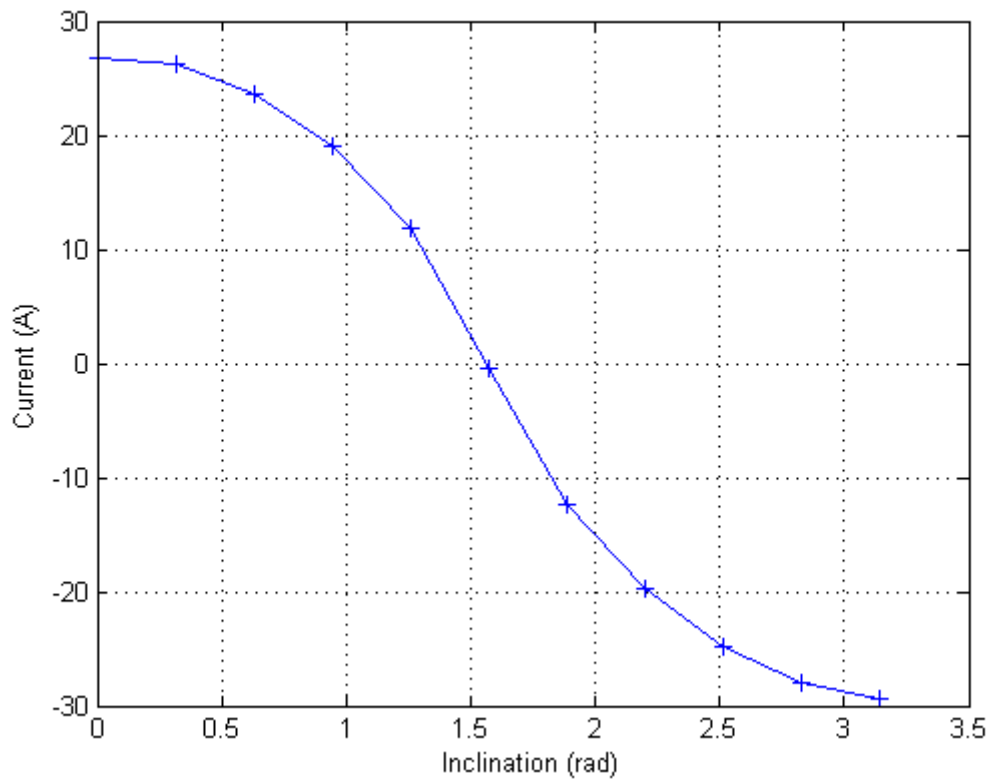


Figure 3.71 – The acceleration on the Y' axis for insulated tether from 0 to  $\pi$  rad of inclination.

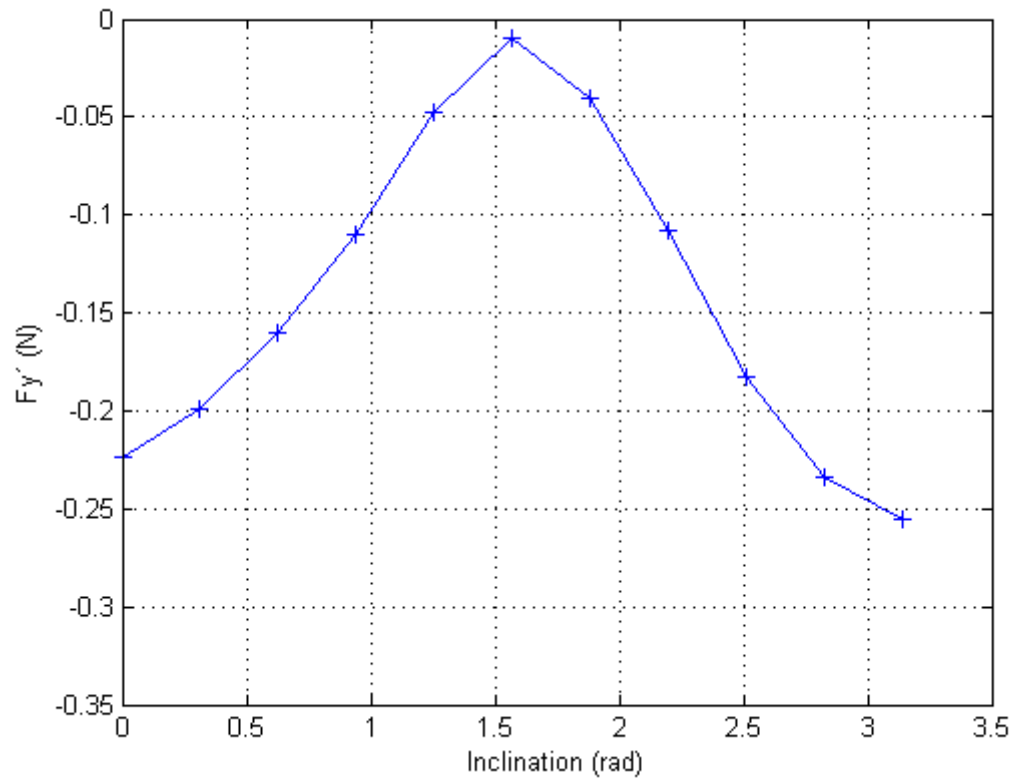


Figure 3.72 – The acceleration on the Y' axis for bare tether from 0 to  $\pi$  rad of inclination.

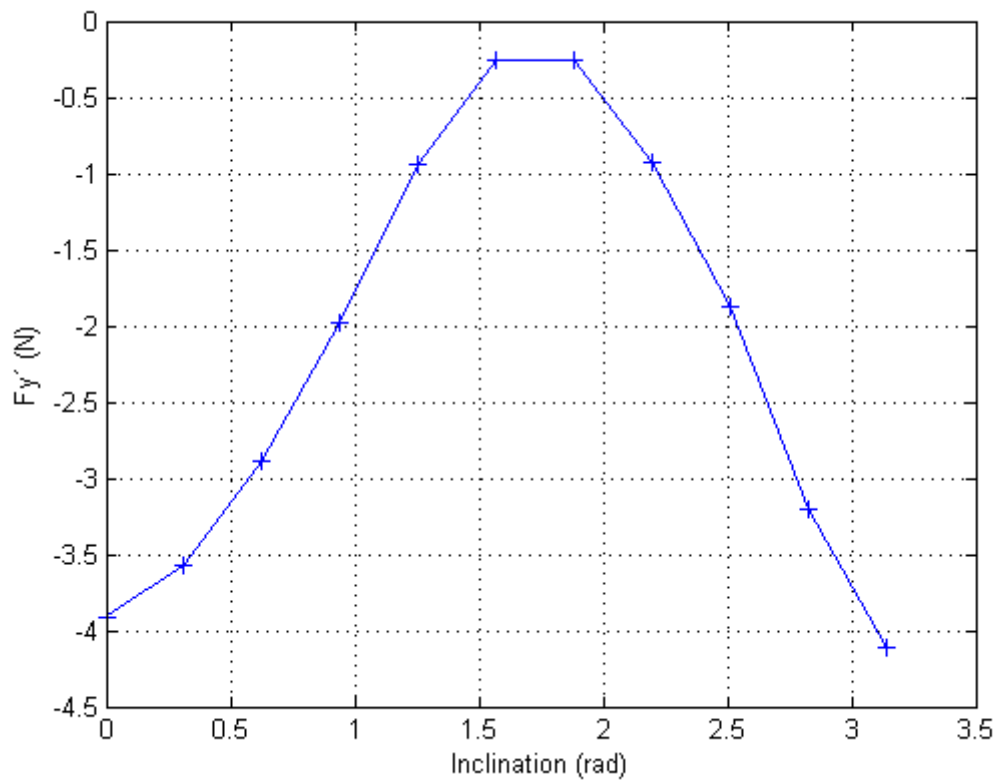


Figure 3.73 – The acceleration on the Z' axis for insulated tether from 0 to  $\pi$  rad of inclination.

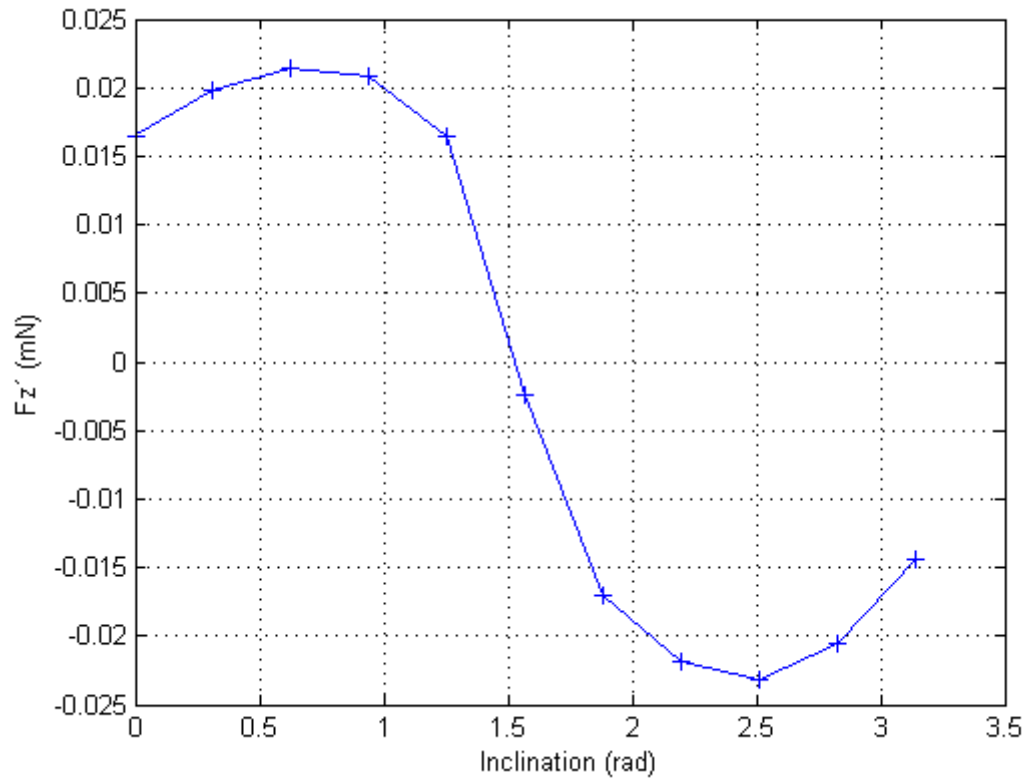
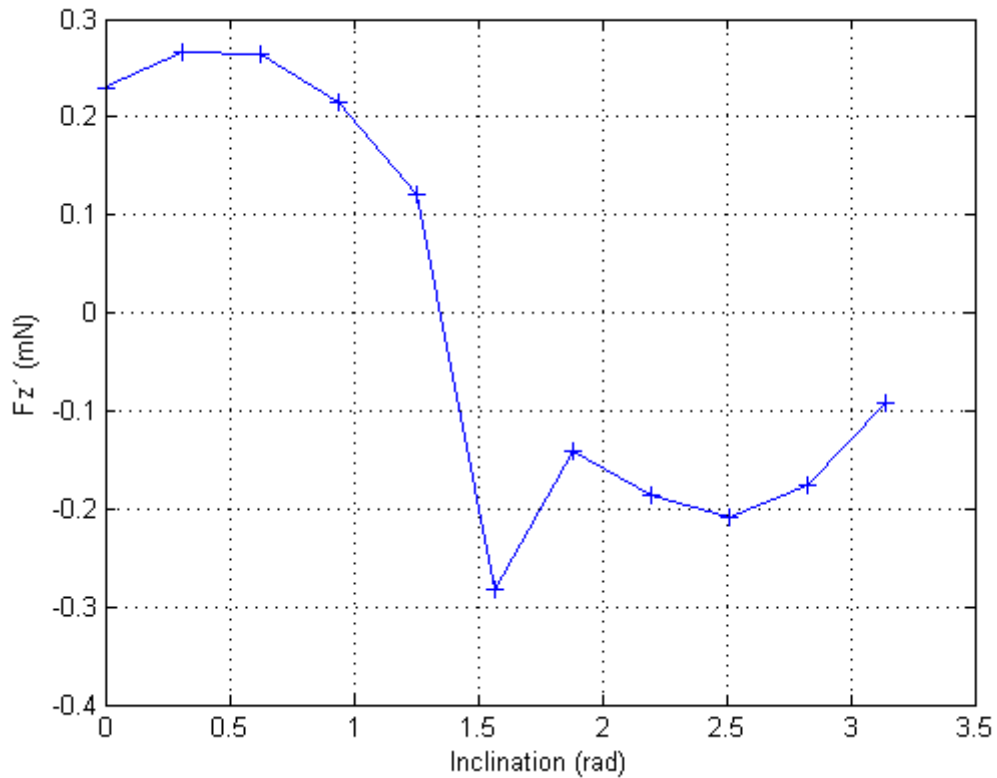


Figure 3.74 – The acceleration on the Z' axis for bare tether from 0 to  $\pi$  rad of inclination.



The study encloses the de-orbit study with the  $F_y'$  negative for most of the cases.  $F_y'$  positive means that the EDT is used to apply thrust and raise the altitude of the system.

For altitudes above the geostationary orbit, the relative speed of the magnetic field becomes greater than the orbital velocity and the EDT has an induced current flowing in the direction of the EMF can be used as a thrust and an electrical power. Altitudes under the geostationary orbit can use the induced current flowing in the direction of the EMF as a drag/de-orbiter. Furthermore, if there is a power supply that overcomes the EMF and allows the current to flow in the opposite direction of the EMF, then the EDT below the GEO can be used as a thrust with the consumption of the electrical power.

This first study of the EDT presented so far includes only the de-orbit case. But the thrust EDT with power consumption for orbits below the GEO presents the same pattern of the EDT tether, like EMF, current and force. The only difference is that it is assumed that the system has a power supply that can overcome the EMF and allow the current to flow in the opposite direction of the EMF. Since the tether resistance is neglected, the average EMF multiplied by the average current presented in the results, in the average power the power supply must apply.

### 3.3.4. The De-Orbiter EDT Effect In Orbital Motion And Perturbation Integrals

This section presents the perturbation integrals and the effect of the EDT in the altitude change in the orbital motion.

The EDT used as a de-orbiter can also be included in the estimative of the orbit decay using Perturbation Integrals.

The estimative of the orbit decay can also be applied for eccentric orbits. The mathematical model should be different, as given in the previous section for circular orbits. It is necessary to evaluate the time of the orbit decay with the help of Equation 3.4. After some manipulations, Equation 3.4 can be written as

$$\Delta E_N = \frac{F_N}{m} v_N \Delta t_N \quad (3.16)$$

where  $E_N$  is the energy of the orbit N.

For each interaction N,  $T_N$  is the period of the orbit N, and  $PI_N$  is given by  $\frac{F_N}{m} T_N$ . In order to make this estimative more precise, it is possible to use a little trick.

For eccentric orbits, the estimation of the time decay can consider the initial position of the spacecraft. Considering the changes of the energy of the orbit

that occurs when the orbit is decaying, the position of the spacecraft in the eccentric orbit can be found by solving the Kepler's equation:

$$n\Delta t = u - e\sin(u) \tag{3.17}$$

where  $n$  is the mean motion,  $e$  is eccentricity of the orbit and  $u$  is the eccentric anomaly (which gives the position of the spacecraft).

Equation 3.17 allows the estimative of the orbit decay to be more precise, especially for highly eccentric orbits with high apogee distance. The Equation 3.1 is not a must, but it helps to reduce the error of the estimation.

The torques on the motion of the conductive tether are neglected. Nevertheless, since high currents (from 0.5 to 5 Amp) generates larger Lorentz induced torques that can destabilize the system, the maximum current imposed for this study is given as follows

$$I = (0.2 + 0.1 * \sin(3j)) \tag{3.18}$$

where  $j$  is the true anomaly of the orbit of the spacecraft. The  $3j$  helps the tether to be stabilized in the roll oscillations.

The results presented next are based in one circular and two eccentric orbits, with eccentricity equal to 0, 0.1 and 0.15, respectively. The results are based on Tables 3.10 to 3.13 , except for the different eccentricities. The attitude of the tether was considered to be radial. In addition, it is necessary to consider a constraint for the estimated time of the orbit decay. The constraint is that when the position of the spacecraft reaches the Earth's surface, the simulation stops. The same constraint is considered for the orbit propagator.

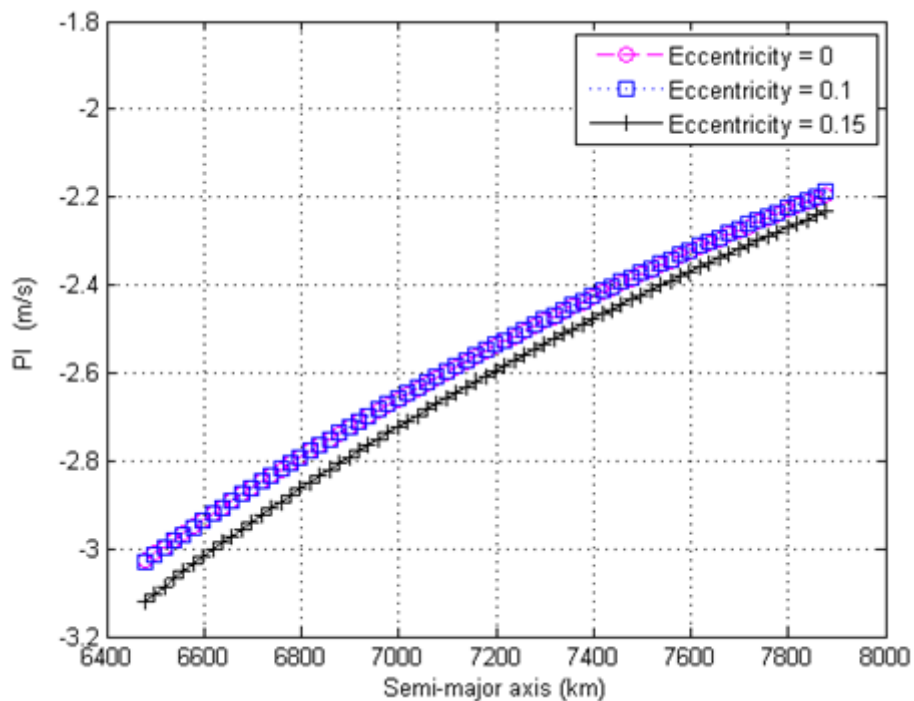
Table 3.14 – Time of decay for different eccentricities.

	Estimated Time	Orbit Propagator

	(days)	(days)
Eccentricity = 0	20.03	19.69
Eccentricity = 0.1	11.27	10.77
Eccentricity = 0.15	5.96	5.94

Figure 3.75 shows the PI values for these three different equatorial orbits.

Figure 3.75 – The PI of the disturbing forces for different eccentric orbits as a function of the semi-major axis from 6500 to 7900 km.

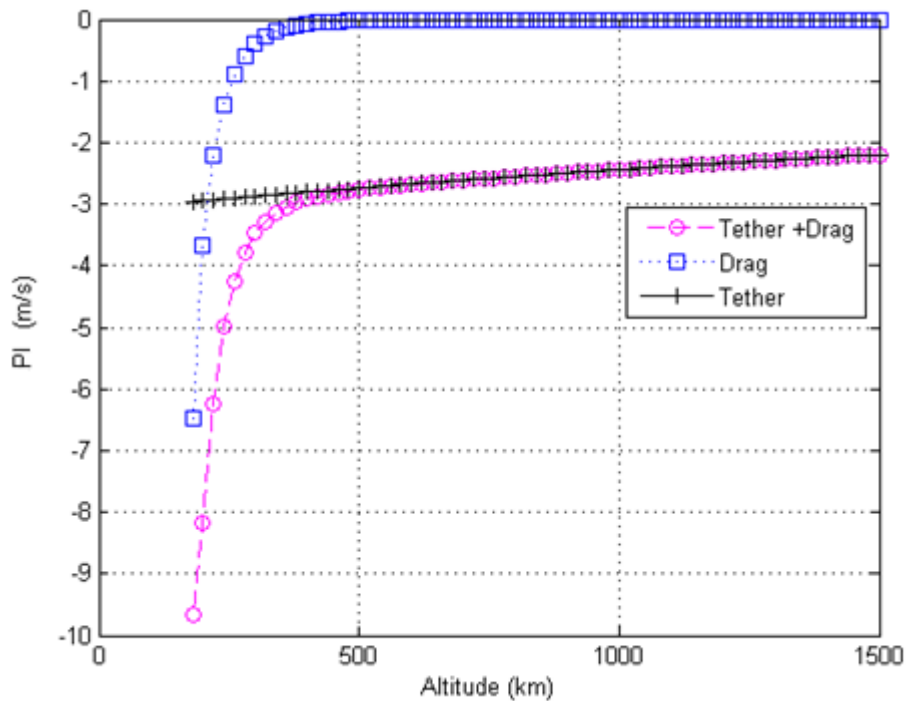


As we can see from Figure 3.75, when the eccentricity of the orbit increases, the magnitude of the PI value of the tether perturbation also increases. As the magnitude of the PI value increases, the time of orbit decay is shortened (as we can see in the table above). The eccentricity also decreases the apogee of the

orbit. Equation 3.17 is essential to guarantee the estimate time of the decay of the orbit with minimum error.

The orbit studied is a LEO. Therefore, the atmospheric drag can be included in the PI with the EDT. The result below shows the PI integrals with the atmospheric drag included as a perturbation. The results are based in the initial parameters in Tables 3.10 to 3.13

Figure 3.76 – The PI of the disturbing forces for different eccentric orbits as a function of the altitude from 150 to 1500 km..



It is possible to note that the magnitude of the drag perturbation increases exponentially as the altitude of the orbit decreases.

The estimate time for the orbit decay of Figure 3.69 is shown below.

Table 3.15 – Time of decay for different eccentricities.

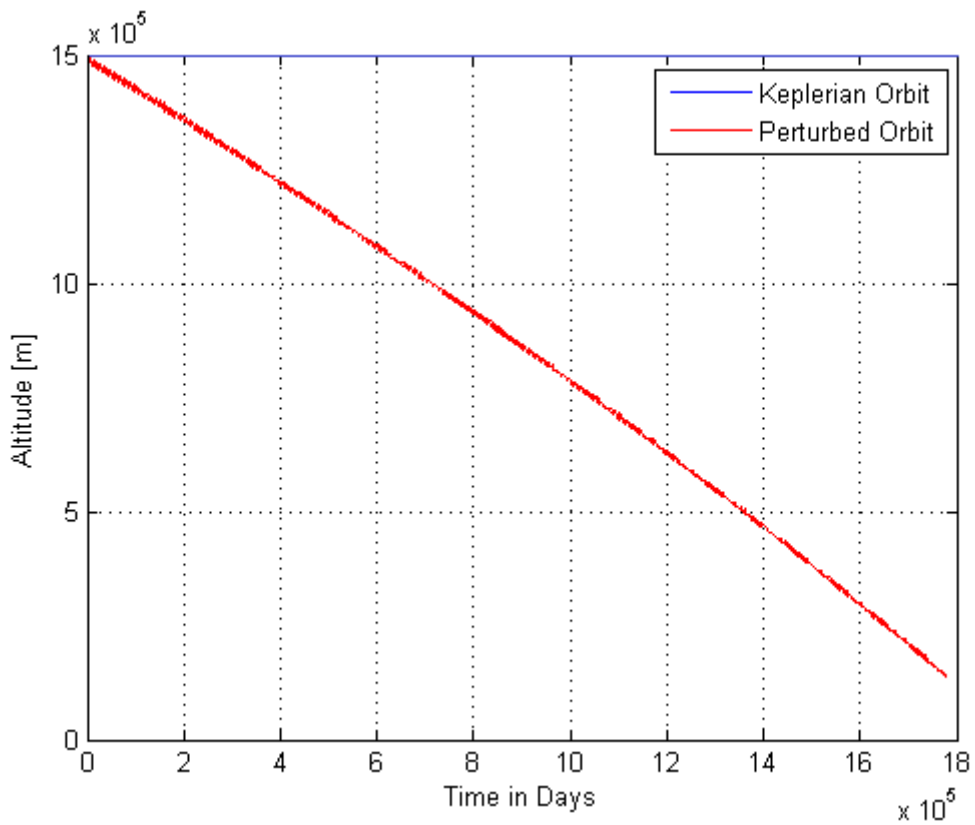
	Estimated Time (days)	Orbit Propagator (days)

Tether	20.03	19.69
Tether + Drag	18.90	18.12

The estimative of the orbit decay with the PI is an easy method to estimate the orbit decay without making numerical integration.

Figure 3.77 shows the decay of the system based on Tables, for an initial altitude of 1500km. The EDT and the atmospheric drag were considered as the forces to de-orbit the spacecraft, but the other disturbing forces were also in the model.

Figure 3.77 – The decay of the tethered system over the days from zero to 18 days.



### 3.4. The Electrodynamic Tether Use For Reducing The Disturbing Forces

This section presents the use of the EDT to reduce the disturbing forces effects. The results present here are based on one orbital period of the spacecraft. The analysis is performed by assuming that the spacecraft is in a Keplerian orbit all the time. It is also assumed that a thrust is applied to compensate the disturbing forces effects that the tether cannot compensate.

The initial parameters of the simulation are based on Tables 3.10 to 3.13 . The initial time and date for this simulation is 01/01/2014 12:30 GMT. The pitch and roll angles are not zero in this case. The idea of using the solar sail to reduce the disturbing forces effects is also applied in the EDT study. The disturbing forces that needs to be reduced are computed and the optimal angle of pitch and roll are found to guarantee that the Lorentz force can reduce the effects of the disturbing forces. The computation of the angles is based on the centre of the mass of the system. This system has the direction for the magnetic field and the direction of the force to be reduced. The direction of the attitude of the tether, given by  $dL$ , is then found.

The tether used for this studied is the bare tether, because it has been proved that this tether is capable of larger currents and Lorentz forces. As the atmospheric drag needs to be reduced in all the simulations, the tether must run a current in the opposite direction of the induced EMF. So is necessary a battery to overcome the EMF to allow the current to flow in the correct direction.

Figure 3.78 shows the acceleration considering only the atmospheric drag and on the Y axis of the OXYZ reference frame. The orbit is circular and Keplerian, therefore, the Y axis is actually the direction of the orbital motion.

Figure 3.78 – The acceleration of the tether and the disturbing forces for one orbital period.

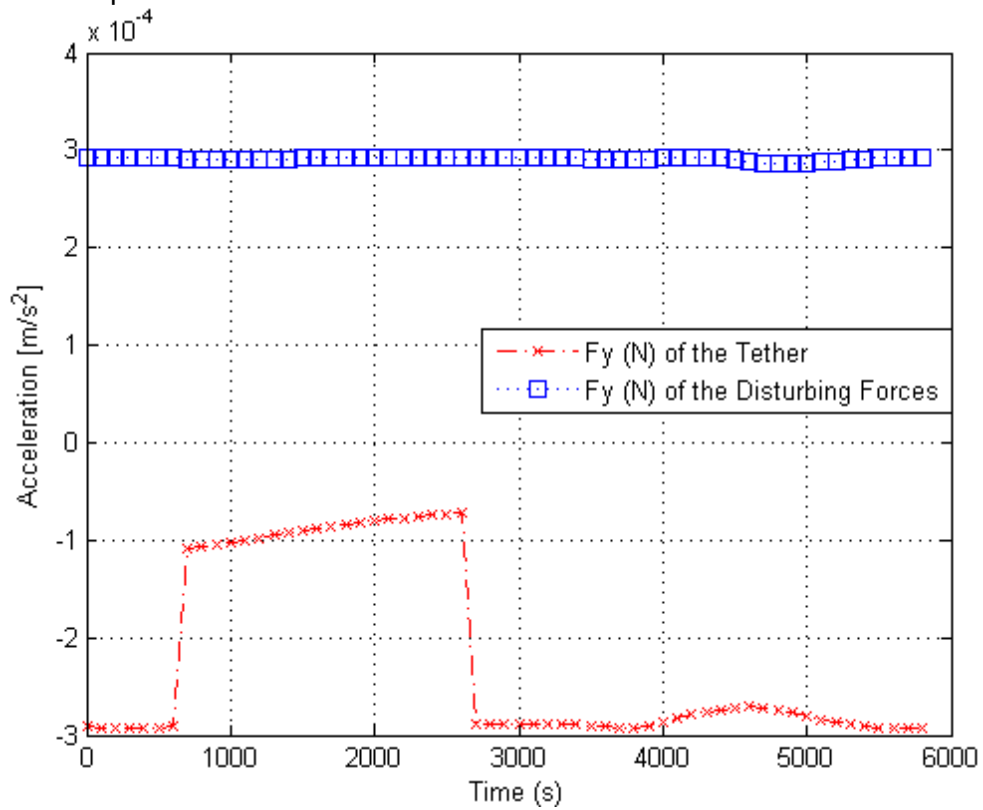


Figure 3.78 shows that the tether can apply a disturbing force at the opposite direction of the atmospheric drag with almost the same magnitude. There are some intervals where the tether cannot reach the required magnitude. Figure 3.79 provides the explanation for this limitation.

Figure 3.79 – The ionospheric density, umbra and illuminated areas for one orbital period.

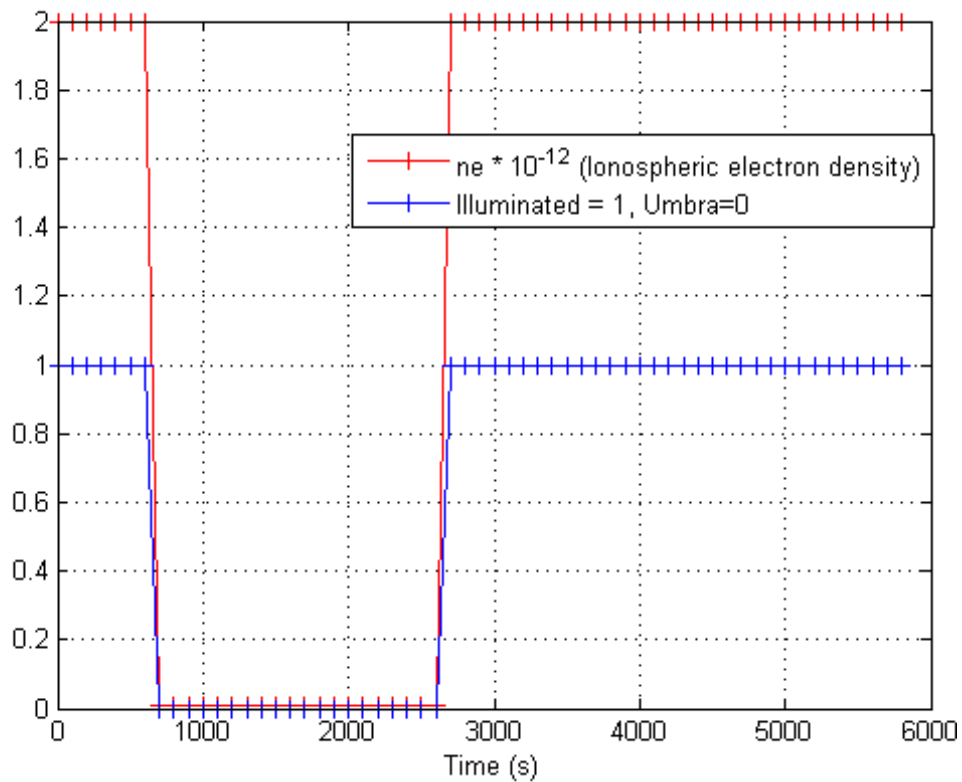
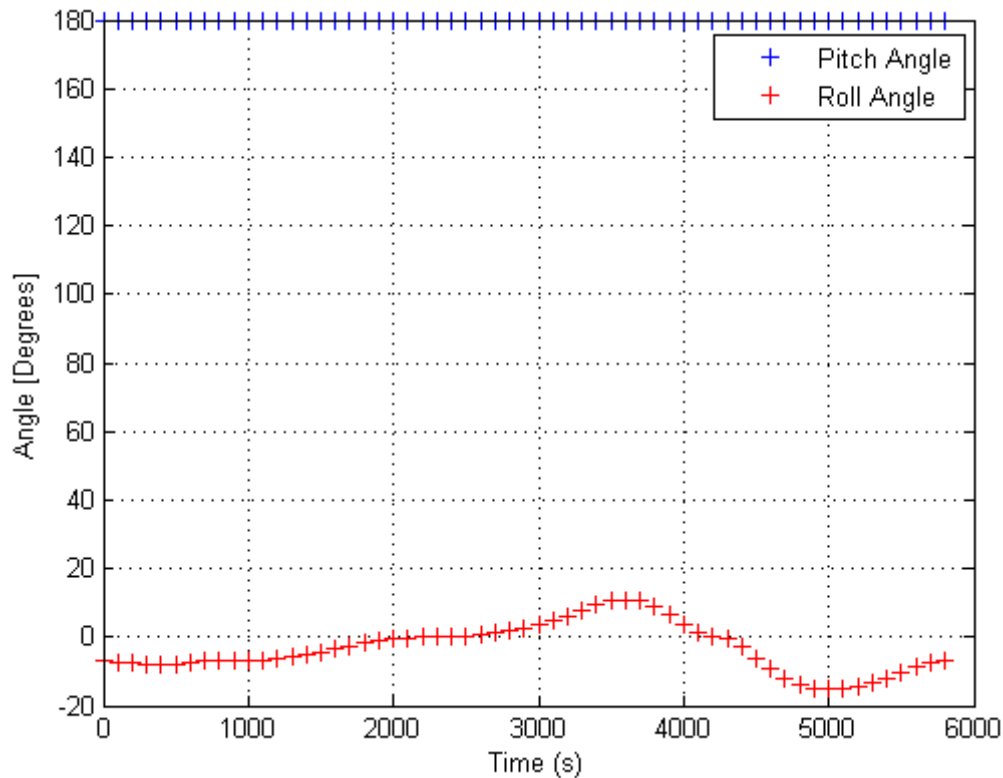


Figure 3.79 shows the ionospheric electron density  $n_e$ . The  $n_e$  is strictly related to the incident of solar rays. The electron density also defines the current that flows in the tether, as given by Equations 2.39 and 2.41. The current is related to the magnetic force (see Equation 2.37) and, if the current is not sufficient to guarantee the optimal magnitude, the tether cannot fully control the disturbing force.

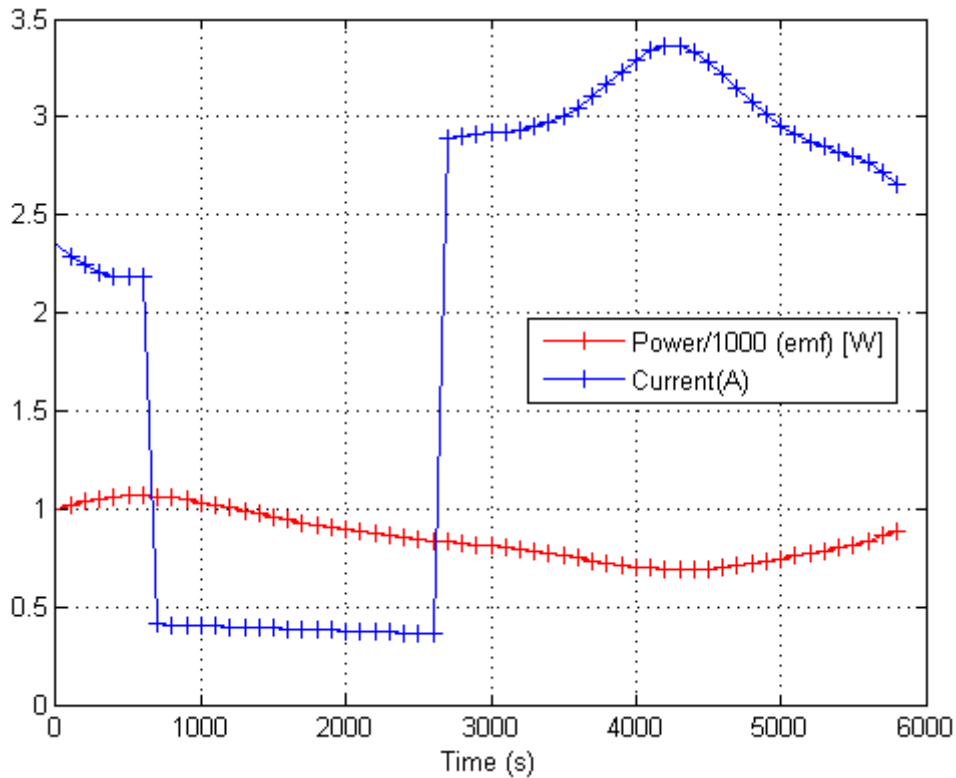
The attitude that the tether must have, in this case, to reduce the disturbing force effects of the atmospheric drag is shown in Figure 3.80 .

Figure 3.80 – The pitch and roll angles for one orbital period.



The pitch angle remains steady all the time, at 180 degrees. The 180 degrees means that the direction of the tether remains parallel to the position vector, as expected. The current flow requires a battery to drive the current into the opposite direction of the induced EMF, therefore the pitch angle is 180 degrees. In the case of a de-orbit, the tether would be required to act as a drag, so the pitch angle should be zero. The roll angle is not zero. The attitude direction of the tether is based on the centre of mass of the system. At that point, the roll is optimal and guarantees that the direction of the electromagnetic tether force along with the pitch angle is opposite to the direction of the disturbing forces. The power and the current that the tether must provide in order to perform this maneuver is shown in Figure 3.81.

Figure 3.81 – The power and current of the tether for one orbital period.



The power shown in Figure 3.81 is the power that the battery must apply in order to guarantee that the current flows in the right direction. The current is the one that must flow in the tether to guarantee that the magnitude of the tether force is coherent with the magnitude of the disturbing force. The current shown in Figure 3.81 is not the maximum value that the tether can deliver to the system (see Equation 2.41 for the maximum current definition). For this simulation, the maximum current is around 20 A. This means that the tether itself can also allow a current flow larger than the one shown in Figure 3.81 to overcome the gap of the current through the passage by the umbra region.

The PI integral, without the averaging technique, as given by Equation 2.1, can provide the amount of the magnitude reduction of the disturbing force for this maneuver. Table 3.16 provides the *PI* values without the averaging technique for the tether and for the disturbing force.

Table 3.16 – PI values based on Equation 2.1.

	PI values
Atmospheric Drag	1.7127 m/s
Tether only	1.2173 m/s
Atmospheric Drag + Tether	0.6299 m/s

Table 3.16 shows the efficiency of the tether proposed in this context. The atmospheric drag has the *PI* value of 1.7127 m/s. This means that the velocity delivered to the spacecraft due to this disturbing force, for one orbital period, is 1.7127 m/s. It would be required a thrust with a total velocity variation of this magnitude for one orbital period to guarantee that the spacecraft does not deviates from its orbit. The tether itself delivers a *PI* value of 1.2173 m/s to the system. The combination of the atmospheric drag and the tether has a *PI* value of 0.6299 m/s. The optimal direction of the tether requires a long processing time for the computer. The method of defining the attitude of the tether based on the centre of mass of the system is fast, but it involves also some errors due to the asymmetry of the magnetic field and its fluctuations. The price of not computing the fluctuations on the magnetic field of the Earth is that the subtraction of the *inte* value of the atmospheric drag and the tether itself is not the *inte* value of the atmospheric drag and the tether. The passage through a umbra region also reduces the efficiency of the tether to zero the atmospheric drag

The tether proposed in this work for this specific maneuver could reduce the magnitude of the disturbing force effects of the atmospheric drag up to 63.22 %. The tether has 5 km length, which is enough for the proposed mission. The

current necessary to reduce the magnitude of the disturbing force effect ( $\approx 3 A$ ) is far lower from the maximum value ( $\approx 20 A$ ).

Drag-free missions are missions that use a drag-free control system, more essentially the atmospheric drag to be eliminated from the equations of motion of the spacecraft. The proposed use of the EDT to reduce the atmospheric drag can be understood as a drag-free control mission and it is extremely important for LEO. The reduction or the elimination of the drag can reduce significantly the cost of orbital maneuvers to overcome the altitude decay. The atmospheric drag must be counteracted continuously as this disturbing force causes the orbital decay and its magnitude increases exponentially and the altitude decays ([LANGE, 1964](#); [VAILLON ET AL., 1990](#))

The next step is to study the case where the tether will not only reduce the atmospheric drag effect, but also the other disturbing forces effects: third-body perturbation from the Sun and the Moon and the solar radiation pressure.

Satellites at LEO experience several disturbing forces: predominantly high order of gravitational components, such as  $J_2$  and  $C_{22}$ , the third-body effects, solar radiation pressure and the atmospheric drag ([EISNER ET AL., 1982](#)). The control of these disturbing forces is extremely important for space missions that require a great accuracy of the trajectory. The reduction of the fuel consumption is highly recommended in order to increase the life-time of the system.

Figures 5 and 6 show the acceleration of the tether and the sum of all disturbing forces as a function of time. The component of the Z axis was omitted, because the magnitude of the disturbing force on this axis is much smaller compared to the other two components.

Figure 3.82 – Acceleration of the tether and all the perturbations on the X axis for one orbital period.

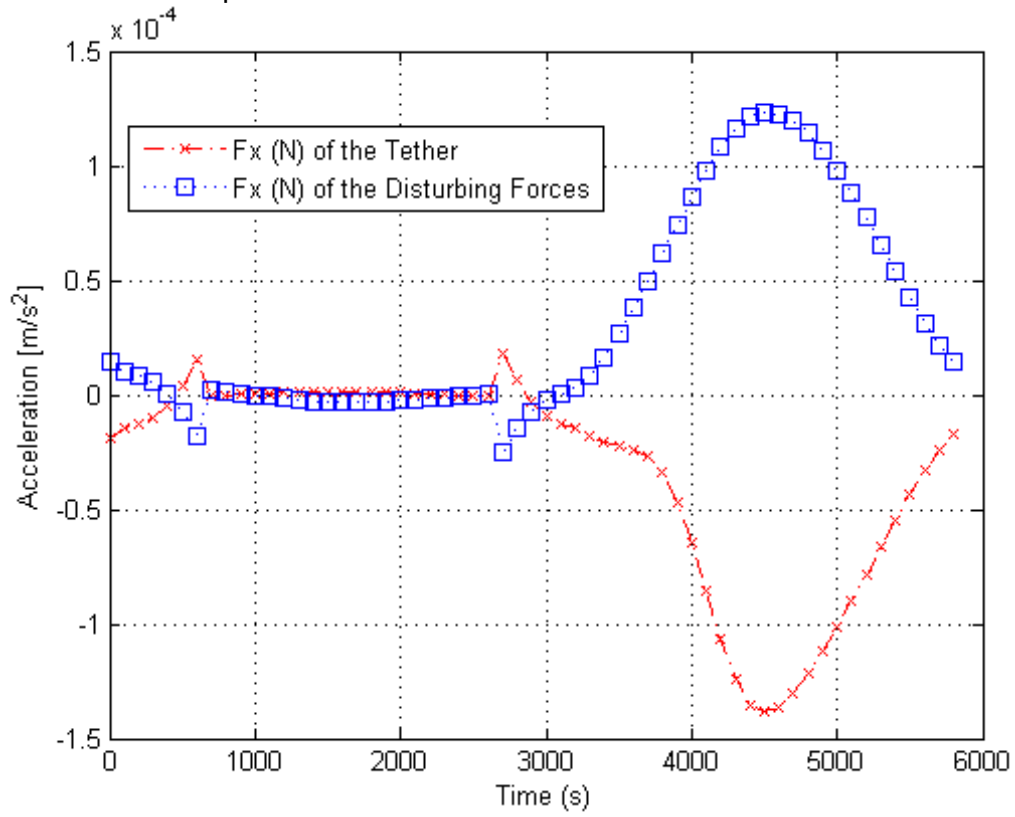
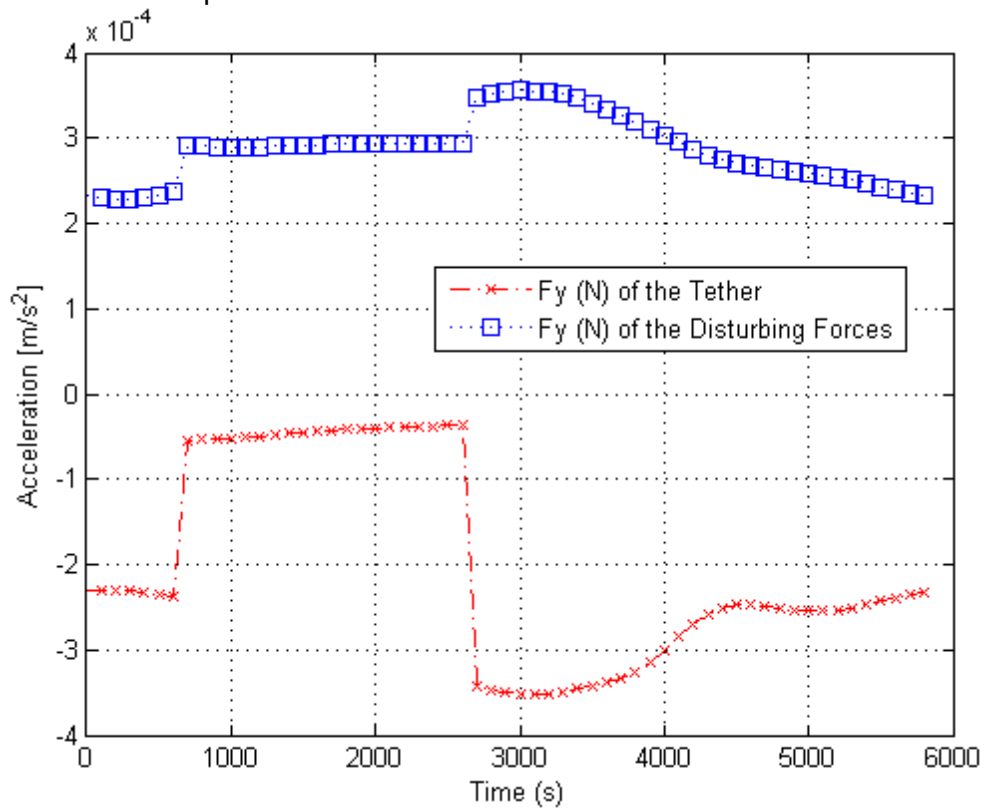


Figure 3.83 – Acceleration of the tether and all the perturbations on the Y axis for one orbital period.

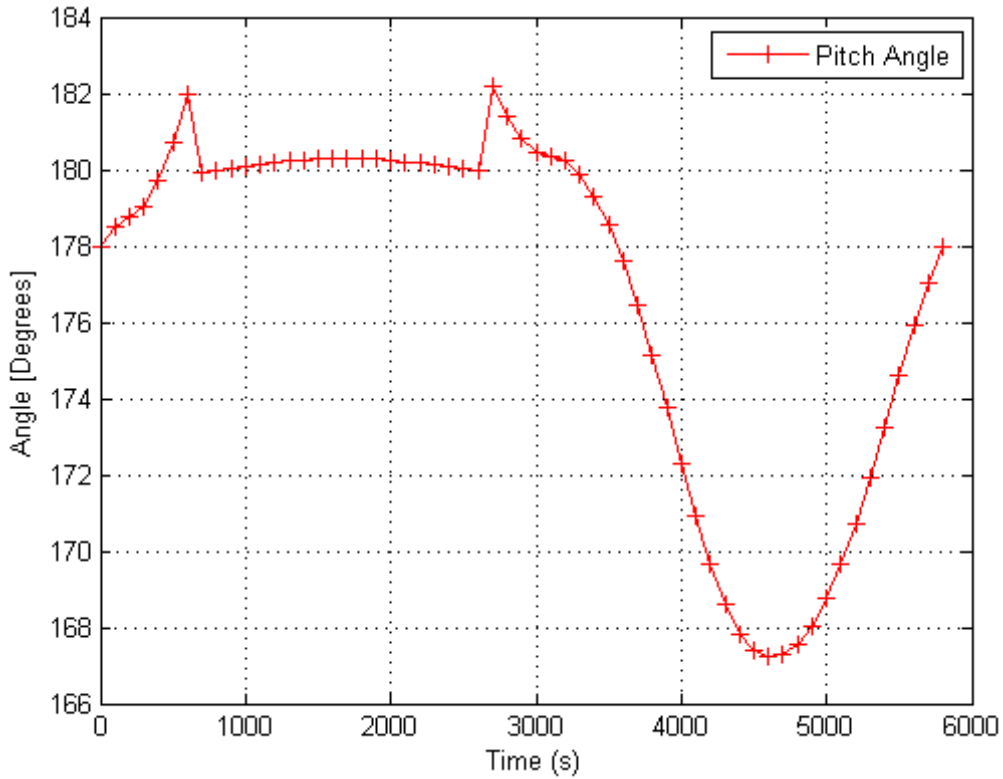


It is clear that the accelerations of the tether and the disturbing forces are almost opposite. Since the initial time of the simulation and the initial parameters are the same, it is possible to note that there is the same gap of the acceleration of the tether for an interval of the time. This occurs, as shown in Figure 3.79, due to the passage of the spacecraft by the shadow of the Earth. It is also interesting to note that the acceleration of the disturbing forces shown in Figures 3.82 and 3.83 also have a discontinuity. The passage by the shadow area reduces the solar radiation pressure perturbation effect to zero and, therefore, there is a decrease in the sum of all the perturbations for this interval as well.

The attitude of the tether, given by the pitch and the roll angles, is different from the previous maneuver. Now, the sum of all the disturbing forces changes the direction that the tether force must be applied. Figure 3.84 shows the pitch

angle that the tether must have for this maneuver. The roll was neglected, since it does not play an important role in this simulation.

Figure 3.84 – Pitch angle for one orbital period.



There is a discontinuity in the pitch angle, due to the decrease of the solar radiation pressure perturbation at the shadow region. Besides this discontinuity, the change of the pitch angle is smooth and changes from 180 to 167 degrees. If it is possible to build a tether that can change and control of the pitch angle, then it is possible to reduce all disturbing forces effects included in this paper. The advantage of reducing all the disturbing forces is to reduce the secular and periodic variations effects. The PI reduction with this maneuver is given in Table 6. The reduction of the magnitude of the disturbing forces is 62.46 %.

Table 3.17 – PI value based on Equation 2.1.

	PI values
--	-----------

Atmospheric Drag	1.7177 m/s
Tether only	1.2223m/s
Atmospheric Drag + Tether	0.6449 m/s

### 3.4.1. The Perturbation Integrals Results For The EDT

This section shows the PI obtained using the averaging technique.

The first result, shown in Figure 3.85 , changes the semi-major axis of the orbit from 6678 to 6978 km (300 to 600 km of altitude). The integration for one orbital period is multiplied by the period of a nominal reference orbit and divided by the period of the current orbit. This procedure avoids time dependence in the results. The nominal reference orbit is 6978 km of semi-major axis. Figure 3.85 shows the PI when the tether is used only to reduce the atmospheric drag effect.

Figure 3.85 – PI of several disturbing forces and the tether as a function of the semi-major axis from 6678 to 6978 km.

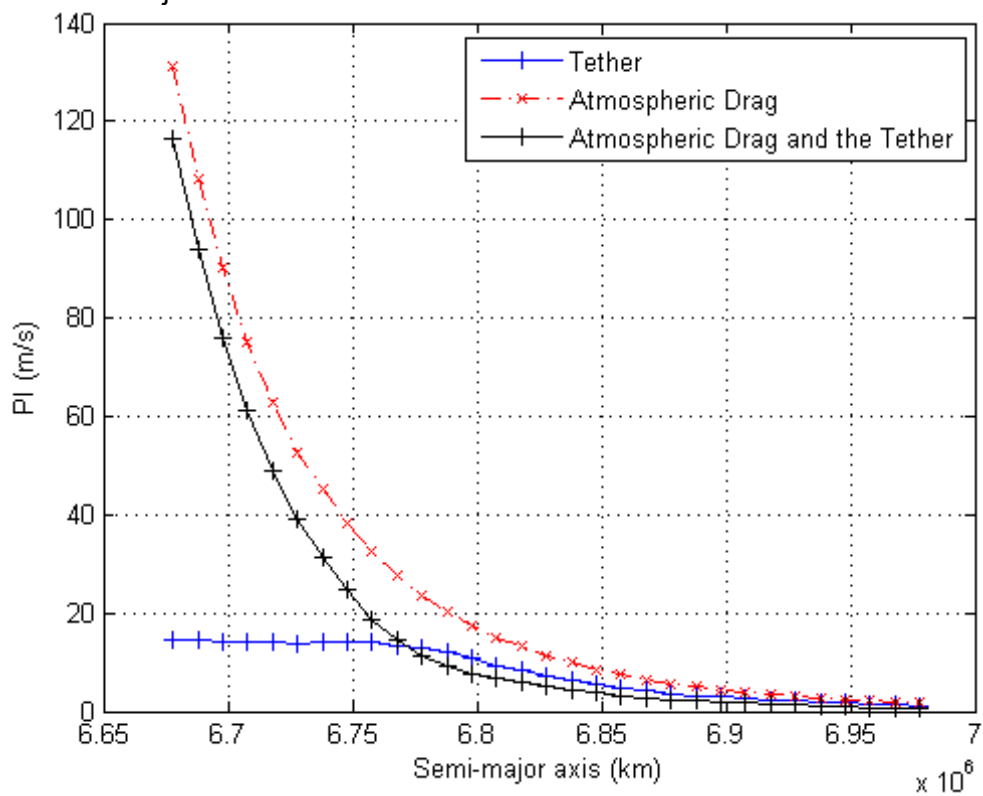


Figure 3.85 shows that the tether is efficient in reducing the magnitude of the disturbing forces. This reduction could be better, if different tether lengths are considered for each semi-major axis interval. The reduction of the magnitude close to the 6678 km semi-major axis is low, due to the magnitude of the atmospheric drag. The magnitude is so large that, even using the maximum current  $I_{max}$ , the tether is not able to guarantee that the disturbing forces can have the same magnitude (Figure 3.86).

Figure 3.86 – Current and power of the tether as a function of the semi-major axis from 6678 to 6978 km.

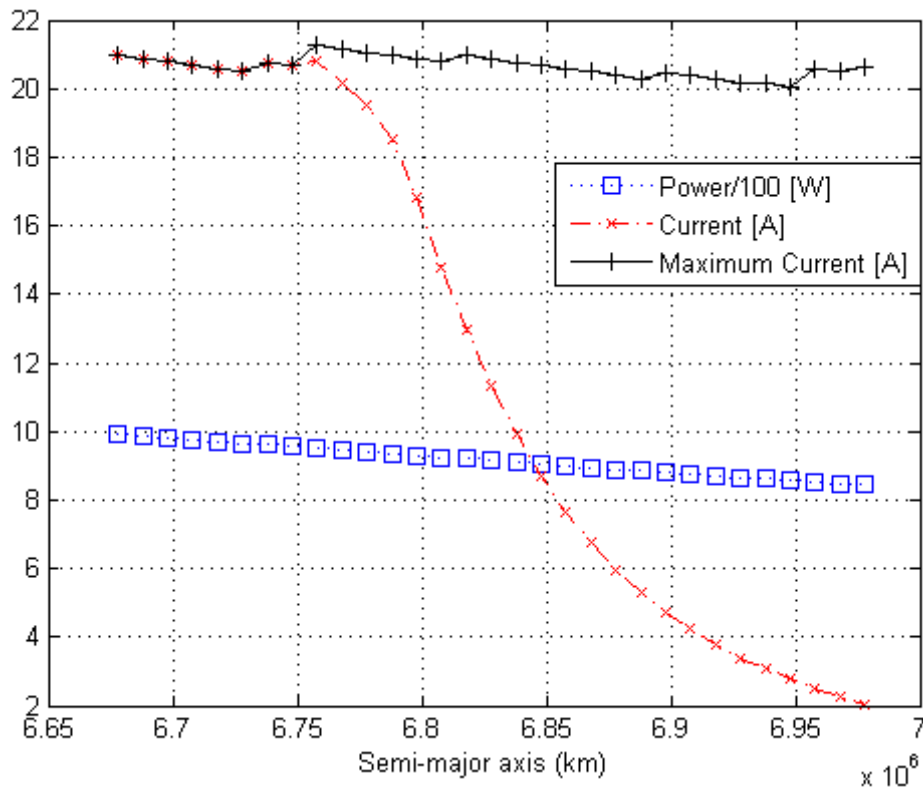


Figure 3.86 shows the maximum current and the nominal current to reduce the disturbing forces effects. From 6678 to 6750 km of semi-major axis, the nominal current of the tether is at the maximum value. Therefore, for this case, the magnitude of the tether cannot be the magnitude of the disturbing force due to the current restriction of the bare tether.

Figures 3.87 - and 3.88 show the use of the tether to reduce all the disturbing forces effects that this work considers. The range of the semi-major axis goes from 6978 to 7278 km.

Figure 3.87 - PI for several disturbing forces as a function of the semi-major axis from 6978 to 7278 km.

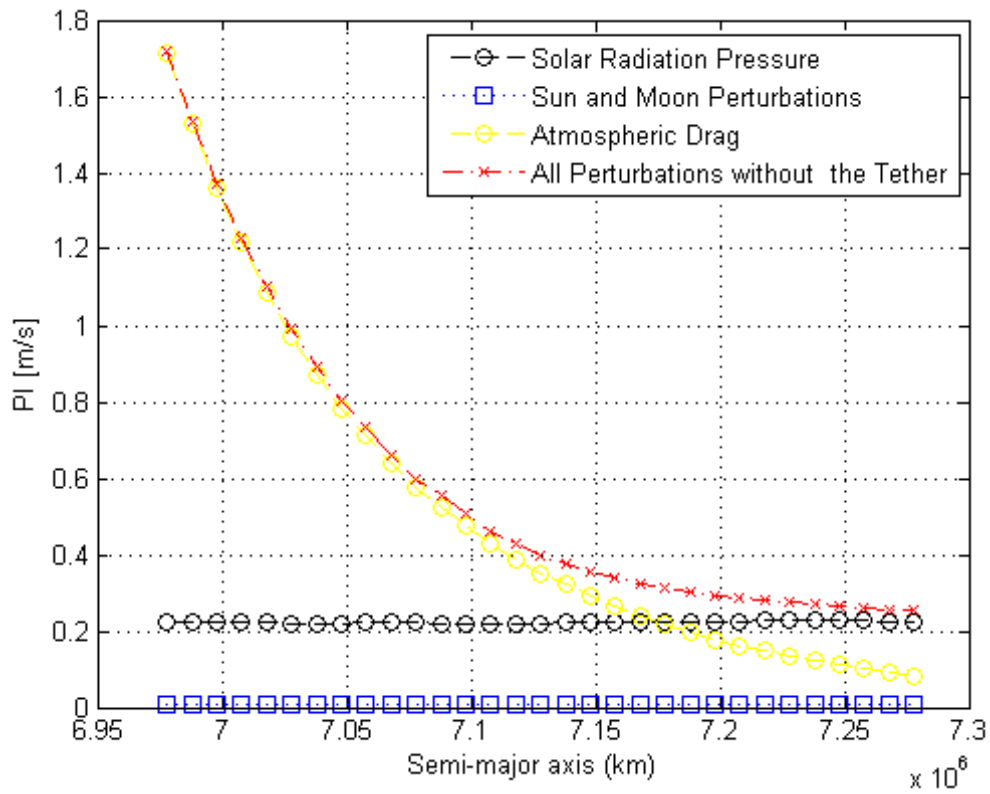
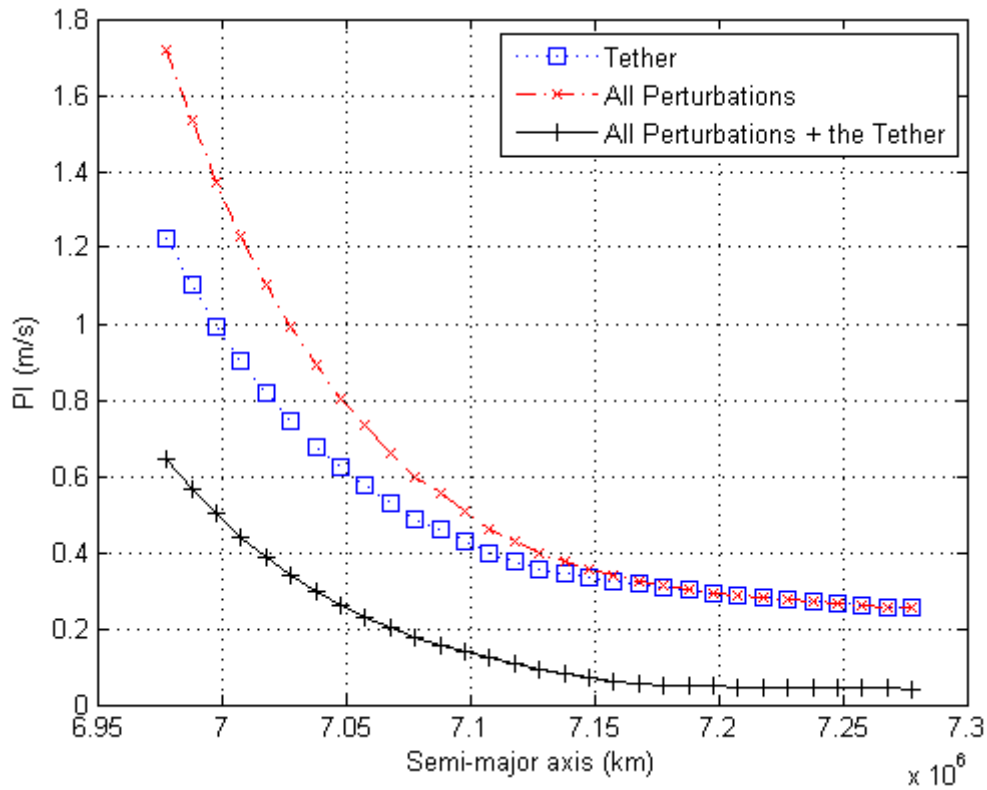


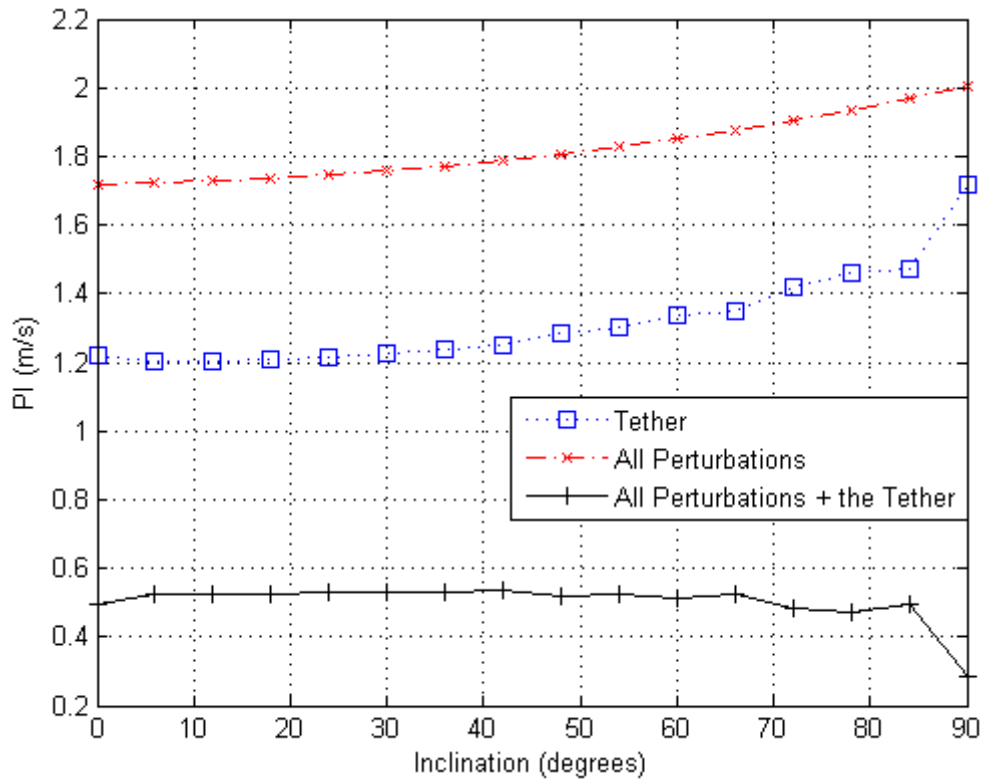
Figure 3.88 – PI for several disturbing forces and the tether as a function of the semi-major axis from 6978 to 7278 km.



The tether can reduce better the disturbing forces effects when the semi-major axis increases, because there are fewer passages by the umbra region, so the spacecraft has more electron density to reduce the disturbing forces effects.

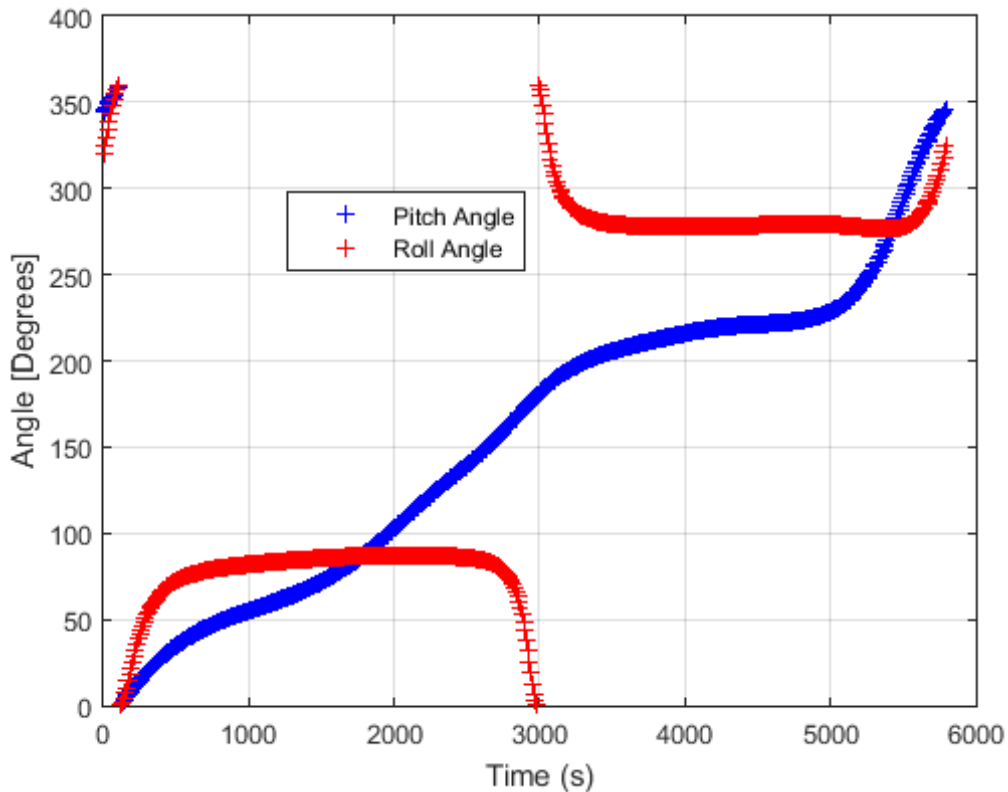
The next simulation shows the study of the PI as a function of the inclination of the orbit. When the inclination of the orbit increases, the induced EMF decreases. The power used to drive a current on the opposite direction of the induced EMF decreases. Figure 3.89 shows a simulation with the initial parameters given in Tables 3.10 to 3.13 , except for the orbit inclination, which in this case varies from 0 to 90 degrees.

Figure 3.89 – PI for the disturbing forces and tether as a function of the inclination from 0 to 90 degrees.



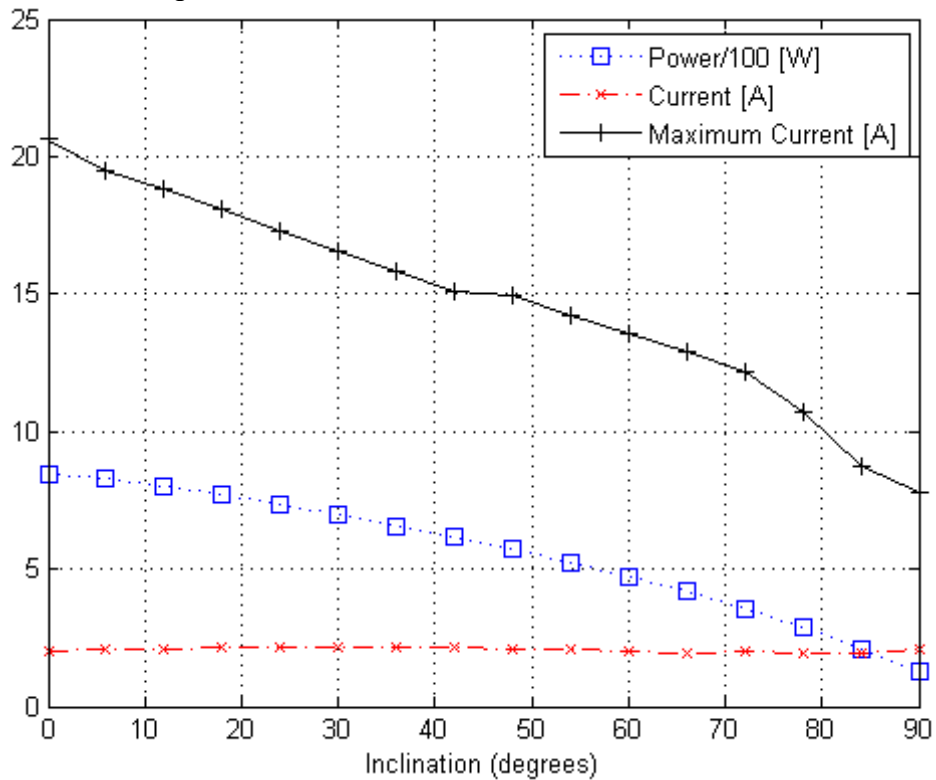
The magnitude of the force due to the tether increases when the inclination increases. The induced EMF decreases when the inclination of the orbit increases. Therefore, there is less power that the battery must provide to overcome the EMF. Nevertheless, although the tether works as an efficient way to reduce the disturbing forces effects, the roll attitude at the orbital inclination of 90 degrees varies from 0 to 90 and from 270 to 360 degrees along one orbital period and the pitch angles varies from 0 to 360 degrees. This occurs due to the geometry of the magnetic field. Although it seems promising the application of this method for highly inclined orbits, the pitch angle variation demands more challenges from the attitude control. Figure 3.90 shows the pitch and roll angles for the simulation with 90 degrees of inclination.

Figure 3.90 – Pitch and roll angles for one orbital period.



The pitch angle varies from 0 to 360 degrees. It means that the direction of the current changes. This change occurs with the signal change of the EMF as well. This means that, even if the current changes the direction, the battery still has to provide power to overcome the EMF. In this case, it is assumed that the current can flow in both directions of the tether and that both end masses can emit electrons. The drastically change of the pitch angle is related to the direction of the magnetic field at the poles of the Earth. At the poles, the direction of the magnetic field becomes radial and this fact results in a change of the tether direction from mainly radial to the direction of the orbital velocity, to guarantee that the tether can reduce the disturbing forces effects, mainly the atmospheric drag. Figure 3.91 shows the power that the battery must provide or the induced EMF and the current to perform the maneuver for different orbital inclinations.

Figure 3.91 – Current and power of the tether as a function of the inclination from 0 to 90 degrees.

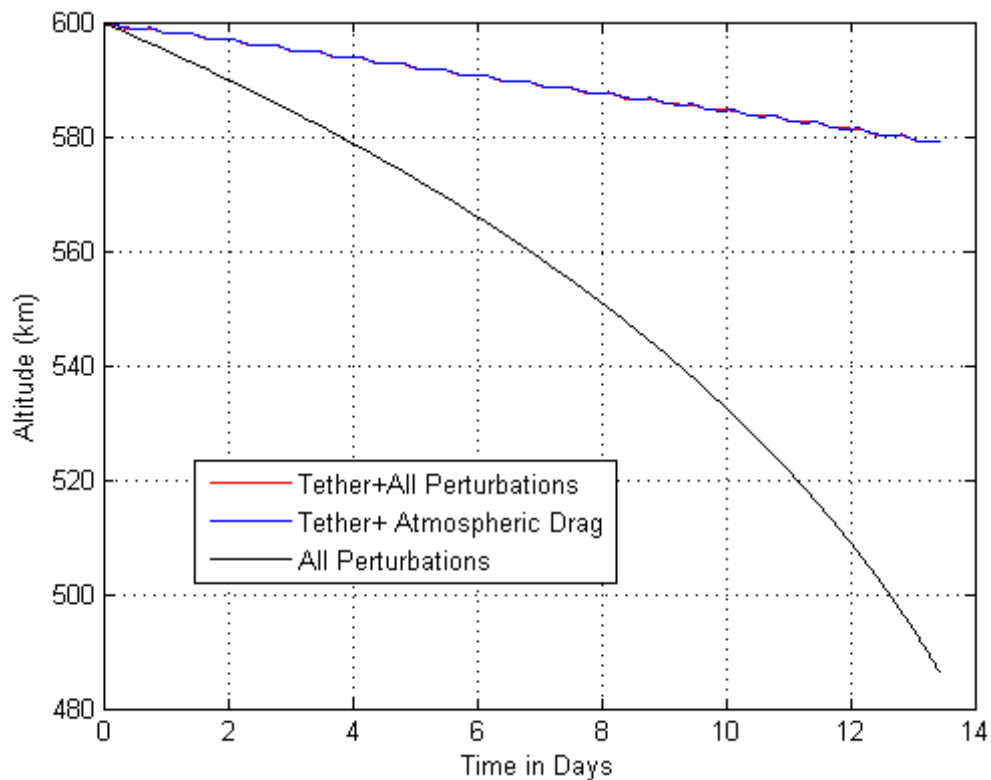


The current required for the station-keeping maneuver is almost constant, although the power required from the battery decreases when the inclination increases. The maximum current decreases, as well as the inverse EMF and the motional electric field decreases (see Equations 2.34, 2.39 and 2.41).

### 3.4.2. The Orbital Propagator Results

This section simulates the spacecraft trajectory with an orbit integrator. The initial parameters of the simulation are given in Tables 3.10 to 3.13 . Figure 3.92 shows three trajectories: i) considering only the external perturbations (no tether), ii) considering the external perturbations and the tether to reduce only the atmospheric drag effect; iii) considering the external perturbations and the tether to reduce all the perturbations effects. The integration is performed for 13.5 days (20 orbital periods of the nominal orbit).

Figure 3.92 – Altitude decay in days due to the disturbing forces with and without the tether control.



It is clear that the tether reduces the deviations caused by the atmospheric drag. The decay of the orbit using the tether is much smaller for the same integration time. The situation where the tether is used to control the atmospheric drag and all the disturbing forces provides almost the same results. This occurs because the atmospheric drag is the main perturbing force in this trajectory.

Let's estimate in a fast and easy way how much fuel consumption the EDT can save based on Figure 3.92. Let's suppose that after the approximately 14 days, the final orbit is a circular one with the altitude decayed. Then a Hohmann transfer is computed based on the circular initial orbit with altitude of 600 km. The final orbits are, therefore, a circular one with altitude of 580 km and another one with 485 km. The  $\Delta v$  required to increase the altitude of the orbit would be 0.4426 km/s for the initial altitude orbit of 580 km and 3.0328 km/s for the initial altitude orbit of 485 km.

The estimative of the fuel consumption can be obtained as

$$\Delta m = m_0(1 - e^{-\Delta v / I_{sp} g_0}) \quad (3.18)$$

where  $\Delta m$  is the amount of propellant expended to produce the velocity increment  $\Delta v$ ,  $m_0$  is the initial mass of the system,  $I_{sp}$  is the specific impulse of the system and  $g_0$  is  $9.81 \text{ m/s}^2$ .

Then, if we consider that the propulsion system has a specific impulse of 200 s, then the fuel consumption would be 0.1622 kg for the inner orbit and 0.0237 for the orbit with altitude of 580 km.

If the propulsion system is more efficient, around 1000 s, then the consumption would be 0.0325 and 0.0047 kg.

This fast calculation demonstrates that the EDT can be used to reduce the atmospheric drag decay and lower the fuel-consumption in orbital maneuvers that has a drag-free control.

## 4 CONCLUSION

The perturbation integrals showed to be an effective method to evaluate the magnitude of the disturbing forces. The maps based on the PI as a function of the Keplerian elements are important to study the pattern of the disturbing forces and to search for the best orbits in the sense of receiving less perturbation.

It has been proved that the PI is also capable of analyzing the efficiency of an electrodynamic tether or a solar sail, if they are used to reduce the effects coming from the disturbing forces or to de-orbit the spacecraft.

The solar sail used to reduce the disturbing forces have been proven to be efficient. The magnitude reduction of the disturbing forces varied from 30% to 70% in some cases. There are many factors that influence the efficiency of the solar sails, like the passages through the umbra region, the magnitude of the disturbing forces and the area of the solar sail.

The EDT could reduce the magnitude of the disturbing forces, especially the atmospheric drag, up to 80% in some cases. The efficiency of the EDT tether depends also of many factors, such as the magnitude of the disturbing forces, the maximum current of the tether, the magnetic field of the earth, the number and duration of the passages through the umbra region, and so on.

The PI could be used to estimate the efficiency of these two free-fuel thrusters easily and map many orbits as a function of their Keplerian elements.

The estimation of the orbital decay based on the PI was proven to be close to the values obtained from the numerical integrations. The estimation of the orbital decay based on the PI has the great advantage of computing an estimate time of the orbital decay with no numerical integration, just by analyzing the PI as a function of the semi-major axis. The error obtained was smaller than 10% when compared to the results coming from the orbit

integrator. The estimation of the time of the orbital decay is based on the atmospheric drag effect with or without the EDT. The estimative of the orbital decay of eccentric orbits were also included.

The spacecraft trajectory simulator enables to make a study related to the solar sail in a complex and more realistic environment. The parameters of the propulsion system allow the possibility to include errors that the sensors or the propulsion systems may have. This work included, in the STRS, the solar sail subsystem that can be used now in the simulator. The results shown in this thesis proves that the solar sail subsystem works well. The STRS user can now study many solar sail maneuvers with different parameters for several missions. The PHALL2, a Brazilian electric propulsion system, was included in some STRS results and the magnitude of this thruster was able to eliminate the disturbing forces effects with the solar sail use. The reduction of the fuel consumption based on the STRS results can achieve up to 30%.

The electrodynamic tether, whether used to de-orbit or to reduce the effects of the disturbing forces, is a powerful idea that can save fuel in orbital maneuvers and also help the control of the space debris (if used as a drag). The electrodynamic tether is still a non-practical and highly-costly system nowadays. But, as the technology develops, the EDT can be used as an efficient system that may save fuel and investments in futures missions.

The solar sail idea is the same. In the future, the solar sail can be used to reduce and control viably the disturbing forces with no fuel consumption.

The use of the EDT to reduce the disturbing forces have been proved to be efficient as the orbital decay of the system were lower and the estimative of the fuel consumption to regain attitude was optimistic for future drag-free missions.

## REFERENCES

ANDERSON, J.; ARNOLD, D.; COLOMBO, G.; GROSSI, M.; KIRSHNER, L. Orbiting tether's electrodynamic interactions. **American Geophysical Union**, v. 13, n.3, p. 417- 424, 1979. 19

ANDERSON, J. D. **Fundamentals of Aerodynamics**. 3. ed. New York: McGraw Hill, 2001. 892 p. ISBN 0-07-237335-0. 36

ARNOLD, D. A.; GROSSI, M. D. Natural damping in the electro-dynamic tether. **Smithsonian Astrophysical Observatory**, p. 1 - 47, 1983. 19

ASLANOV, V. S.; LEDKOV, A. S. **Dynamics of tethered satellite system**. 1. ed. Woodhead Publishing, 2012. 331 p. ISBN: 978-0-85709-156-7. 15, 15, 16, 16, 17, 17

BATTEN, S.; FULLER-ROWELL, T. J.; REES, D. A numerical data base for VAX and personal computers for storage, reconstruction, and display of global thermospheric and ionospheric models, **Planet. Space Sci.** v. 35, n. 9, p. 1167, 1987. 47

BAKER, R. M. L. **Astrodynamics, applications and advanced topics**. 1. ed. New York :Academic Press, 1967. 540 p. ISBN 10- 0120756560. 25

BORGRAAFE, A.; HEILIGERS, J.; CERIOTTI, M.; MCINNES, C. Optical control of solar sails using distributed reflectivity. In: SPACECRAFT STRUCTURES CONFERENCE, 2014, National Harbor, Maryland. **Proceedings...** Reston, VA: AIAA, 2014. p. 13-17. DOI: 10.2514/6.2014-0833,13-17. 36

CAPÓ-LUGO, P. A.; BAINUN, P. M. **Orbital mechanics and formation flying: a digital control approach**, 1. Cambridge: Woodhead Publishing, 2011, 414 p. ISBN: 978-0-85709-054-6. 33,36,37, 100

CARROLL, K.A. Economical planetary space science using small solar sail propelled spacecraft. In: **New directions in a global environment** :

proceedings of the 10th conference on astronautics. Ottawa: Canadian Aeronautics and Space Institute, 1998. 12

CARVALHO, J. P. S.; MORAES, V.; PRADO, A. F. B. A. Searching less perturbed circular orbits for a spacecraft travelling around Europa. **Mathematical Problems in Engineering**, v. 2014, ID 529716, p. 1-10, 2014. doi:10.1155/2014/529716. 6

CHOBOTOV, V. A. Orbital mechanics. Washington, DC: AIAA, 1991. 447p. ISBN 978-1563475375. AIAA Education Series. 25, 25

COSMO, M. L.; LORENZINI, E. C. **Tethers in space handbook**. 3. ed. Cambridge: Smithsonian Astrophysical Observatory, 1997, 241 p. 15, 16, 18, 18, 18, 18, 19, 19, 25, 25, 25, 26, 26, 62, 147

COMMITTEE ON EXTENSION TO THE STANDARD ATMOSPHERE (COESA), **U.S. standard atmosphere 1962**. Washington, DC: U.S. Government Printing Office, 1962. 49

COMMITTEE ON EXTENSION TO THE STANDARD ATMOSPHERE (COESA), **U.S. standard atmosphere 1976**. Washington, DC: U.S. Government Printing Office, 1976. 49

DAVIS, J. **Mathematical modeling of earth's magnetic field**. Blacksburg, VA: Virginia Tech., 2004. 21 p. 55, 56, 56, 56, 57

EDWARDS, B. C. The space elevator development program. In: INTERNATIONAL ASTRONAUTICAL CONGRESS, 55., 2004, Vancouver. **Proceedings...** Vancouver: IAA, 2004. p. 1-9, IAC-04-IAA.3.8.2.01. 15

EISNER, A.; YIONOULIS S. M., NOVA-1 - The 'drag-free' navigation satellite. In: NATIONAL AEROSPACE METING, 1982, Moffett Field, CA. **Proceedings...** Washington, DC: Institute of Navigation, 1982. p. 26-31. (A83-28776 11-04). 167

ESTES, R. D.; SANMARTIN, J. R.; MARTINEZ- SANCHEZ, M. **Technology of bare tether current collection**. In: TETHER TECHNOLOGY INTERCHANGE MEETING, 1997, Huntsville. Proceedings... Huntsville: NASA Marshall Space Flight Center, 1997. p. 1 -20. 26, 26, 57, 59, 61, 61, 62, 132

FERREIRA, J. L.; MARTINS A. A.; MIRANDA R.; SCHELLING A.; ALVES L. S.; COSTA, E. Permanent magnet Hall Thruster development and applications on future Brazilian space missions. **Journal of Physics Conference Series**, v. 641, n. 1, p. 012016, 2016. DOI: 10.1088/1742-6596/641/1/012016. 23, 121

FIESELER, P. D. A method for solar sailing in a low earth orbit. **Acta Astronautica**, v. 43, n. 9-10,p. 531-541, 1998. 36

FIMPLE, W.R. Generalized three-dimensional trajectory analysis of planetary escape by solar sail. **American Rocket Society Journal**, n. 32, p. 883-887, 1962. 11

FORWARD, R. L; HOYT, R. P. AND UPHOFF, C. **The terminator tether™**: a low-mass system for end-of-life deorbit of LED spacecraft. In: TETHER TECHNICAL INTERCHANGE MEETING, 1997, Huntsville. **Proceedings...** Huntsville: NASA Marshall Space Flight Center, 1997. 15, 26, 26, 133

FORWARD, R. L. Statite: a spacecraft that does not orbit. **Journal of Spacecraft and Rockets**, n. 28, v. 5, p. 606-611, 1991. 11

GARWIN, R.L. Solar sailing - a practical method of propulsion within the solar system. **Jet Propulsion**, n. 28, p. 188-190, 1958. 10, 10

GONÇALVES, L. D.; ROCCO, E. M.; MORAES, R. V. Analysis of the influence of orbital disturbances applied to an artificial lunar satellite. **Journal of Physics: Conference Series**, 2015a. To be Published. 24

GONÇALVES, L. D.; ROCCO, E. M.; MORAES, R. V. Evaluation of a spacecraft trajectory deviation due to the lunar albedo. In: INTERNATIONAL

CONGRESS OF MECHANICAL ENGINEERING, 22., 2013, Ribeirão Preto.  
**Proceedings...** Rio de Janeiro: ABCM, 2013b. ISSN 2176-5480. 23

GONÇALVES, L. D.; ROCCO, E. M.; MORAES, R. V. Evaluation of the uncertainty in the trajectory simulations of a lunar satellite due to the adopted model for the lunar gravitational field. **Journal of Physics: Conference Series**, 2015b. To be Published. 24

GONÇALVES, L. D.; ROCCO, E. M.; MORAES, R. V. Orbital disturbance analysis due to the lunar gravitational potential and deviation minimization through the trajectory control in closed loop. **Journal of Physics: Conference Series**, v. 465, n. 1, p. Article number 012013, 2013a. doi:<10.1088/1742-6596/465/1/012013>. 23

GROSSI M. D. **On the feasibility of electric power generation and electromagnetic wave injection by electrodynamic tethers**. Smithsonian Astrophysical Observatory, 1983. (Tech. Note TP 83-003). 19

HACKER B. C.; GRIMWOOD J. M. On the shoulders of Titan: a history of project Gemini. **NASA Special Publication**, n. 4203 in the NASA History Series, 1977. 16

HEDIN, A. E. Extension of the MSIS thermospheric model into the middle and lower atmosphere. **J. Geophys. Res.** v. 96, n. A2, p. 1159-1172, 1991. 47

HUGHES, P. C. **Spacecraft attitude dynamics**. 1. ed. New York: Dover Publications, 1986. 570 p. ISBN 978-0486439259. 25

12th generation international geomagnetic reference field Schmidt semi-normalized spherical harmonic coefficients, degree  $n=1,13$ . IAGA Division V-MOD Geomagnetic Field Modeling. Available at:<  
<http://www.ngdc.noaa.gov/IAGA/vmod/igrf12coeffs.txt> >. Accessed in: 02 mar. 2014. 56

JACCHIA L. G. **Revised static models of the thermosphere and exosphere with empirical temperature profiles**. *Smithson. Astrophys. Obs.*, 1971. Spec. Rept. No. 332. 47

JACCHIA L. G. Static diffusion models of the upper atmosphere with empirical temperature profiles. **Smithsonian Contributions to Astrophysics**, v. 8, p. 215-257 1964. 47

JACCHIA, L. G. **Thermospheric temperature, density and composition: new models**. Smithsonian Astrophysical Observatory, Cambridge, p. 1–106, 1977. Special Report 375. 25, 25, 47

**JAPAN AEROSPACE EXPLORATION AGENCY**. Ongoing Missions –

IKAROS. Available from:

<<http://www.isas.jaxa.jp/e/enterp/missions/ikaros/index.shtml>>. Accessed on: September 30th, 2015. 13

JIN, Z.; TIANSHU, W.; SHENGPING, G. Influence of attitude control on transfer mission for a flexible solar sail. **Acta Astronautica**, v. 97, p.73-91. doi:10.1016/j.actaastro.2013.12.018. 13

JOHNSON, L.; HERRMANN, M. **International Space Station electrodynamic tether Reboost study**. Huntsville: Marshall Space Flight Center, 1998. p. 1 – 42. NASA TM—1998-208538. 26, 26, 59, 132

KAPLAN, M. H. **Modern spacecraft dynamics and control**. 1. ed. New York: John Wiley and Sons, 1976. 427 p. ISBN 978-0471457039. 25

KOESTLER, A. **The sleepwalkers: a history of man's changing vision of the universe**. 1. London: MacMillan, 1986. p. 623. 8

KRISTIN L. M. **A nonlinear magnetic controller for three-axis stability of nanosatellites**. 126 f. Master's thesis. Faculty of the Virginia Polytechnic Institute and State University, Blacksburg, Virginia, 2001.56, 56

KUGA, H. K.; CARRARA, V.; RAO, K. R. **Satélites artificiais** - movimento orbital. São José dos Campos: INPE, 2011. 103 p. (sid.inpe.br/mtc-m19/2011/11.22.18.25-PUD). Disponível em: <<http://urlib.net/8JMKD3MGP7W/3ARJ3NH>>. Acesso em: 27 nov. 2015. 41, 42, 42, 43, 43, 50, 50, 100

KUMAR, K. D.; BANG, H. C.; TAHK, M. J. Formation flying using solar radiation pressure, ISTS 2004-d-25. In: INTERNATIONAL SYMPOSIUM ON SPACE TECHNOLOGY AND SCIENCE, 24., 2004, Miyazaki, Japan, May 30- June 6. **Proceedings...**Miyazaki: ISTS Secretariat, 2004. 36

LANGE, B. The drag free satellite. **AIAA Journal**, v. 2, n. 9. p. 1590-1606, Sept. 1964. 167

LANOIX, E. L. M. **A mathematical model for the long-term dynamics of tethered spacecraft**. f. 130, Doctoral thesis, department of mechanical engineering, McGill University, Montreal, June 1999. 19, 26, 51, 52, 53, 54, 57, 58, 58, 58, 58, 59, 59, 60, 60, 62, 62, 62

LARA, M. Equivalent delta-v per orbit of gravitational perturbations. **Journal of guidance, control and dynamics**, 2016. To be published. 8

LE FAURE, G.; DE GRAFFIGNY, H. **Aventures extraordinaires d'un savant russe**. Paris: Les editions Fayard, 1889. 537p. 9

LEBEDEW, P. Untersuchungen über die Druckkräfte des Lichtes. **Annalen der Physik**, v. 311, n.11, p. 443-458, 1901. 9

LIU, J.; RONG, S.; SHEN, F.; CUI, N. N. Dynamics and control of a flexible solar sail. **Mathematical Problems in Engineering**, v. 2014, p. 1-25, 2014. doi:10.1155/2014/868419. 12

LONDON, H.S. Some exact solutions of the equations of motion of a solar sail with a constant setting. **American Rocket Society Journal**, n. 30, p. 198-200, 1960. 11

LONGO, C. R. O.; RICKMAN, S. L. **Method for the calculation of the spacecraft umbra and penumbra shadow terminator points**. Houston, TX: NASA, 1995. NASA Technical Paper, n. 3547. 37, 38, 38

LORENZINI, E. C.; ESTES, R. D.; COSMO, M. C. **Electrodynamic tethers for the International Space Station, In-Space Transportation with Tethers**. Cambridge, MA: Smithsonian Astrophysical Observatory, 1997. p. 1-23. Annual Report for NASA Grant NAG9-1303. 26, 26, 132

MACCONE, C. Space missions outside the solar system to exploit the gravitational lens of the sun. **Journal of the British Interplanetary Society**, n. 47, p. 45-52, 1994. 12

MARCELINO, E. W. **Controle de trajetória orbital em manobras de empuxo contínuo de longo prazo**. 2009. 186 p. (INPE-15757-TDI/1500). Dissertação (Mestrado em Mecânica Espacial e Controle) - Instituto Nacional de Pesquisas Espaciais, São José dos Campos, 2009. Disponível em: <<http://urlib.net/8JMKD3MGP8W/35CFG4P>>. Acesso em: 04 nov. 2015. 21

MAXWELL, J. C. **A Treatise on Electricity and Magnetism**. 1. ed. London: MacMillan, 1873, p. 504. 9

MCINNES, C. R. **Solar sailing: technology, dynamics and mission applications**. 1. ed. New York: Springer, 2004, p. 296. ISBN 3-540-21062-8. 9, 9, 9

MCINNES, C. R. et al. Solar sail parking in restricted three-body systems. **Journal of Guidance Dynamics and Control**, n. 17, v. 2, p. 399-406, 1994. 12

NATIONAL AERONAUTICS AND SPACE ADMINISTRATION. **Small Satellite Missions**. 2012. Available from:

<[http://www.nasa.gov/mission\\_pages/smallsats/nanosaild.html](http://www.nasa.gov/mission_pages/smallsats/nanosaild.html)>. Accessed on: September 30th, 2015. 14

OLIVEIRA, T. C.; PRADO, A. F. B. A. Evaluating orbits with potential to use solar sail for station-keeping maneuvers. In: IAA CONFERENCE ON DYNAMICS & CONTROL OF SPACE SYSTEMS, 2. (DYCOSS)., 2014, Roma. **Proceedings...**, 2014b. p. 20. Disponível em:<<http://www.dycoSS.com/program/final/IAA-AAS-DyCoSS2-14-16-03.pdf>>. Acesso em: 26 abr. 2016. 7, 12, 28, 39, 40

OLIVEIRA, T. C.; PRADO, A. F. B. A.; MISRA, A. K. Determining orbits that can be controlled by natural forces. **Advances in the Astronautical Sciences**, v. 152, p. 3081-3100, 2014. 6, 38

OLIVEIRA, T. C.; PRADO, A. F. B. A.; MISRA, A. K. Searching for orbits that can be controlled by natural forces. **Advances in the Astronautical Sciences**, v. 150, p. 2407-2426, 2013a. 4, 7, 38,

OLIVEIRA, T. C.; PRADO, A. F. B. A. Mapping orbits with low station keeping costs for constellations of satellites based on the integral over the time of the perturbing forces. **Acta Astronautica**, v. 104, n. 1, p. 350-361, 2014a. doi:10.1016/j.actaastro.2014.06.035. 7

OLIVEIRA, T. C.; PRADO, A. F. B. A. Study of the fuel consumption for station-keeping maneuvers for GEO Satellites based on the integral of the perturbing forces over time. **Mathematical Models in Engineering and Computer Science**, v.1, p. 90-95, 2013. ISBN: 978-1-61804-194-4. 4

OLIVEIRA, T. C.; PRADO, A. F. B. A. Using electrodynamic tethers to perform station-keeping maneuvers in LEO satellites. In: INTERNATIONAL SYMPOSIUM ON SPACE FLIGHT DYNAMICS, 25., 2015. Munich, 2015. To be published. 26, 28

OLIVEIRA, T. C.; PRADO, A. F. B. A. Using radiation pressure to control orbits around a triple asteroid. In: INTERNATIONAL ASTRONAUTICAL CONGRESS, 65., 2014, Toronto, Canada. **Proceedings...** 2014c, v. 1. p. 1-10. DVD. 7, 13

OLIVEIRA, T. C.; ROCCO, E. M.; PRADO, A. F. B. A.; FERREIRA, J. L. A Study of the duration of the passage through the Van Allen Belts for a spacecraft going to the moon. **Journal of Physics: Conference Series**, v. 465, n. 1, p. Article number 012019, 2013b. doi: <10.1088/1742-6596/465/1/012019>. 23

PARKER, L. W.; MURPHY, B. L. Potential buildup on an electron-emitting satellite. **Journal of Geophysical Research**, v. 72, n. 5, p. 1631 – 1636, 1976. DOI 0.1029/JZ072i005p01631. 60

PARKS, D.; KATZ, I. Theory of plasma contactors for electrodynamic tethered satellite system, **Journal of Spacecraft and Rockets**, v. 24, n. 3, v. 8, p. 245-245, 1987. doi: 10.2514/3.25906. 17

PEARSON, J.; LEVIN E. AND CARROLL J. **Enhancing space elevator safety by active debris removal**. In: SPACE ELEVATOR CONFERENCE, 2010, Redmond. **Proceedings...** Redmond, Washington, USA: Sponsored by Microsoft Corporation, 2010. 15

PEARSON, J. **Space elevators for earth and moon**. In: INTERNATIONAL SPACE DEVELOPMENT CONFERENCE, 2007, Dallas. **Proceedings...** Dallas: NASA, 2007. 15

PLANETARY SOCIETY. Available from: <<http://sail.planetary.org/>>. Accessed on: September 30th, 2015. 14

POLYAKA, Y. N. Solar radiation pressure and the motion of earth satellites, **AIAA Journal**, v. 1, n. 12, pp. 2893-2909, 1963. 36

PRADO, A. F. B. A. Mapping orbits around the asteroid 2001SN263.

**Advances in Space Research**, v. 53, n. 5, p. 877-889, 2014.

doi:10.1016/j.asr.2013.12.034. 5

PRADO, A. F. B. A. Searching for orbits with the minimum fuel consumption for station-keeping maneuvers: application to luni-solar perturbations.

**Mathematical Problems in Engineering**, v. 2013, ID 415015, 2013, p. 1-10,

doi:10.1155/2013/415015. 2, 4, 27,29, 30, 32,32,45,45, 83

ROCCO, E.M. Analysis of the deviations of the trajectory due to the terrestrial albedo applied to some scientific missions. In: INTERNATIONAL

CONFERENCE ON MATHEMATICAL PROBLEMS IN ENGINEERING, 2008,

Genova. **Proceedings...** Genova, 2008b. 22

ROCCO, E. M. Automatic correction of orbital elements using continuous thrust

controlled in closed loop. **Journal of Physics: Conference Series**, v. 465, n. 1,

p. Article number 012007, 2013. doi: <10.1088/1742-6596/465/1/012007>. 23

ROCCO, E. M. Earth albedo evaluation and analysis of the trajectory 187

deviation for some drag-free missions. Bauru, SP, 2009. In: BRAZILIAN

CONFERENCE ON DYNAMICS, CONTROL AND APPLICATIONS, 8., 2009,

Bauru, SP. **Proceedings...** Bauru, 2009. p. 18- 22. 22, 34

ROCCO, E. M. Gravitational disturbances generated by the Sun, Phobos and

Deimos in orbital maneuvers around Mars with automatic correction of the semi-major axis. **Journal of Physics: Conference Series**, v. 641, p. 012027, 2015.

doi: <[10.1088/1742-6596/641/1/012027](https://doi.org/10.1088/1742-6596/641/1/012027)>. 24

ROCCO, E. M. **The earth albedo model**. Bremen: Center of Applied Space

Technology and Microgravity (ZARM), 2008a. 91p. 22, 22, 23

RUGGIERO, M. A. G.; LOPES, V. L. R. **Cálculo numérico**: aspectos teóricos e computacionais. 2.ed. São Paulo: Pearson Makron Books, 1996, 405 p. ISBN

85-346-0204-2. 39

SANCHEZ D. M.; PRADO, A. F. B. A.; YOKOYAMA, T. Gravitational capture and maintenance of a spacecraft around Pluto. In: AIAA/AAS ASTRODYNAMICS SPECIALIST CONFERENCE, 2014, San Diego, CA. **Proceedings...** 2014b, p. 1-12, 2014. ISBN 9781624103087. 6

SANCHEZ, D. M.; PRADO, A. F. B. A.; YOKOYAMA, T. On the effects of each term of the geopotential perturbation along the time I: quasi-circular orbits. **Advances in Space Research**, v.54, n. 6, p.1008-1018, 2014a. doi:10.1016/j.asr.2014.06.003. 5

SANDS, N. Escape from planetary gravitational fields by use of solar sails. **American Rocket Society Journal**, n. 31, p. 527-531, 1961. 11, 11

SANMARTIN, J. R.; MARTINEZ- SANCHEZ, M.; AHEDO, E. Bare wire anodes for electrodynamic tethers. **Journal of Propulsion and Power**, v. 9, p. 353-360, 1993. 57, 59, 62, 132

SANTOS, W. G. **Simulação de manobras aeroassistidas de um veículo espacial controlado por placas aerodinâmicas reguláveis e sistema propulsivo**. 2011. 272 p. (sid.inpe.br/mtc-m19/2011/01.26.16.55-TDI). Dissertação (Mestrado em Mecânica Espacial e Controle) - Instituto Nacional de Pesquisas Espaciais, São José dos Campos, 2011. 23,25,25

SANTOS, W. G.; ROCCO, E. M. Controle de Manobras de um Veículo Espacial por meio de Variações Aerodinâmicas. In: WORKSHOP EM ENGENHARIA E TECNOLOGIA ESPACIAIS, 1. (WETE)., 2010, São José dos Campos. **Anais...** São José dos Campos: INPE, 2010. v. IWETE2010-1017. DVD. ISSN 2177-3114. 23

SANTOS, W. G.; ROCCO, E. M.; CARRARA, V. Aeroassisted coplanar transfer from geostationary orbit to low earth orbit. In: WORKSHOP EM ENGENHARIA E TECNOLOGIA ESPACIAIS, 2.São José dos Campos. **Proceedings...**, São José dos Campos: INPE, 2011. DVD. ISSN 2236-2606. Disponível

em: <<http://urlib.net/J8LNKAN8RW/3BA98PL>>. Acesso em: 04 nov. 2015. doi: 10.5018/jatm.v6i2.351. 23

SIMPSON, D. G. An alternative Lunar ephemeris model for on-board flight software use. In: FLIGHT MECHANICS SYMPOSIUM, 1999, Greenbelt. **Proceedings...** Greenbelt, MD: NASA GSFC, 1999. p. 175-184. 33

SUNJAMMER. Available from: <<http://www.sunjammermission.com/AboutSunjammer>>. Accessed on: September 30th, 2015. 14

SVITEK, T. ET AL. Solar sail concept study. In: INTERNATIONAL ASTRONAUTICAL CONGRESS, 33., 1982, Paris. **Proceedings...** IAF-ST-82-12. 11

TAMBURRO, M. B.; ABBOTT, A. S.; TOWNSEND, G. E. **Coordinate systems and time measure**, Vo. 1, Guidance, flight mechanics and trajectory optimization, National Aeronautics and Space Administration, p. 105, 1968. 33

TEWARI, A. **Atmospheric and space flight dynamics**: modeling and simulation with MATBAL and simulink. 1. ed. Boston: Birkhauser, 2007. 556 p. ISBN-10: 0-8176-4373-7. 37, 43, 43, 43, 45, 45, 46, 46, 49, 49, 50, 50

THOMPSON, D.C.; BONIFAZI, C.; GILCHRIST, B.E.; WILLIAMS, S.D.; RAITT, W.J.; LEBRETON, J.-P.; BURKE. **The current-voltage characteristics of a large probe in low ear1h orbit**: TSS-1R results, <http://setswww.sprt.umich.edu/sets/publicpapers/publications/grl97/IV-characteristics/IV-char.html>, 1997. 60

TORCZYNSKI, D. M.; AMINI, R.; MASSIONI, P. Magnetorquer based attitude control for a nanosatellite testplatform, **AIAA Infotech@Aerospace 2010**, AIAA 2010-3511, Atlanta, p. 1-9, 2010. DOI: 10.2514/6.2010-3511. 26

TSANDER, F. A. Perelet na drugie planetc, **Tekhnika i zhzn**, n. 13, 1924. 9

- TSIOLKOVSKY, K. E. **Extension of man into outer space**, n. 2, United Scientific Technical Presses, 1936 (1921). 9
- TSIOLKOVSKY, K. E. **Speculations between earth and sky, and on Vesta**. Izd-vo AN SSR, Moscow, 1959 (reprint), p. 35. 15, 15
- TSU, T.C. Interplanetary travel by solar sail. **ARS Journal**, v. 29, p. 442-447, 1959. 10, 11
- VAILLON, L. J.; BORDE, T. D.; DAMILANO, P. Drag-free control systems and technologies. **Space Technology**, v. 16, n. 5/6, p. 245-254, 1990. 167
- VENDITTI, F. C. F.; PRADO, A. F. B. A. Mapping Orbits regarding Perturbations due to the Gravitational Field of a Cube. **Mathematical Problems in Engineering**, v. 2015, ID 493903, p. 1-11, 2015. doi:10.1155/2015/493903. 7
- VENDITTI, F. C. F.; ROCCO, E. M.; PRADO, A. F. B. A. Trajectory control around non-spherical bodies modelled by parallelepipeds. **Journal of Physics: Conference Series**, v. 465, n. 1, p. Article number 012008, 2013. doi: <10.1088/1742-6596/465/1/012008>. 23
- VISAGIE, L., LAPPAS, V., ERB, S. Drag sails for space debris mitigation. **Acta Astronautica**, v. 109, 2015, p.65-77. doi:10.1016/j.actaastro.2014.12.013. 13
- TIESENHAUSEN, G. v. **The roles of tethers on space station**. Huntsville: Marshall Space Flight Center, 1985. p. 1-154. NASA, TM-86519. 16
- WARNOCK, T. W. AND COCHRAN, J. E. Predicting the orbital lifetime of tethered satellite systems, **Acta Astronautica**, v. 35, n. 213, p. 193-203, 1995. doi:10.1016/0094-5765(94)00265-N. 25, 25
- WILBUR P. J.; LAUPA, T. G. Plasma contactor design for electrodynamic tether applications. **Advances in Space Research**, v. 8, n.1, p. 1-19, 1988. doi:10.1016/0273-1177(88)90366-3. 17

WILEY, C. [pseudonym SANDERS, R.], Clipper ships of space, **Astounding Science Fiction**, p. 135, 1951. 10

WILLIAMS, P.; HYSLOP, A.; STELZER, M.; KRUIJFF, M. YES2 Optimal trajectories in presence of eccentricity and aerodynamic drag. **Acta Astronautica**, n. 64, v. 7-8, p. 745-769, 2009. 17

WILLIAMS, T. AND WANG, Z. S. Potential Uses of Solar Radiation Pressure in Satellite Formation Flying, In: AAS/AIAA SPACEFLIGHT MECHANICS MEETING, 2000, Clearwater, Florida. **Proceedings...** Clearwater: AAS, 2000. P. 1599-1611. AAS 00-204.36

WRIGHT, J.L.; WARMKE, J.M. Solar sail mission applications. In: AIAA-AAS ASTRODYNAMICS CONFERENCE, 1976, San Diego. **Proceedings...** San Diego: AIAA, 1976. AIAA-76-808. doi: 10.2514/6.1976-808. 11

ZANARDI, M. C.; ASSIS, S. C.; QUIRELLI, I. M. P.; KUGA, H. K. **Influência do torque residual na deriva do eixo de rotação de satélites artificiais em órbitas circulares.** In: Congresso Nacional de Matemática Aplicada e Computacional, 27., 2004, Porto Alegre. **Anais...** Porto Alegre: PUC, 2004. 26

ZENG, X.; GONG, S.; LI, J. Fast solar sail rendezvous mission to near Earth asteroids. **Acta Astronautica**, v. 105, n.1, 2014, p. 40-56. doi:10.1016/j.actaastro.2014.08.023. 13